

**INVESTIGATION ON LOCAL STRUCTURES OF  
DILUTE MAGNETIC SEMICONDUCTOR THIN  
FILMS BY FLUORESCENCE BASED EXAFS  
MEASUREMENTS**

*By*

**ASHOK KUMAR YADAV**

**PHYS01201304026**

**Bhabha Atomic Research Centre**

*A thesis submitted to the  
Board of Studies in Physical Sciences  
In partial fulfillment of requirements  
for the Degree of*

**DOCTOR OF PHILOSOPHY**

*of*

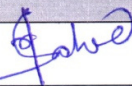
**HOMI BHABHA NATIONAL INSTITUTE**



**September, 2018**

**HOMI BHABHA NATIONAL INSTITUTE**  
**Recommendations of the Viva Voce Committee**

As members of the Viva Voce Committee, we certify that we have read the dissertation prepared by Shri A.K. Yadav entitled “**Investigation on local structures of dilute magnetic semiconductor thin films by Fluorescence based EXAFS measurements**” and recommend that it may be accepted as fulfilling the thesis requirement for the award of Degree of Doctor of Philosophy.

Sr.No.	Name	Designation	Signature	Date
1.	Dr. N.K. Sahoo	Chairman		29/8/2018
2.	Dr. D. Bhattacharyya	Guide & Convener		29/8/18
3.	Dr. Harish C. Barshilia	Examiner		29/08/2018
4.	Dr. A. Das	Member		29.8.18
5.	Dr. M. K. Chattopadhyay	Member		29/08/2018

Final approval and acceptance of this thesis is contingent upon the candidate's submission of the final copies of the thesis to HBNI.

I hereby certify that I have read this thesis prepared under my direction and recommend that it may be accepted as fulfilling the thesis requirement.

Date: 29/08/18  
Place: Mumbai

  
Dr. Dibyendu Bhattacharyya  
(Guide)

## **STATEMENT BY AUTHOR**

This dissertation has been submitted in partial fulfillment of requirements for an advanced degree at Homi Bhabha National Institute (HBNI) and is deposited in the Library to be made available to borrowers under rules of the HBNI.

Brief quotations from this dissertation are allowable without special permission, provided that accurate acknowledgement of source is made. Requests for permission for extended quotation from or reproduction of this manuscript in whole or in part may be granted by the Competent Authority of HBNI when in his or her judgment the proposed use of the material is in the interests of scholarship. In all other instances, however, permission must be obtained from the author.

ASHOK KUMAR YADAV

## **DECLARATION**

I, hereby declare that the investigation presented in the thesis has been carried out by me. The work is original and has not been submitted earlier as a whole or in part for a degree / diploma at this or any other Institution / University.

ASHOK KUMAR YADAV

## List of Publications arising from the thesis

### Journals:

1. "X-ray absorption spectroscopy of Mn doped ZnO thin films prepared by rf sputtering technique", Ashok Kumar Yadav, Sk Maidul Haque, Dinesh Shukla, Ram Janay Choudhary, S.N. Jha and D.Bhattacharyya, *AIP Advances*, **2015**,5, 117138.
2. "Investigation of Fe doped ZnO thin films by X-ray absorption spectroscopy", Ashok Kumar Yadav, Sk Maidul Haque, Shilpa Tripathi, Dinesh Shukla, Md. A. Ahmed, D. M. Phase, S. Bandyopadhyay, S.N. Jha and D. Bhattacharyya, *RSC Adv.*, **2016**, 6, 74982-74990.
3. "Local structure studies of Ni doped ZnO/PVDF composite free-standing flexible thin films using XPS and EXAFS studies", Ashok Kumar Yadav, Rajkumar Dey, Ritamay Bhunia, Shamima Hussain, Shambhu Nath Jha, Dibyendu Bhattacharyya, Radhaballav Bhar, and Arun Kumar Pal, *J. Poly. Res.*, **2016**, 23, 265.
4. "Probing Local structure of Co doped Polyvinylidene fluoride (PVDF)-ZnO thin films using X-ray Absorption Spectroscopy", Rajkumar Dey, Ashok Kumar Yadav, Ritamay Bhunia, Shambhu Nath Jha, Dibyendu Bhattacharyya, Shamima Hussain, Radhaballav Bhar and Arun Kumar Pal, *Spectrochimica Acta Part B: Atomic Spectroscopy*, **2017**, 131, 115-123.
5. "Local structure investigation of Ni doped ZnO thin films by X-ray absorption spectroscopy", A. K. Yadav, S M Haque, Rajnarayan De, N Pathak, D K Shukla, R J Choudhary, D M Phase, S N Jha, Dibyendu Bhattacharyya, *Thin Solid Films*, **2018**, 647, 70-79.
6. "Local Structure Investigation of Mn And Co Doped TiO<sub>2</sub> Thin Films by X-Ray Absorption Spectroscopy", Ashok Kumar Yadav, Sk Maidul Haque, Rajnarayan De, Md Azaharuddin Ahmed, Velaga Srihari, Mukul Gupta, Deodatta M. Phase, Sudipta Bandyopadhyay, Shambu Nath Jha and Dibyendu Bhattacharyya, *Chem. Select.*, **2017**, 2, 11012-11024.
7. "Probing local structures in (Ni/Co) co-doped ZnO/PVDF composite flexible and free standing films by using XAS and XPS studies", Ashok Kumar Yadav, Rajkumar Dey, Shambhu Nath Jha, Dibyendu Bhattacharyya, Shamima Hussain, Radhaballav Bhar and Arun Kumar Pal, X-ray spectrometry (2018) (in press).

### Conference publications

1. "X-ray absorption spectroscopy of Mn doped ZnO thin films prepared by rf sputtering technique", A.K. Yadav, S. M. Haque, Sanjay Rai, S.N. Jha and D.Bhattacharyya XAFS-16, 23-28 August **2015**, Karlshure, Germany.

2. "X-ray absorption spectroscopy of Co doped ZnO thin films prepared by rf sputtering technique", Ashok Kumar Yadav, Sk Maidul Haque, Dinesh Kumar Shukla, S.N. Jha and D.Bhattacharyya, *AIP Conf. Proc.* 1731 (2015) 060008-1–060008-3.
3. "Local structure investigation on Mn and Co doped TiO<sub>2</sub> thin films by X-ray absorption spectroscopy", A. K. Yadav, S. M. Haque, R. De, Md. A. Ahmed, V. Srihari, M. Gupta, D. M. Phase, S. Bandyopadhyay, S.N. Jha and D.Bhattacharyya, *AIP Conference Proceedings* 1942, 080012 (2018).

ASHOK KUMAR YADAV

*Dedicated*

*To*

*My Parents and My wife*

## ACKNOWLEDGEMENTS

I would like to gratefully and sincerely thank my supervisor Dr. Dibyendu Bhattacharyya, Head Synchrotron Science & Multilayer Physics Section, Atomic & Molecular Physics Division, BARC, for his guidance, understanding and patience during my doctoral studies. I am extremely grateful to Dr. N.K. Sahoo, Associate Director, Physics Group and Head, Atomic & Molecular Physics Division, BARC for his continuous encouragement throughout this thesis work. I would like to thank all of the members of my XAFS research group, Dr. Shambhu Nath Jha, Ashwini Kumar Poswal, Dr. Arup Biswas, Chandrani Nayak, Nidhi Tiwari, Ankur Agrawal, Ashutosh Dwivedi and Nirmalendu Patra and other colleagues who have helped me in every possible way. A special mention for Dr. (Smt.) Sohini Basu (formerly at Atomic & Molecular Physics Division at BARC, Mumbai, and now at UOP-Honeywell, Gurugram, Haryana), Chandrani Nayak and Nidhi Tiwari, who made my long working hours worthwhile and for the stimulating discussions on XAFS.

I would also like to thank members of my doctoral committee for their input and valuable discussions. I am also thankful to my principal collaborators, Prof. (Dr.) A. K. Pal, Dr. R. Bhunia, R. Dey, R. Bhar (Department of Instrumentation Science, Jadavpur University, Kolkata), Dr. D. M. Phase, Dr. R. Choudhary, Dr. D. K. Shukla, Dr. Mukul Gupta (UGC-DAE CSR, Indore), Dr. K. Divakar Rao, Dr. S. M. Haque, Dr. Shilpa Tripathi, Rajnarayan De (Atomic & Molecular Physics Division, BARC, Visakhapatnam), Dr. S. Bandopadhyay, Dr. Md. A. Ahmed (Calcutta University, Kolkata), Dr. Nimai Pathak (Radiochemistry Division, Bhabha Atomic Research Centre, Mumbai), Dr. P. D. Babu (UGC-DAE CSR, Mumbai), Dr. P. K. Mishra, Dr. C.L. Prajapat (Technical Physics Division, Bhabha Atomic Research Centre, Mumbai), Dr. V. Srihari (High Pressure & Synchrotron Radiation Physics Division, Bhabha Atomic Research Centre, Mumbai), Dr. Sanjay Rai, Dr. S. D. Singh, Dr. (Smt.) P. Gupta and their group members. Last but not the least; I acknowledge all my teachers, friends and family members for their inspiration and silent support during the course of this thesis work.

# CONTENTS

<b>Synopsis</b>	<b>01</b>
<b>List of Figures</b>	<b>09</b>
<b>List of Tables</b>	<b>24</b>
<b>Chapter 1: INTRODUCTION</b>	<b>27</b>
1.1 Potential DMS materials:	29
1.2 Spintronic devices and application of DMSs:	31
1.2.1 Spin diode:	32
1.2.2 Spin Field Effect Transistor	33
1.3 Model for Magnetism in DMS:	34
1.3.1 Carrier exchange interaction models:	35
1.3.2 The bound magnetic polaron model:	36
1.3.3 Transition metal clustering or secondary phase models:	37
1.4 Challenges of oxide DMSs & Motivation of the thesis:	37
1.5 Outline of the thesis:	45
<b>Chapter 2: EXPERIMENTATION AND DATA ANALYSIS</b>	<b>47</b>
2.1 Sample preparation:	47
2.1.1 Deposition of thin films by rf sputtering:	47
2.1.2 Free standing polymer films:	52
2.2 XAS measurements and data analysis:	55
2.2.1 Theoretical formulation:	55
2.2.2 XAS measurements:	65
2.2.3 EXAS data analysis:	71
2.3 Other characterisation techniques:	85
2.3.1 Grazing Incidence X-ray Diffraction (GIXRD):	85
2.3.2 Spectroscopic Ellipsometry:	89
2.3.3 Photoluminescence studies:	92
2.3.4 Field Emission Scanning Electron Microscope (FESEM):	92
2.3.5 X-ray Photoelectron Spectroscopy (XPS):	94

2.3.6 Magnetic measurements:	96
<b>Chapter 3: Mn DOPED ZnO THIN FILMS</b>	<b>98</b>
3.1 Introduction:	98
3.2 Experimental:	98
3.2.1 Preparation of samples:	98
3.2.2 Characterization of samples:	99
3.3 Results and discussion:	99
<b>Chapter 4: Fe, Co AND Ni DOPED ZnO THIN FILMS</b>	<b>114</b>
4.1 Fe doped ZnO:	114
4.1.1 Experimental:	114
4.1.2 Results and discussions:	115
4.2 Co doped ZnO thin films:	129
4.2.1 Experimental:	129
4.2.2 Results and discussion:	130
4.3 Ni doped ZnO:	138
4.3.1 Experimental:	138
4.3.2 Results and discussion:	140
<b>Chapter 5: TM (Mn, Co AND Ni)-DOPED NANOCRYSTALLINE-ZnO/PVDF COMPOSITE THIN FILMS</b>	<b>160</b>
5.1 Ni doped ZnO/PVDF:	160
5.1.1 Experimental:	161
5.1.2 Results and discussion:	163
5.2 Co doped ZnO/PVDF:	176
5.2.1 Experimental:	176
5.2.2 Results and discussion:	177
5.3 (Ni,Co) co-doped PVDF-ZnO thin films:	190
5.3.1 Experimental:	191
5.3.2 Results and Discussion:	191
5.4 Mn doped ZnO/PVDF:	203
5.4.1 Experimental:	203

5.4.2 Results and discussion:	204
<b>Chapter 6: Mn AND Co DOPED TiO<sub>2</sub> THIN FILMS</b>	<b>212</b>
6.1 Introduction:	212
6.2 Experimental:	212
6.2.1 Preparation of samples:	212
6.2.2 Characterisation of samples:	213
6.3 Results and discussion:	214
6.3.1 Grazing Incidence X-ray Diffraction:	214
6.3.2 X-ray Absorption Spectroscopy:	215
6.3.3 Magnetization studies on Mn and Co doped TiO <sub>2</sub> samples:	232
<b>Chapter 7: SUMMARY, CONCLUSION AND FUTURE WORK</b>	<b>235</b>
7.1 Summary and conclusion:	235
7.1.1 TM doped ZnO thin films:	235
7.1.2 TM doped nanocrystalline-ZnO/PVDF composite thin films:	238
7.1.3 TM doped TiO <sub>2</sub> thin films:	241
7.2 Future work:	241
<b>References</b>	<b>243</b>
<b>Appendices</b>	
<b>Appendix-A: Tauc-Lorentz dispersion mode</b>	<b>255</b>
<b>Appendix-B: Bruggeman Effective Medium Approximation</b>	<b>258</b>

# SYNOPSIS

## **Investigation on local structures of dilute magnetic semiconductor thin films by Fluorescence based EXAFS measurements**

Dilute magnetic semiconductors which are formed by incorporating small amount of transition metals (TM) in semiconductor hosts are considered to be potentially important materials for spintronics applications. Spintronics is an emerging field where the spins of electrons of a material are used simultaneously with their charges for the realisation of more efficient and advanced devices [1-3]. Following the theoretical prediction by Dietl et. al. about room temperature ferromagnetism (RTFM) in 5% Mn doped ZnO [4] not only TM doped ZnO but other doped oxide semiconductors (DMS) such as SnO<sub>2</sub> [5], TiO<sub>2</sub> [6] and HfO<sub>2</sub> [7] were also explored both experimentally as well as theoretically for the RTFM.

Origin of RTFM in DMS materials is not unique and has been attributed to a variety of intrinsic and extrinsic reasons. Different research groups have reported different reasons for the origin of ferromagnetism in these DMS systems and contradictory reports are available in the literature regarding whether FM arises due to the precipitation of metallic cluster in a homogenous ZnO host matrix [8] or due to the uniformly distributed TM cations in the semiconductor lattice or due to the presence of an entirely separate magnetic phase [8,9] or due to the defects [10].

Thus origin of FM in DMS is still a fairly unresolved question and further experimental and theoretical studies are required particularly to explore the local environment around the host and the dopant cations carefully to obtain unambiguous results regarding the origin of FM in these systems. X-ray Absorption Spectroscopy

(XAS), which comprises of both X-ray Near Edge Structure (XANES) and Extended X-ray Absorption Fine Structure (EXAFS) techniques, is a perfect tool to study the local environments around impurities and defects due to its short range nature. Due to its element specific and short range nature, X-ray absorption spectroscopy (XAS) is increasingly been useful for local structural investigation of complex, disordered materials in a variety of scientific fields such as physics, chemistry, bioscience, materials science and engineering, energy science, environmental science, geoscience, metallurgy, mineralogy etc. In this thesis work thus synchrotron radiation based XAS, measurements have been extensively used to understand the origin of FM. The obtained results are additionally supported by other alternative experimental and theoretical techniques i.e. photoluminescence, XPS, FEFF9 calculations etc.

Chapter-1 of the thesis gives a brief introduction and motivation behind the work carried out under this doctoral programme. Initially various potential DMS materials alongwith different proposed spintronics devices which can be realized with these materials have been discussed. Subsequently brief history of research carried out for the two specific systems which have been studied in this thesis work, viz., TM doped ZnO and TM doped TiO<sub>2</sub>, have been discussed. Various theoretical models given to understand the origin of magnetism in DMS are briefly discussed. Subsequently, since dilute amount of dopant materials has been used to prepare these DMS materials, the importance of using a local structure analysis tool like X-ray absorption spectroscopy, instead of X-ray diffraction has been emphasized. Subsequently, structural and magnetic properties of the various systems discussed in this thesis in subsequent chapters have been described briefly. In summary the contents of this chapter provides the basis for the works presented in subsequent chapters.

Chapter-2 deals with experimental techniques and XAFS data analysis used in this thesis work. In the experimental section, various sample preparation techniques used for the

preparation of samples for the present thesis work have been described. Two type of methods have been used to prepare thin films for the present work. TM (Mn, Fe, Co, Ni) doped ZnO and TM (Co, Mn) doped TiO<sub>2</sub> thin films are deposited on Si substrates using an in-house built magnetron sputtering system and TM doped ZnO/PVDF free standing flexible polymer films are prepared using spin coating. In the second part of this experimental section, various thin film characterization techniques that have been employed to investigate the properties of thin films in this thesis have been briefly discussed. The techniques of grazing incidence X-ray diffraction (GIXRD), spectroscopic ellipsometry (SE), Photoluminescence (PL) and magnetic measurement techniques have been described shortly. Finally the XAS technique, including both EXAFS and XANES, which has been used in this thesis work extensively for hard X-ray and soft X-ray regions have been discussed in details. It is started with brief introduction of synchrotron source and various beamlines used for various measurements for present thesis. Finally the XAFS data analysis procedure is described elaborately which involves extensive use of the IFEFFIT software package including ATHENA and ARTEMIS subroutines [11] for EXAFS analysis and FEFF9 software package for XANES simulations [12].

Next chapters (Chapters 3-6) of the thesis work deals with local structural investigation using EXAFS and XANES on various DMS thin films with varying dopant concentration. These chapters are divided based on magnetic and non magnetic dopant case for ZnO host lattice. The origin of magnetic properties in different systems are explained on the basis of local structure findings.

Chapter-3, is devoted to correlation of local structure and magnetic properties of Mn doped ZnO thin films with different Mn doping concentrations deposited by r.f. sputtering technique. GIXRD measurements show pure phase of the samples with preferential directional growth. XANES and EXAFS measurements have been performed at Zn, Mn and

O K edges and Mn L<sub>2,3</sub> edges for details local structure investigations at the host and dopant sites. XAFS results confirm that Mn substitutes Zn in ZnO lattice with indication of Mn clustering at relatively higher Mn doping concentration. Mn K edge XANES measurements show that oxygen vacancies in the samples increase with increase in Mn doping concentration which is also supported by O K edge XANES measurements [13]. Magnetic measurements show room temperature ferromagnetism in the samples at lower Mn doping concentration which is destroyed at higher Mn doping concentration of ~10%. These results have been explained using findings of EXAFS and XANES measurements.

In Chapter-4, studies on a set of Fe, Co and Ni doped ZnO thin films deposited with rf magnetron sputtering technique on c-Si substrates with varying Fe, Co and Ni doping concentrations have been reported. GIXRD measurements show pure wurtzite structure of the all the samples. XANES measurements show that Fe is present in the samples with mixed oxidation states of Fe<sup>2+</sup> and Fe<sup>3+</sup> and quantitative ratio of the two contributions have been obtained using linear combination fitting of the XANES spectra [14], however, it has been found that Co and Ni are present in +2 oxidation state only. XAFS measurements at Zn and dopant K edges have been used to identify location and oxidation state of the dopants in host site. Magnetization measurement shows the room temperature ferromagnetic behaviour of the samples. The obtained magnetic behaviour have been explained based on the XAFS results and occasionally supported with other alternative techniques i.e. PL study and XANES simulations. Ferromagnetism observed in the samples is thus believed to be originated from intrinsic origin with possible mediation by oxygen vacancies [15-16].

In Chapter-5, the studies on a set of free standing and flexible nano-ZnO/PVDF and Mn, Ni and Co-doped nano-ZnO/PVDF composite films prepared by sol-gel technique have been reported. The poled and unpoled films have been subjected to FESEM, XPS and XANES/EXAFS studies. FESEM micrographs showed highly oriented nanocrystals of ZnO

embedded in free standing PVDF matrix in the poled samples. The XPS spectra recorded for the poled samples from the fluorine terminated surface showed a very strong peak at ~695 eV for F1s arising due to C-F bonds. This peak was of very low intensity for the reversed surface (hydrogen terminated surface). The FTIR spectra for unpoled films contained assorted peaks related both to  $\alpha$ -phase and  $\beta$  phase [17].

For the Mn doped samples, XANES measurements show that Zn K edge positions of the samples agree well with that of ZnO bulk sample which shows that Zn is present only in  $Zn^{2+}$  state in the samples which is also supported by core level XPS spectra of the samples. Difference in core level XPS peaks of Zn  $2p_{3/2}$  and Zn  $2p_{1/2}$  on fluorine-terminated and hydrogen terminated surfaces of the poled samples further suggests presence of highly aligned ZnO nanocrystallites in the poled PVDF matrix which would effectively modulate the piezoelectric behaviour of the composite. Core level XPS peaks of Mn  $2p_{3/2}$  and Mn  $2p_{1/2}$  are attributed to the existence of  $Mn^{4+}$  and  $Mn^{2+}$  species in the samples, though Mn K edge XANES studies indicate the presence of Mn in 2+ states for all the films studied here. Zn K edge EXAFS analysis suggests that there is no significant change in the local structure surrounding Zn due to Mn doping since both ions are in +2 oxidation state and are of similar size. However, Mn edge EXAFS data suggest that the Mn doped ( $x = 0.01$ ) sample is more likely a composite of ZnO and Mn acetate tetrahydrate where proper Mn substitution at Zn sites has not been taken place, though Mn doped ( $x = 0.03$  and  $0.05$ ) samples show signature of proper Mn substitution at Zn sites in ZnO lattice.

XANES measurements of Ni doped nano-ZnO/PVDF show that Zn K edge positions of the samples agree well with that of ZnO bulk sample which shows that Zn is present only in  $Zn^{2+}$  state in the samples and which is also supported by core level XPS spectra of the samples [18]. However, Co-doped nano-ZnO/PVDF Zn Kedge XANES studies show that Zn

is present in the samples in  $Zn^{+2}$  oxidation state though poled samples shows the position of Zn K absorption edge at higher energies than that corresponding to  $Zn^{+2}$  state possibly due to increase in effective positive charge at Zn sites due to poling effect which is also supported by core level XPS spectra of the samples [19]. XANES measurements and core level XPS peaks of Ni (Ni  $2p_{3/2}$  and Ni  $2p_{1/2}$ ) and Co (Co  $2p_{3/2}$  and Co  $2p_{1/2}$ ) have been used for detailed discussion on valance state. EXAFS analysis recorded from Zn K edge and dopant K edge confirm that dopant atoms primarily substitute Zn atoms in the ZnO lattice.

In Chapter-6, the study on Mn and Co doped  $TiO_2$  thin films prepared by rf magnetron sputtering technique on c-Si substrates, has been described. GIXRD measurements show anatase phase for undoped  $TiO_2$  and Mn doped  $TiO_2$  films at lower Mn doping concentration and mixed anatase and rutile phases for Co doped  $TiO_2$ . The above structural results have also been corroborated by EXAFS measurements at host (Ti) and dopant (Mn,Co) K-edges. EXAFS measurements at the dopant edges further indicate creation of oxygen vacancies in the samples due to TM doping, which is also confirmed by XANES measurements at O K-edge and by FEFF calculations. The oxidation states of the dopants in the host matrix have been confirmed by K and L-edge XANES measurements of dopant edges which rules out the presence of any other metal cluster or ferromagnetic oxide phases in the samples. Ferromagnetism obtained in the doped samples has thus been attributed to the defect (oxygen vacancy) mediated interaction between the TM ions [20].

Finally in Chapter-7 the conclusions drawn in all the previous chapters in the different set of thin films have been summarized and future directions of the works have been mentioned. As a future prospective it is proposed to carry out X-ray Magnetic Circular Dichroism (XMCD) measurements on doped and co-doped DMS materials using the XMCD setup being developed at the BL-08 Energy dispersive EXAFS beamline at Indus-2 SRS to understand magnetic behaviour of individual magnetic components.

## References

- [1]. A. Prinz *Science* 282, (1998) 1660-1663.
- [2]. S. A. Wolf, D. D. Awschalom, R. A. Buhrman, J. M. Daughton, S. V. Molnár, M. L. Roukes, A. Y. Chtchelkanova, D. M. Treger, *Science* 294, (1998) 1488–1495.
- [3]. H Ohno, *Science* 281, (1998) 951–956.
- [4]. T. Dietl, H. Ohno, F. Matsukura, J. Cibert, D. Ferrand, *Science* 287, (2000) 1019-1022.
- [5]. X. L. Wang, Z. X. Dai, Z. Zeng, *J. Phys.: Condens. Matter.* 20, (2008) 045214.
- [6]. H. Zhang, T. Ji, L. Li, X. Qi, Y. Liu, J. Cai, H. Du, J. Sun, *Acta Phys. Sin.*, 24 (2008) 607-611.
- [7]. M. S. R. Rao, D. C. Kundaliya, S. B. Ogale, L. F. Fu, S. J. Welz, N. D. Browning, V. Zaitsev, B. Varughese, C. A. Cardoso, A. Curtin, S. Dhar, S. R. Shinde, T. Venkatesan, S. E. Lofland, S. A. Schwarz, *Appl. Phys. Lett.* 88 (2006) 142505.
- [8]. D. Wang, Z. Q. Chen, D. D. Wang, J. Gong, C. Y. Cao, Z. Tang, L. R. Huang, *Journal of Magnetism and Magnetic Materials* 322 (2010) 3642-3647.
- [9]. X. Z. Li, J. Zhang, D. J. Sellmyer, *Solid State Communications* 141 (2007) 398-401.
- [10]. W. Yan, Z. Sun, Q. Liu, Z. Li, Z. Pan, J. Wang, S. Weia, D. Wang, Y. Zhou, X. Zhang, *Appl. Phys. Lett.* 91 (2007) 062113.
- [11]. M. Newville, B. Ravel, D. Haskel, J. J. Rehr, E. A. Stern and Y. Yacoby, *Physica B* 154 (1995) 208.
- [12]. J. J. Rehr, J. J. Kas, F. D. Vila, M. P. Prange, K. Jorissen, *Phys. Chem. Chem. Phys.* 12 (2010) 5503-5513.
- [13]. Ashok Kumar Yadav, Sk Maidul Haque, Dinesh Shukla, Ram Janay Choudhary, S. N. Jha and D. Bhattacharyya, *AIP Advances* 5 (2015) 117138.

- [14]. Ashok Kumar Yadav, Sk Maidul Haque, Shilpa Tripathi, Dinesh Shukla, Md. A. Ahmed, D. M. Phase, S. Bandyopadhyay, S.N. Jha and D. Bhattacharyya, RSC Adv. 6 (2016) 74982.
- [15]. A K Yadav, S M Haque, Rajnarayan De, N Pathak, D K Shukla, R J Choudhary, D M Phase, S N Jha, Dibyendu Bhattacharyya, Thin Solid Films (2017) in press.
- [16]. Ashok Kumar Yadav, Sk Maidul Haque, Dinesh Kumar Shukla, S.N. Jha and D.Bhattacharyya, AIP Conf. Proc. 1731, 060008-1–060008-3, [2015].
- [17]. R. Bhunia, A.K. Yadav, S.N. Jha, D. Bhattacharyya, S. Hussain, R. Bhar, A.K. Pal, Polymer 78 (2015) 1-12.
- [18]. Ashok Kumar Yadav, Rajkumar Dey, Ritamay Bhunia, Shamima Hussain, Shambhu Nath Jha, Dibyendu Bhattacharyya, Radhaballav Bhar, and Arun Kumar Pal, J. Poly. Res, 23 (2016) 265.
- [19]. Rajkumar Dey, Ashok Kumar Yadav, Ritamay Bhunia, Shambhu Nath Jha, Dibyendu Bhattacharyya, Shamima Hussain, Radhaballav Bhar and Arun Kumar Pal, Spectrochimica Acta Part B: Atomic Spectroscopy 131 (2017) 115-123.
- [20]. Ashok Kumar Yadav, Sk Maidul Haque, Rajnarayan De, Md Azaharuddin Ahmed, Velaga Srihari, Mukul Gupta, Deodatta M. Phase, Sudipta Bandyopadhyay, Shambu Nath Jha and Dibyendu Bhattacharyya, Chem. Select., 2017, 2, 11012-11024.

# List of Figures

	Page No.
Figure 1.1: Schematic of spin polarized light emitting diode. Spin polarized holes of Mn doped GaAs region recombine with electrons in the InGaAs region, with emission of circularly polarized light.	32
Figure 1.2: Datta-Das spin FET. Spin polarized electron emitted from the source are travel through narrow channel and collected at drain, if source and drain have parallel alignment of spin. When gate volatage is on, spin of channel is parallel to gate and source, allows current to pass, when channel spin are antiparallel, current will not pass.	34
Figure 1.3: Schematic representation of a spin-FET based on TM doped ZnO. Source and drain are made of Co doped ZnO. With gate voltage, holes are injected in Mn doped ZnO makes it half metallic ferromagnet which allows a spin polarized current to flow from source to drain.	34
Figure 1.4: Representation of bound magnetic polarons proposed by Coey et. al. Small circles are cation sites and unoccupied oxygen sites are represented by squares.	37
Figure 2.1: Schematic representation of sputter deposition technology.	48
Figure 2.2: Schematic of R.F. Magnetron sputtering system.	50
Figure 2.3: In-house built R.F. Magnetron sputtering deposition system at BARC-VIZAG, Visakapatnam.	51

Figure 2.4:	Actual picture of spin coater.	53
Figure 2.5:	Schematic diagram and actual picture of (a) poling unit used, (b) Schematic view of two of the PVDF phases. The a-phase consists of a series of non-polar anti-parallel chains, whereas b-phase phase consists of a series of polar parallel chains.	54
Figure 2.6:	Photo absorption cross section for different phenomenon of interaction of X-ray with matter.	55
Figure 2.7:	A typical X-ray absorption spectrum.	59
Figure 2.8:	Schematic of scattering.	59
Figure 2.9:	Typical characteristic of photoelectron mean free path vs. wave number	63
Figure 2.10:	Indus-2 Synchrotron Source (2.5 GeV, 100 mA) at Raja Ramanna Centre for Advanced Technology (RRCAT), Indore, India.	66
Figure 2.11:	Schematic layout of Scanning EXAFS Beamline BL-09.	68
Figure 2.12:	Photograph of (a) optics hutch and (b) experimental station of Scanning EXAFS Beamline BL-09.	68
Figure 2.13:	Experimental set-up for transmission mode of XAFS measurement.	69
Figure 2.14:	Experimental set-up for fluorescence mode of XAFS measurement.	69
Figure 2.15:	Schematic layout of Soft X-ray Absorption Beamline BL-01.	71
Figure 2.16:	The main window of ATHENA program.	73
Figure 2.17:	Pre-edge and post-edge polynomial subtraction.	73
Figure 2.18:	Typical normalised spectrum.	74
Figure 2.19:	Pre-edge, post-edge polynomial and background subtraction.	75
Figure 2.20:	$k$ space EXAFS spectrum with hanning window.	76
Figure 2.21:	Fourier transformed EXAFS spectra alongwith real and imaginary	76

	contribution.	
Figure 2.22:	Main window of ARTEMIS program.	78
Figure 2.23:	GUI window of FEFF9 program.	85
Figure 2.24:	Schematic of GIXRD set-up in $2\theta$ scan mode.	87
Figure 2.25:	Bruker D8 Discover diffractometer used for experiment.	88
Figure 2.26:	Rigaku SmartLab diffractometer used for experiment.	88
Figure 2.27:	Photograph of the experimental station at AD/EDXRD beamline BL-11.	89
Figure 2.28:	Photograph of spectroscopic ellipsometer (SOPRA GES5E) .	91
Figure 2.29:	Photograph of Edinburgh spectroscopic Photoluminescence instrument.	92
Figure 2.30:	Schematic diagram of a FESEM.	93
Figure 2.31:	Carl Zeiss SUPRA <sup>®</sup> 55 FESEM.	94
Figure 2.32:	Block diagram of XPS instrument.	95
Figure 2.33:	Photograph of XPS instrument.	96
Figure 2.34:	Photograph of SQUID-vibrating sample magnetometer.	97
Figure 3.1:	GIXRD plots of Mn doped ZnO thin films (1%, 2%, 4%, 6% and 10% doping).	100
Figure 3.2:	(Left panel) Normalised XANES spectra of pure ZnO and Mn doped ZnO (1%, 2%, 4%, 6% and 10% doping) at Mn K-edge along with reference Mn metal, MnCl <sub>2</sub> and Mn <sub>2</sub> O <sub>3</sub> . (Right panel) Theoretically simulated XANES spectra by Yan et al. assuming different defect models.	101
Figure 3.3:	Normalised XANES spectra of pure ZnO and Mn doped ZnO (1%, 2%, 4%, 6% and 10% doping) at Zn K-edge.	102

Figure 3.4:	Normalised EXAFS spectra of pure ZnO and Mn doped ZnO (1%, 2%, 4%, 6% and 10% doping) samples measured at Zn K-edge.	103
Figure 3.5:	Normalised EXAFS spectra of Mn doped ZnO (1%, 2%, 4%, 6% and 10% doping) samples measured at Mn K-edge.	103
Figure 3.6:	Fourier transformed EXAFS spectra of (a) ZnO (b) 1% Mn doped ZnO (c) 2% Mn doped ZnO (d) 4% Mn doped ZnO (e) 6% Mn doped ZnO and (f) 10% Mn doped ZnO samples measured at Zn K-edge along with best fit theoretical plots.	104
Figure 3.7:	Variation of bond length (R), coordination number (N) and disorder factor ( $\sigma^2$ ) with doping concentration for Zn K-edge (left panel) and Mn K-edge (right panel).	104
Figure 3.8:	Fourier transformed EXAFS spectra of (a) 1% Mn doped ZnO (b) 2% Mn doped ZnO (c) 4% Mn doped ZnO (d) 6% Mn doped ZnO and (e) 10% Mn doped ZnO samples measured at Mn K-edge along with best fit theoretical plots.	106
Figure 3.9:	O K edge XANES spectra of undoped and Mn doped ZnO samples (1%, 2%, 4%, 6% and 10% doping). Inset (b) shows theoretically simulated XANES spectra by Yan et al. for different defect models and Inset (c) shows the part of feature A in expanded scale.	107
Figure 3.10:	Mn $L_{2,3}$ edge XANES spectra for Mn doped ZnO thin films (1%, 2%, 4%, 6% and 10% doping). Inset shows spectra from Thakur et al.	109
Figure 3.11:	Room temperature M-H curve of Mn doped ZnO thin films (2%, 4% and 10% doping).	110
Figure 3.12:	Magnetic moment versus temperature plots for 1%, 2% and 6% Mn	111

doped ZnO thin films.

- Figure 3.13: First principle calculations by Basu et al. for mixing energy versus percentage of substitution of Zn atoms by Mn atoms. 112
- Figure 3.14: Room temperature M-H curves of 4% Mn doped ZnO thin films deposited in pure Ar ambient and in Ar+O<sub>2</sub> mixed ambient. 113
- Figure 4.1: GIXRD plots of undoped ZnO and Fe doped ZnO thin films (1%, 2%, 4%, 6% and 10% doping). Inset: Variation of the (100) peak position with increase in Fe doping concentration. 116
- Figure 4.2: Variation of lattice constant (a) and FWHM of the diffraction peak (100) with Fe doping concentration. 117
- Figure 4.3: Normalised XANES spectra of undoped ZnO and Fe doped ZnO thin films (1%, 2%, 4%, 6% and 10% doping) at Fe K-edge. The reference spectra of Fe metal, FeO, Fe<sub>3</sub>O<sub>4</sub> and Fe<sub>2</sub>O<sub>3</sub> are given for comparison. The inset figure (i) shows the expanded part of the pre-edge region and (ii) shows the XANES spectra reported by Wei et al.. 118
- Figure 4.4: Normalised XANES spectra of undoped ZnO and Fe doped ZnO thin films (1%, 2%, 4%, 6% and 10% doping) measured at Zn K-edge along with Zn metal foil. 120
- Figure 4.5: Normalised EXAFS spectra of undoped ZnO and Fe doped ZnO (1%, 2%, 4%, 6% and 10% doping) thin films measured at Zn K-edge. 121
- Figure 4.6: Normalised EXAFS spectra of Fe doped ZnO (1%, 2%, 4%, 6% and 10% doping) thin films measured at Fe K-edge. 121
- Figure 4.7: Fourier transformed EXAFS spectra of (a) ZnO (b) 1% Fe doped 122

ZnO (c) 2% Fe doped ZnO (d) 4% Fe doped ZnO (e) 6% Fe doped ZnO and (f) 10% Fe doped ZnO (scatter points) at Zn K edge along with best fit theoretical plots (solid line).

- Figure 4.8: Fourier transformed EXAFS spectra of (a) 1% Fe doped ZnO (b) 2% Fe doped ZnO (c) 4% Fe doped ZnO (d) 6% Fe doped ZnO and (e) 10% Fe doped ZnO (scatter points) at Fe K edge along with best fit theoretical plots (solid line). 122
- Figure 4.9: Variation of bond length (R) and disorder factor ( $\sigma^2$ ) with doping concentration for Zn K-edge (left panel) and Fe K-edge (right panel). 125
- Figure 4.10: O K edge XANES spectra of undoped and Fe doped ZnO samples (1%, 2%, 4%, 6% and 10% doping). 126
- Figure 4.11: Room temperature M-H curve of Fe doped ZnO thin films (2%, 4% and 10% doping). 128
- Figure 4.12: GIXRD spectra of the ZnO and Co doped ZnO thin films. 130
- Figure 4.13: Normalised XANES spectra of pure ZnO and Co doped ZnO (1%, 2%, 4% and 10% doping) at (a) Co K-edge and (b) Zn K-edge. 131
- Figure 4.14: Fourier transformed EXAFS spectra (scatter points) of (i) ZnO, (ii) 1% Co doped ZnO (iii) 2% Co doped ZnO (iv) 4% Co doped ZnO and (v) 10% Co doped ZnO measured at (a) Co K edge and (b) Zn K edge and theoretical fits (Solid line).. 131
- Figure 4.15: Variation of bond length (R) and disorder factor ( $\sigma^2$ ) with doping concentration for Zn K-edge (left panel) and Co K-edge (right panel). 133
- Figure 4.16: O K-edge XANES spectra of Co doped ZnO samples. 134

Figure 4.17:	L2,3 edge XANES spectra for Co K edge. The inset shows the spectra obtained by Chiou et al.	135
Figure 4.18:	M-H curve of Co doped ZnO at room temperature.	136
Figure 4.19:	GIXRD plots of pure ZnO and Ni doped ZnO thin films (1%, 2%, 4%, 6% and 10% doping).	140
Figure 4.20:	Normalised XANES spectra of Ni doped ZnO thin films (1%, 2%, 4%, 6% and 10% doping) at Ni K-edge. Reference spectra of Ni metal and NiO are also given for comparison. The inset (a) shows the extended part of the pre edge region. The inset (b) shows Ni K-edge XANES simulation with the defect model of substitutional Ni and oxygen vacancy ( $\text{Ni}_{\text{Zn}}+\text{V}_{\text{O}}$ ).	142
Figure 4.21:	Normalised XANES spectra of pure ZnO and Ni doped ZnO thin films (1%, 2%, 4%, 6% and 10% doping) at Zn K-edge along with that of Zn metal foil.	143
Figure 4.22:	Normalised EXAFS spectra of pure ZnO and Ni doped ZnO (1%, 2%, 4%, 6% and 10% doping) at Zn K-edge.	144
Figure 4.23:	Normalised EXAFS spectra of Ni doped ZnO (1%, 2%, 4%, 6% and 10%).	144
Figure 4.24:	Fourier transformed EXAFS spectra (a) ZnO, (b) 1% Ni doped ZnO, (c) 2% Ni doped ZnO, (d) 4% Ni doped ZnO, (e) 6% Ni doped ZnO and (f) 10% Ni doped ZnO (scatter points) at Zn K edge along with best fit theoretical plots (solid line). Red line is for magnitude and blue line is imaginary part of $\chi(\text{R})$ .	145
Figure 4.25:	Fourier transformed EXAFS spectra of (a) Ni metal foil and NiO, (b) 1% Ni doped ZnO, (c) 2% Ni doped ZnO, (d) 4% Ni doped	145

ZnO, (e) 6% Ni doped ZnO and (f) 10% Ni doped ZnO (scatter points) at Ni K edge along with best fit theoretical plots (solid line). Red line is for magnitude and blue line is imaginary part of  $\chi(R)$ .

- Figure 4.26: Variation of bond length (R) and disorder factor ( $\sigma^2$ ) with doping concentration for Zn K-edge (left panel) and Fe K-edge (right panel). 147
- Figure 4.27: O K-edge XANES spectra of undoped and Ni doped ZnO samples (1%, 2%, 4%, 6% and 10% doping). (Inset shows extended part of the low energy region). 150
- Figure 4.28: Simulated XANES spectra of ZnO at O K edge with different model clusters. (Inset shows extended part of the low energy region). 150
- Figure 4.29: Simulated XANES spectra of ZnO at O K edge with Ni atoms replacing Zn atoms in first coordination shell. 152
- Figure 4.30: (a) Experimental Ellipsometry spectra (scatter points) alongwith best fit theoretical curves (solid line) over a wavelength range of 200-900 nm for a representative 1% Ni doped ZnO thin film deposited on Si substrate. (b) Variation of band gap of the films (obtained from ellipsometric measurements) as a function of Ni doping concentration. 153
- Figure 4.31: PL spectra of 4% and 10% Ni doped ZnO thin films 156
- Figure 4.32: Room temperature M-H curves of 4% and 10% Ni doped ZnO thin films. 157
- Figure 5.1: FESEM pictures of poled: (a)  $Zn_{1-x}Ni_xO/PVDF$  ( $x=0.01$ ) sample, 164  
 (b)  $Zn_{1-x}Ni_xO/PVDF$  ( $x=0.04$ ) and (c)  $Zn_{1-x}Ni_xO/PVDF$  ( $x=0.09$ )

sample, Insets show the corresponding FESEM pictures of unpoled films.

- Figure 5.2: (a) Core level XPS spectra for Zn2p peak of a representative unpoled  $Zn_{1-x}Ni_xO/PVDF$  ( $x=0.04$ ) sample, (b) O1s peak and (c) Core level spectra of Ni2p peak. Corresponding insets show the same for poled samples recorded from H-terminated (right hand insets) and F-terminated (left hand insets) surfaces 165
- Figure 5.3: (a) Normalised XANES spectra of unpoled and poled  $Zn_{1-x}Ni_xO/PVDF$  ( $x=0.01(S_1)$ ,  $0.04(S_2)$  and  $0.09(S_3)$ ) at measured Zn K-edge with along with the spectra for reference Zn metal and commercial ZnO powder sample. (b) Normalised XANES spectra of unpoled and poled  $Zn_{1-x}Ni_xO/PVDF$  ( $x=0.01(S_1)$ ,  $0.04(S_2)$  and  $0.09(S_3)$ ) measured at Ni K-edge along with the reference Ni metal and NiO sample. 168
- Figure 5.4: (a) Normalised EXAFS spectra of unpoled and poled  $Zn_{1-x}Ni_xO/PVDF$  ( $x=0.01(S_1)$ ,  $0.04(S_2)$  and  $0.09(S_3)$ ) at Zn K-edge. (b) Normalised EXAFS spectra of unpoled and poled  $Zn_{1-x}Ni_xO/PVDF$  ( $x=0.01(S_1)$ ,  $0.04(S_2)$  and  $0.09(S_3)$ ) at Ni K-edge with along with reference NiO sample 169
- Figure 5.5: (a) Fourier transformed EXAFS spectra of unpoled  $Zn_{1-x}Ni_xO/PVDF$  at Zn K-edge (Scatter points) and theoretical fit (Solid line): (I)  $x=0.01$  (II)  $x=0.04$  and (III)  $x=0.09$ . (b) Fourier transformed EXAFS spectra of Poled  $Zn_{1-x}Ni_xO/PVDF$  at Zn K-edge (Scatter points) and theoretical fit (Solid line): (I)  $x=0.01$  (II)  $x=0.04$  and (III)  $x=0.09$  170

- Figure 5.6: (a) Fourier transformed EXAFS spectra of unpoled  $Zn_{1-x}Ni_xO/PVDF$  at Ni K-edge (Scatter points) and theoretical fit (Solid line): (I)  $x=0.01$  (II)  $x=0.04$  and (III)  $x=0.09$ . (b) Fourier transformed EXAFS spectra of Poled  $Zn_{1-x}Ni_xO/PVDF$  at Ni K-edge (Scatter points) and theoretical fit (Solid line): (I)  $x=0.01$  (II)  $x=0.04$  and (III)  $x=0.09$  172
- Figure 5.7: FESEM pictures of poled: (a) pristine PVDF film, (b)  $Co_xZn_{1-x}O/PVDF(x = 0.01)$  sample, (c)  $Co_xZn_{1-x}O/PVDF(x = 0.04)$  and (d)  $Co_xZn_{1-x}O/PVDF(x = 0.07)$  sample. Insets show the corresponding FESEM pictures of unpoled films. 178
- Figure 5.8: General survey XPS spectra of  $Co_xZn_{1-x}O/PVDF(x=0.07)$  for (a) unpoled Surface, (b) poled sample of the same film when recorded from fluorine terminated surface and (c) shows the same when recorded from hydrogen terminated surface. 179
- Figure 5.9: Normalised XANES spectra of unpoled and poled  $Co_xZn_{1-x}O/PVDF$  films (with  $x=0.01(S_1)$ ,  $x = 0.04(S_2)$  and  $x= 0.07(S_3)$ ) measured at Zn K-edge with along with the spectra for reference Zn metal and commercial ZnO powder sample. 180
- Figure 5.10: Core level XPS spectra for Zn2p peaks showing doublet structure for: (a) unpoled  $Co_xZn_{1-x}O/PVDF (x=0.07)$  films. Insets show the core level spectra of  $Co_xZn_{1-x}O/PVDF$  film for  $x= 0.01$ (left hand side) and  $x=0.04$ (right hand side), (b) poled  $Co_xZn_{1-x}O/PVDF (x=0.07)$  film when recorded from fluorine terminated side and Inset shows the same film from hydrogen terminated side. 182
- Figure 5.11: Normalised XANES spectra of unpoled and poled  $Co_xZn_{1-x}O/PVDF$  183

films (with  $x = 0.01(S_1)$ ,  $x = 0.04(S_2)$  and  $x = 0.07(S_3)$ ) measured at Co K-edge along with the reference Co metal and CoO sample.

- Figure 5.12: Core level Co2p peaks showing doublet structure for (a) unpoled  $\text{Co}_x\text{Zn}_{1-x}\text{O/PVDF}$  ( $x=0.07$ ) films, Insets show the core level spectra of  $\text{Co}_x\text{Zn}_{1-x}\text{O/PVDF}$  film for  $x= 0.01$ (left hand side) and  $x=0.04$ (right hand side), (b) poled  $\text{Co}_x\text{Zn}_{1-x}\text{O/PVDF}$  ( $x=0.07$ ) film when recorded from fluorine terminated side and Inset shows the same film from hydrogen terminated side.(c) Core level O1s peaks for unpoled  $\text{Co}_x\text{Zn}_{1-x}\text{O/PVDF}$  ( $x=0.07$ ) films and Insets show same films recorded from fluorine terminated side(left hand side) and hydrogen terminated side(right hand side). 185
- Figure 5.13: Radial structure functions of  $\text{Co}_x\text{Zn}_{1-x}\text{O/PVDF}$  films with: (i)  $x=0.01$ , (ii)  $x=0.04$  and (iii)  $x=0.07$  measured at Zn K-edge (scatter points) and theoretical fit (solid line) for (a) unpoled surface and (b) poled surface. 187
- Figure 5.14: Radial structure functions of  $\text{Co}_x\text{Zn}_{1-x}\text{O/PVDF}$  films with: (i)  $x=0.01$ , (ii)  $x=0.04$ , (iii)  $x=0.07$  and (iv) Co metal measured at Co K-edge (scatter points) and theoretical fit (solid line) for (a) unpoled surface (b) poled Surface. 189
- Figure 5.15: Normalised XANES spectra of Co/Ni codoped PVDF\_ZnO at measured Zn K-edge with along with the spectra for reference Zn metal and commercial ZnO powder sample (solid line). Dash line is for poled samples. 192
- Figure 5.16: Normalised XANES spectra of Ni/Co codoped PVDF\_ZnO measured at Co K-edge along with the reference CoO sample (solid 193

line). Dash line is for poled samples. Inset shows the extended portion of pre edge.

- Figure 5.17 : Normalised XANES spectra of Ni/Co codoped PVDF\_ZnO measured at Ni K-edge along with the reference NiO sample (solid line). Dash line is for poled samples. Inset shows the extended portion of pre edge. 194
- Figure 5.18: Normalised EXAFS spectra of Co/Ni codoped PVDF\_ZnO at Zn K-edge (solid line). Dash line is for poled samples. 195
- Figure 5.19: Normalised EXAFS spectra of Co/Ni codoped PVDF\_ZnO at Co K-edge (solid line). Dash line is for poled samples. 195
- Figure 5.20: Normalised EXAFS spectra of Co/Ni codoped PVDF\_ZnO at Ni K-edge (solid line). Dash line is for poled samples. 196
- Figure 5.21: Fourier transformed EXAFS spectra of Co/Ni codoped PVDF\_ZnO at Zn K-edge (Scatter points) and theoretical fit (Solid line). 198
- Figure 5.22: Fourier transformed EXAFS spectra of Co/Ni codoped PVDF\_ZnO at Co K-edge (Scatter points) and theoretical fit (Solid line). 198
- Figure 5.23: Fourier transformed EXAFS spectra of Co/Ni codoped PVDF\_ZnO at Ni K-edge (Scatter points) and theoretical fit (Solid line). 200
- Figure 5.24: (a) XANES spectra of unpoled and poled  $Mn_xZn_{1-x}O/PVDF$  with  $x = 0.01, 0.03$  and  $0.05$  Mn doping measured at Zn K-edge along with spectra for reference Zn metal and ZnO/ PVDF film; (b) Normalised XANES spectra for unpoled and poled  $Mn_xZn_{1-x}O/PVDF$  with  $x=0.01, 0.03$  and  $0.05$  Mn doping measured at Mn K-edge along with the reference Mn metal,  $MnCl_2$  and  $Mn_2O_3$  samples. (Inset of (b) shows extended pre-edge part). 205

- Figure 5.25: (a) Normalised EXAFS spectra of poled  $\text{Mn}_x\text{Zn}_{1-x}\text{O}/\text{PVDF}$  samples with  $x = 0.01, 0.03$  and  $0.05$  Mn doping measured at Zn K-edge along with the spectra for poled ZnO/PVDF film and reference Zn metal. (b) Normalised EXAFS spectra for poled  $\text{Mn}_x\text{Zn}_{1-x}\text{O}/\text{PVDF}$  samples with  $x = 0.01, 0.03$  and  $0.05$  Mn doping measured at Mn K-edge along with the reference Mn metal and  $\text{Mn}_2\text{O}_3$  sample. 206
- Figure 5.26: (I) Fourier transformed EXAFS spectra of unpoled Mn doped ZnO/PVDF samples measured at Zn K-edge (Scatter points) and theoretical fit (Solid line): (a)  $x = 0$  Mn, (b)  $x = 0.01$  Mn; (c)  $x = 0.03$  Mn and (d)  $x = 0.05$  Mn. (II) Fourier transformed EXAFS spectra of unpoled  $\text{Mn}_x\text{Zn}_{1-x}\text{O} / \text{PVDF}$  samples measured at Mn K-edge (Scatter points) and theoretical fit (Solid line): (a)  $x = 0.01$  Mn, (b)  $x = 0.03$  Mn and (c)  $x = 0.05$  Mn. (III) Fourier transformed EXAFS spectra of poled  $\text{Mn}_x\text{Zn}_{1-x}\text{O} / \text{PVDF}$  measured at Zn K-edge (Scatter points) and theoretical fit (Solid line): (a)  $x = 0.01$  Mn, (b)  $x = 0.03$  Mn and (c)  $x = 0.05$  Mn. (IV) Fourier transformed EXAFS spectra of poled  $\text{Mn}_x\text{Zn}_{1-x}\text{O} / \text{PVDF}$  measured at Mn K-edge (Scatter points) and theoretical fit (Solid line): (a)  $x = 0.01$  Mn, (b)  $x = 0.03$  Mn and (c)  $x = 0.05$  Mn. 207
- Figure 6.1: GIXRD plots of Mn doped  $\text{TiO}_2$  and Co doped  $\text{TiO}_2$  thin films. The XRD spectra of pure anatase and rutile phase are also plotted for reference. 215
- Figure 6.2: Normalised XANES spectra of  $\text{TiO}_2$  and Mn doped  $\text{TiO}_2$  thin films at Ti K-edge. The inset figure shows the extended part of the pre edge region. 216

Figure 6.3:	Normalised XANES spectra of TiO <sub>2</sub> and Mn doped TiO <sub>2</sub> thin films at Mn K-edge. The reference spectrum of Mn metal, MnCl <sub>2</sub> and Mn <sub>2</sub> O <sub>3</sub> are given for comparison.	216
Figure 6.4:	Normalised XANES spectra of TiO <sub>2</sub> and Co doped TiO <sub>2</sub> thin films at Ti K-edge. The inset figure shows the extended part of the pre edge region.	218
Figure 6.5:	(Upper) Normalised XANES spectra of TiO <sub>2</sub> and Co doped TiO <sub>2</sub> thin films at Co K-edge. The reference spectrum of Co metal and CoO are given for comparison. (Lower) The derivative of XANES spectra.	218
Figure 6.6:	Normalised EXAFS spectra of (a) TiO <sub>2</sub> and Mn doped TiO <sub>2</sub> at Ti K-edge (b) Mn doped TiO <sub>2</sub> at Mn K-edge (c) TiO <sub>2</sub> and Co doped TiO <sub>2</sub> at Ti K-edge and (d) Co doped TiO <sub>2</sub> at Co K-edge.	219
Figure 6.7:	Fourier transformed EXAFS spectra of (a) TiO <sub>2</sub> (b) 1% Mn doped TiO <sub>2</sub> (c) 4% Mn doped TiO <sub>2</sub> and (d) 10% Mn doped TiO <sub>2</sub> (scatter points) at Ti K-edge along with best fit theoretical plots (solid line).	221
Figure 6.8:	Fourier transformed EXAFS spectra of (a) 1% Mn doped TiO <sub>2</sub> (b) 4% Mn doped TiO <sub>2</sub> and (c) 10% Mn doped TiO <sub>2</sub> (scatter points) at Mn K-edge along with best fit theoretical plots (solid line).	221
Figure 6.9:	Variation of bond length (R) and disorder factor ( $\sigma^2$ ) with doping concentration at Co K-edge.	223
Figure 6.10:	Fourier transformed EXAFS spectra of (a) TiO <sub>2</sub> (b) 2% Co doped TiO <sub>2</sub> (c) 4% Co doped TiO <sub>2</sub> and (d) 10% Co doped TiO <sub>2</sub> (scatter points) at Ti K-edge along with best fit theoretical plots (solid line).	224
Figure 6.11:	Fourier transformed EXAFS spectra of (a) 2% Co doped TiO <sub>2</sub> (b)	224

4% Co doped TiO<sub>2</sub> and (c) 10% Co doped TiO<sub>2</sub> (scatter points) at Co K edge along with best fit theoretical plots (solid line).

- Figure 6.12: Variation of bond length (R) and disorder factor ( $\sigma^2$ ) with doping concentration at Co K-edge. 226
- Figure 6.13: Soft X-ray absorption spectra of TiO<sub>2</sub> and Mn doped TiO<sub>2</sub> at Ti L<sub>2,3</sub> edge. 228
- Figure 6.14: Soft X-ray absorption spectra of TiO<sub>2</sub> and Co doped TiO<sub>2</sub> at Ti L<sub>2,3</sub> edge. 228
- Figure 6.15: Soft X-ray absorption spectra of TiO<sub>2</sub> and Mn doped TiO<sub>2</sub> at Oxygen K-edge. The inset shows the theoretically calculated XANES spectra using FEFF9. 230
- Figure 6.16: Soft X-ray absorption spectra of TiO<sub>2</sub> and Co doped TiO<sub>2</sub> at Oxygen K-edge. 230
- Figure 6.17: Soft X-ray absorption spectra of TiO<sub>2</sub> and Mn doped TiO<sub>2</sub> at Mn L<sub>2,3</sub> edge. 231
- Figure 6.18: Soft X-ray absorption spectra of TiO<sub>2</sub> and Co doped TiO<sub>2</sub> at Co L<sub>2,3</sub> edge. 231
- Figure 6.19: M Vs H plot for Mn doped TiO<sub>2</sub> at room temperature. 232
- Figure 6.20: M Vs H plot for Co doped TiO<sub>2</sub> at room temperature. 232

# List of Tables

	Page No.
Table 3.1: Bond length, coordination number and disorder factor obtained by fitting of the FT-EXAFS data measured at Zn-K edge.	105
Table 3.2: Bond length, coordination number and disorder factor obtained by theoretical fitting of EXAFS data measured at Mn K edge .	105
Table 4.1: Contribution of Fe+2 and Fe+3 oxidation states obtained from Linear Combination Fitting of XANES spectra.	119
Table 4.2: Bond length, coordination number and disorder factor obtained by fitting of FT-EXAFS data measured at Zn K edge.	123
Table 4.3: Bond length, coordination number and disorder factor obtained by fitting of FT-EXAFS data measured at Fe K edge.	124
Table 4.4: EXAFS parameters at Zn K edge of Co doped ZnO.	132
Table 4.5: EXAFS parameters at Co K edge of Co doped ZnO.	133
Table 4.6: Bond length, coordination number and disorder factor obtained by EXAFS fitting at Zn K-edge. (Same values for the amplitude reduction factor ( $S_0^2$ ) and $\Delta E_0$ have been used for all the coordination shells. The values of $S_0^2$ and $\Delta E_0$ obtained by fitting the FT-EXAFS spectrum of a pure ZnO sample are $1.01 \pm 0.07$ and $3.62 \pm 1.63$ eV, respectively. These values have been kept fixed for rest of the samples).	146
Table 4.7: Bond length, coordination number and disorder factor obtain by EXAFS fitting at Ni K-edge. (Same values for the amplitude reduction factor ( $S_0^2$ ) and $\Delta E_0$ have been used for all the coordination shells. The values of $S_0^2$ and $\Delta E_0$ obtained by fitting the FT-EXAFS spectrum of a pure NiO	148

sample are  $0.77 \pm 0.08$  and  $-5.5 \pm 1.33\text{eV}$ , respectively. These values have been kept fixed for rest of the samples).

Table 5.1:	Bond length, coordination number and disorder factor obtain by EXAFS fitting for unpoled Zn <sub>1-x</sub> Ni <sub>x</sub> O/PVDF at Zn K edge.	171
Table 5.2:	Bond length, coordination number and disorder factor obtain by EXAFS fitting for Poled Zn <sub>1-x</sub> Ni <sub>x</sub> O/PVDF at Zn K edge.	171
Table 5.3:	Bond length, coordination number and disorder factor obtain by EXAFS fitting for unpoled Zn <sub>1-x</sub> Ni <sub>x</sub> O/PVDF at Ni K edge.	172
Table 5.4:	Bond length, coordination number and disorder factor obtain by EXAFS fitting for Poled Zn <sub>1-x</sub> Ni <sub>x</sub> O/PVDF at Ni K edge.	173
Table 5.5:	Bond length, coordination number and disorder factor obtained by EXAFS fitting of unpoled and poled Co doped PVDF-ZnO films at Zn K edge.	188
Table 5.6:	Bond length, coordination number and disorder factor obtain by EXAFS fitting for unpoled and poled Co doped PVDF-ZnO films at Co K edge	190
Table 5.7:	Sample name code for Ni and Co codoped ZnO/PVDF.	191
Table 5.8:	Bond length, coordination number and disorder factor obtain by EXAFS fitting for unpoled Co/Ni codoped PVDF-ZnO at Zn K edge.	197
Table 5.9:	Bond length, coordination number and disorder factor obtain by EXAFS fitting for poled Co/Ni codoped PVDF-ZnO at Zn K edge.	197
Table 5.10:	Bond length, coordination number and disorder factor obtain by EXAFS fitting for unpoled Co/Ni codoped PVDF-ZnO at Co K edge.	199
Table 5.11:	Bond length, coordination number and disorder factor obtain by EXAFS fitting for poled Co/Ni codoped PVDF-ZnO at Co K edge.	199
Table 5.12:	Bond length, coordination number and disorder factor obtain by EXAFS	201

fitting for unpoled Co/Ni codoped PVDF-ZnO at Ni K edge.	
Table 5.13: Bond length, coordination number and disorder factor obtain by EXAFS fitting for unpoled Co/Ni codoped PVDF-ZnO at Ni K edge.	202
Table 5.14: Bond length, coordination number and disorder factor obtained by EXAFS fitting for unpoled samples at Zn K edge.	208
Table 5.15: Bond length, coordination number and disorder factor obtained by EXAFS fitting for unpoled samples at Mn K edge	209
Table 5.16: Bond length, coordination number and disorder factor obtained by EXAFS fitting for poled samples at Zn K edge.	211
Table 5.17: Bond length, coordination number and disorder factor obtained by EXAFS fitting for poled samples at Mn K edge.	211
Table 6.1: Bond length, coordination number and disorder factor obtain by EXAFS fitting at Ti K edge.	222
Table 6.2: Bond length, coordination number and disorder factor obtain by EXAFS fitting at Mn K edge.	222
Table 6.3: Bond length, coordination number and disorder factor obtain by EXAFS fitting at Ti K edge.	225
Table 6.4: Bond length, coordination number and disorder factor obtain by EXAFS fitting at Co K edge.	226

# Chapter 1

## INTRODUCTION

### **1. Introduction:**

Today our life is surrounded by various gadgets and equipments developed based on semiconductors technology. Semiconductor based computer technology, cell phones, medical and engineering equipments have shaped the modern society. Transistors packed by millions in integrated circuits are the building blocks of virtually every electronic device. Processing speed and integration density of silicon chips have been increasing following Moors law<sup>1</sup>, which postulates that transistor density on integrated circuits doubles about every 2 years. Current storage areal density on a disk surface has approached to its limit with smallest transistor of ~10nm scale<sup>2</sup>. It is now impossible to create smaller transistors as electrons experience quantum tunneling through gate. This places limit on the historical Moores law since the materials which are currently used are reaching their functional limit. The conventional electronics based on electron charge and its transport is reaching a dead end. However, the electron has another degree of freedom that can be used, namely spin and the solution of this dead end is either use of spin as an additional degree of freedom or by using the spin alone. Spintronics or spin electronics is the emerging research area, where spin of the electron will also be used with charge of the electron<sup>3, 4</sup>. Spintronics promises a new generation of devices with the advantage of non-volatility and higher processing speed, integration density and power efficiency<sup>5</sup>. The concept of spintronics is emerged from the independent discovery of giant magnetic resonance (GMR) by Albert Fert<sup>6</sup> and Peter Grunberg<sup>7</sup>. Spintronics has already shown its success with the application of ferromagnetic metals in the computer industry, in the form of hard disk drive read heads which use the giant magnetoresistance (GMR) effect, revolutionizing data storage technology. However, in this

first form of spintronics, data are stored in metal-based magnetic devices, and processed in semiconductor-based electronic devices. Exchanging data between these two costs both time and energy, which could be saved if storage and processing could be integrated in a single device. This essentially translates to evolving from metal-based to semiconductor-based spintronics. Doing so requires a material which displays electrically tunable ferromagnetism at room temperature and which can be incorporated into complex integrated circuits<sup>8</sup>. However, even though ferromagnetic and semiconducting behaviors do coexist in some materials, such as europium chalcogenides and chromium spinals, their ordering temperatures (Curie temperatures) are well below room temperature ( $< 100$  K), limiting their use in practical applications.

Thus significant research is now being performed on exploring the possibilities of introducing ferromagnetism in the non magnetic semiconductors by doping dilute amount of magnetic impurity in semiconductors, the corresponding subject is characterized as the field of dilute magnetic semiconductors (DMS)<sup>9</sup>. A large volume of reports are published annually in the literature on this topic with the hope that manipulation of spin in semiconducting devices will improve the conventional technology and will help to produce high speed and low power consumption devices<sup>10</sup>.

As it is mentioned, the primary goal in DMS is to produce ferromagnetic semiconductor with ordering temperature well above room temperature to realize the devices to use in daily life. Theoretical predictions of various systems have been done to produce Room Temperature Ferromagnetism (RTFM), for example, narrow band gap Mn doped InAs and GaAs<sup>11</sup>, wide band gap Co doped TiO<sub>2</sub><sup>12</sup> and TM doped ZnO<sup>9, 13, 14</sup> and so on. Narrow band gap semiconductors like InAs, GaAs etc. are well established semiconductor with wide application in the electronics and optoelectronics industries. With such a strong technology background this class of material is the most promising candidate for the implementation of

DMS. However, despite the intense research since concept of DMS emerged, maximum curie temperature in these materials could not be achieved above 185K<sup>10</sup>. For wide band gap DMS, the situation is still unclear. There are many reports of RTFM in these DMS, however this RTFM is also challenged<sup>10, 14, 15</sup>. Despite the many promising results reported in literature, this field of DMS has contained to be challenged by the concerns regarding the origin of it, whether it is intrinsic or extrinsic.

### **1.1 Potential DMS materials:**

The initial research of DMS was extensively based on III-V semiconductors doped with transition metals<sup>10</sup>. It is found that magnetic ions are located at substitution sites or interstitial or both in a single system of the semiconductor host. The early discovery of carrier induced ferromagnetism is found in Mn doped GaAs and InAs led to the extensive effort to understand the physics of semiconductor spintronics<sup>11</sup>. It is well established by experimental as well as the theoretical ground that the ferromagnetism in such systems are mediated by the holes generated by substitution Mn through RKKY exchange interaction<sup>10</sup>. However, III-V system is extensively used to understand the physics and concept of spintronics which led to the significant enhancement to understanding about the behavior of spins in semiconductor host, their exchange interaction. This research led to the development of spin based devices such as spin polarized light emitters, spin valves, spin FET<sup>16-19</sup>. The main drawback of III-V DMS, however, is the Curie temperature, which is much below the room temperature and even the values reported by best research groups are not above 180-190K<sup>20-23</sup>. Currently III-V DMS's are basically studied as model systems for understanding on spintronics which can be applied to other systems.

Theoretical predications by several groups motivated the search of DMS in II-VI metal oxide based DMS with large band gap. This include ZnO, TiO<sub>2</sub>, SnO<sub>2</sub>, and In<sub>2</sub>O<sub>3</sub> etc<sup>9, 12, 24, 25</sup>. The oxide semiconductor are different from conventional elemental or compound

semiconductors in their structural form and bonding characteristics, nature and type of defect states, anisotropies and their implications for properties and having broad phase diagram of structural-stoichiometry property relationship<sup>26-28</sup>. ZnO and TiO<sub>2</sub> are the two most extensively studied systems for DMS applications. The first reason for this is that it has been theoretically proven that they can show room temperature ferromagnetism (RTFM).<sup>9, 12, 29</sup> The second reason is expected large amount of dopant incorporation in host lattice, without generating any extra phase leading to stronger magnetic field<sup>30, 31</sup>.

ZnO is a wide band gap (3.37 eV) semiconductor with large exciton energy (60 meV) and had several favourable properties, including good transparency, high electron mobility, wide bandgap, and strong room-temperature luminescence<sup>32</sup>. ZnO crystal structure is wurzite (hexagonal) with lattice parameter  $a=3.25 \text{ \AA}$  and  $c=5.12 \text{ \AA}$ <sup>33</sup>. In general ZnO is n-type semiconductor, but p-type conductivity can also be induced<sup>27, 32</sup>. Doped ZnO is one of the promising DMS materials that simultaneously exhibit ferromagnetic and semiconductor properties and have immense potential in spintronic device application<sup>9, 13, 34</sup>. Research on doped ZnO systems (both in thin film and bulk form) gained pace since the theoretical prediction by Dietl et. al.<sup>9</sup> that 5% Mn doped ZnO could exhibit room temperature (RT) ferromagnetism (FM) followed by theoretical demonstration by first-principle electronic structure calculations by Sato and Katayama-Yoshida<sup>13</sup> who suggested that transition-metal (TM = Ti, V, Cr, Mn, Fe, Co, Ni) doped ZnO compounds are ferromagnetic provided that the carriers produced by the TM doping formed a partially filled spin-split impurity band. Coey et al. predicated that ferromagnetic exchange in dilute magnetic semiconductors is mediated by shallow donor electrons<sup>35</sup>. A large volume of reports have been published in last one decade on transition metal doped ZnO both in nanocrystalline and thin film form. Pan et. al. reviewed experimental and theoretical results of transition metal doped ZnO thin films deposited by various deposition technique under different experimental conditions<sup>14</sup>.

Recently Yang have reviewed progress in TM doped ZnO, particularly focussing on spin coherence, free carrier type to understand the origin of ferromagnetic ordering and future prospective of controllable ZnO dilute magnetic semiconductor.<sup>36</sup> Giuli et al.<sup>37</sup> very recently reported that transition metal-doped zinc oxide can be used as a new lithium-ion anode material to increase the energy density of high power lithium-ion batteries.

Following the theoretical prediction by Dietl et. al. about room temperature ferromagnetism (RTFM) in 5%Mn doped ZnO,<sup>9</sup> not only TM doped ZnO but other doped oxide semiconductors (DMS) such as SnO<sub>2</sub>,<sup>38-40</sup> TiO<sub>2</sub><sup>41-45</sup> and HfO<sub>2</sub><sup>46</sup> were also explored both experimentally as well as theoretically for the RTFM. RTFM observed in Co doped TiO<sub>2</sub> by Matsumoto et al.<sup>12</sup> gave a thrust in the research on TM doped TiO<sub>2</sub> systems. Successively, Hong et al. reported RTFM in V, Cr, Fe, Co and Ni doped TiO<sub>2</sub> thin films and there is no secondary phase or cluster formation is obtained, and suggested that ferromagnetic character is due to the transition metal doping only<sup>47</sup>.

## **1.2 Spintronic devices and application of DMSs:**

The spin-transport properties in Dilute Magnetic Semiconductors (DMS) have many possible potentially interesting device applications<sup>8, 9, 12, 48, 49</sup>. Spintronic devices such as spin-valve transistors, spin light-emitting diodes, non-volatile memory, logic devices, optical isolators and ultrafast optical switches are some of the areas of interest for application of the ferromagnetic properties at room temperature in a semiconductor switches<sup>50, 51</sup>. There are two different approaches for realizing spintronic devices, one is ferromagnetic metal based spintronics and another is semiconductor based spintronics. Metal based spintronics has been the basis of information storage devices based on giant magnetic resistance (GMR) such as read heads for magnetic hard disk drives. In case of semiconductor based spintronics, the challenge is to produce ferromagnetism in semiconductor above room temperature. Two of such potential semiconductor spintronic devices viz., Spin field effect transistor (Spin-

FET) and Spin light emitting diode (spin-LED) are discussed in this section. The overall requirement for achieving practical spintronic devices are the efficient electrical injection of spin polarized carriers, the ability to transport the carriers with high transmission efficiency within the host semiconductor, the ability to detect or collect the spin polarised carriers and all these process should be performed at room temperature<sup>52, 53</sup>. All this requires development of a material with high Curie temperature which would also be compatible with presently available semiconductor device fabrication technology.

### 1.2.1 Spin diode:

There are reports of use of spin polarized electrons in light emitting diodes with efficiency up to 90%<sup>4, 53</sup>. These kinds of diodes can emit circularly polarized light. The spin LED based on Mn-doped GaAs is demonstrated, where Mn doping is accompanied by holes (p-type doping) in the valance band which couple their spins to the moments of the Mn atoms, producing spin polarized carriers<sup>54</sup>. An n-type doped region is separated from the p-type doped region by a GaAs layer (Fig. 1.1). When the voltage is applied, spin polarized holes of the p-type region travel over the GaAs layer to recombine with electrons in n-type region. Since the holes are spin polarised, the light emitted in the recombination process has a specific helicity in order to conserve angular momentum.

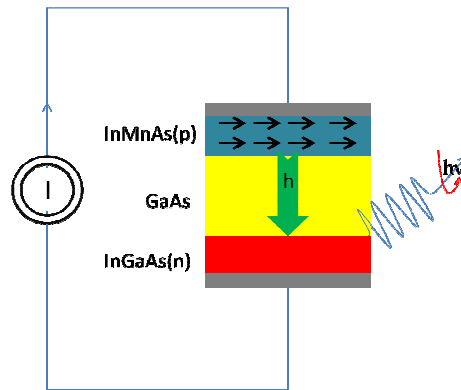


**Figure 1.1:** Schematic of spin polarized light emitting diode. Spin polarized holes of Mn doped GaAs region recombine with electrons in the InGaAs region, with emission of circularly polarized light.

### 1.2.2 Spin Field Effect Transistor

The spin field effect transistor proposed by Datta and Das<sup>55</sup> has motivated extensive study of novel spin controlled electronic devices. Later Huang et al. has demonstrated a silicon spin-FET in which spin polarized electrons are modulated by external gate voltage with 37% electron current spin polarization after transport through 10  $\mu\text{m}$  of undoped single crystal silicon<sup>56</sup>. Source is used as the spin polarized electrode to inject the carrier of definite spin orientation and this source can be ferromagnetic metal or DMS. Similarly drain will be used to collect these spin and worked as a second magnetically polarized electrode. The source-drain current depends on relative orientation of the carrier spins and the magnetization direction of the source and drain. If source and drain magnetization direction is parallel, then current become maximum, however if it is antiparallel transistor will be shut off. The gate voltage is used to control the spin alignment of carriers in the channel and consequently control the current. The spin flip of carriers in gate region are expected to occur at lower voltages than conventional charge controlled transistors. This leads to potential application of spin FETs in very low power microprocessors. There are some reports of developing the III-V based spin FET<sup>18,57</sup>, however no such report on oxide based spin FET is available yet. One of the major obstacles is the inability to achieve high spin injection and detection efficiency at the interfaces, because any scattering at the interfaces between the ferromagnet and the semiconductor could result in spin relaxation<sup>14</sup>. The alternative approach suggested for oxide based DMS is by using fully epitaxial techniques during device fabrication. For example, a ZnO-based Spin FET can be specially designed as follows to allow epitaxial growth of the device: (Zn,Co)O DMS can be used as injector and detector and a half-metallic (Zn,Mn)O can be used as channel with an insulating ZnO as gate oxide<sup>14</sup>.

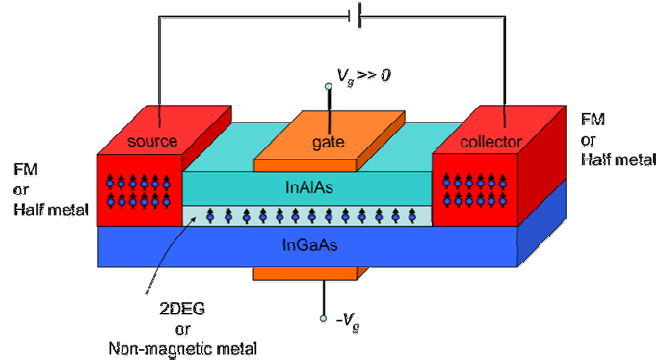


**Figure 1.2:** Datta-Das spin FET. Spin polarized electron emitted from the source are travel through narrow channel and collected at drain, if source and drain have parallel alignment of spin. When gate voltage is on, spin of channel is parallel to gate and source, allows current to pass, when channel spin are antiparallel, current will not pass<sup>55</sup>.

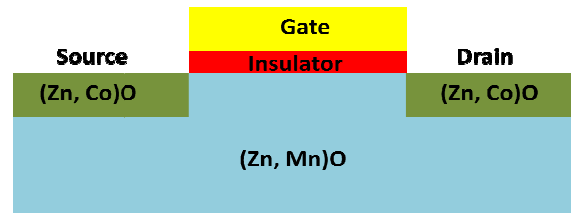


**Figure 1.3:** Schematic representation of a spin-FET based on TM doped ZnO. Source and drain are made of Co doped ZnO. With gate voltage, holes are injected in Mn doped ZnO makes it half metallic ferromagnet which allows a spin polarized current to flow from source to drain<sup>58</sup>.

### 1.3 Model for Magnetism in DMS:

The presence of ferromagnetism is reported in many TM doped ZnO and TiO<sub>2</sub> systems and the origin of this ferromagnetism is debated over large number of research papers. Many mechanisms are proposed for magnetism in these systems, however it is hard to experimentally characterize and quantitatively analyze the nature of RTFM due to many factors affecting the magnetic behavior i.e. microstructure, local structure, electronic structure, coupling between localized magnetization and trace amount of TM clustering. The most popular mechanism suggested for magnetic in TM doped ZnO and TiO<sub>2</sub> are carrier

mediated exchange and the bound magnetic polaron (BMP) model, which are described in details below.

### **1.3.1 Carrier exchange interaction models:**

The RTFM arising from carrier exchange interaction has been predicted in several TM doped ZnO systems<sup>9, 13</sup>. The early publications up to 2004 generally favored carrier exchange interactions<sup>14, 59, 60</sup>. The carrier exchange interaction is characterized by strong coupling between localized d electrons of TM ions and the extended s-p carriers of ZnO. The term carrier-mediated exchange refers to interactions between localized magnetic moments that are mediated by free carriers in the system, which can be divided into three cases: the Rudermann–Kittel–Kasuya–Yosida (RKKY) interaction; Zener carrier-mediated exchange; and Zener double exchange. The RKKY (Ruderman-Kittel-Kasuya-Yosida) model explains magnetic interaction between a single localised magnetic ion and delocalised conduction band electrons<sup>61, 62</sup>. Due to RKKY interaction, conduction electrons close to the magnetic ion get magnetized and act as an effective field to influence the polarization of neighboring magnetic ions, with the oscillatory polarization decaying with distance from the magnetic ion and causing indirect super exchange interaction (RKKY) between two magnetic ions on nearest or next nearest magnetic neighbors. This coupling results in a parallel (ferromagnetic) or an anti-parallel (antiferromagnetic) setting of moments dependent on separation of the interacting atoms. This RKKY model is efficient when a high concentration of delocalized carriers is present in the host material. Zener carrier-mediated exchange proposes that carriers can mediate FM interaction between local moments in the sample and both local magnetic moments and itinerant carriers<sup>9</sup>. FM ordering is driven by a decrease in carrier energy due to redistribution between spin sub-bands split by the exchange interaction. Finally, the Zener double-exchange model refers to indirect coupling mediated by oxygen atoms between neighboring FM ions in different states. The kinetic energy of the system decreases if the

magnetic moments align in parallel, since parallel alignment allows electron transfer from ions in the low state to those in the higher state<sup>15</sup>.

### 1.3.2 The bound magnetic polaron model:

The Coey model first explains the role of defects i.e. vacancy, interstitial, grain boundaries, in the origin of ferromagnetism in DMS oxides<sup>35</sup>. A bound magnetic polaron (BMP) is a collection of electrons (or holes) bound to impurity atoms through exchange interactions within an orbit. Ferromagnetic exchange can be mediated by shallow donor electrons that form bound magnetic polarons (BMPs) which overlap to create a spin split impurity band. The electrons associated with particular defects remain localized in terms of hydrogenic orbits, until a critical donor concentration is reached, at which point the impurity band becomes delocalized. The donors tend to form BMPs, coupling the 3d magnetic moments of the TM dopants within their orbits. Depending upon the system, the interaction can make carrier parallel or anti parallel to the magnetic impurity. These two configurations differ in energy, and this results in a non zero spin flip energy that is a characteristic of BMPs. The interaction of ions with carriers is same, the net energy of the system can be lowered if the ions are aligned parallel to each other. If there is sufficiently large orbital radius, overlap between hydrogenic electron and the cation within its orbit leads to FM supercoupling between them, as shown in figure 1.4. Interaction between the hydrogenic electron and the cation is represented by a Heisenberg exchange Hamiltonian<sup>63</sup>

$$\hat{H}_{ij} = \sum_{ij} J_{ij} \hat{S}_i \hat{S}_j \quad (1.1)$$

Where, S is the spin of dopant cation and s is the doner electron spin.

The Hamiltonian of a two-polaron subsystem is given by Eq. (1.1), where the donor electron spin index j takes only two values, j<sub>1</sub> and j<sub>2</sub>, corresponding to the two polarons under consideration. The hydrogenic orbital tends to spread out sufficiently to overlap with a large

number of BMPs, but some isolated polarons cannot be covered and thus cannot achieve macro-FM ordering.

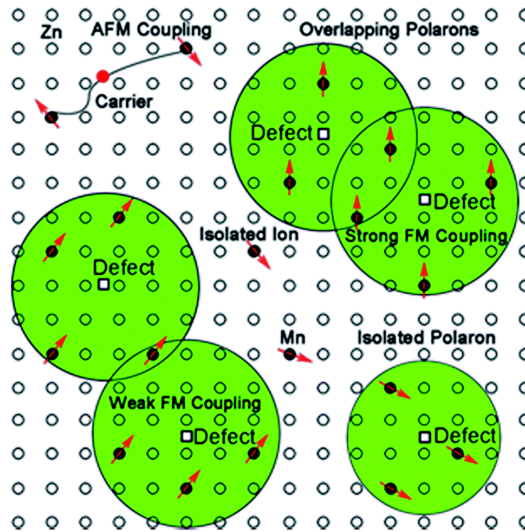


**Figure 1.4:** Representation of bound magnetic polarons proposed by Coey et. al.<sup>35</sup>. Small circles are cation sites and unoccupied oxygen sites are represented by squares.

### 1.3.3 Transition metal clustering or secondary phase models:

There are also many reports which attribute the observed ferromagnetism to extrinsic causes. The separate metallic cluster just a few atoms in dimension<sup>64-66</sup>, magnetic contamination<sup>67</sup> or secondary phases<sup>68-73</sup> can also be possible reason for presence of ferromagnetism. The key requirement in explaining ferromagnetism in DMS systems is to judge whether magnetism present in the system is originated from substitution dopants at host site or formation of secondary phase.

### 1.4 Challenges of oxide DMSs & Motivation of the thesis:

Since thin film form of DMS will be used as a final device fabrication, study of thin film DMS is equally important as bulk DMS. The processing of materials into thin films allows simple integration into various types of devices. Thin film materials are the key elements of continued technological advances made in the fields of optoelectronic, photonic

and magnetic devices. Thin film studies have directly or indirectly advanced many new areas of research in solid state physics and chemistry which are based on phenomena uniquely characteristic of the thickness, geometry and structure of the film.

Brittleness and high loss factors with highly hysteretic behavior are the general characteristic features of piezo-ceramics like ZnO<sup>74</sup>. The increasing demand of printable resistance, transistors and sensor devices, etc. on flexible substrates<sup>75, 76</sup> has accelerated the search for new materials in free-standing and flexible form for application in flexible electronics device technology. There exists a challenge for synthesizing ZnO based DMS material in a freestanding flexible form in cost effective, scalable and reproducible method. Polymer-based composites with high dielectric constant<sup>77-82</sup> or high permeability<sup>83-86</sup> are treated as a possible candidate for the above due to their flexible nature. In this regard, polyvinylidene fluoride (PVDF) has become one of the most suitable and potential materials for advanced applications. This is basically due to the extraordinary electroactive properties among other polymer systems. Inherent combination of properties conducive to various device applications like: processability, mechanical and chemical resistance, and low mechanical and acoustic impedance<sup>87, 88</sup> are present in PVDF material. These properties have ushered in hope of utilizing it for various device applications, especially in the fields of sensors and actuators<sup>89, 90</sup>.

Although, oxide DMSs have been studied by many researches for significant new science and understanding, this field lack of same level of maturity and clarity about the observed phenomena as compared to that of the III-V semiconductor based DMS. Since last decade, the research field of oxide-based DMSs is rapidly progressing and varieties of compounds are discovered and reported, from room temperature to high temperature, from low to high moment. For further progress in this field, minimum requirements are the fabrication of high quality materials with high  $T_C$  value, its detail characterization, and the

clarification of origin of observed FM, since the properties of oxide DMSs are strongly influenced by various growth parameters, TM concentration, host morphology, doping techniques, and other factors. Also various defects (vacancy, interstitial, grain boundary) inside oxide magnetic semiconductors have very serious effects on FM interaction. Pinpointing these defects are an exciting challenge to face off, as it is difficult to characterize defects and to measure it quantitatively. As a result, though an oxide doped with TM and/or non-magnetic elements can exhibit RT FM, there are still lots of open questions regarding the origin of the observed FM. To elucidate this point further, in the following we give a glimpse of the wide variations present among the reports available in the literature in attributing the reason of RTFM observed in various transition metal doped ZnO and TiO<sub>2</sub> semiconductors.

Mn doped ZnO deposited by chemical vapor deposition shows room temperature ferromagnetism which is found to be induced by Zn vacancies in the samples<sup>91</sup>. Cheng and Chien<sup>92</sup> have observed paramagnetic behavior at room temperature for thin films of Mn doped ZnO deposited by r.f. magnetron sputtering, while thin films prepared by pulsed laser deposition shows paramagnetic<sup>93, 94</sup> as well as ferromagnetic<sup>25, 48</sup> behavior at room temperature. Kundaliya et. al.<sup>68</sup> studied both Mn doped ZnO bulk and thin film systems and suggested that RTFM is induced by oxygen vacancies based on thermogravimetric analysis (TGA). Mn-doped ZnO thin films grown by spin coating technique exhibits room temperature FM which decreases with increase in Mn concentration due to segregation of Mn on grain boundaries<sup>95</sup>. Thin films deposited by sol-gel technique also show well defined ferromagnetism<sup>96</sup>. Ferromagnetism induced by zinc and oxygen defects has been observed in thin films prepared by spray technique and in this case also ferromagnetism is found to decrease at higher Mn concentration due to Mn clustering.<sup>97</sup> Similar to Mn doped ZnO, the origin of ferromagnetism in Fe doped ZnO DMS is also an open question. Different groups have reported different reasons for the origin of ferromagnetism in these DMS systems,

particularly whether FM arises due to the precipitation of metallic cluster in a homogenous ZnO host matrix<sup>98</sup> or due to the uniformly distributed TM cations in the semiconductor lattice or due to the presence of an entirely separate magnetic phase<sup>69,70</sup> or due to the defects.<sup>91</sup>

Co doped ZnO is also a potential candidate for spintronics devices<sup>9</sup>. Search for DMS in Co doped ZnO is also started parallel to Mn doped ZnO and it is reported the material to be ferromagnetic below RT with the curie temperature ~280K for doping concentration up to 25%<sup>60</sup>. Room-temperature ferromagnetism in ZnO:Co has been widely reported<sup>60, 99-101</sup>, but paramagnetic or antiferromagnetic behavior has also been observed<sup>102-105</sup>. In case of thin films, there are many reports of RTFM, some of which attributed the observed RTFM to Co clustering<sup>98, 99</sup> and in some cases it is thought to be intrinsic in nature<sup>106-108</sup>, where double exchange interaction has been proposed as an explanation of RTFM<sup>108</sup>, and no observed ferromagnetism at all<sup>109</sup>. Yang et al. prepared Co doped ZnO thin films on sapphire (0001) substrates by PLD at various substrate temperatures in oxygen ambient condition. All samples exhibited room-temperature ferromagnetism, However the average moment per Co atom was much smaller than that of Co<sup>2+</sup> (3d<sup>7</sup>) is attributed due to the different distribution of Co<sup>2+</sup> ions and defects, as well as the different defect concentrations in thin films<sup>110</sup>. Li et al. grown Co-doped ZnO thin film by molecular beam epitaxy and only the Co composition of 20% shows ferromagnetism at room temperature and it is due to hydrogen facilitated interaction, which is supported experimentally by magnetic measurements on hydrogen-treated ZnO:Co as well as theoretically by first-principles calculation<sup>111</sup>.

Different magnetic properties like RTFM, diamagnetism or paramagnetism have been observed in Ni doped ZnO thin films also. Liu et. al.<sup>112</sup> have observed RTFM behaviour in Ni-doped ZnO films synthesized by pulse laser deposition while Wakano et. al.<sup>113</sup> have observed ferromagnetic properties only at low temperature. Different reasons have been attributed also in the literature to the origin of ferromagnetism in Ni doped ZnO films. While

Liu et. al. reported that defect states are responsible for the RTFM in Ni doped ZnO<sup>114</sup>, Srinet et. al. suggested that oxygen rich stoichiometry with enhanced Zn-O bonding favours the indirect Ni-O-Ni ferromagnetic exchange coupling and is responsible for RTFM<sup>115</sup>. Yin et. al. have reported paramagnetic and no ferromagnetic behaviour for Zn<sub>0.86</sub>Ni<sub>0.14</sub>O<sup>116</sup>. A detailed structure-property correlation and analysis done by Snure et. al. revealed that ferromagnetism in ZnO:Ni films is not an inherent property of the material but results due to a strong tendency of Ni to precipitate out in the ZnO matrix<sup>117</sup>.

Subsequently, many researchers explored the possibility of RTFM in Co doped TiO<sub>2</sub> systems. For example, Co doped TiO<sub>2</sub> rutile powder samples prepared by Nakai et al.<sup>118</sup> shows room temperature ferromagnetism and ilmenite-type anti-ferromagnetic component. The ferromagnetic character has been attributed to the presence of oxygen vacancies near dopant sites. Griffin et al.<sup>119</sup> performed TEM and XAS measurements on anatase Co doped TiO<sub>2</sub> films and found that the observed ferromagnetism is not carrier mediated, but due to the co-existence of another dielectric phase, while Kim et al. found that room temperature ferromagnetism in Co doped TiO<sub>2</sub> anatase thin films is due to the presence of Co clusters.<sup>120</sup> Detailed X-ray fluorescence holography and XAS experiments done on rutile paramagnetic and ferromagnetic Co doped TiO<sub>2</sub> films show that CoO<sub>2</sub>Ti<sub>4</sub> type of auboxidic phase is formed around Co which are responsible for high curie temperature in the samples.<sup>121</sup> Chambers et al. performed detailed analysis on Co doped TiO<sub>2</sub> anatase and found that Co atoms are substituting Ti atoms and no secondary phase is present.<sup>122</sup> Sol-gel derived Co doped rutile TiO<sub>2</sub> nanoparticles prepared by Jiang et al.<sup>123</sup> exhibit room temperature ferromagnetism due to the substitution of Co<sup>2+</sup> ions at TiO<sub>2</sub> host matrix which increases with an increase in Co doping concentration. Co doped rutile thin films fabricated on Al<sub>2</sub>O<sub>3</sub> substrates show the co-existence of Co in metallic as well as oxide valance state and the origin of the observed ferromagnetism has been attributed to interaction between doped Co ions and TiO<sub>2</sub> lattice.<sup>124</sup>

Theoretical calculations done by Anisimov et al.<sup>125</sup> showed that  $\text{Co}^{2+}$  doped rutile  $\text{TiO}_2$  shows weak ferromagnetism due to the large impurity-impurity distance, however stronger ferromagnetic character appeared after inclusion of oxygen vacancies. The effect of oxygen vacancies on the ferromagnetism of DMS materials have been directly observed by Wang et al.<sup>126, 127</sup> where the authors have found that saturation magnetization of Co doped and (Co,Cu) co-doped ZnO thin films decrease when annealed under oxygen ambient while it increases by annealing under hydrogen atmosphere. Roberts et al. have also found by density-functional calculations that activation of RTFM in highly insulating Co-doped anatase  $\text{TiO}_2$  is defect mediated and involves the formation of ordered  $\text{Co-Ti}^{+3}\text{-V}_\text{O}$  defect complexes.<sup>128</sup> Geng et al. performed ab-initio density functional calculations on Co doped rutile  $\text{TiO}_2$  and found that interstitial Co near the substitution impurities can reduce the spin polarization.<sup>129</sup>

Comparatively fewer reports are available on Mn doped  $\text{TiO}_2$  systems. Xu et al. prepared Mn doped  $\text{TiO}_2$  thin films by sol gel spin coating in which RTFM is found to increase with vacuum annealing of the samples, which is attributed to the increase in the oxygen vacancies or defects.<sup>130</sup> Similarly, ferromagnetic nature of Mn (>5%) doped  $\text{TiO}_2$  thin films on fused quartz silica substrates by spray pyrolysis technique is explained by the formation of bound magnetic polarons by Sharma et al.<sup>131</sup> Wang et al.<sup>132</sup> however showed that RTFM in Mn doped  $\text{TiO}_2$  thin film deposited on  $\alpha\text{-Al}_2\text{O}_3$  substrate by pulse laser deposition is hole mediated between the Mn magnetic moments. Room-temperature ferromagnetism has been found by Kim et al. in Mn doped  $\text{TiO}_2$  thin films prepared by sol gel method which is attributed to magnetic polaron formed by trapped electrons in oxygen vacancies and magnetic ions around them.<sup>133</sup> Xu et al. prepared Mn doped  $\text{TiO}_2$  thin film on  $\text{SrTiO}_3$  substrate by plasma assisted molecular beam epitaxy, in which ferromagnetism is attributed to a variety of reasons like growth condition, oxygen vacancy and interfacial defects and the bound magnetic polarons.<sup>134</sup>

Several studies have also been performed with simultaneous or co-doping of ZnO nanoparticles by two TM ions. For example, Jefferson et. al.<sup>135</sup> have found that co-doping of (Fe,Ni) into ZnO nanoparticles exhibits higher magnetization than that of Fe doped ZnO and Ni doped ZnO nanoparticles. They have suggested that the observed ferromagnetism in (Fe, Ni) co-doped ZnO nanoparticles could be the result of exchange interaction between conductive electron with local spin polarized electron on Ni<sup>+2</sup> or Fe<sup>+2</sup> ions. Co-doping of TM and rare earth (RE) ions simultaneously in ZnO has also been explored by several authors including one by our group also.<sup>136-138</sup>

Thus it is clear from the above examples that different groups have reported different reasons for the origin of ferromagnetism in a same DMS system and contradictory reports are also available in the literature regarding whether ferromagnetism observed in these system is due to the precipitation of metallic cluster in a homogenous oxide host matrix<sup>70</sup> or due to the uniformly distributed TM cations in the semiconductor lattice or due to the presence of an entirely separate magnetic phase<sup>69, 70</sup> or due to the defects<sup>91</sup>. Thus, the origin of ferromagnetism in TM doped ZnO and TiO<sub>2</sub> is still a fairly unresolved question and seeks further investigations through both experimental and theoretical approach towards this.

A systematic investigation of the local environment around the host and the dopant cations can yield unambiguous results regarding the origin of FM in these systems and synchrotron based X-ray Absorption Spectroscopy (XAS), which comprises of both X-ray Near Edge Structure (XANES) and Extended X-ray Absorption Fine Structure (EXAFS) techniques, is a perfect tool to study the local environments around impurities and defects due to its short range nature. XAS is an element specific tool and thus can yield local structural results separately surrounding all metal species present in a material. Moreover DMS materials being discussed here are generally nanocrystalline or thin films with very small amount of the dopant materials. Since single-phase domains are not sufficiently large in these

materials, X-ray diffraction, which acts on the principle of long range order, might not give the correct phase information and for such systems, EXAFS which basically probes the local order and does not depend on the long range order can yield better result so far microscopic behaviour of the samples is concerned. It has been observed by us and other groups also that in case of polycrystalline/amorphous oxide films, where GIXRD data cannot yield much quantitative result, EXAFS measurements can give useful information regarding structural aspects of the samples.<sup>139-141</sup>

Thus keeping the above challenges in mind, in this thesis work we have prepared a range of transition metal doped and co-doped ZnO and TiO<sub>2</sub> DMS thin films by r.f. sputtering technique on c-Si substrates and also free-standing flexible transition metal doped nano ZnO embedded polyvinylidene fluoride (PVDF) thin films by sol gel technique. As mentioned above these DMS thin films have primarily been characterised by EXAFS and XANES measurements. In all the above cases apart from the transition metal dopants (Mn,Fe,Ni,Co) and host metal (Zn and Ti) K edges, wherever was possible, measurements have also been carried out at the metal L edges and oxygen K edges. The data analysis has been aimed to the investigation of whether the dopant ions goes to the substitutional sites in the host matrix, whether any metallic cluster of the dopants have been formed in the host material, whether any other impurity phases are formed, what is the oxidation state of the dopant in the host lattice and whether any defect or vacancies are created in the host material due to the doping. The results have also been complemented with other measurements viz., grazing incidence X-ray diffraction (GIXRD), spectroscopic ellipsometry (SE), Photoluminescence (PL) or X-ray photoelectron spectroscopy (XPS) measurements whenever was required. In most of the cases the XANES features observed in the samples have also been compared with theoretically simulated results obtained from ab-initio first principle calculations which is

either available in the literature or has been simulated for this thesis work. These results have subsequently been used to explain the observed magnetic properties of the samples.

### **1.5 Outline of the thesis:**

The subsequent chapters of the thesis are arranged as follows. Chapter-2 deals with various experimental techniques used in this thesis work with brief descriptions of different equipments used and also describes the XAS data analysis technique in detail. In the beginning of this chapter, various sample preparation techniques used for the preparation of the samples studied in the present thesis work have been described. Subsequently, different thin film characterization techniques that have been employed in this thesis have been briefly discussed. The techniques of grazing incidence X-ray diffraction (GIXRD), spectroscopic ellipsometry (SE), Photoluminescence (PL) and magnetic measurement techniques have been described shortly. Finally the XAS technique, including both EXAFS and XANES, which has been used in this thesis work extensively in both hard X-ray and soft X-ray regions have been discussed in details. It is started with brief introduction of synchrotron source and various beamlines used for XAS measurements of the samples for present thesis and finally the XAS data analysis procedure has been described.

In the next chapters (Chapters 3-6) of the thesis work, we have presented the results of the above investigations on various DMS thin films with varying dopant concentrations. These chapters are divided based on magnetic and non magnetic dopant case for ZnO host lattice. Chapter-3, is devoted to correlation of local structure and magnetic properties of Mn doped ZnO thin films deposited by r.f. sputtering technique with different Mn doping concentrations. In Chapter-4, studies on a set of Fe, Co and Ni doped ZnO thin films deposited with rf magnetron sputtering technique on c-Si substrates with varying Fe, Co and Ni doping concentrations have been reported. In Chapter-5, the studies on a set of free standing and flexible films of ZnO nanocrystals embedded in polyvinylidene fluoride

(PVDF) matrix prepared by sol-gel technique have been presented. The samples discussed in this chapter include Ni, Co and Mn doped and (Ni,Co) co-doped nano-ZnO/PVDF composite films. In this study both poled and unpoled doped nano-ZnO/PVDF films have been subjected to FESEM, XPS and XANES/EXAFS studies and the results are presented in this chapter. In Chapter-6, the study on Mn and Co doped TiO<sub>2</sub> thin films prepared by rf magnetron sputtering technique on c-Si substrates, has been described. Finally in Chapter-7 the conclusions drawn in all the previous chapters in the different set of thin films have been summarized and future direction of the work has been mentioned.

## Chapter 2

### **EXPERIMENTATION AND DATA ANALYSIS**

In the first part of this chapter we describe the different experimental techniques used for preparation of the samples studied in this thesis. Two type of transition metal (TM) doped ZnO thin film samples are prepared for present thesis. TM doped ZnO and TM doped TiO<sub>2</sub> thin films on Si(111) substrate using r.f. magnetron sputtering system and TM doped ZnO flexible polymer composite films prepared by sol-gel technique. The second section of this chapter deals with different characterizations techniques used for these samples focusing mainly on X-ray Absorption Spectroscopy technique.

#### **2.1 Sample preparation:**

##### **2.1.1 Deposition of thin films by rf sputtering:**

TM doped ZnO thin films and TM doped TiO<sub>2</sub> thin films studied for the present thesis work have been deposited with varying doping concentration using an in-house built magnetron sputtering system<sup>142</sup>. Brief description and working principal of sputtering technique of thin film deposition is given below. Thin film deposition technology is becoming increasingly popular due to the fact that all microelectronic solid state devices are based on thin film deposition<sup>143</sup>. Thin film deposition techniques fall into two major categories viz., chemical vapour deposition (CVD) and physical vapour deposition (PVD). In case of CVD, the substrate is exposed to one or more volatile precursors which react and decompose on the substrate surface to produce the desired deposit. During this process, volatile by-products are also produced, which are removed by gas flow through the reaction chamber. PVD, on the other hand, comprises of a group of surface coating technologies where atom (or molecule) by atom transfer of material from the solid phase (target) to the

vapour phase and back to solid phase takes place, gradually building a film on a surface to be coated (substrate). Sputtering is also a physical vapour deposition (PVD) process in which a plasma is created between two electrodes in an inert gas atmosphere (generally argon) using an electric field. The momentum transfer theory can be used to understand the physics of sputtering, where kinetic momentum of incident ions are transferred to the atoms at the target surface upon collision and a collision cascade takes place within the top few layers in the material which results ejection of the target surface species<sup>144</sup>. The efficiency of sputtering is quantified by *sputtering yield* which is defined as the average number of ejected target atoms/molecules per single ion hitting the target. The yield of sputtering depends upon ion/target atomic mass, ion energy, target crystallinity and angle of incidence. The schematic of basic sputtering process is given in figure 2.1.

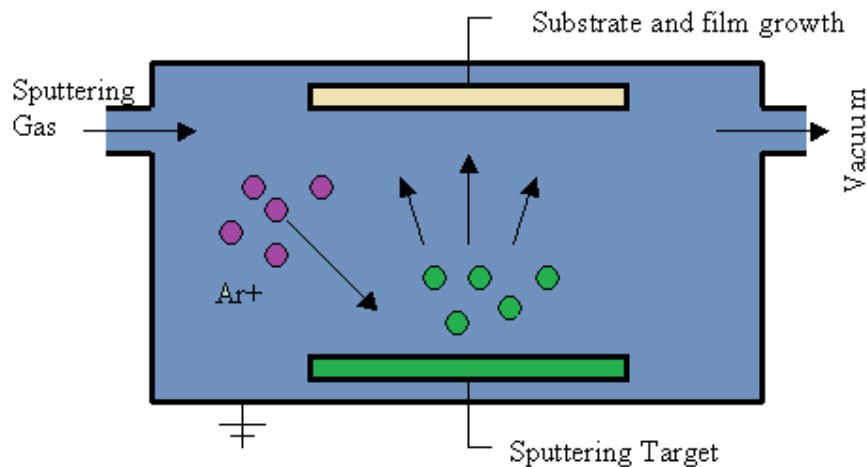


**Figure 2.1:** Schematic representation of sputter deposition technology.

Sputtering technique had different variants. The simplest variant of sputtering deposition is dc sputtering. In case of dc sputtering, positively charged ions ( $\text{Ar}^+$ ) from the plasma are accelerated towards the negatively charged electrode where the material to be deposited or the “target” is kept<sup>145</sup>. The positive ions are accelerated by potentials ranging from a few hundred to a few thousand electron volts and strike the negative electrode with sufficient force to dislodge and eject atoms from the target. These atoms (cluster of atoms or

ad-atoms) condense on substrate surface that is placed in proximity to the sputtering cathode and is generally kept grounded. In DC sputtering, there is a low concentration of secondary electrons. So, there will be fewer collisions in the plasma and thus large voltage and higher chamber ambient pressure are required to sustain the plasma. Another problem of DC sputtering is that it is only effective for deposition of conductive materials, since if an insulating target is used, a sheath of positive charge get accumulated in front of the target surface, thus prohibiting further  $\text{Ar}^+$  ions to reach the target and thus stops the sputtering process. This problem of sputtering of insulating material is solved in RF sputtering by a mechanism called the 'self bias'. In this process, an alternative electric field of megahertz frequency is applied to the target. In the presence of this alternating field both electrons and ions in the plasma oscillate and alternatively hit the target surface. However due to the fact that electrons are lighter in mass than ions, during positive cycle of RF field more numbers of electrons reach the target surface than ions in the negative half cycle. As a consequence, a net negative potential is produced in front of the target surface which drives positive ions towards the target surface and repels electrons in opposite way. This is called self biasing of the target. Once this happens, it behaves as a DC target where positive ions continuously bombard the target surface and sputtering takes place. In case of rf sputtering technique, which is used to sputter insulators like in the oxide semiconductors deposited in this thesis, sputtering conditions prevail at both target and substrate regions, however, target sputtering is made much more significant by reducing its effective area compared to the substrate since the self bias developed near any electrode is inversely proportional to the fourth power of electrode surface area i.e.  $V \propto A^{-4}$ . Typical RF frequency exploited for this purpose is in the range of 5-30 MHz. In practice, 13.56 MHz is used due to government communications regulations (International Telecommunications Union).

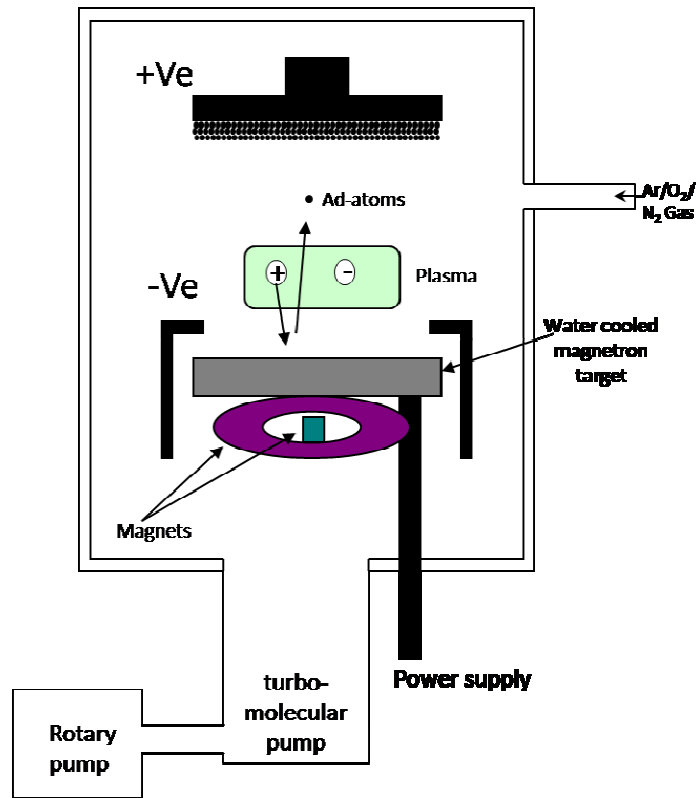


**Figure 2.2:** Schematic of R.F. Magnetron sputtering system.

In DC, or RF sputtering process discussed above, the secondary electrons have relatively longer mean free path (10's cm) and that's why the processes suffer from inefficient secondary electron process and thereby low ionization levels. This leads to slow etching of target surface and therefore lower deposition rate at relatively higher pressure. Magnetron sputtering technique, additionally uses a closed magnetic field around the target material so that electrons undergo helical movement near the target, enhancing the efficiency of the ionization process. This allows creation and sustention of plasma at relatively lower pressures which reduces both contamination in the growing film and energy loses of the sputtered atoms through collision with gas molecules. The main advantages of sputtering compared to other thin film deposition techniques are (i) higher kinetic energy of sputtered particles compared to energy of evaporated adatoms, resulting in higher surface mobility in

condensing particles and thus enabling smooth two-dimensional growth of the film compared to columnar growth in case of evaporation techniques, (ii) possibility of large area deposition, (iv) feasibility of alloy sputtering with required stoichiometry due to smaller difference in sputtering yields among elements of alloys compared to the difference in vapour pressure, (v) lower substrate temperature, (vi) feasibility of sputtering the materials with high melting point and (vii) better adhesion.



**Figure 2.3:** In-house built R.F. Magnetron sputtering deposition system at BARC-VIZAG, Visakapatnam.

TM doped ZnO thin films and TM doped TiO<sub>2</sub> thin films studied for present thesis work have been deposited with varying doping concentration using an in-house built DC/RF magnetron sputtering system available at A&MPD, BARC, Visakhapatnam Centre<sup>142</sup>. This system consists of two magnetrons cathodes (make-Edwards) of 3” diameter, each of which can be powered by either RF power supply (Make-Huttinger, Max 1.5 kW ) or DC power supply (Make-Millman, Max. 2.5 KW). The vacuum chamber is evacuated using a turbo molecular pump (Make:Alcatel) with backing Rotary pump (Make: Alcatel). The vacuum

chamber is equipped with one pirani (Make:HHV ) and penning gauge (Make:Pfeiffer ) for monitoring the chamber pressure. A quartz crystal thickness monitor (Make: Inficon ) is provided to monitor deposited thickness online. Cold water supply is provided with a custom made chiller in order to cool power supply, magnetron, quartz crystal head etc. Fig. 2.3 shows the picture of this in-house built dual magnetron sputtering system. This system can be used for the deposition of both metallic and dielectric samples.

High purity target discs of 75mm diameter were used as the target materials in the present system. Substrates used for all the depositions are crystalline silicon (111) having dimension of 25mm x 11mm, kept at room temperature and the depositions have been carried out under high purity argon ambient. The Ar flow rate was controlled by using a mass flow controller. The substrate holder is also water-cooled to cancel out the temperature rise by the plasma during the sputtering process. A quartz crystal thickness monitor has been used in the deposition system near the target for *in-situ* monitoring of the rate of deposition and total thickness deposited. The crystal monitor is calibrated by *ex-situ* thickness measurement of a ZnO/TiO<sub>2</sub> thin film by spectroscopic ellipsometry. The other deposition parameters used are sputtering pressure of  $\sim 10^{-3}$  mbar, substrate to target distance of 4.5 cm, RF power of 100 W and all the films were deposited for 20 minutes. In all cases, prior to deposition a base vacuum of  $\sim 10^{-6}$  mbar was archived. The substrates were not intentionally heated during deposition; however it has been observed that during deposition, the substrate temperature reaches up to 50–80°C due to the presence of the magnetron plasma.

### **2.1.2 Free standing polymer films:**

Zinc acetate dihydrate, transition metal acetate tetrahydrate, N-N dimethyl formamide, diethanolamine, and PVDF were used for synthesis of free standing TM doped ZnO/PVDF composite films. Protocol for obtaining the requisite sol for the deposition of TM doped nano-ZnO/PVDF films is as follows:

(i) Appropriate amount of Zn-acetate was taken in a conical flask to obtain a 10 wt% (0.275 M) sol with 4 ml dimethyl formamide (DMF). The above sol was refluxed for 1 h with constant stirring at 30°C for complete dissolution of the solute. Such stock solutions were obtained in different conical flasks for different doping concentrations.

(ii) Different amounts of transition metal-acetate were added to the above flasks to form  $Zn_{1-x}TM_xO$ . These mixtures were refluxed for 3 h with constant stirring at 150°C for complete dissolution of the solute with resultant formation of intermediate products of  $Zn(OH)_2$  and  $TM(OH)_2$ . We have added appropriate amount of dimethyl amine acting as a reducing agent to the above sol while keeping the heating and stirring for another 30 min.

(iii) A fixed amount of PVDF (15 wt%) was then added to the above sols which was cooled down to 60°C keeping stirring constant for another 2 h. A semi-gel sol with a brownish tinge was obtained.

The above sol was spin-casted uniformly on glass substrates at room temperature at a low spin (60 rpm) for depositing the TM-doped nano-ZnO/PVDF composite films. A photograph of the spin coater used for this is given in figure 2.4.



**Figure 2.4:** Actual picture of spin coater.

A microwave oven was used to heat the as-coated films at 100 W for 3 min. The films so obtained could be easily peeled out from the glass substrate. The flexible free-standing

films thus obtained were used for characterizations. Conventional hot plate heating of the as-deposited spin-cast films was avoided to ensure uniform heating of the films. Conventional heating of the as-spin casted films on glass substrate were prone to have pores arising out of bubbles emanating from the substrate/film interface. Low thermal conductivity of glass substrates prevents homogeneous heating of the as-cast films. The glass/film interface gets heated before the heat could be transmitted uniformly throughout the film volume. This uneven heating associated with the hot plate heating was completely eliminated by microwave heating which imparted uniform heat throughout the bulk of the film. The quality of the films so obtained was extremely good and the process was completely reproducible. The thicknesses of the composite films as measured were ~10 mm and the active film area was ~5 mm x 5 mm.

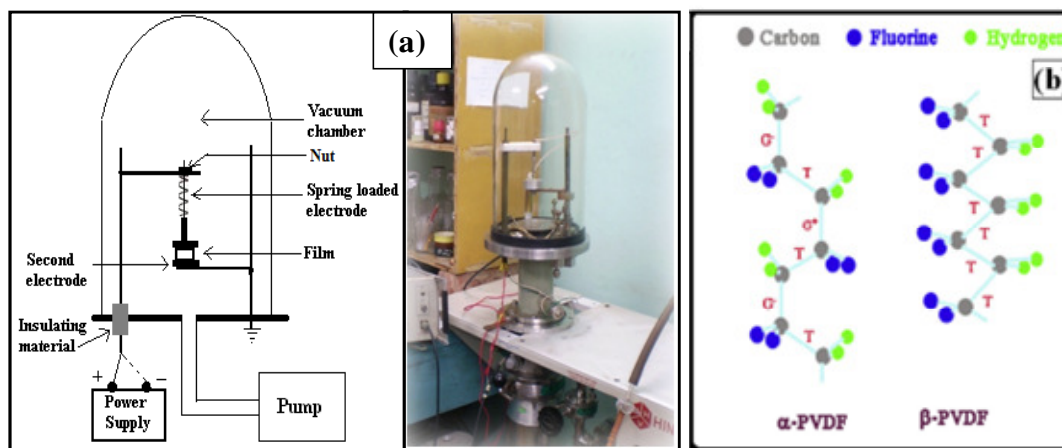


**Figure 2.5:** Schematic diagram and actual picture of (a) poling unit used, (b) Schematic view of two of the PVDF phases. The a-phase consists of a series of non-polar anti-parallel chains, whereas b-phase phase consists of a series of polar parallel chains.

As has been mentioned in Chapter-1, to generate poled films with hydrogen terminated and fluorine-terminated surface on opposite faces, the films were poled in vacuum ( $\sim 10^{-6}$  Torr) at a field of 5 MV/m for 2 h. Fig. 2.5 (a) shows an illustrative schematic diagram of the same<sup>146</sup>. The poling unit consisted of a spring loaded electrode and a film holder, which acted as the second electrode. The above assembly was housed in a pyrex glass

vacuum chamber which could be evacuated to a level of  $\sim 10^{-6}$  Torr. Appropriate feed-through allowed the HT connections. The electrodes were connected to a regulated d.c. power supply (0-10 kV at 50 mA) with appropriate protection for short circuit. Fig. 2.5(b) gives the schematic representation of the structure of the unpoled and poled PVDF films, respectively. It can be seen that, upon poling the as-deposited ( $\alpha$ -phase) PVDF film converts to  $\beta$  phase PVDF with one side preferentially hydrogen terminated while the other side preferentially fluorine terminated.

## 2.2 XAS measurements and data analysis:

### 2.2.1 Theoretical formulation:

X-ray can interact with material either by scattering or absorption phenomena. Interaction of X-ray with matter (figure 2.6) is primarily divided in three processes depending on energy of X-ray and the elemental composition: Thomson scattering, Compton scattering and Photoelectric effect.

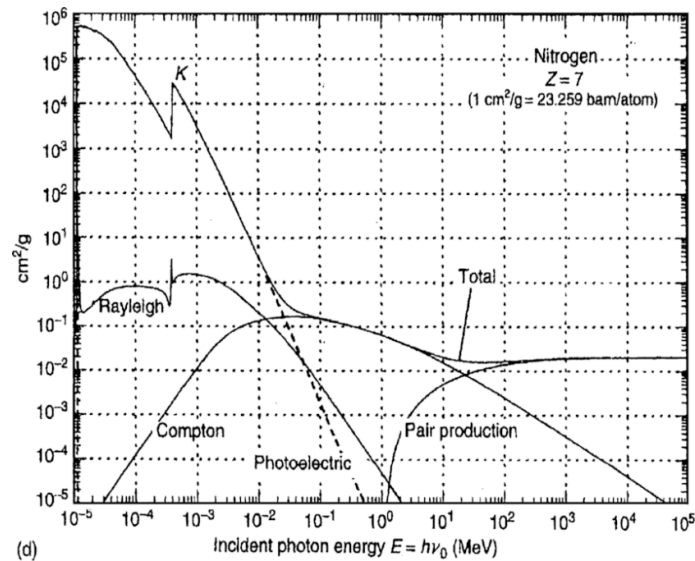


**Figure 2.6:** Photo absorption cross section for different phenomenon of interaction of X-ray with matter <sup>147</sup>.

Thomson scattering is an elastic scattering of photons by the free or bound charged particles (electrons) in the medium. For most of the materials Thomson scattering is dominant when the energy of the photon is less. According to classical theory, In the low-energy limit, the electric field of the incident wave (photon) accelerates the charged particle, causing it, in turn, to emit radiation at the same frequency as the incident wave. Thus, the particle is behaving like small radiating dipole, consequently emitting radiation. Compton scattering is the result of a high-energy photon colliding with a free electron or with an atom having loosely bound electrons. The scattered radiation experiences a wavelength or energy shift due to transfer of momentum to the electron. Compton scattering is purely quantum mechanical phenomena, which can be explained by assuming particle nature of light.

In photoelectric process an X-ray is absorbed by an atom ejecting a core level electron (K, L or M shell) out of the atom and into the continuum. This phenomenon occurs when energy of the incident photon matches with the binding energy of one of the core level electron. The atom is then left in an excited state with an empty electronic level (a core hole). The electron ejected from the atom is called the photo electron and this phenomenon is known as photo electric effect. Following the photoelectric effect, secondary processes such as emission of fluorescence or Auger electrons can also occur. The excited core hole will relax back to a ground state by another core level electron jumping into the ground level. This can be accompanied by either emission of X-ray in which excess energy of electron is emitted as X-ray called fluorescence or ejection of electron in which excess energy is transferred to another core level electron and prompting that electron to emit out of the material is called Auger emission. In the hard X-ray regime ( $> 2$  keV), X-ray fluorescence is more likely to occur than Auger emission, but for lower energy X-ray absorption, Auger processes dominate<sup>148</sup>.

In different energy regime of X-ray, the probabilities of occurrence of the above processes are different and it is defined by absorption cross section which represents the probability of a specific type of X-ray interaction with matter. Fig. 2.6 depicts the cross section of different processes while interaction of X-ray with matter. In general, the absorption cross section smoothly decreases as the energy increases as  $\sim E^{-3}$ , however at specific energies there are sharp increase in absorption cross section, defined as X-ray absorption edge. These absorption edges occur due to photoelectric effect, i.e. when energy of incident X-ray photon matches with binding energy of one of the core level electron and it knocks out this electron by photoelectric process. These absorption edges are characteristics of element present in the material. A closer look near the absorption edge reveals fine oscillations near and above the absorption edge is called X-ray Absorption Fine Structure (XAFS) and it contains information related to the physical and chemical state of absorbing element. The experimental technique used to study these oscillation to obtain the various information like formal oxidation state, coordination chemistry, near neighbour distances, coordination number and species of the atoms immediately surrounding the selected element is called X-ray Absorption spectroscopy (XAS).

X-ray absorption spectroscopy (XAS) measures the energy-dependent fine structure of the X-ray absorption coefficient near the absorption edge of a particular element to study the local structure. Since it is local structure technique and element specific, XAS can be applied not only to crystals, but also to materials that possess little or no long-range translational order: amorphous systems, glasses, quasicrystals, disordered films, membranes, solutions, liquids, metalloproteins – even molecular gases. This versatility allows it to be used in a wide variety of disciplines: physics, chemistry, biology, biophysics, medicine, engineering, environmental science, materials science, and geology<sup>149-152</sup>.

Fine structure oscillations in X-ray absorption spectra is known since 1920 when it was first observed<sup>153, 154</sup>. A milestone to use these as an accurate and quantitative structural technique is k-space Fourier transform (FT) proposed by Sayers, Stern and Lytle in 1971 to separate peaks corresponding to various atomic shells<sup>155</sup>. The Fourier transform has also prompted another key development in the XAS theory, namely, the treatment of the multiple-scattering (MS) effects in terms of effective path length first proposed by Lee and Pendry in 1975<sup>156</sup>. Later, the path-by-path XAS theory was greatly developed by Rehr and Albers who proposed a separable representation of the Green's-function propagators to overcome all the computational difficulties<sup>157</sup>. So far, various advancements in the theoretical models have been obtained such as full multiple-scattering (FMS)<sup>158</sup>, self-consistent field and fully relativistic calculations<sup>159</sup> especially for a quantitative analysis of the near-edge regime. The EXAFS theory is implemented in various ab initio codes like EXCURV<sup>160</sup>, FEFF<sup>161</sup>, GNXAS<sup>162</sup>, WIEN2k<sup>163</sup>, NSRL-XAFS<sup>164</sup> etc.

A typical X-ray absorption spectrum is shown in figure 2.7. The X-ray absorption spectrum is typically divided into two regimes: X-ray Absorption Near Edge Spectroscopy (XANES) and Extended X-ray Absorption Fine Structure spectroscopy (EXAFS). Though the two have the same physical origin, this distinction is convenient for the interpretation and provides different information about the system. XANES is strongly sensitive to formal oxidation state and coordination geometry (e.g., octahedral, tetrahedral coordination) of the absorbing atom, while the EXAFS is used to determine the distances, coordination number, and species of the neighbors of the absorbing atom.

EXAFS is a quantum mechanical phenomenon that is based on X-ray photoelectric effect, in which X-ray photon incident on an atom within a sample is absorbed and liberates a photoelectron from an inner atomic orbital. The photoelectron wave scatters from the atoms around the X-ray absorbing atom, creating interferences between the outgoing and scattered

parts of the photoelectron wave function. These quantum interference effects cause an energy-dependent variation in the X-ray absorption probability, which is proportional to the X-ray absorption coefficient, a measurable quantity. Since the EXAFS oscillations arise due to the presence of neighboring atoms, these oscillations can be analyzed to extract information like bond distances, coordination numbers and disorder factor of neighboring atoms with respect to the absorbing atom.

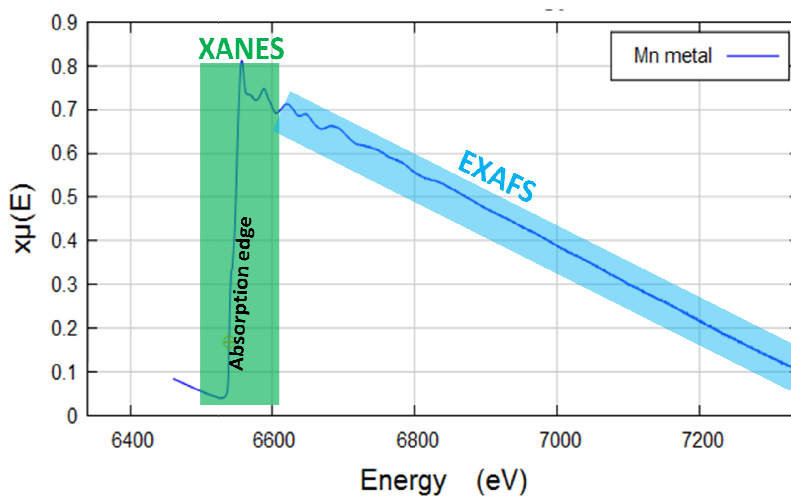


**Figure 2.7:** A typical X-ray absorption spectrum.

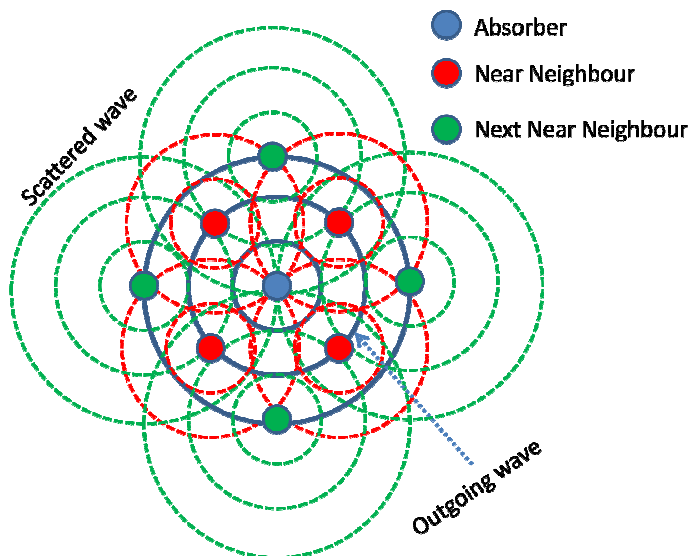


**Figure 2.8:** Schematic of scattering.

The observed oscillations can be described by EXAFS equation. The derivation of EXAFS equation is given in many books and reviews<sup>148-150, 165-167</sup>. X-ray absorption is a transition between two quantum states, absorption coefficient in this process is proportion to transition probability and can be written using Fermi Golden's rule as:-

$$\mu \propto \left| \langle i | H | f \rangle \right|^2 \quad (2.1)$$

Where  $\langle i |$  represents the initial state with an X-ray, a core electron, and no photo-electron to a final state and  $| f \rangle$  represents the final state with no X-ray, a core hole, and a photo-electron. The photoelectron emitted from absorbing atom will travel in material and backscattered by electron cloud of nearby atoms (Fig. 2.8). This backscattered photoelectron wave will interfere with the outgoing wave and change the final state, however the initial state will be same since the core level electron is very tightly bound to the absorbing atom. The final state now can be written using two terms, "bare atom" portion  $| f_0 \rangle$  and one that is the effect of neighbouring atoms  $| \Delta f \rangle$ , i.e.  $| f \rangle = | f_0 \rangle + | \Delta f \rangle$ . Thus,

$$\begin{aligned} \mu ( E ) &\propto \left( \langle i | H | f_0 \rangle + \langle i | H | \Delta f \rangle \right) \times \left( \langle i | H | f_0 \rangle + \langle i | H | \Delta f \rangle \right)^* \\ &\propto \left| \langle i | H | f_0 \rangle \right|^2 + \left| \langle i | H | \Delta f \rangle \right|^2 + \langle i | H | f_0 \rangle \times \langle i | H | \Delta f \rangle^* + \langle i | H | \Delta f \rangle \times \langle i | H | f_0 \rangle^* \\ &\propto \left| \langle i | H | f_0 \rangle \right|^2 + 2 \operatorname{Re} \left[ \langle i | H | \Delta f \rangle \times \langle i | H | f_0 \rangle^* \right] \end{aligned}$$

Neglecting the small contribution due to  $\left| \langle i | H | \Delta f \rangle \right|^2$  term, one gets-

$$\mu ( E ) \propto \left| \langle i | H | f_0 \rangle \right|^2 \left[ 1 + \frac{2 \operatorname{Re} \left[ \langle i | H | \Delta f \rangle \times \langle i | H | f_0 \rangle^* \right]}{\left| \langle i | H | f_0 \rangle \right|^2} \right] \quad (2.2)$$

By rearranging above equation,

$$\mu(E) = \mu_0(E)[1 + \chi(E)] \quad (2.3)$$

Comparing equation (2.3) with equation (2.2) we can write-

$$\chi(E) = \frac{\mu(E) - \mu_0(E)}{\Delta\mu_0(E)} \quad (2.4)$$

So, EXAFS oscillation can be written as,

$$\chi(E) \propto \langle i | H | \Delta f \rangle \quad (2.5)$$

As per quantum radiation theory, the interaction term H is proportional to  $e^{ikr}$ . The initial state is a tightly bound core level which can be approximated as a delta function. The change in final state is same as the wave function of scattered photo electron  $\psi_{scatt}(r)$ . Putting all these terms, one can write the expression for EXAFS as

$$\chi(E) \propto \int \delta r e^{ikr} \psi_{scatt}(r) dr = \psi_{scatt}(0) \quad (2.6)$$

To say it in words, the EXAFS function is proportional to the scattered photoelectron at the absorbing atom. Now if we consider the outgoing photo electron wave function  $\psi(k, r)$  as spherical wave, we can write-

$$\psi(k, r) = \frac{e^{ikr}}{kr} \quad (2.7)$$

where  $k$  is the photoelectron wave vector, defined as  $k = \sqrt{\frac{2m(E-E_0)}{\hbar^2}}$ , where  $E$  is the incident photon energy and  $E_0$  is the binding energy of the core shell electron. This photoelectron travels a distance  $R$  to the neighbouring atom, gets scattered from neighbouring atoms and then traverses back to the absorbing atom. The amplitude of scattered photo electron at the position of absorbing atom then becomes

$$\psi_{scatt}(k, r=0) = \frac{e^{ikR}}{kR} \left[ 2kf(k) e^{i\delta(k)} \right] \frac{e^{ikR}}{kR} + C.C. \quad (2.8)$$

where,  $f(k)$  and  $\delta(k)$  are back scattering amplitude and scattering phase shift due to the scattering atom. The scattering factors  $f(k)$  and  $\delta(k)$  depends upon the atomic number,  $Z$  of the neighbouring atom. These scattering factors make EXAFS sensitive to the presence of neighbouring atoms. Combing equation 2.6 and 2.8 we get, after few more simplification

$$\chi(k) = \frac{f(k)}{kR^2} \sin [2kR + \delta(k)] \quad (2.9)$$

This represents EXAFS equation considering one pair of absorbing atom and scattering atoms. However, in real scenario, often there is large number of scattering atoms are present at approximately same distance, called coordination shells. However, the distance of each atom in coordination shell is not same due to the effect of thermal or static disorder in the bond distances and we need to average over their contribution. As a first approximation i.e. assuming one type of neighbouring atoms and Gaussian distributions of neighbouring atom's disorder, the EXAFS equation becomes:

$$\chi(k) = \frac{Ne^{-2k^2\sigma^2} f(k)}{kR^2} \sin [2kR + \delta(k)] \quad (2.10)$$

where,  $N$  is the coordination number in one coordination shell at a distance of  $R$  and  $\sigma^2$  is the mean-square-displacement in the bond distance  $R$ . Summing over the contribution due to different coordination shells, EXAFS equation becomes

$$\chi(k) = \sum_j \frac{N_j f_j(k)}{kR_j^2} \sin [2kR_j + \delta_j(k)] e^{-2k^2\sigma_j^2} \quad (2.11)$$

where,  $j$  stands for the individual coordination shell of identical atoms at approximately the same distance from the central atom. In principle there could be many such shells, but as shells of similar  $Z$  become close enough (i.e., within a  $0.05\text{\AA}$  of each other), they become difficult to distinguish from one another and they are often represented by a single shell having equivalent multiple degeneracy.

Before applying the EXAFS equation (2.11) to any practical case, it needs an important correction. At the start of the derivation, we assumed that photoelectron wave traverses the distance between absorbing and neighbouring atom as spherical wave. In reality, these photoelectrons can undergo inelastic scattering with the conduction electrons; phonons etc. and its energy may get changed. The criteria for a photo electron to participate in the XAFS is that the photo-electron has to elastically scatter from the neighbouring atom and return to the absorbing atom and also, the photoelectron has to return back before the excited state decays. To take inelastic scattering and the core-hole lifetime into account one should rather use a damped spherical wave like:

$$\psi(k, r) = \frac{e^{ikr} e^{-2r/\lambda(k)}}{kr} \quad (2.12)$$

where,  $\lambda$  is the mean free path that represents the distance that a photoelectron can traverse without undergoing inelastic scattering and before the core hole is filled. The mean free path typically falls in the range of 5-30 Å and has a fairly universal functional relationship with photo electron wave number,  $k$  as shown in fig. 2.9.

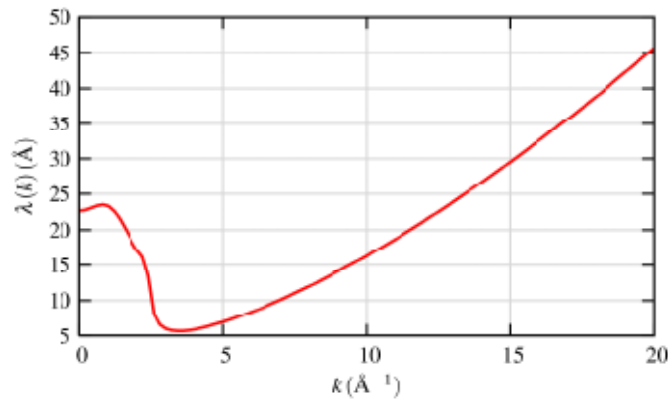


**Figure 2.9:** Typical characteristic of photoelectron mean free path vs. wave number.

One more correction is added to the final equation is called passive electron effect. As a consequence of absorption of the incident photon, a core electron is knocked out from the excited atom. The atomic electrons of this excited atom perceive a modified potential, which

can be approximated by that of an atom with its  $Z$  increased by 1. Thus the many body relaxation effect reduces the value of  $\mu$  by the factor  $S_0^2$ . This usually has a value between 0.7 and 1.0 and does not depend on  $k$ .

Taking the mean free path correction into account, the EXAFS equation becomes-

$$\chi(k) = \sum_j \frac{N_j S_0^2 f_j(k)}{k R_j^2} \sin [2kR_j + \delta_j(k)] e^{-2k^2 \sigma_j^2} e^{-2R_j/\lambda(k)} \quad (2.13)$$

This is the EXAFS equation which widely used for simulating theoretical EXAFS spectra of any species in order to carry out the analysis of experimental EXAFS data. Certainly, this requires a priori knowledge about scattering factors  $f(k)$  and  $\delta(k)$ . These scattering factors are function of atomic number  $Z$  and are usually calculated theoretically with very high accuracy. One important corollary that can be drawn from EXAFS equation follows that because of  $\lambda(k)$  term and  $R^{-2}$  term in the equation, EXAFS is inherently a local probe i.e. EXAFS cannot see much further than  $\sim 8 \text{ \AA}$ . The contribution of different terms in EXAFS oscillation is as follows:

(1)  $N_j$ : Coordination number  $N_j$  contributes in amplitude of EXAFS signal and does not have  $k$  dependence.

(2)  $S_0^2$ : This term basically contributes in amplitude of EXAFS oscillation. It is different for different elements, but the value is generally transferable between different species from the same element and the same edge.

(3)  $R_j$ : The term  $R_j$  is the half path length of the photoelectron (i.e., the distance between the absorber and a coordinating atom for a single-scattering event). The term  $\sin(2kR_j + \delta_j(k))$  defines the oscillation frequency of each coordination shell. The EXAFS oscillations are convolution from all the coordination shells. It is this sine term in the EXAFS equation that makes the Fourier transform (FT) of the XAFS signal such a powerful tool, because a FT results in peaks at distances related to  $R_j$ .

(4) $\sigma^2$ : This term has contributions from dynamic (thermal) disorder as well as static disorder (structural heterogeneity) as stated above. A distribution of distances within a single shell decreases the amplitude of the EXAFS signal because the phase differences between outgoing and scattered photoelectrons are shifted slightly for each atom in the coordination shell.

## **2.2.2 XAS measurements:**

### **2.2.2.1 Indus-2 Synchrotron source:**

It is evident that X-ray absorption spectroscopy measurements needs a bright and tunable X-ray source and presently only synchrotron radiation sources are used to carry out XAS measurements world-wide. When a charged particle traverses a magnetic field it is forced to change its direction of motion thereby emitting electromagnetic radiation. In a synchrotron, electrons of relativistic speed are forced to circulate in a storage ring by a series of bending magnets<sup>168</sup>. The radiation thus created is characterized by a continuous energy spectrum over a wide range of wavelengths (from infrared to hard X-rays), high intensity, strong polarization and a pulsed nature. Modern synchrotron facilities also have additional elements, so-called insertion devices, placed in the straight sections between the bending magnets. These devices constitute a series of alternating magnetic fields that force the electron beam to perform either strong (wiggler) or gentle (undulator) oscillations. The wiggler emits a broad beam of incoherent radiation characterized by increased intensity and a continuous energy spectrum extending to much higher X-ray energies compared to a bending magnet. The undulator emits a narrow beam of coherent radiation the intensity of which is amplified up to 10,000 times but only at certain energies. Based on these characteristics, the source (bending magnet, wiggler or undulator) best suited for a particular experimental technique is chosen. For the present thesis work, all XAS measurements have been carried out at Indus-2 Synchrotron facility at RRCAT, Indore, India.<sup>169</sup> The schematic of Indus-2

synchrotron source is shown in figure 2.10. The electron produces in a source are first accelerated using linear accelerator or microtron before their energy is further increased in the booster ring. From here they are transferred to the storage ring where they circulates over million times each second, creating intense electromagnetic radiation. The synchrotron source Indus-2 was commissioned in 2005 and is presently being operated with 2.5 GeV electron energy at 200 mA beam current and a critical wavelength of about  $2\text{\AA}$ , providing a spectrum from infra-red to hard X-ray regime. The storage ring of Indus-2 is 172.4 meter (circumference) consisting of 8 unit cells each providing a 4.5 m long straight section. Each of the eight super periods has two dipole bending magnets (1.502 T), four focusing and five defocusing quadrupoles and six sextupoles. Four RF cavities are used for RF voltage of 1.5 MV to achieve 2.5 GeV energy with beam emittance of  $X=5.81 \times 10^{-8} \text{m}\cdot\text{rad}$  and  $Y=5.81 \times 10^{-9} \text{m}\cdot\text{rad}$ . The insertion devices which are going to be installed on Indus-2 in near future include two planar undulators, one APPLE type undulator and one super conducting wavelength shifter.

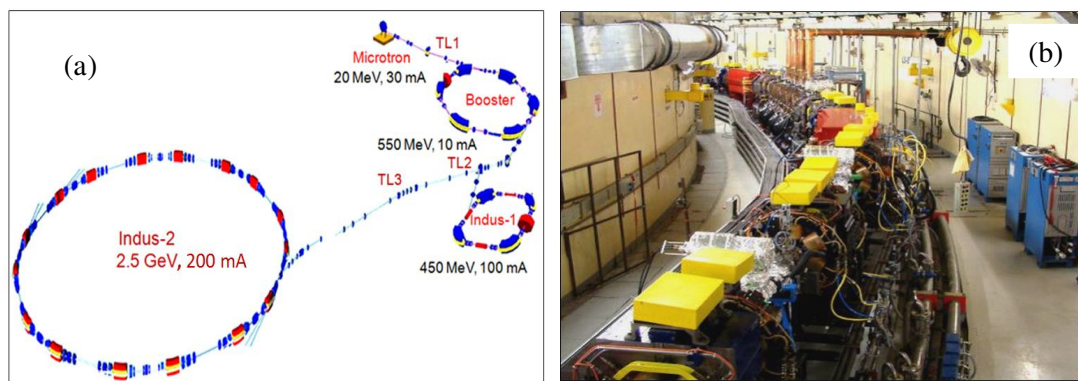


**Figure 2.10:** Indus-2 Synchrotron Source (2.5 GeV, 100 mA) at Raja Ramanna Centre for Advanced Technology (RRCAT), Indore, India<sup>170-172</sup>

XAS measurements on the samples studied in this thesis have been carried out at the Energy Scanning EXAFS beamline (BL-09) and Soft X-ray EXAFS beamline (BL-01) at Indus-2 SRS<sup>170</sup> both built at bending magnet ports. XAS measurements at transition metal

dopants (Mn,Fe,Ni,Co) and host metal (Zn and Ti) K edges have been carried out with hard X-rays at the Energy Scanning EXAFS beamline (BL-09), whereas soft X-ray XAS measurements at metal L edges and oxygen K edges have been carried out at the Soft X-ray EXAFS beamline (BL-01). Beamlines deliver the radiation at the end station where it can be used for variety of experimental techniques. Beamlines are complex instruments that perform a variety of functions, preparing the beam for the experiment by precollimating, filtering, splitting, monochromating and focusing, using proper X-ray optics and performing precisely timed data acquisition that is synchronized to the motions of beamline optics.

#### **2.2.2.2 Energy Scanning EXAFS beamline (BL-09):**

As has been mentioned above all XANES and EXAFS measurements presented in this thesis in the hard X-ray regime have been carried out at the Energy-Scanning EXAFS beamline (BL-9) of Indus-2 SRS<sup>170-172</sup>. This beamline operates in the energy range of 4 keV-25 keV. The beamline optics consist of a Rh/Pt coated collimating meridional cylindrical mirror and the collimated beam reflected by the mirror is monochromatized by a Si(111) ( $2d = 6.2709 \text{ \AA}$ ) based double crystal monochromator (DCM). The second crystal of DCM is a sagittal cylinder used for horizontal focussing while a Rh/Pt coated bendable post mirror facing down is used for vertical focusing of the beam at the sample position. Rejection of the higher harmonic content in the X-ray beam is performed by detuning the second crystal of the DCM to an extent so that the intensities of the higher harmonics are reduced by 99% with the loss of about half intensity of the incident flux. The energy resolution ( $\frac{E}{\Delta E}$ ) of the beamline at 10 KeV is  $\sim 10^4$ .

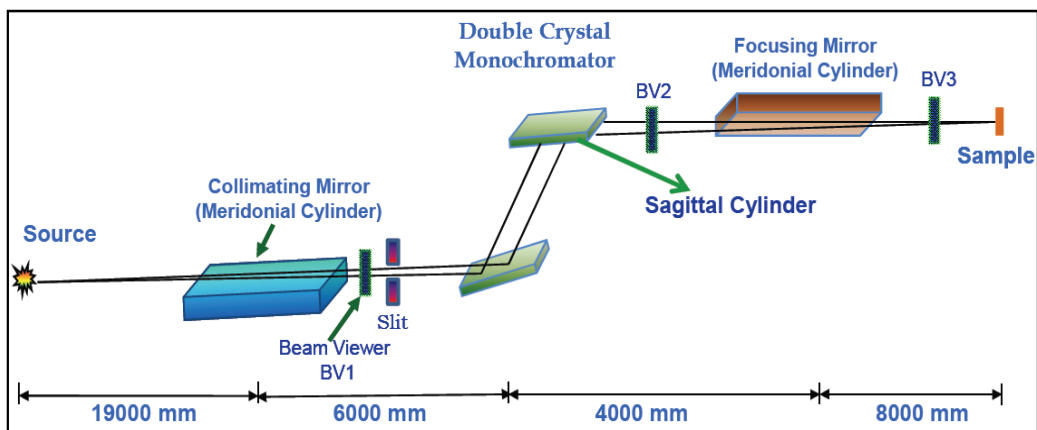


**Figure 2.11:** Schematic layout of Scanning EXAFS Beamline BL-09.

In this thesis work, hard X-ray XAFS measurements are done in transmission as well as in fluorescence mode. All the samples deposited on Si substrate ( Mn, Co, Ni and Fe doped ZnO; Mn and Co doped TiO<sub>2</sub> ) are measured in fluorescence mode only. In case of free standing flexible polymer films host edge (Zn edge) is measured in transmission mode and dopant edge (Mn, Co, Ni ) is measured in fluorescence mode.

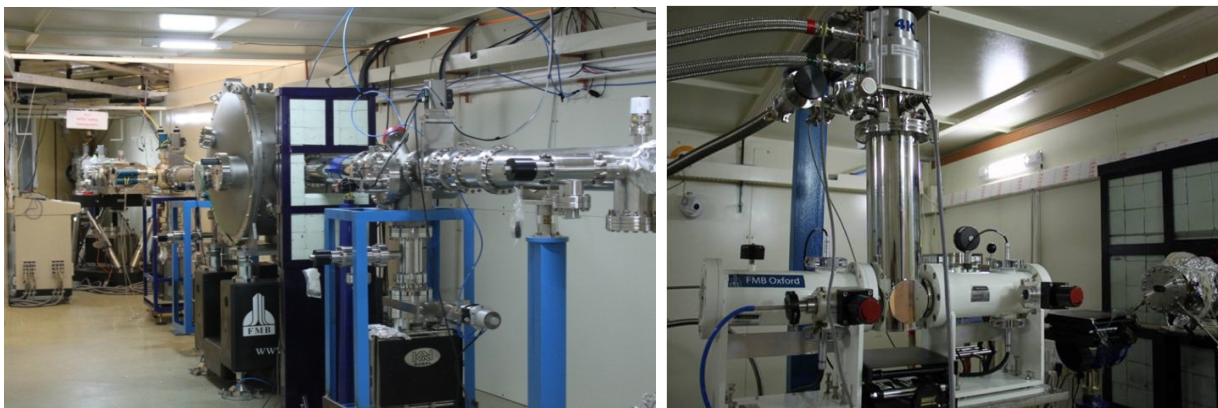


**Figure 2.12:** Photograph of (a) optics hutch and (b) experimental station of Scanning EXAFS Beamline BL-09.



**Figure 2.13:** Experimental set-up for transmission mode of EXAFS measurement.

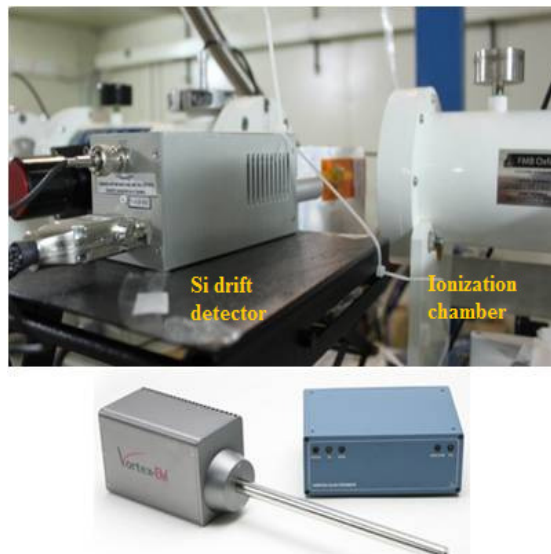


**Figure 2.14:** Experimental set-up for fluorescence mode of XAFS measurement.

For recording the X-ray absorption spectra in transmission mode, the sample is placed between two 30 cm long ionization chamber detectors as shown in fig. 2.13 The first ionization chamber measures the incident flux ( $I_0$ ) and the second ionization chamber measures the transmitted intensity ( $I_t$ ). Absorption ( $\mu$ ) is calculated using formula,

$\mu t = \log\left(\frac{I_0}{I_t}\right)$ . A third ionization chamber is also used after the second ionization chamber

where reference metal foils are measured for energy calibration. Appropriate gas pressure and gas mixture have been chosen to achieve 10-20% absorption in first ionization chamber and 70-90% absorption in second ionization chamber to obtain better signal to noise ratio.

For recording the X-ray absorption spectra in fluorescence mode, the sample is placed at  $45^\circ$  to the incident X-ray beam. For measuring the fluorescence spectrum from the sample, a single channel Si drift detector is placed in front of the sample at  $45^\circ$ .

The detector is placed at right angle to the incident beam as shown in fig. 2.14 so that the scattered X-ray is largely suppressed as the incident X-ray is polarized in the plane of synchrotron. An ionization chamber filled with a pre-defined gas mixture to absorb 10-20% of the incident beam was placed prior the sample stage to measure the incident beam ( $I_0$ ). A proper region of interest (ROI) is selected in the detector output to selectively measure the fluorescence intensity of the absorbing atomic species ( $I_f$ ). Thus the absorption coefficient of the sample was determined by the relation ( $\mu = I_f / I_0$ ) and the spectrum was obtained as a function of the energy by scanning the DCM of the beam line over the specified energy range.

### **2.2.2.3 Soft X-ray EXAFS beamline (BL-01):**

Soft X-ray absorption spectroscopy beamline (SXAS) BL-01 is located at bending magnet source of Indus-2 synchrotron source<sup>173</sup>. This beamline covers energy ranges of 100-1200 eV with option of polarization selectivity using a water cooled polarization selection aperture of 200 micron width. Spherical grating monochromator (SGM) with three interchangeable gratings (290, 660, 1500 gr/mm) is used for monochromatic beam at sample position. The pre mirror is used to focus the beam at slit S1 (Virtual source) and post mirror is used to focus the beam at sample position. The exit slit of the monochromator is movable in horizontal as well as lateral direction. During the energy scan, exit slit is moved to

minimize the defocus effect of monochromator. The beam size at sample position is  $\sim 500 \mu\text{m}$  x  $500 \mu\text{m}$ . The sample is kept in the vacuum and photoelectrons are measured in Total electron yield mode (TEY).

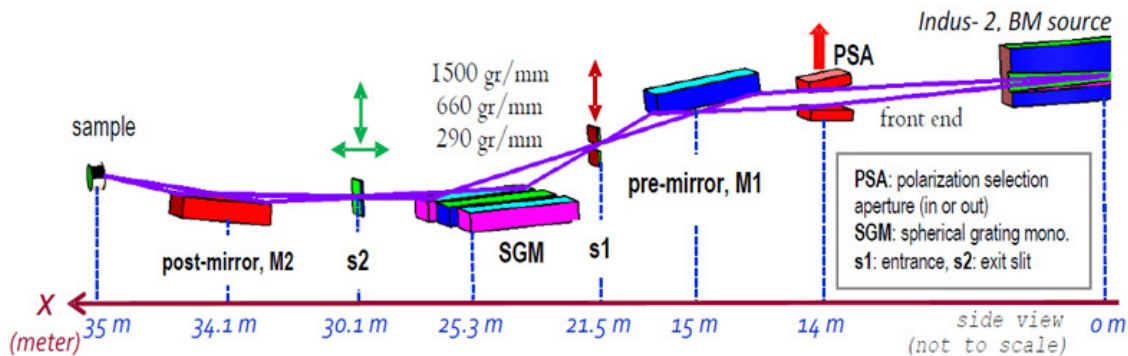


**Figure 2.15:** Schematic layout of Soft X-ray Absorption Beamline BL-01<sup>173</sup>.

### 2.2.3 EXAS data analysis:

The standard order of operations in EXAFS data analysis consists of the following steps:

- (1) Normalization of the data to unit edge step
- (2) Background subtraction
- (3) Conversion from energy to k-space
- (4) Fourier transformation to R-space and generation of experimental  $\chi(R)$  vs. R spectra
- (5) Windowing and inverse transformation
- (6) Generation of theoretical  $\chi(R)$  vs. R spectra using a crystallographic/amorphous model
- (7) Fitting of the experimental spectra with the theoretical spectra by nonlinear least squares fitting.

EXAFS data analysis step 1-5 is performed in ATHENA subroutine and step 6 and 7 is performed in ARTEMIS subroutines, which are discussed later.

### 2.2.3.1 Software package:

Demeter is a comprehensive system programme for processing and analyzing X-ray Absorption Spectroscopy data. These computer codes have been developed by Dr. Bruce Ravel and co-workers over the years<sup>174</sup> providing a rich graphical interface to the extensive analytical and numerical capabilities of the popular IFEFFIT library<sup>175</sup>. Demeter is freely available and actively developed and maintained. This package is based on the IFEFFIT library of numerical and XAS algorithms and it is written in the Perl programming language. This package includes : (i) ATHENA, a program for XAS data processing, (ii) ARTEMIS, a program for analysis of extended X-ray absorption fine structure (EXAFS) data using theoretical standards computed by the FEFF program<sup>159, 176</sup> and (iii) HEPHAESTUS, a collection of beamline utilities based on tables of atomic absorption data.

### 2.2.3.2 Data reduction using Athena:

ATHENA is used for all the main steps in data processing as:

- (1) Normalization of the data to unit edge step
- (2) Background subtraction
- (3) Conversion from energy to k-space
- (4) Fourier transformation to R-space and generation of experimental  $\chi(\mathbf{R})$  vs.  $\mathbf{R}$  spectra
- (5) Windowing and inverse transformation

As such ATHENA is useful for data visualization at the beamline as well as for processing of data such as conversion of raw data to  $\mu(E)$  spectra, plotting, energy calibration, alignment of data, use of reference spectra, deglitching and merging of data etc. The normal view of the ATHENA window is shown in Fig. 2.16.

Data conversion from its raw form is executed, creating  $\mu(E)$  spectra from transmission, fluorescence or electron yield experiments. Edge-step normalization of the data is determined by a linear pre-edge subtraction and regression of a quadratic polynomial

beyond the edge. The absorption edge  $E_0$ , the threshold energy (muffin tin zero level in the theory) is determined automatically as the data is imported by finding the first large peak in the first derivative of the  $\mu_0(E)$  spectrum, but can also be set interactively. Typically the half-maximum point on the edge is taken, or the first maxima of the derivative of the EXAFS signal.

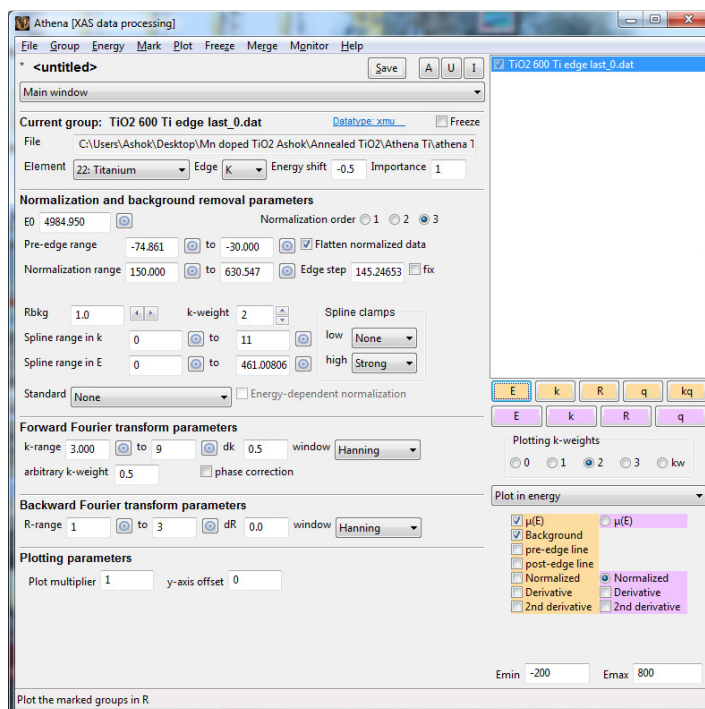


**Figure 2.16:** The main window of ATHENA program.

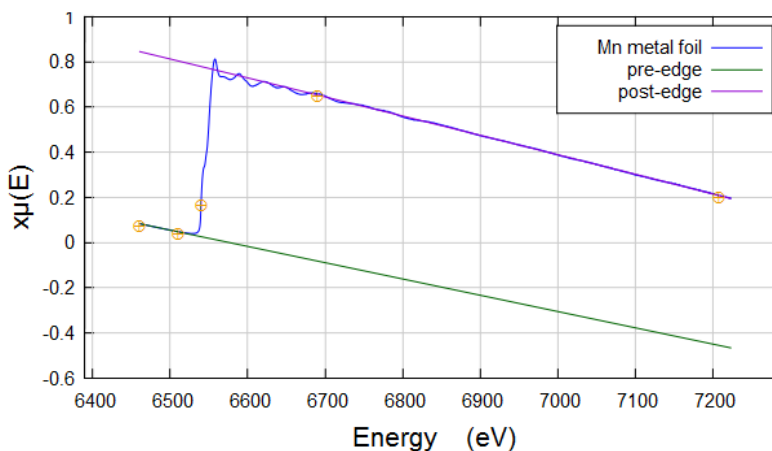


**Figure 2.17:** Pre-edge and post-edge polynomial subtraction.

Normalized data are typically presented after subtracting the curvature of the regressed quadratic and the difference in slope between the post- and pre-edge polynomials after the edge. The normalization procedure, by which the data are divided by the size of the edge step, compensates for the uncertainties in the concentration and sample thickness.

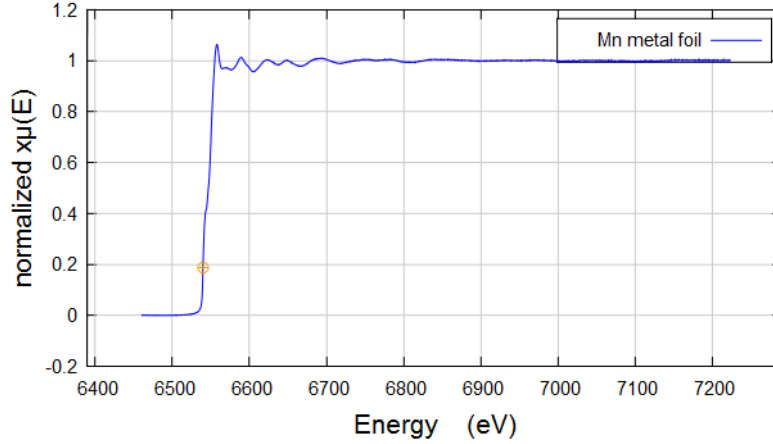


**Figure 2.18:** Typical normalised spectrum.

In the next step, background subtraction is performed, to isolate the oscillations in EXAFS from the atomic part of the absorption  $\mu_o(E)$ , and the background absorption or scatter from other elements in the beam path. AUTOBK algorithm<sup>177</sup> is used for background subtraction, which determines an empirical background spline based on a distinction between data and background in terms of Fourier components. In principle, the isolated atom absorption  $\mu_o(E)$  (which is generally unknown) is subtracted from the absorption of the atom in condensed matter  $\mu(E)$ , and the result is divided by  $\mu_o(E)$ , which is a slow function of energy in the EXAFS region. Background subtraction is accomplished by ordinary linear least squares fitting, typically using cubic spline functions. The difference between pre-edge and post-edge polynomials extrapolated to the edge energy  $E_0$  is used as the normalization constant in the definition of:

$$\chi(E) = \frac{\mu(E) - \mu(E_0)}{\mu_o(E_0)} \quad (2.14)$$

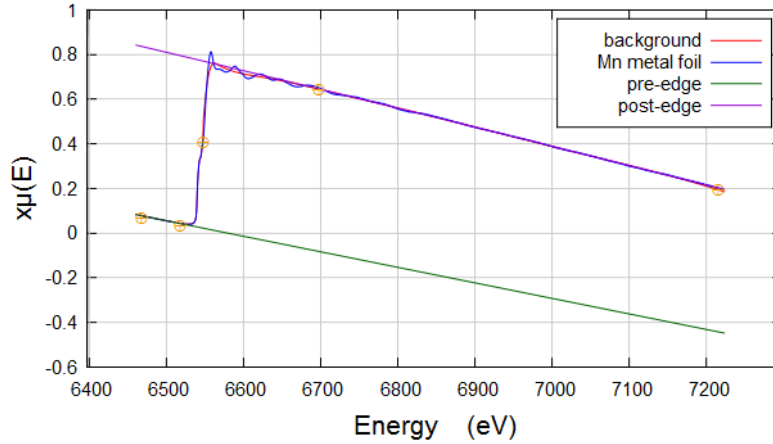


**Figure 2.19:** Pre-edge, post-edge polynomial and background subtraction.

Subsequently the data in E-space is converted to k-space and  $\chi(k)$  is obtained by the formula

$$k = \sqrt{\frac{2m(E-E_0)}{\hbar^2}} \quad (2.15)$$

The converted  $k$  space spectrum is generally weighted by an increasing function of  $k$  (such as  $k$ ,  $k^2$  or  $k^3$ ) so that the data at high  $k$  (which are of small amplitude) becomes significant. At this point, the data consist of sums of damped sine waves corresponding to the different shells of atoms and hence Fourier transformation is carried out to generate the radial distribution function. The region below  $k=2\text{\AA}^{-1}$  is excluded because of possible complications from multiple scattering etc. The transformed data ( $\chi(R)$  vs.  $R$ ) actually consist of a complex function, which has real and imaginary parts, or alternatively a modulus and phase. The modulus is the most frequently used quantity, but the real and imaginary parts are also useful. They exhibit significantly more structure than the modulus does, and they don't suffer from nonlinear interference and hence during the fitting, modulus as well as real and imaginary parts should be monitored. Once the raw data has been processed appropriately, it is used in ARTEMIS for theoretical modeling and fitting.

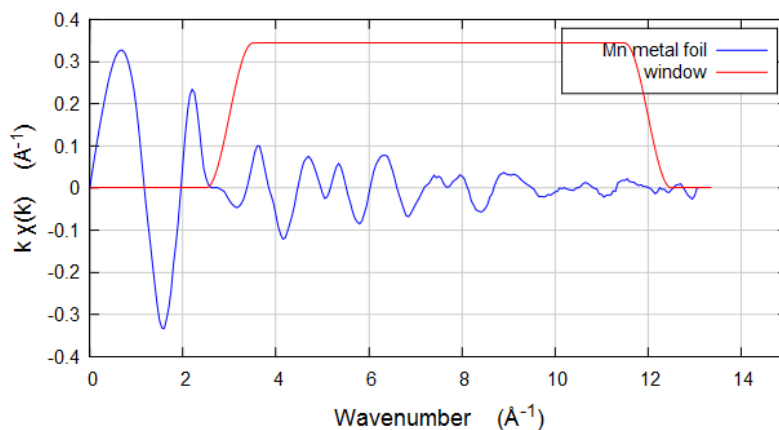


**Figure 2.20:**  $k$  space EXAFS spectrum with hanning window.

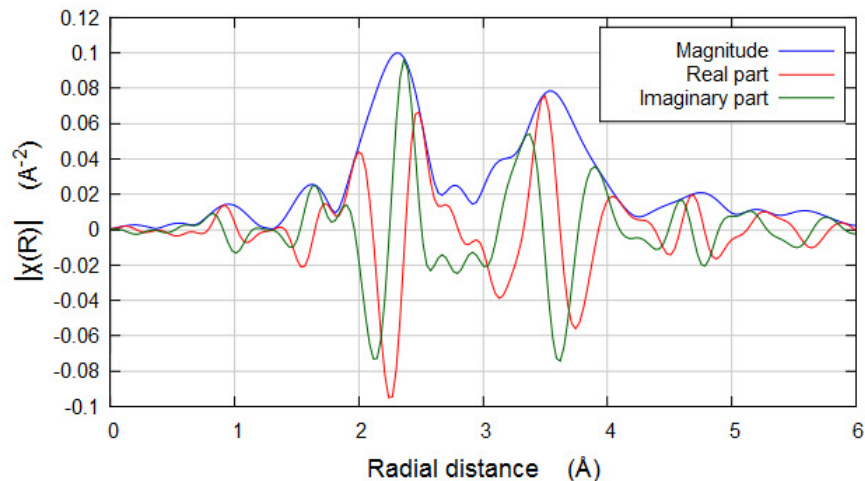


**Figure 2.21:** Fourier transformed EXAFS spectra alongwith real and imaginary contribution.

Apart from data processing, ATHENA provides utilities for linear combination fitting, principal component analysis, peak fitting using different line shapes (arctangent, Gaussian, Lorentzian), log ratio/phase difference analysis and generating the difference spectra. ATHENA can also import and display the results of FEFF8 calculations<sup>159</sup> for comparison with measured data. A significant feature of ATHENA is that processing and displaying many data sets simultaneously is as simple as for a single data set. The parameters controlling background removal and Fourier transforms can be adjusted for each data set individually or constrained in a flexible manner between data sets. Additional features self-absorption

corrections for fluorescence data using different algorithms. The self-absorption correction tool offers four different algorithms to approximate the effect of self-absorption using tables of x-ray absorption coefficients. One of them works on XANES data, while all four can be used to correct EXAFS data.

### 2.2.3.3 Data fitting using Artemis:

ARTEMIS is a graphical interface for EXAFS data analysis and a front-end for FEFF and IFEFFIT built using DEMETER. ARTEMIS includes access to the functionality of the ATOMS program, which generates input file format suitable for FEFF. Shown in Fig. 2.22 is the ARTEMIS window in its data view.

In EXAFS analysis, a theoretical model of the data is constructed containing unknown parameters and their values are determined by fitting. ARTEMIS can read crystallographic data either in the form of an ATOMS input file or a crystallographic information file (.cif) or can be supplied structure information interactively. These data are then converted into a FEFF input file. ARTEMIS includes access to the functionality of the ATOMS program, which converts crystallographic data into a format suitable for FEFF. FEFF is an *ab initio* multiple scattering code used to generate theoretical fitting standards for EXAFS analysis and simulation of XANES spectra<sup>161</sup>. FEFF performs its calculation in real-space on a specified cluster of atoms provided by ATOMS subroutine.  $f(k)$  and  $\delta(k)$  (the scattering amplitude and phase shift due to the neighboring backscattering atom respectively) and the photoelectron mean free path  $\lambda(k)$  are calculated theoretically. After the FEFF run, ARTEMIS displays a page containing a concise interpretation of the paths computed by FEFF including the path distances, degeneracy, atomic species in the path, whether the path is single or multiple-scattering. Each scattering path has variable parameters such as degeneracy  $N$  (the number of equivalent atoms in single scattering paths), an effective distance  $R$  (half path-length), and a mean square variation parameter  $\sigma^2$ , as mentioned in the canonical EXAFS (equation 2.6).

Once calculated, each of these paths can be easily modified to give a different  $N$ ,  $R$ ,  $\sigma^2$ , and even  $E_0$  (if that is necessary).

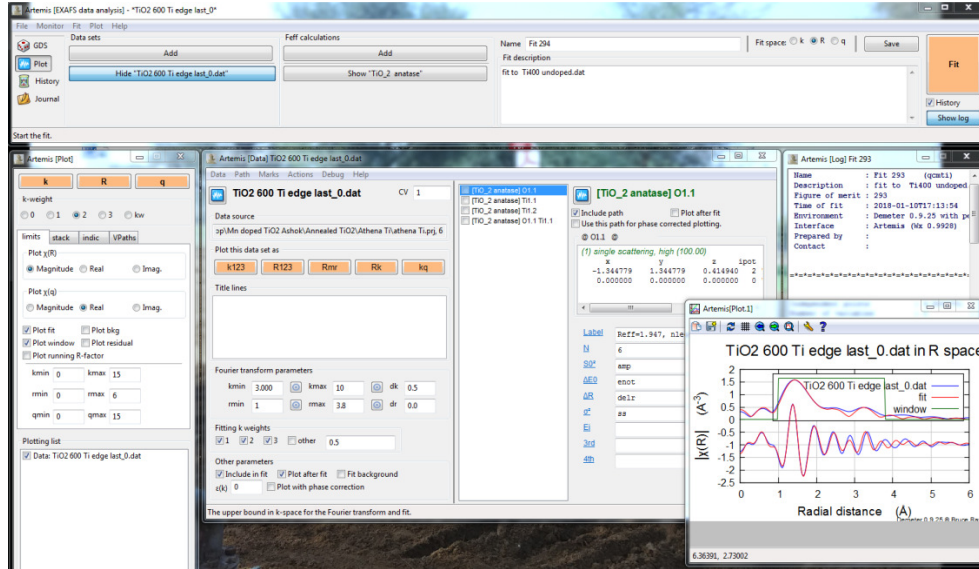


**Figure 2.22:** Main window of ARTEMIS program.

Artemis/IFEFFIT<sup>175</sup> works in this way where, the user needs to devise a set of fitting parameters that are adjusted by IFEFFIT to give the best fit to the data (usually over a selected region in  $r$ -space). This approach is particularly good for analyzing simple structures in which only a few paths (mostly single scattering) are important, and also for refining complex structures that are pretty much known, except for a few details. Although reasonable ad hoc assumptions or constraints can be made to limit the degrees of freedom, it is also best to start with the simplest hypothetical structure while modelling, and if the fit is inadequate for all rational choices of the parameters, further complexity can be introduced into the model.

Some of the fitting parameters are correlated. For example,  $N$  and  $\sigma^2$ , however their effect on spectrum is different. The coordination number affects the amplitude parameter uniformly as a function of  $k$  and on the other hand  $\sigma^2$  also affects the amplitude, but it has a

greater effect at high  $k$  than at low  $k$ . A similar correlation is observed between  $\Delta E_0$  and the distance  $R$ . Both affect the slope of the phase, but in different ways. In case of high correlations, the fitting problem becomes poorly determined and numerically unstable and introduces large error in parameter values. To avoid this problem different strategy can be adopted, such as multiple  $k$  weight fit or multiple data sets fit. The number of independent parameters that can be varied during a fitting is limited by information available. Adding unnecessary parameters may introduce correlations that will cause the error bars to inflate, so the information about the original parameters is masked. EXAFS data exist over a finite range in both  $k$ -space and  $r$ -space, and therefore they have limited information content. It is known from a Fourier series expansion that only a finite number of coefficients are needed to represent a signal of fixed bandwidth. All of the data in the FT exist on an array of  $N$  points in size. If we assume that the  $k$  window width is  $\Delta k$  wide, and the  $r$ -space data are contained in total width  $\Delta R$ , the grid spacing's respectively are  $\delta k$  and  $\delta r$  where  $\delta r = \pi/(N\delta k)$ . The maximum  $r$  value in the  $r$  space is  $(N/2)\delta r = \pi/(2\delta k)$ , where the factor of two comes in because half the space is allocated to negative frequencies which offer no new information. The fraction of the total information contained within  $\Delta R$  is then  $2\delta k\Delta R$ . The number of  $k$ -space data points in the window is (about)  $\Delta k/\delta k$ . But most of these data points actually carry no information, because the signal can be accurately represented within only a fraction of the total  $r$ -space. Therefore the actual information content in the data is number of  $k$ -space points  $\Delta k/\delta k$  times the compression factor  $2\delta k\Delta R$ . This gives a total “independent point” count of  $N_{\text{ind}} = 2\Delta k\Delta R/\pi$ , also called the Nyquist theorem. Stern<sup>178</sup> has however, argued that a more precise value is  $N_{\text{ind}} = 2\Delta k\Delta R/\pi + 2$ .

More advanced data fitting can be done using methods such as:

- (i) Simultaneous refinement of multiple data sets.
- (ii) Refinement using multiple  $k$ -weightings for any data set.

(iii) Co-refinement of a background spline to reveal correlations between the spline and the fitting parameters.

(iv) Constraints and restraints using prior knowledge.

(v) Debye and Einstein models for  $\sigma^2$

#### **2.2.3.4 Results and Goodness of Fit:**

The experimental data fitting process based on some theoretical modelling invariably includes some presumably known or determinable experimental uncertainties from random noise and other influences. These can be divided into random noise (such as photon counting) and non-random (systematic) errors. It is important to track and eliminate the systematic errors, but they cannot be completely eliminated. While fitting data we systematically vary the hypothetical values of the “unknown” (i.e. only partially known) parameters to give the best agreement with the experimental data. We will not achieve perfect agreement with the data, because of the noise and other uncertainties (“errors”), but we can determine how far we can vary the parameters around the best-fit values while still getting an acceptable fit to within the experimental (and theoretical) errors. The quality of a fit can be quantified by a comparison between the experimental data and the theoretical fit. The simplest approach is to calculate the squared deviation between the data and theory. The deviation (“residual”) is squared so that both positive and negative deviations contribute positively to the error statistic. If there are many data points the squared deviations are summed:

$$\chi^2 = \sum_{i=\min}^{\max} [\chi_d(r_i) - \chi_t(r_i)]^2 \quad (2.16)$$

where  $\chi_d(r_i)$  is the  $i$ th measured data point,  $\chi_t(r_i)$  represents the theory function, which depends on the independent variable. For EXAFS fitting the goodness of fit can be determined by the following quantities:

- **Chi-square:**

$$\chi^2 = \frac{N_{idp}}{\varepsilon N_{data}} \sum_{i=\min}^{\max} [Re(\chi_d(r_i) - \chi_t(r_i))^2 + Im(\chi_d(r_i) - \chi_t(r_i))^2] \quad (2.17)$$

Where,  $\chi(r)$  is the FT EXAFS data (which is a complex quantity) and the subscripts  $d$  and  $t$  denote data and theory respectively and  $\varepsilon$  = measurement uncertainty

- **Reduced chi-square:**

Chi square scaled by degrees of freedom  $\nu$

$$\chi^2_{\nu} = \frac{\chi^2}{\nu} \quad (2.18)$$

where

$$\nu = N_{idp} - N_{var} \quad (2.19)$$

The values of  $\chi^2_{\nu} \sim 10$  or higher typically for good quality EXAFS data.

- **R-factor:**

It is the fractional misfit between experimental data and the theoretical fit.

$$R_{factor} = \frac{\sum_{i=\min}^{\max} [Re(\chi_d(r_i) - \chi_t(r_i))^2 + Im(\chi_d(r_i) - \chi_t(r_i))^2]}{\sum_{i=\min}^{\max} [Re(\chi_d(r_i))^2 + Im(\chi_d(r_i))^2]} \quad (2.20)$$

IFEFFIT also estimate errors and correlation coefficient for the fitted parameters. During the estimation each parameter is varied about its best fit value until the value of  $\chi^2$  increased by one from its minimum<sup>179</sup>. The correlation coefficient range from zero to one and express the degree to which each parameter depends on other parameter. There are different methods for breaking these correlations depending on the type of parameters that are correlated. The amplitude parameter  $S_0^2$  and  $\sigma^2$  and the phase parameter  $\Delta E_0$  and  $\Delta R$  are often strongly correlated. For the present thesis, the  $k$  dependency is used for phase parameters and chemical transferability is used for amplitude parameters to break the correlation between these parameters. In all the EXAFS fittings presented in this thesis, correlations in the fitting parameters have been kept below 80%. In all the EXAFS fittings presented in this thesis,

uncertainties in the fitting parameters have been estimated and typical values are  $\pm 0.05 \text{ \AA}$  in  $R$ ,  $\pm 10\%$  in CN and  $\pm 0.001$  in DW factor ( $\sigma^2$ ).

#### 2.2.3.5 XANES interpretation:

The region near to the absorption edge (about  $\pm 50\text{eV}$ ) is called X-ray Near Edge Structure or XANES. This region is often contain additional features like intense peak just after the edge position called white line and features before absorption edge called pre-edge. Since the absorption edge is result of electronic transition of core level electron to continuum, the additional features just before the absorption edge (pre edge) are due to the transition of this electron in partially filled or empty bound state.

One of the most useful quantitative analysis of XANES spectra is linear combination fitting (LCF). The underlying principal of LCF is the additive nature of the absorption from each species in the sample, which means total absorption coefficient can be written as a weighted sum of coefficient for all the elements in the sample. Comparing the spectra of the samples of interest with those of known standards yields qualitative assessment of the chemical and structural environment of the absorbing atom, provided the spectra of the standards are sufficiently different from each other. The spectrum of the sample of interest is modelled by weighting the spectrum of each known standard  $i$  with a factor  $f_i$  and adding them together

$$\mu_{cal} = \sum f_i \mu_i \quad (2.21)$$

The factors  $f_i$  represent the fraction with which each standard is present in the sample and are obtained by minimizing the difference between the calculated and measured spectrum using least square fitting. The most crucial part of LCF is consistent normalisation. Ideally, they should sum to one. However, structural disorder can sometimes broaden the XANES features and the sum rule needs to be relaxed in these cases<sup>167</sup>. Linear combination fitting works well if the number of potential chemical and structural environments for the absorbing

atom in the sample, and thus the number of standards is small and if the spectra of these standards exhibit unique features that allow to differentiate between them. The limitation of LCF is the need of reference spectra of all the species having similar energy resolution. Therefore, it can be used only for systems where the species in the sample are well known. Linear combination fitting subroutines are available in XAS data analysis programs ATHENA.

Another important XANES analysis technique is principal component analysis (PCA). The PCA approach provides insight on the number of unique components present in a set of samples without any priori knowledge about the identity of species. This approach is commonly combined with LCF to help determining the number of standard spectra and to define the standard spectra. Principal component analysis is used with a set of spectra that are meaningfully related. Principal component analysis uses matrix operations to determine eigenvectors that represent the variation in the set of spectra. The maximum number of eigenvectors is equal to the number of sample spectra. The first eigenvector is defined as a vector along the greatest variation in some aspect of the data set. The second vector is extracted orthogonally to the first one to account for the highest remaining variation. Additional eigenvectors are orthogonally extracted until all the variation in the dataset is captured. There are several criteria that can be used to statistically separate the significant eigenvectors from those representing noise in the data set. The significant eigenvectors are called principle components and are statistical abstractions with no physical relationship to the chemical components or species in the samples. This technique is very popular among the time resolved studies performed under different environment and conditions<sup>180, 181</sup>.

Characteristic features such as white lines or pre-edge features can also be quantified by peak fitting procedures. For peak fitting the absorption edge itself is typically approximated by an arctangent function while the peaks are modelled by Lorentzian lines

convoluted with a Gaussian function (Voigt function) to account for experimental broadening<sup>148</sup>. Such an analysis could yield, for example, the change in edge position related to a change in first nearest neighbour distances for a series of samples or the fraction of different oxidation states (characterized by different white line positions) of the absorbing atom within a sample.

#### **2.2.3.6 Ab initio simulations:**

The XANES spectra is generated using ab initio simulations for fingerprinting. XANES is considerably harder to fully interpret like EXAFS<sup>182</sup>, since interaction of ejected photoelectron with the potential of the neighbouring atoms are still strong so the simplifying single scattering approach used in EXAFS is not possible. In the near-edge (XANES) region the muffin-tin approximation is less satisfactory for quantitative analysis and the interpretation of XANES is complicated. Precise and accurate calculations of all spectral features are still difficult, time-consuming, and not always reliable. This situation is improving, but at this point, quantitative analyses of XANES using ab initio calculations are very rare, though few programmes for theoretical simulation of XANES such as FEFF9<sup>159</sup>,<sup>161</sup>, MXAN<sup>183</sup>, FDMNES<sup>184</sup> etc are available.

FEFF9 programme has been used to simulate the XANES spectra in the present thesis. The FEFF9 theory predicts the XANES spectra based on the production of a core hole during electron excitation, the density of states of the molecular orbitals of the coordinated atoms in this excited state, and multiple scattering of the photoelectron at energies near the absorption edge. The use of a real-space multiple scattering approach for ab-initio calculations of XAS spectra unifies the description of both the XANES and EXAFS regions of the spectra. The theoretical calculation of the XANES spectrum is based on a cluster of atoms surrounding the absorber. The theoretical spectrum is then compared with the experimental spectrum, and the molecular structure is refined as needed to provide the best

match between theory and experiment. Due to the long mean free path of the photoelectron at the absorption edge, the cluster of atoms needed for an accurate XANES calculation can be greater than 10 Å. Usually a small cluster is used first, and then the size is incremented to determine the effect on the XANES spectra. An exact match implies that the local molecular structure has been solved. To develop the original molecular structure, additional information such as interatomic distances and coordination numbers provided by EXAFS analysis or molecular dynamics simulations are useful. The use of ab-initio simulations of XANES data are presently useful for characterizing the fine details of XANES with rich structural features.

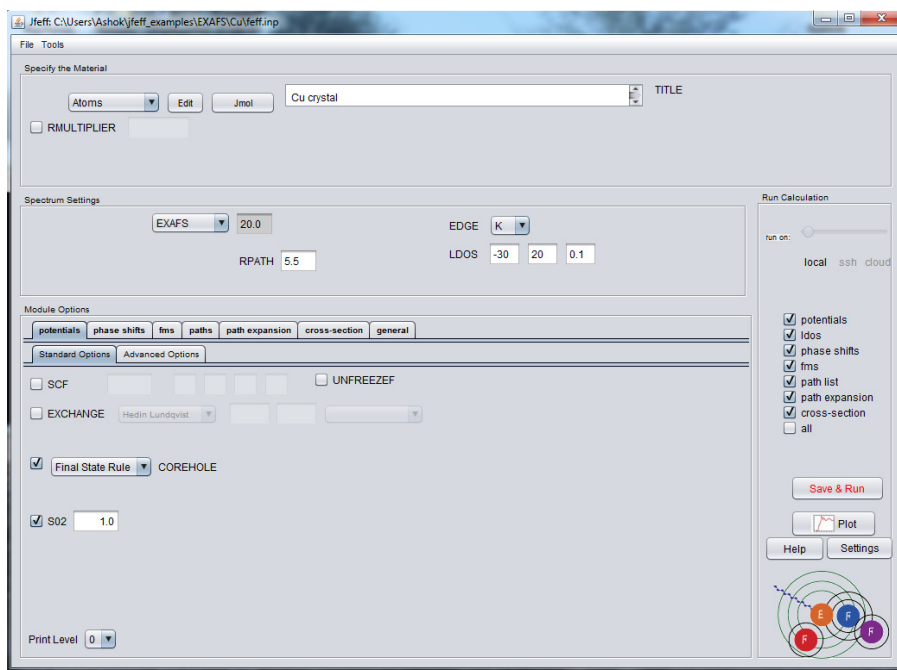


**Figure 2.23:** GUI window of FEFF9 program.

## 2.3 Other characterisation techniques:

### 2.3.1 Grazing Incidence X-ray Diffraction (GIXRD):

X-ray wavelength is comparable to the inter-atomic distances in material which makes it most useful for structural detection. X-ray diffraction (XRD) is the most widely used characterization technique for crystalline material characterization. The XRD peak position, intensity and width provide the information regarding crystalline phase, lattice parameters,

strain and preferred growth direction in crystalline solids. The collimated beam of X-ray incident on the sample and it is diffracted following the 'Bragg's diffraction law'

$$2d\sin\theta=n\lambda \quad (2.22)$$

where,  $d$  is the interplaner spacing,  $\theta$  is the angle of incidence,  $n$  is the diffraction order and  $\lambda$  is the wavelength of incident photon.

Different type of geometry is used for XRD measurements depending on the sample requirements. Grazing incidence X-ray diffraction (GIXRD) is specifically used for investigating structural properties of thin films coated on bulk substrates. In contrast to wide angle X-ray diffraction where angle of incidence  $>10^\circ$ , here the X-ray beam is made incident on the sample at a fixed and small grazing angle of incidence. This is to ensure that the penetration depth of incident X-ray lies almost within the thickness of the thin film so that X-rays will interact mostly with the thin film and not with the underlying substrate. To collect the GIXRD pattern for thin film, the grazing angle of incidence of X-rays is kept fixed and the diffracted X-ray is measured in the wide angular range by rotating the detector arm across the intended angular range. This is often called as detector scan mode of measurement. One of the prime difference of detector scan mode with conventional  $\theta$ - $2\theta$  mode of XRD measurement is that in  $\theta$ - $2\theta$  mode, only the family of crystallographic planes which are parallel to the sample surface can take part in diffraction whereas in detector scan mode ( $2\theta$  mode), all the crystallographic planes in the sample takes part in diffraction. The schematic of grazing incidence X-ray diffraction measurement configuration is shown in fig. 2.24. One of the prerequisites for recording noise free GIXRD measurement is that incident X-ray beam should be sufficiently collimated. Otherwise the X-ray beam will have spread of incident angle rather than having a definite well-defined angle of incidence. Monochromatic Cu  $K_\alpha$  X-ray being originated from X-ray tube is collimated using collimating mirror by cross beam

optics (CBO) technique. X-rays diffracted from the sample is passed through a soller slit and detected by a scintillation detector followed by photomultiplier tube.

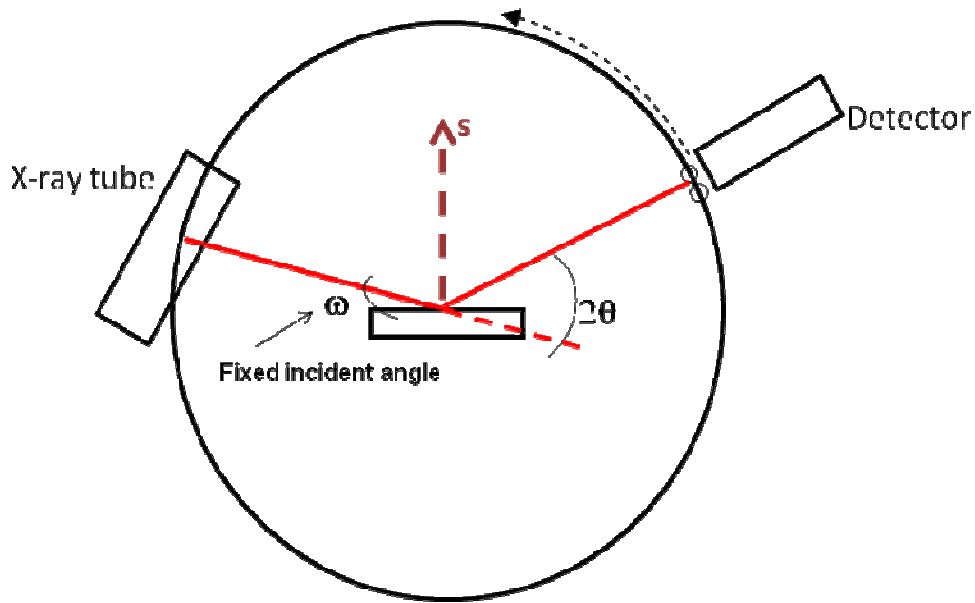


**Figure 2.24:** Schematic of GIXRD set-up in  $2\theta$  scan mode.

As mentioned above, the information about the single or multiple phases in sample is identified by assigning the “ $d$ ” values of the diffraction peaks and monitoring their relative intensity. These peaks are compared with the standard JCPDS data (The International Centre for Diffraction Data (<http://www.icdd.com/>)) for various known crystal structure of material. JCPDS powder diffraction files is a huge collection of XRD data base and it is used for identify the crystalline phase of material by comparing the XRD peak positions.

Preliminary structural characterizations of the Mn doped ZnO and Co doped ZnO films were carried out by GIXRD measurements using a Bruker D8 Discover diffractometer while structural chataerisation of Fe doped ZnO and Ni doped ZnO films were carried out by GIXRD measurements using a Rigaku SmartLab diffractometer. In both the cases

measurements were done with monochromatic Cu  $K_{\alpha}$  X-rays at a grazing angle of incidence of  $0.5^{\circ}$  and with a wavelength of  $1.54\text{\AA}$ .



**Figure 2.25:** Bruker D8 Discover diffractometer used for experiment.



**Figure 2.26:** Rigaku SmartLab diffractometer used for experiment.

GIXRD measurement of Mn and Co doped  $\text{TiO}_2$  thin films are measured using AD/ED-XRD beamline (BL-11) in ADXRD mode, which is a bending magnet beamline at Indus-2 RRCAT Indore.<sup>185</sup> This beamline works in two different modes Viz. Angle dispersive X-ray diffraction (ADXRD) and energy dispersive X-ray diffraction (EDXRD).

The beam from bending magnet is transported to the experimental station through various components viz. Beam stopper, primary slit and precision slit. In case of ADXRD mode (used in present thesis) X-ray is monochromatized using at Si(111) channel cut monochromator. Mar345 area detector with pixel size of  $0.1 \times 0.1 \text{ mm}^2$  is used for data collection.

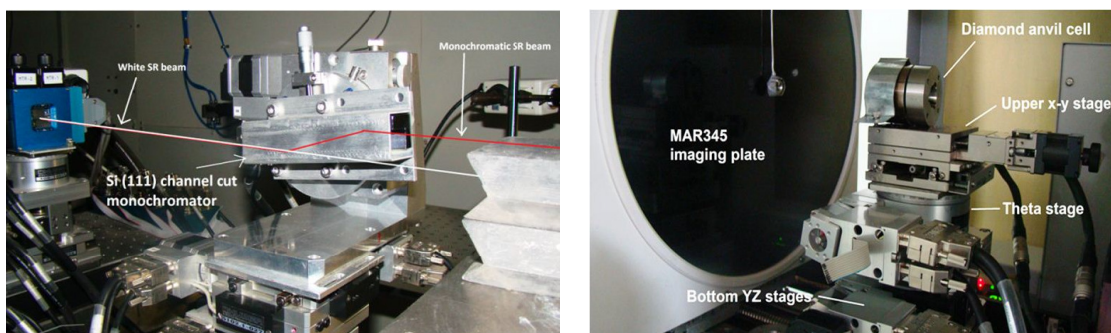


**Figure 2.27:** Photograph of the experimental station at AD/EDXRD beamline BL-11.

### 2.3.2 Spectroscopic Ellipsometry:

Ellipsometry is an optical technique for investigation of refractive index, roughness, thickness and band gap of thin films. The thickness and bandgap of the samples have been determined from spectroscopic ellipsometry measurements by using a rotating polarizer type spectroscopic ellipsometer. The ellipsometry measurements were performed at  $70^\circ$  angle of incidence and in the wavelength range of 200 to 900 nm. In ellipsometry, the variation of the amplitude and the phase difference between the parallel (p) and perpendicular (s) components of the reflected light polarized with respect to the plane of incidence are measured. In general reflection causes a change in the relative phase of p and s waves and in the ratio of their amplitudes. The effect of reflection is measured by the two quantities, viz.  $\psi$  (which measures the amplitude ratio) and  $\Delta$  (which measures the relative phase change).

These are given by<sup>186</sup>:

$$\rho = \frac{r_p}{r_s} = \tan(\Psi) \exp(i\Delta) \quad (2.23)$$

where,  $r_p$  and  $r_s$  are the reflection coefficients for the p and s component of the waves respectively. In rotating polarizer spectroscopic ellipsometry, the time dependent signal  $I(t)$  at each wavelength is described by the general formula<sup>187</sup>:

$$I(t) = I_0(1 + \alpha \cos(2\omega t) + \beta \sin(2\omega t)) \quad (2.24)$$

where,  $\omega$  is the rotational frequency of the polarizer and  $\alpha$  and  $\beta$  are the normalized Fourier coefficients from which the ellipsometric parameters  $\Psi$  and  $\Delta$  can be determined using following expression:

$$\alpha = \frac{\tan^2\Psi - \tan^2 A}{\tan^2\Psi + \tan^2 A} \quad ; \quad \beta = \frac{2 \tan\Psi \cos\Delta \tan A}{\tan^2\Psi + \tan^2 A} \quad (2.25)$$

where,  $A$  is the angle of analyzer.

Even though  $\Psi$  and  $\Delta$  are physically more meaningful ellipsometric parameters, the more directly obtained ellipsometric parameters  $\alpha$  and  $\beta$  (at analyser angle of  $45^\circ$ ) are also used for ellipsometry data analysis. Therefore, measured ellipsometry data consists of either the normalized Fourier coefficients  $\alpha$  and  $\beta$  or derived from the measured data  $\tan \Psi$  and  $\cos \Delta$  as a function of wavelength.

The experimental ellipsometric spectra of the samples are fitted with appropriate models consisting of one single layer of pure/doped ZnO film on top of a silicon substrate having some amount of void. Optical constants of the bulk material (ZnO) are assumed to follow the Tauc-Lorentz dispersion model<sup>188</sup> which is common for such oxide dielectric films and the mixture of material and void has been treated under the Bruggeman Effective Medium Approximation<sup>189</sup>. The Tauc-Lorentz dispersion model<sup>188</sup> and Bruggeman Effective Medium Approximation<sup>189</sup> have been briefly described in Appendixes A & B of this thesis. The optical constants of silicon substrate have been estimated through a separate ellipsometric measurement and have been supplied in the above fitting process. Various

parameters of the sample layer structure and dispersion relations are varied in the analysis software and the simulated ellipsometry parameters are fitted with the measured ellipsometric spectra by minimizing the Root Mean Squared Error (RMSE) value between the measured and calculated values of the ellipsometric parameters ( $\alpha$  and  $\beta$ ) given by:

$$RMSE = \sqrt{\frac{1}{2N-P} \sum_i^N \{(\alpha_i^{exp} - \alpha_i^{cal})^2 + (\beta_i^{exp} - \beta_i^{cal})^2\}} \quad (2.26)$$

where,  $N$  is the number of data points and  $P$  is the number of model parameters. The optical constants of the ZnO layers have been obtained from the best fit of the experimental and simulated ellipsometric spectra.



**Figure 2.28:** Photograph of spectroscopic ellipsometer (SOPRA GES5E)

Optical characterization of all the films have been carried out by spectroscopic ellipsometry measurement using a rotating polarizer type spectroscopic ellipsometer (M/s. Semilab, model: GES5E). Ellipsometry spectra were measured for all the samples in the wavelength range of 200-900 nm at 70° angle of incidence.

### 2.3.3 Photoluminescence studies:

Photoluminescence spectroscopy is used to measure the radiative defects present in the sample. Photon on specific energy causes generation of electron-holes within the material and excitation of this electron to higher allowed states. When these electron return to their equilibrium states, the excess energy is released and electron and holes can either recombine non-radiatively by emitting phonons (or collision transfer to other particles) or radiatively by emitting the photons, the later phenomenon is called photo-luminescence. Photoluminescence (PL) spectra of the samples were recorded using an Edinburgh FL920 instrument.

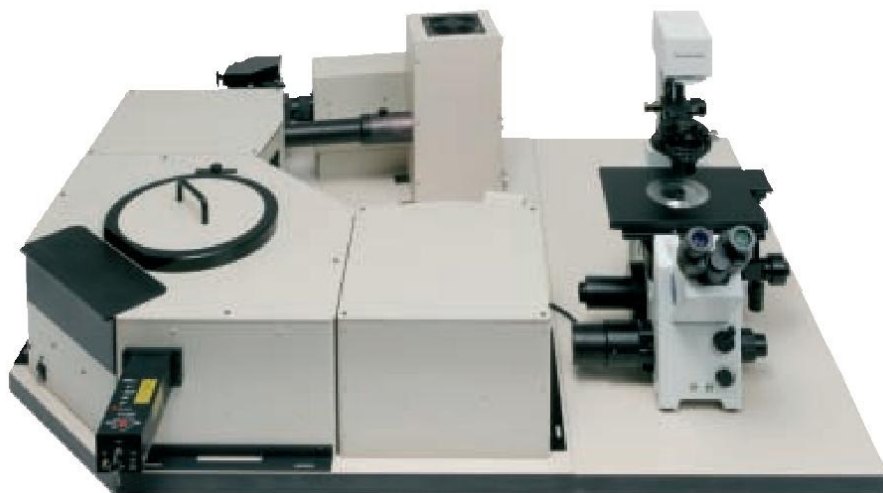


**Figure 2.29:** Photograph of Edinburgh spectroscopic Photoluminescence instrument.

### 2.3.4 Field Emission Scanning Electron Microscope (FESEM):

The Field Emission Scanning Electron Microscope (FESEM) is a scanning electron microscope that uses a field-emission cathode in the electron gun. The combination of higher magnification, larger depth of focus, greater resolution, and simplicity of sample observation makes the FESEM one of the most widely used instruments in today's context.

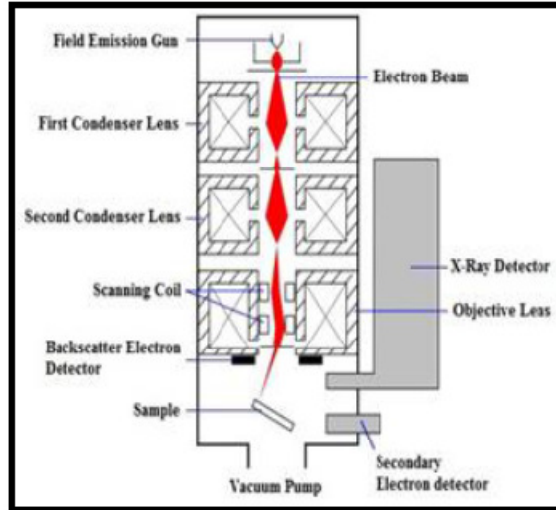


**Figure 2.30:** Schematic diagram of a FESEM.

A field-emission cathode in the electron gun of a scanning electron microscope provides narrower probing beams at low as well as high electron energy, resulting in both improved spatial resolution and minimized sample charging and damage. The anode, which is positive with respect to the sharply etched monocrystalline tungsten or lanthanum hexaboride ( $\text{LaB}_6$ ) field emission gun tip, causes electrons to accelerate. Electrons accelerate in the space between the anode and the cathode and move down the evacuated column towards the sample. The electron beam is then collimated by the condenser and focused by the condenser lens on the sample. The scan coils are energized by varying the voltage produced by the scan generator for creating a magnetic field, which deflects the electron beam back and forth in a controlled manner. The electron beam hits the sample, producing secondary electrons from the sample, which are collected by a secondary electron detector or a backscatter electron detector. The amplified detector signal is applied to the grid of the cathode ray tube and causes the intensity to change. The image consists of thousands of spots of varying intensity on the cathode ray tube (CRT) or LCD monitor that represent the topography of the sample. The pattern of deflection of the electron beam is the same as the pattern of deflection of the spot of light on the CRT.



**Figure 2.31:** Carl Zeiss SUPRA<sup>®</sup> 55 FESEM.

A field emission scanning electron microscope (Carl Zeiss SUPRA<sup>®</sup> 55 with GEMINI<sup>®</sup> Technology) was used to study the growth and morphology of TM doped ZnO/PVDF composite films (thickness > 200 nm) (Figure 2.27). The FESEM (SUPRA<sup>®</sup> 55) has been designed to operate on voltages between 0.1– 30 kV. The design allows the operator to choose the optimum voltage for a particular specimen. The instrument has a resolution of ~ 2 nm and magnification could be varied from 12 – 900000x.

### **2.3.5 X-ray Photoelectron Spectroscopy (XPS):**

XPS is based on photoelectric effect. It can be applied to a broad range of materials and provides valuable quantitative and chemical state information from the surface of the material being studied. When the sample is irradiated with X-rays of energy  $h\nu$ , photoelectrons are emitted from the sample surface. Photoelectrons emitted with a specific kinetic energy K.E., which is measured by an electron energy analyzer.

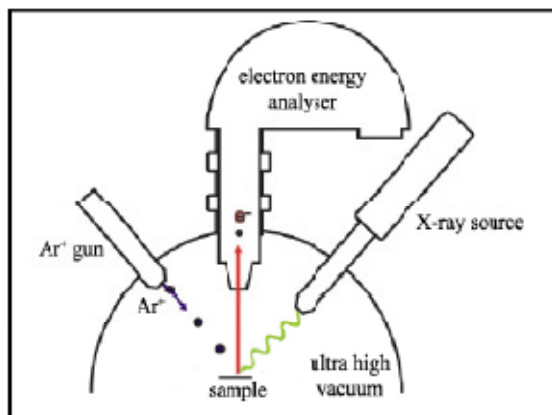


**Figure 2.32:** Block diagram of XPS instrument.

This kinetic energy of the emitted photoelectron is given by,

$$K.E. = h\nu - B.E. - \Phi_s \quad (2.27)$$

where,  $B.E.$  is the binding energy of the electron in atomic orbital from which the electron originates and  $\Phi_s$  is the work function dependent on both the spectrometer and the material. The schematic representation of the working principle of an XPS instrument is shown in fig. 2.32. The spectrum is obtained as a plot of the number of detected electrons per energy interval versus their kinetic energy. Since the mean free path of the electrons in solids is very small, a majority of the detected electrons originate from the top few atomic layers makes this technique surface sensitive. Since the core levels of each element have unique binding energies, XPS can be used to identify and determine the concentration of the elements at the surface. Variation in the elemental binding energies (chemical shifts), arising from differences in the chemical potential (Madelung potential) and polarizability of compounds can be used to identify chemical states of the elements in materials being analyzed. XPS experiments in this thesis work were conducted in a VG Microtech system (Fig.2.33) with the base pressure of  $10^{-10}$  Torr. The XPS system is equipped with a hemispherical analyzer and a dual anode Mg-Al X-ray source. The system is equipped with a EX03 Ar ion sputtering gun for sample etching.



**Figure 2.33:** Photograph of XPS instrument.

The analyzer was operated with a pass energy of 200 eV for large size survey scan of 0-1000 eV binding energy region. For high resolution scans a pass energy of 20 eV was utilized. Non monochromatic Mg-K( $\alpha$ ) 1256.6 eV radiation was used at 300W for all the XPS measurements reported here.

### **2.3.6 Magnetic measurements:**

In DMS materials, the magnetic moment is very small since the doping concentration was very small (<10%) and samples are thin (<200 $\mu$ m). The magnetic moment of typical DMS system is usually between  $10^{-7}$  to  $10^{-4}$  emu, thus require a highly sensitive magnetometry. The various field dependent and temperature dependent magnetic properties of the DMS thin films and bulk wafers are measured by VSM and SQUID.

SQUID magnetometer measures the magnetic moment of a sample by moving it through superconducting detection coils. The detection coils are connected to the SQUID device through superconducting wires, allowing the current from the detection coils to inductively couple to a SQUID sensor (based on a Josephson junction). As the sample moves through the detection coils, the magnetic moment of the sample induces an electric current in the detection coils. The detection coils, the connecting wires and the SQUID input coil form a

closed superconducting loop. Any change in the magnetic flux in the detection coils produces a change in the persistent current in the detection circuit, proportional to the change in magnetic flux. Since the SQUID works as a highly linear current-to-voltage converter, the variations in the current in the detection coils produce corresponding variations in the SQUID output voltage which are proportional to the magnetic moment of the sample.

Magnetization measurements as functions of magnetic field were performed by employing two different commercial SQUID systems, 7-Tesla SQUID-vibrating sample magnetometer (SVSM; Quantum Design Inc., USA) and a SQUID-Vibrating Sample Magnetometer (SQUID-VSM-050 MPMS), Quantum Design, USA. M vs H measurements on all the samples were carried out at room temperature.



**Figure 2.34:** Photograph of SQUID-vibrating sample magnetometer.

# Chapter 3

## **Mn DOPED ZnO THIN FILMS**

### **3.1 Introduction:**

In this chapter we have discussed the experimental findings on Mn doped ZnO DMS thin films which have primarily been characterised by X-ray absorption spectroscopy (XAS) technique comprising of both XANES and EXAFS measurements. Mn-doped ZnO thin films have been reported to be grown by various techniques viz., spin coating,<sup>11,12</sup> sol-gel,<sup>13-15</sup>, spray,<sup>16</sup> metal organic chemical vapour deposition,<sup>17,18</sup> rf magnetron sputtering<sup>19,20</sup> and pulsed laser deposition.<sup>21-24</sup> In the present study we have prepared Mn doped ZnO thin films by r.f. sputtering of a doped target as discussed below. The objective of using XAS techniques in probing the local structure around the host and dopant atoms in these materials and in the interpretation of their magnetic properties have already been discussed in detail in Chapter-1.

### **3.2 Experimental:**

#### **3.2.1 Preparation of samples:**

Mn doped ZnO thin films have been deposited with different doping concentrations (1, 2, 4, 6, and 10%) using an in-house built magnetron sputtering system described in Chapter 2<sup>142</sup>. High purity Mn doped ZnO (with 1, 2, 4, 6 and 10% of Mn) discs of 75mm diameter were used as target materials in the present system. Substrates used for all the depositions are crystalline silicon (111) having dimension of 25mm x 11mm, kept at room temperature and the depositions have been carried out under high purity argon ambient. The crystal monitor is calibrated by *ex-situ* thickness measurement of a ZnO thin film by spectroscopic ellipsometry (~200nm). The other deposition parameters used are sputtering

pressure of  $4 \times 10^{-3}$  mbar, substrate to target distance of 4.5 cm, RF power of 100 W and all the films were deposited for 20 minutes.

### **3.2.2 Characterization of samples:**

Preliminary structural characterisations of the films were carried out by Grazing Incidence X-ray Diffraction (GIXRD) measurements using a Bruker D8 Discover diffractometer with monochromatic Cu  $K_{\alpha}$  X-rays at a grazing angle of incidence and with a wavelength of 1.54 Å. XANES and EXAFS measurements have been carried out on the Mn doped ZnO thin film samples at the Energy-Scanning EXAFS beamline (BL-09) at the Indus-2 Synchrotron Source at RRCAT, Indore, India as has been described thoroughly in Chapter-2<sup>170, 171</sup>. XANES measurements at the O K edges and Mn  $L_{2,3}$  edges of the Mn doped ZnO samples were performed at room temperature in the total electron yield (TEY) mode at the soft X-ray absorption spectroscopy (SXAS) beamline (BL-01) of the Indus-2 synchrotron radiation source at RRCAT, Indore, India. Magnetization measurements as a function of magnetic field were performed by employing the commercial 7-Tesla SQUID-vibrating sample magnetometer (SVSM; Quantum Design Inc., USA) as mentioned in Chapter-2. M vs H measurements on all the samples were carried out at room temperature.

### **3.3 Results and discussion:**

GIXRD results given in fig.3.1 show no secondary phase other than wurzite hexagonal ZnO phase in the samples. However, we have observed that with the increase in Mn doping concentration preferential growth along [001] direction takes place.

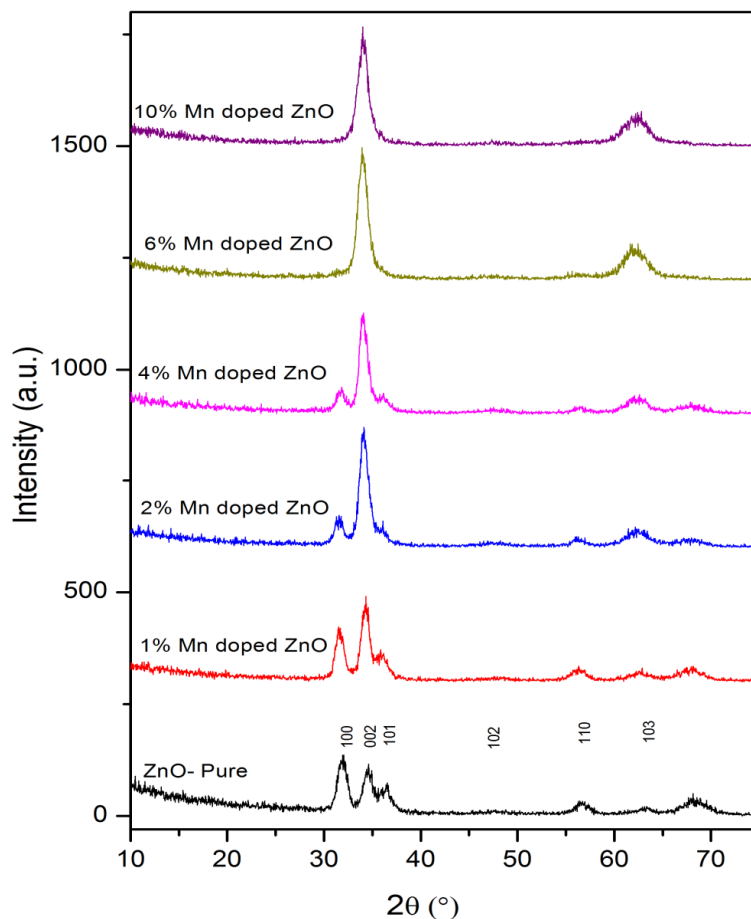


**Figure 3.1:** GIXRD plots of Mn doped ZnO thin films (1%, 2%, 4%, 6% and 10% doping).

The XANES spectra at Mn K edge for Mn doped ZnO films are shown in figure 3.2 along with that of three standard samples viz., Mn metal foil,  $\text{MnCl}_2$  and  $\text{Mn}_2\text{O}_3$  with +0, +2 and +3 oxidation states of Mn respectively. The pre-edge features below the main edge denoted by A are due to Mn 1s transition into unoccupied O 2p-Mn 3d (or Mn 3d/4p) hybridized states, which have p components projected at the Mn site as observed in many transition-metal oxides. Since metallic Mn does not show pre-edge, the presence of pre-edge in Mn doped samples suggest that no metallic content is present in the sample. The main edge (B) at the Mn K-edge corresponds to the high-energy Mn 4p states. It is found that maxima of first derivative in Mn doped ZnO films are closer to that of  $\text{MnCl}_2$  but much lower than  $\text{Mn}_2\text{O}_3$  suggesting that Mn is present in the samples in 2+ oxidation state. We have observed

that for 10% Mn doped sample the edge is marginally (0.5 eV) shifted to higher energy side. The feature indicated by D in figure 3.2 is absent in case of Mn doped samples which also clearly rules out the presence of  $\text{Mn}_2\text{O}_3$ .

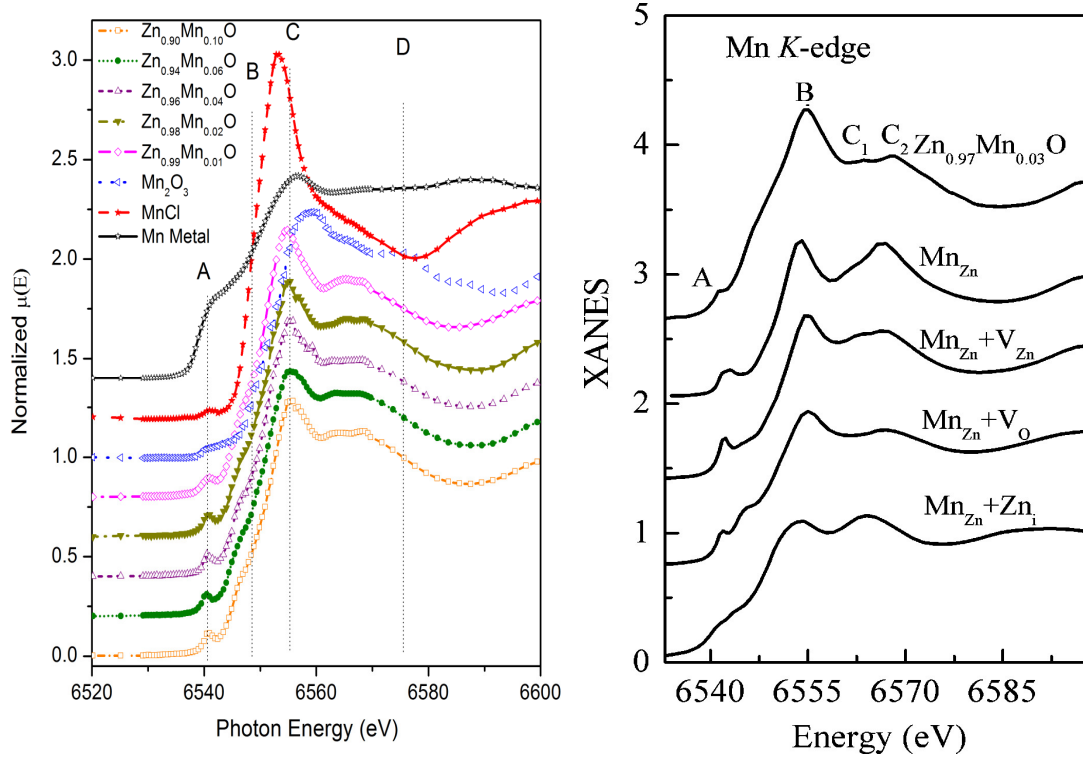


**Figure 3.2:** (Left panel) Normalised XANES spectra of pure ZnO and Mn doped ZnO (1%, 2%, 4%, 6% and 10% doping) at Mn K-edge along with reference Mn metal,  $\text{MnCl}_2$  and  $\text{Mn}_2\text{O}_3$ . (Right panel) Theoretically simulated XANES spectra by Yan et al.<sup>91</sup> assuming different defect models.

Yan et. al.<sup>91</sup> have calculated XANES spectra for different models of Mn doped ZnO system. It can be seen that the main features of our Mn K edge XANES spectra matches with the theoretical spectra obtained by Yan et. al.<sup>91</sup> assuming a model of substitutional Mn and Zn vacancy ( $\text{Mn}_{\text{Zn}}+\text{V}_{\text{Zn}}$ ) or substitutional Mn and oxygen vacancy ( $\text{Mn}_{\text{Zn}}+\text{V}_{\text{O}}$ ), shown in the right panel of fig. 3.2. The spectra also resembles that of PLD grown Mn doped ZnO thin film given by Droubay et al.<sup>190</sup>. The Zn K-edge XANES spectra (fig. 3.3) show that Zn is present in +2 oxidation state and there is no shift with Mn doping concentration.

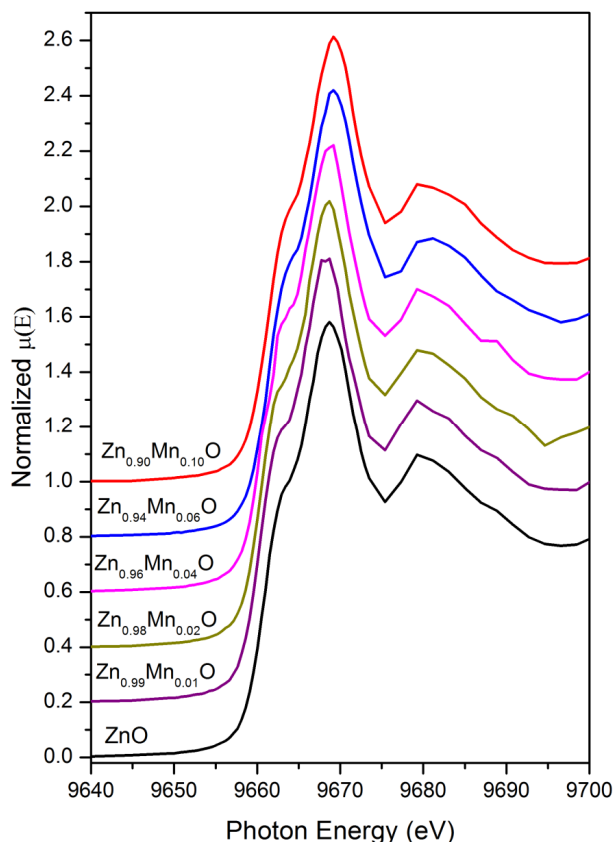


**Figure 3.3:** Normalised XANES spectra of pure ZnO and Mn doped ZnO (1%, 2%, 4%, 6% and 10% doping) at Zn K-edge.

The normalized EXAFS spectra of pure and Mn doped ZnO samples are shown in figures 3.4 and 3.5 at Zn and Mn K edges respectively. A set of EXAFS data analysis codes available within the IFEFFIT software package have been used for EXAFS data analysis as described in details in Chapter-2. The  $\chi(R)$  versus  $R$  plots have been generated (Fourier transform range  $k = 3.0-11.7 \text{ \AA}^{-1}$ ) for all the samples from the  $\mu(E)$  versus  $E$  spectra following the methodology described in Chapter-2 and are shown in figure 3.6 and 3.8 for the data measured at Zn and Mn K edges respectively. The structural parameters (atomic coordination and lattice parameters) of ZnO used for simulation of the theoretical FT-EXAFS spectra of the samples have been obtained from reference<sup>33</sup> and the best fit  $\chi(R)$  versus  $R$  plots (fitting range  $R=1.0-3.5 \text{ \AA}$ ) of the samples have also been shown in figures 3.6 and 3.8 along with the experimental data. The bond distances, co-ordination numbers (including scattering

amplitudes) and disorder (Debye-Waller) factors ( $\sigma^2$ ), which give the mean square fluctuations in the distances, have been used as fitting parameters. The best fit results are summarized in Table 3.1 and 3.2 for Zn and Mn K edge measurements.

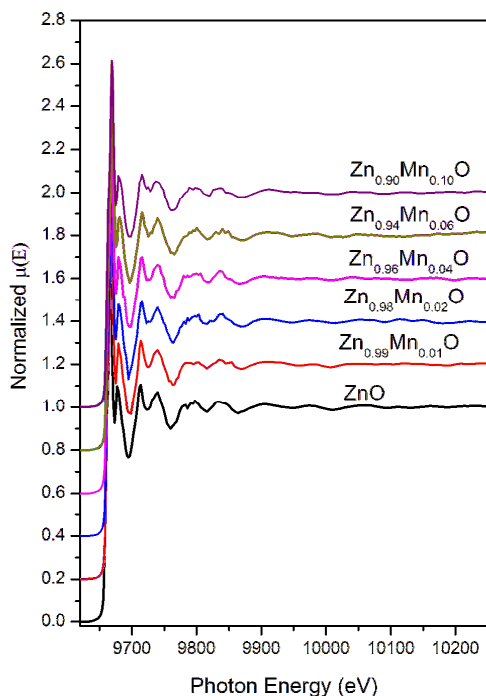


**Figure 3.4:** Normalised EXAFS spectra of pure ZnO and Mn doped ZnO (1%, 2%, 4%, 6% and 10% doping) samples measured at Zn K-edge.

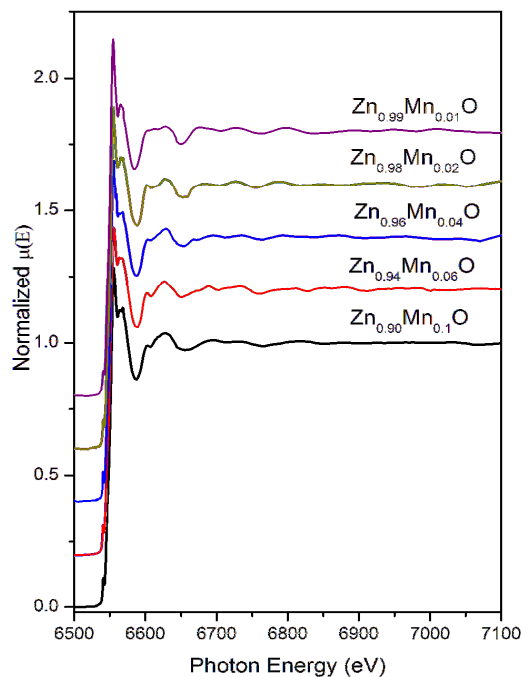


**Figure 3.5:** Normalised EXAFS spectra of Mn doped ZnO (1%, 2%, 4%, 6% and 10% doping) samples measured at Mn K-edge.

The first peak in the Zn K-edge FT-EXAFS spectrum (fig. 3.6) of pure ZnO has contributions from two Zn-O shells each having three and one oxygen at 1.94 Å and 1.95 Å respectively. The bond length obtained is in good agreement with other studies<sup>191</sup>. The second peak is fitted with single Zn-Zn shell with coordination number of 12. As can be seen from Table 3.1 & fig. 3.7, for Zn K-edge data, though there is no change in coordination number and bond length with increase in Mn doping concentration,  $\sigma^2$  value is found to increase for Zn-Zn paths with increase in Mn doping concentration manifesting substitution of Mn ions at Zn sites.

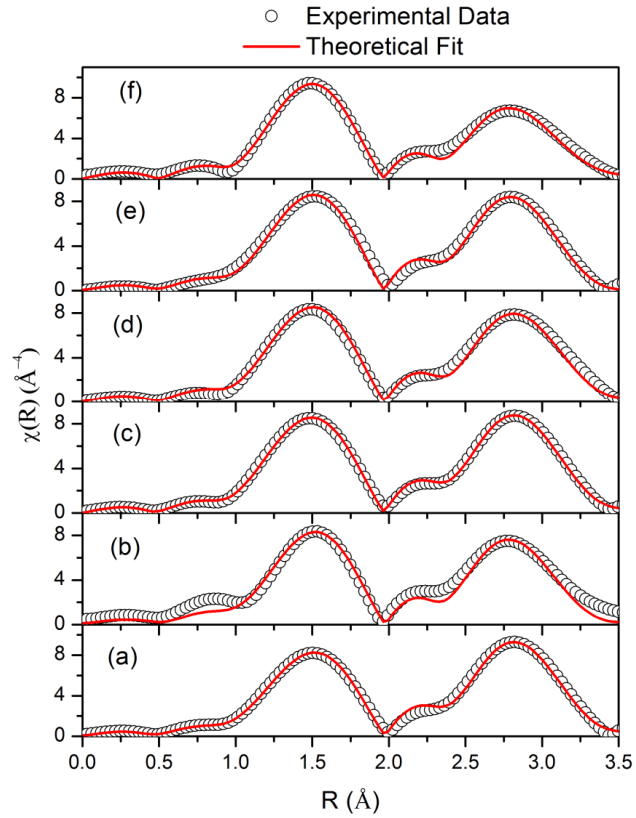


**Figure 3.6:** Fourier transformed EXAFS spectra of (a) ZnO (b) 1% Mn doped ZnO (c) 2% Mn doped ZnO (d) 4% Mn doped ZnO (e) 6% Mn doped ZnO and (f) 10% Mn doped ZnO samples measured at Zn K-edge along with best fit theoretical plots.

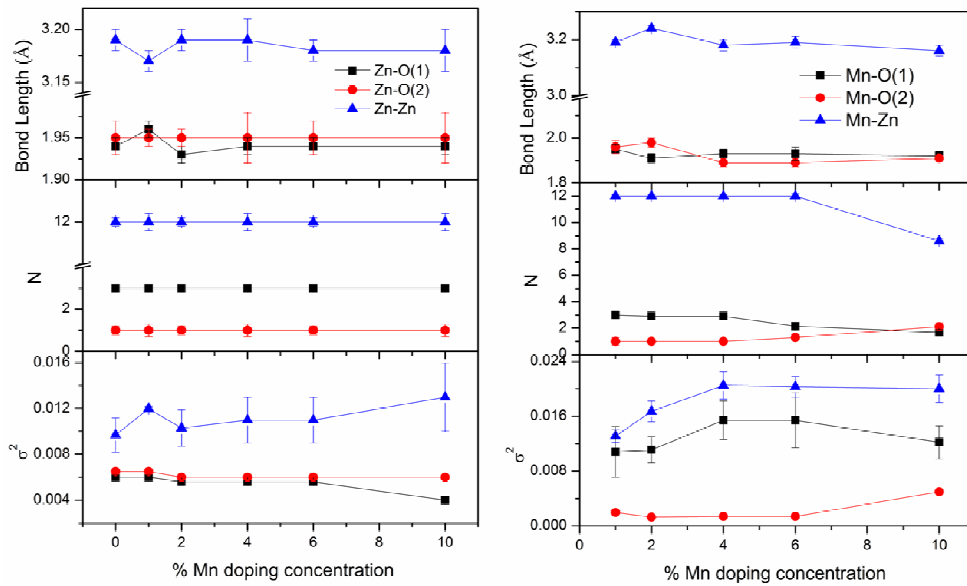


**Figure 3.7:** Variation of bond length (R), coordination number (N) and disorder factor ( $\sigma^2$ ) with doping concentration for Zn K-edge (left panel) and Mn K-edge (right panel).

**Table 3.1:** Bond length, coordination number and disorder factor obtained by fitting of the FT-EXAFS data measured at Zn-K edge.

Path	Parameter	ZnO: Pure	ZnO: 1%Mn	ZnO: 2%Mn	ZnO: 4%Mn	ZnO: 6%Mn	ZnO: 10%Mn
Zn-O	R (Å)	1.94±0.01	1.96± 0.01	1.93±0.01	1.94±0.01	1.94±0.01	1.94± 0.01
	N	3.0±0.010	3.0± 0.10	3.0±0.10	3.0± 0.10	3.0±0.10	3.0± 0.10
	$\sigma^2$	0.0060± 0.0002	0.0060± 0.0002	0.0056± 0.0002	0.0056± 0.0002	0.0056± 0.0002	0.0040± 0.0002
Zn-O	R (Å)	1.95± 0.02	1.95± 0.01	1.95±0.01	1.96±0.03	1.96±0.02	1.96± 0.03
	N	1.0±0.20	1.0± 0.30	1.0± 0.20	1.0± 0.3	1.0± 0.2	1.0± 0.3
	$\sigma^2$	0.0065± 0.0002	0.0065± 0.0002	0.0060± 0.0002	0.0060± 0.0002	0.0060± 0.0002	0.0060± 0.0002
Zn-Zn	R (Å)	3.19±0.01	3.17±0.01	3.19±0.01	3.19± 0.01	3.18±0.01	3.18± 0.02
	N	12.0±0.1	12.0±0.2	12.0±0.1	12.0± 0.2	12.0± 0.1	12.0±0.2
	$\sigma^2$	0.0097± 0.0015	0.0120± 0.002	0.0103± 0.0016	0.011± 0.002	0.011± 0.002	0.013± 0.003

**Table 3.2:** Bond length, coordination number and disorder factor obtained by theoretical fitting of EXAFS data measured at Mn K edge .

Path	Parameter	ZnO: 1%Mn	ZnO: 2%Mn	ZnO: 4%Mn	ZnO: 6%Mn	ZnO: 10%Mn
Mn-O	R (Å)	1.95±0.02	1.91± 0.02	1.93± 0.02	1.93± 0.03	1.92± 0.02
	N	3.0±0.1	2.9±0.1	2.9±0.1	2.1± 0.2	1.7±0.2
	$\sigma^2$	0.0108±0.00 37	0.0111±0.00 19	0.0154±0.00 28	0.0154±0.00 40	0.0122± 0.0024
Mn-O	R (Å)	1.96± 0.03	1.98±0.02	1.89±0.02	1.89±0.02	1.91± 0.01
	N	1.0± 0.3	1.0±0.2	1.0±0.2	1.3± 0.2	2.1±0.3
	$\sigma^2$	0.0020± 0.0002	0.0013± 0.0001	0.0014± 0.0001	0.0014± 0.0001	0.0050±0.00 01
Mn-Zn	R (Å)	3.19± 0.01	3.24±0.01	3.18± 0.02	3.19± 0.02	3.16± 0.02
	N	12.0± 0.1	12.0±0.1	12.0± 0.1	12.0±0.2	8.6±0.1
	$\sigma^2$	0.0131± 0.009	0.0167±0.00 15	0.0205± 0.0020	0.0203± 0.0015	0.020±0.002 0

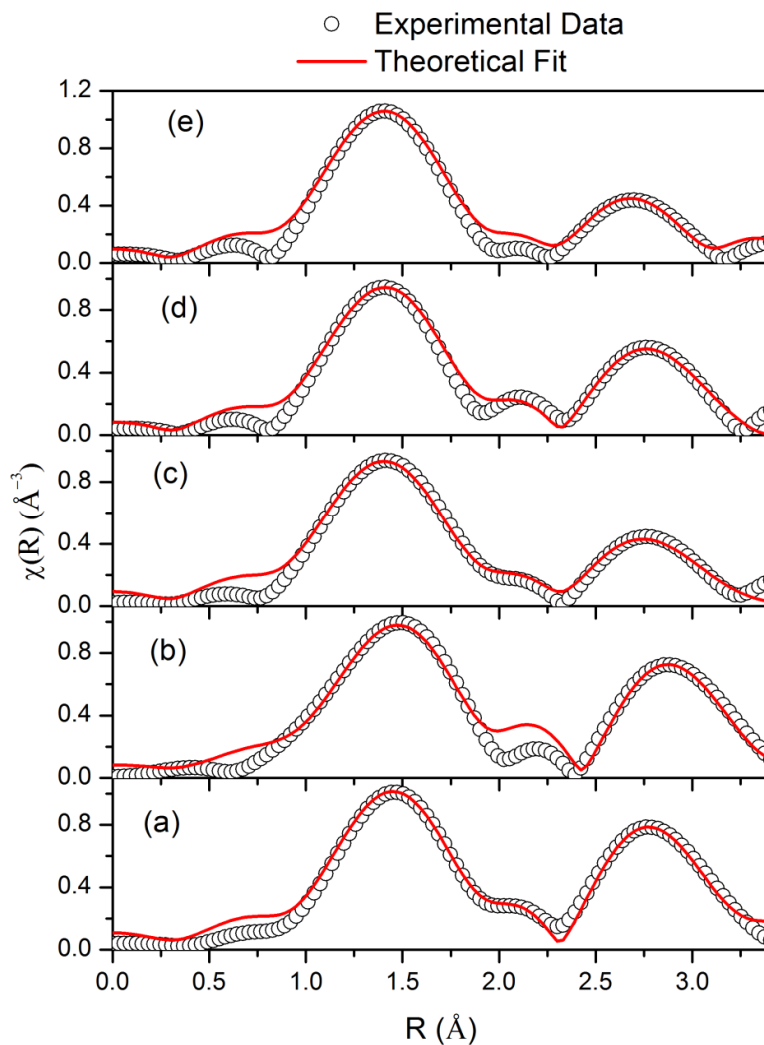


**Figure 3.8:** Fourier transformed EXAFS spectra of (a) 1% Mn doped ZnO (b) 2% Mn doped ZnO (c) 4% Mn doped ZnO (d) 6% Mn doped ZnO and (e) 10% Mn doped ZnO samples measured at Mn K-edge along with best fit theoretical plots.

Based on the XANES results obtained at Mn K-edge, initial structure taken for theoretical FT-EXAFS calculations and fitting of Mn K-edge FT-EXAFS data is Mn atoms substituting Zn sites in ZnO lattice. It can be seen from Table 3.2 that as Mn doping concentration is increased, oxygen coordination decreases, though  $\sigma^2$  increases for all three paths (fig. 3.7). This decrease in oxygen coordination or increase in oxygen vacancies in the samples with increase in Mn doping concentration is also confirmed by O K-edge XANES measurements as discussed later. It is also observed that the second shell Zn coordination for

the 10% Mn doped sample is much lower ( $N=8.6$ ) compared to other doping concentrations manifesting decrease in substitutional Mn and increase in interstitial Mn concentration in the samples which possibly implies creation of Mn clusters in this sample.

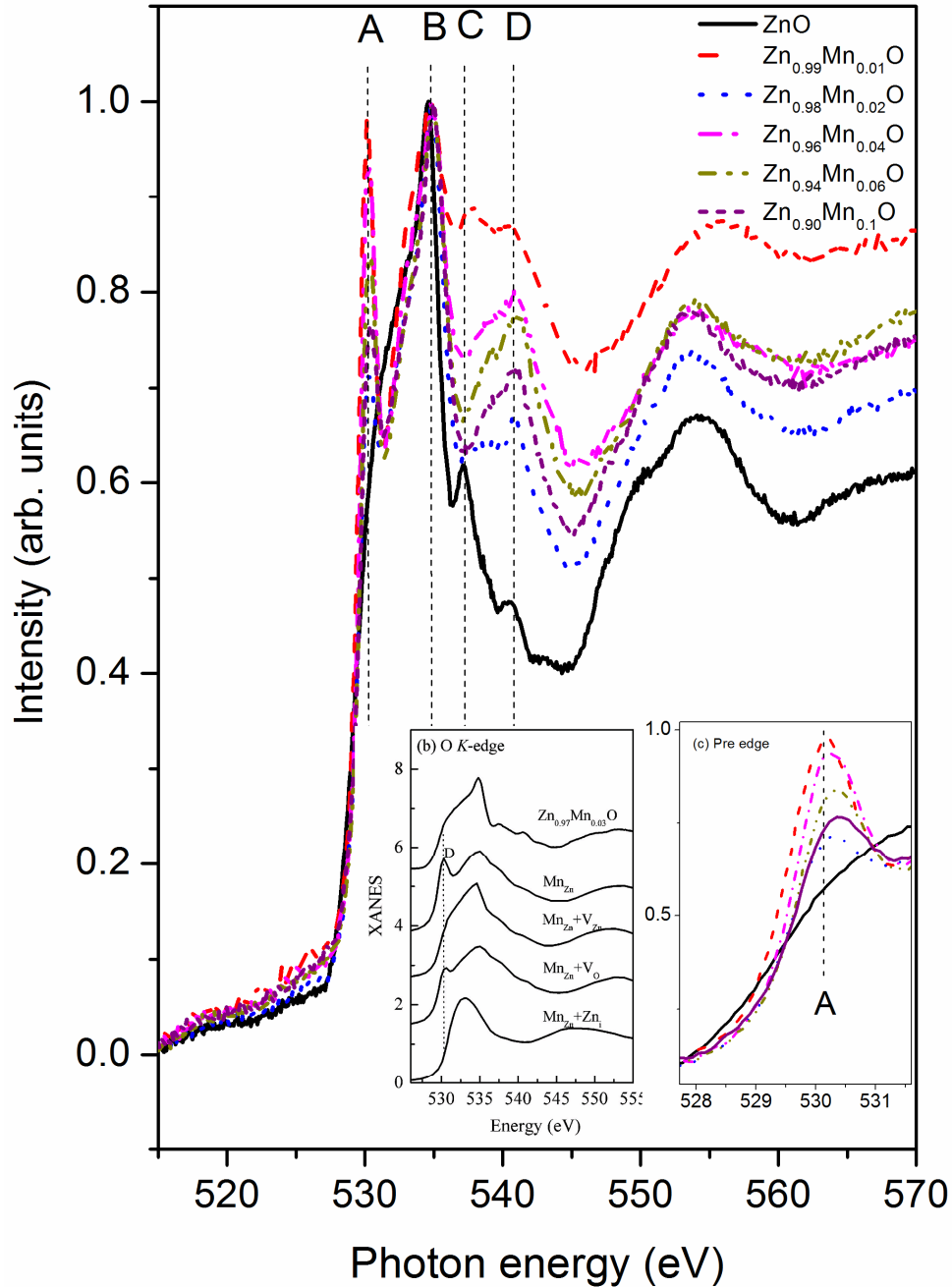


**Figure 3.9:** O K edge XANES spectra of undoped and Mn doped ZnO samples (1%, 2%, 4%, 6% and 10% doping). Inset (b) shows theoretically simulated XANES spectra by Yan et al.<sup>91</sup> for different defect models and Inset (c) shows the part of feature A in expanded scale.

Normalized XANES spectra at O K-edge for samples with different Mn concentrations are shown in figure 3.9. The O K-edge spectra of ZnO obtained here matches well with earlier experimental results<sup>91, 192-195</sup>. The four main structural features in the spectra are denoted by A, B, C and D. The structural feature denoted by B is attributed mainly due to transition of K shell electron to O 2p hybridization with highly dispersive Zn 3d4s/Mn 3d states which forms the bottom of the conduction band<sup>192</sup>. The intensity and position of the peak observed at B is found to be the same for all doping concentrations. Undoped ZnO shows a shallow shoulder at position A in the spectra however in case of Mn doped samples this shoulder grows as a well separated peak. The enlarged portion of this peak A is shown in inset of the figure 3.9 which shows that the peak intensity increases with increase in Mn doping excluding the 1% Mn doped sample for which peak intensity is found to be maximum. The peak position is also shifted to higher energy side with Mn doping. The peak at A is attributed to transition to O2p-Mn3d hybrid state with little contribution from fully occupied Zn 3d shell though it may have some contribution from Zn 4s states also as has been suggested by Guo et al.<sup>193</sup>. The other significant observation from O K edge XANES spectra is that at position C a small peak is present in case of undoped ZnO sample which becomes very weak for 1% Mn doped ZnO and is absent for all other doping concentrations. However the peak intensity at D is found to continuously increase with increase in Mn doping concentration. The spectra are similar for all the samples in the energy region beyond D. The peak denoted by C and D was assigned to O2p hybridization with Zn 4p/Mn 4sp states and the spectrum above D arise due to the O 2p state that extends to Zn/Mn higher states<sup>192</sup>.

As in case of Mn K edge XANES data, we have compared the O K-edge XANES data also with the theoretical spectra generated by Yan et. al.<sup>91</sup> (shown in the inset of fig. 3.9) with different conditions like  $Mn_{Zn}$ ,  $Mn_{Zn}+V_o$ ,  $Mn_{Zn}+V_{Zn}$ , and  $Mn_{Zn}+Zn_i$ . By comparing the

spectra we could rule out the possibilities of  $Mn_{Zn}+V_{Zn}$  and  $Mn_{Zn}+Zn_i$  in the present set of samples. The remaining possibilities are either substitutional Mn and oxygen vacancy ( $Mn_{Zn}+V_O$ ) or only substitutional Mn ( $Mn_{Zn}$ ). On the other hand as reported by Vaithainathan et.al.<sup>194</sup> since the peak at position A is a characteristics of transition to O 2p-Mn3d hybridized state, a strong peak here is a result of significantly high density of unoccupied states or in other words due to high density of oxygen vacancies in the sample giving rise to their n-type semiconducting properties. The increase in the concentration of oxygen vacancies in the samples with Mn doping is also corroborated by the EXAFS results at Mn K-edge described above.

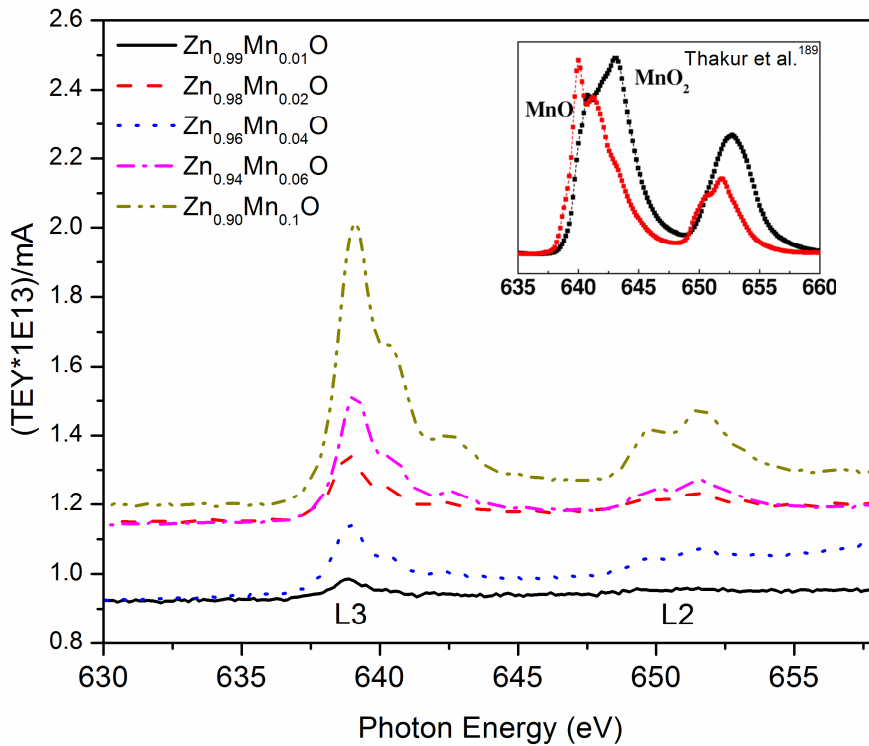


**Figure 3.10:** Mn L<sub>2,3</sub> edge XANES spectra for Mn doped ZnO thin films (1%, 2%, 4%, 6% and 10% doping). Inset shows spectra from Thakur et al.<sup>192</sup>

The Mn L<sub>2,3</sub> EXAFS spectra of the samples are shown in figure 3.10 which matches with that reported in the literatures<sup>193, 195, 196</sup>. The L<sub>3</sub> edge is a result of Mn 2p<sub>3/2</sub>-3d transition

and  $L_2$  edge is the result of  $Mn2p_{1/2-3d}$  transition. Since these transitions involve outer shells of Mn, the change in the oxidation state is more pronounced for  $L_{2,3}$  edges than for Mn K edge. The position and the lineshape of Mn  $L_{2,3}$  peak change when the charge state and crystal field on Mn changes<sup>195</sup>. If we compare our spectra with the spectra of  $Mn^{2+}$  and  $Mn^{3+}$  standard samples as given by Thakur et al.<sup>192</sup>, shown in the inset of fig. 3.10, it clearly suggests that Mn is present in 2+ oxidation state in our Mn doped samples and there is no other oxidation state of Mn present in these samples.

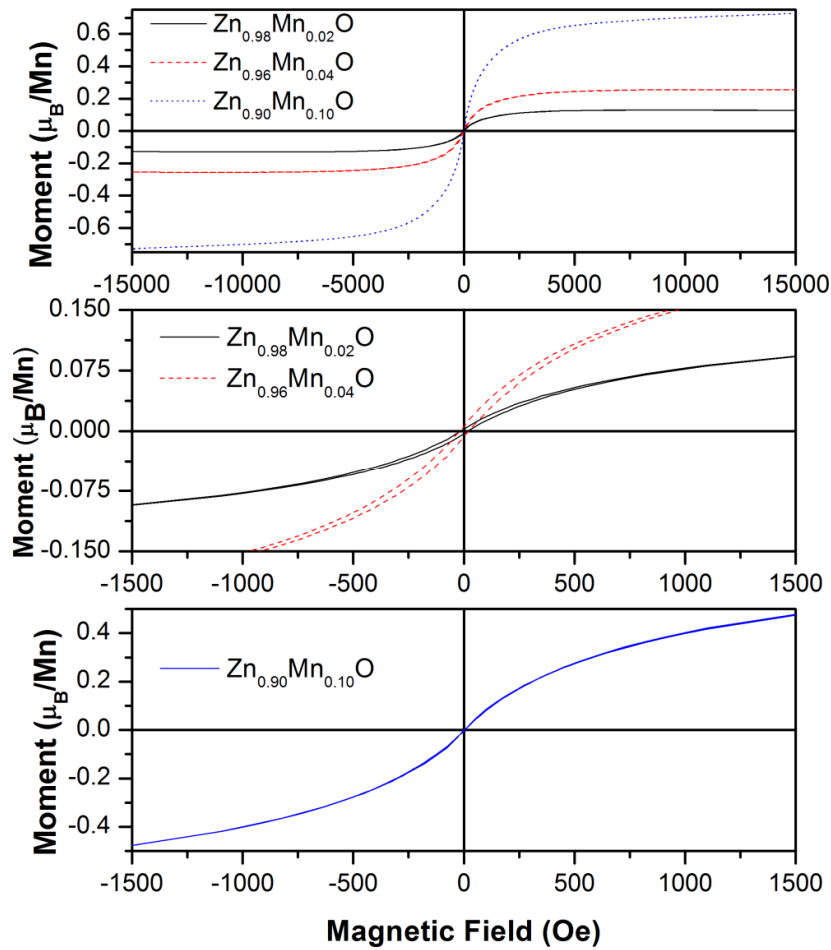


**Figure 3.11:** Room temperature M-H curve of Mn doped ZnO thin films (2%, 4% and 10% doping).

Magnetization versus applied magnetic field (M–H) curves measured at 300K for Mn doped ZnO samples (2%, 4% and 10% Mn doped samples) are shown in Figure 3.11 after removing the contributions from c-Si substrate. Weak hysteresis loops are observed for the samples with the lower (2% and 4%) Mn concentrations which manifest the ferromagnetic ordering at room temperature with saturation magnetisation of  $0.13 \mu_B/\text{Mn}$  for 2% and  $0.25 \mu_B/\text{Mn}$  for 4% doping which are much less than the value of  $5 \mu_B/\text{Mn}$  for a free  $\text{Mn}^{2+}$  ion, though are comparable to the results obtained by other researchers<sup>91, 197</sup>. Fig. 3.12 shows the variation of magnetization as a function of temperature for 1%, 2% and 6% Mn doped ZnO thin film samples, from which it is clear that magnetization follows a convex-like behavior, as normally expected for ferromagnetic materials according to the Weiss mean field theory. Similar trend in the M-T plots for the ferromagnetic Mn doped ZnO nano-wire samples has been reported by Chang et al.<sup>198</sup>.

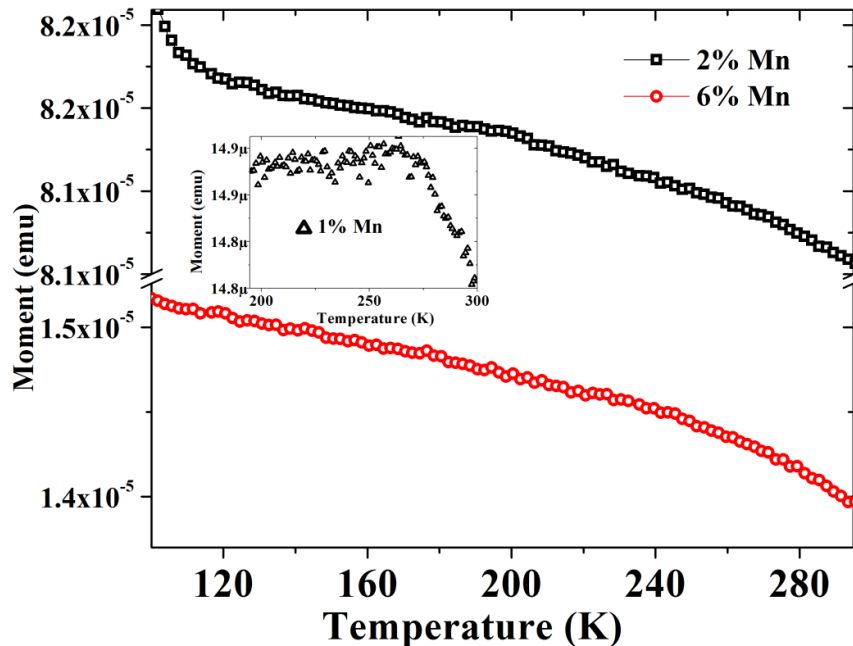


**Figure 3.12:** Magnetic moment versus temperature plots for 1%, 2% and 6% Mn doped ZnO thin films.

However, as can be seen from fig. 3.11 ferromagnetism completely disappears for the sample with 10% Mn concentration as there is no hysteresis observed. Thakur et al.<sup>192</sup> and Fatima et al.<sup>95</sup> have also observed that saturation magnetization decreases with increase in Mn doping concentration in ZnO thin films.

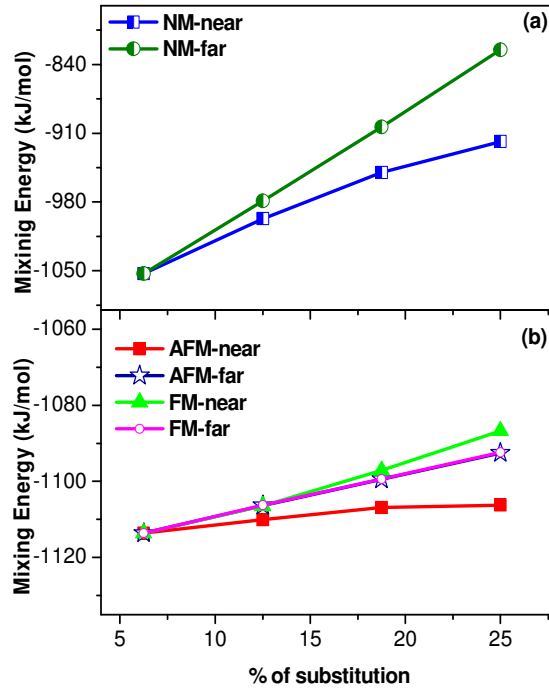


**Figure 3.13:** First principle calculations by Basu et al.<sup>191</sup> for mixing energy versus percentage of substitution of Zn atoms by Mn atoms.

Thus our magnetization result, along with the findings from XANES and EXAFS measurements (which conclusively proves the presence of oxygen vacancies in the samples and that Mn is present in the samples primarily in  $Mn^{+2}$  state), support the proposition that magnetization in Mn doped ZnO is governed by two competing phenomena of FM and AFM interactions. At lower Mn concentration, ferromagnetic interaction dominates which is attributed to indirect interaction among Mn ions through defects (oxygen vacancies) or in other words due to the overlap of unoccupied Mn 3d states with impurity band of oxygen vacancies<sup>199</sup>. However, as Mn concentration increases, Mn clustering takes place which gives rise to AFM ordering<sup>191</sup> and hence the net magnetization of the sample decreases. First

principle calculations done by our group (Basu et al.<sup>191</sup>) earlier have clearly shown (figure 3.13) that in Mn doped ZnO system with relatively high doping concentration, when Mn atoms lie closer to each other, the AFM interaction of the system becomes more probable with significantly lower mixing energy.

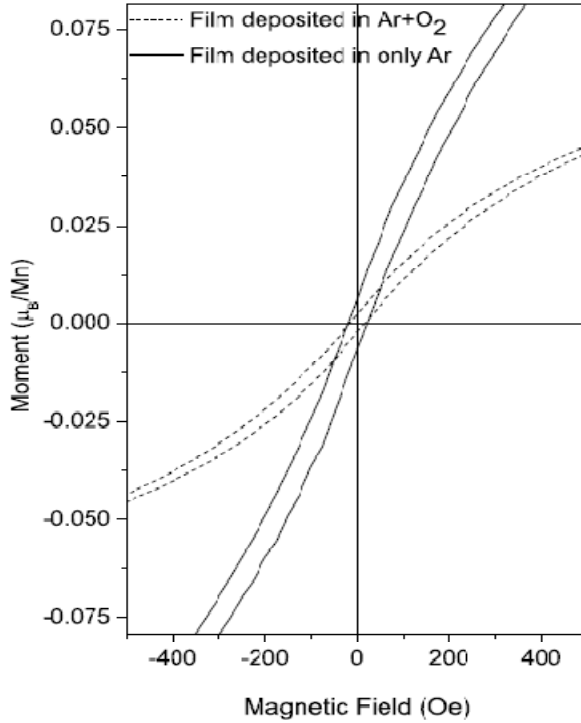


**Figure 3.14:** Room temperature M-H curves of 4% Mn doped ZnO thin films deposited in pure Ar ambient and in Ar+O<sub>2</sub> mixed ambient.

To further probe the role of oxygen vacancies in determining the magnetic properties of the present thin films, a 4% Mn doped ZnO film has been deposited in a mixed Ar +O<sub>2</sub> (50%+50%) ambient instead of in pure Ar ambient. The M-H plot for the film deposited in Ar+O<sub>2</sub> ambient is shown in fig. 3.14 alongwith that of the film deposited in only Ar ambient. It can be seen that coercivity and saturation magnetization in the sample deposited with oxygen reduces significantly, which clearly manifests the role of oxygen vacancies towards the origin of FM in the samples.

# Chapter 4

## **Fe, Co AND Ni DOPED ZnO THIN FILMS**

In the present section of this chapter, we have presented the results of our investigations by XAS measurements on the origin of room temperature ferromagnetism (RTFM) in Fe, Co and Ni doped ZnO thin films. The advantage of using XAS techniques in probing the local structure around the host and dopant atoms in these materials and hence in interpretation of their magnetic properties have already been discussed in detail in Chapter-1.

### **4.1 Fe doped ZnO:**

Several methods have been reported in the literature to produce Fe doped ZnO based DMS nanocrystalline powder and thin films, such as sol gel,<sup>200, 201</sup> solid state reaction,<sup>70</sup> molecular beam epitaxy,<sup>202</sup> laser ablation<sup>203</sup> and radio frequency (rf) sputtering<sup>204</sup> etc. In the present study we have prepared Fe doped ZnO thin films by rf sputtering technique as discussed below.

#### **4.1.1 Experimental:**

##### **4.1.1.1 Preparation of samples:**

Pure and Fe (1, 2, 4, 6 and 10%) doped ZnO thin films have been deposited using the in-house built magnetron sputtering system described in Chapter 2<sup>205</sup>. The target materials are high purity Fe doped ZnO (1, 2, 4, 6 and 10%) discs of 75 mm diameter. Substrates used for all the depositions are crystalline silicon (111) having dimension of 25mm x 10mm and the depositions have been carried out under high purity argon ambient, the Ar flow rate being controlled by using a mass flow controller. The other deposition parameters are sputtering

pressure of  $4 \times 10^{-3}$  mbar, substrate to target distance of 4.5 cm, RF power of 100 W and all the films were deposited for 20 minutes.

#### **4.1.1.2 Characterization of samples:**

Preliminary structural characterisations of the films were carried out by Grazing Incidence X-ray Diffraction (GIXRD) measurements using a Rigaku SmartLab diffractometer with monochromatic Cu  $K_{\alpha}$  X-rays at a grazing angle of incidence and with a wavelength of 1.54 Å. The XANES and EXAFS measurements have been carried out at the Energy-Scanning EXAFS beamline (BL-09) at the Indus-2 Synchrotron Source RRCAT, Indore, India, while XANES measurements at the O K edges of the Fe doped ZnO samples were performed at room temperature in the total electron yield (TEY) mode at the soft X-ray absorption spectroscopy (SXAS) beamline (BL-01) of the Indus-2 synchrotron radiation source. The details of the above beamlines have been described in Chapter-2. M–H measurements at room temperature (RT) were performed with a Superconducting Quantum Interference Device Vibrating Sample Magnetometer (SQUID-VSM-050 MPMS), Quantum Design, USA as described also in Chapter-2.

#### **4.1.2 Results and discussions:**

The phase purity of Fe doped ZnO films has been checked by GIXRD measurement which (Fig.4.1) shows no secondary phase other than wurtzite hexagonal ZnO phase (space group P63mc; JCPDS card no. 36-1451) in the samples. It has been observed from Fig. 4.1 that with an increase in Fe doping concentration, hexagonal crystal structure of ZnO remains preserved and there is no appearance of other impurity peaks, though the diffraction peaks are found to be shifted to lower angles which is also consistent with the other reports on Fe doped ZnO films<sup>73, 204, 206, 207</sup>. The shift in the (100) peak has been shown in enlarged scale in the inset of Fig. 4.1.

Similar shift of the XRD peaks towards lower angles with increase in Fe doping concentration has also been observed by Gautam et al.<sup>208</sup> for Fe doped nanorod samples which has been attributed to slight increase in Zn–O and Zn–Zn bond lengths with increase in Fe doping concentration in the ZnO samples. In wurtzite structure of ZnO unit cell, one oxygen atom neighbouring four Zn atoms form the geometry of a triangular pyramid with oxygen located at the pyramid centre and substitution of Zn<sup>2+</sup> ions (ionic radii 0.60 Å in tetrahedral coordination<sup>209</sup>) by smaller Fe<sup>3+</sup> ions (ionic radii 0.49 Å in tetrahedral coordination<sup>209</sup>) results in a small increase in the Zn–O and Zn–Zn bond distances. We have used the position of (100) diffraction peak to calculate the lattice constant 'a' using the formula given by Wang et al.<sup>207</sup>

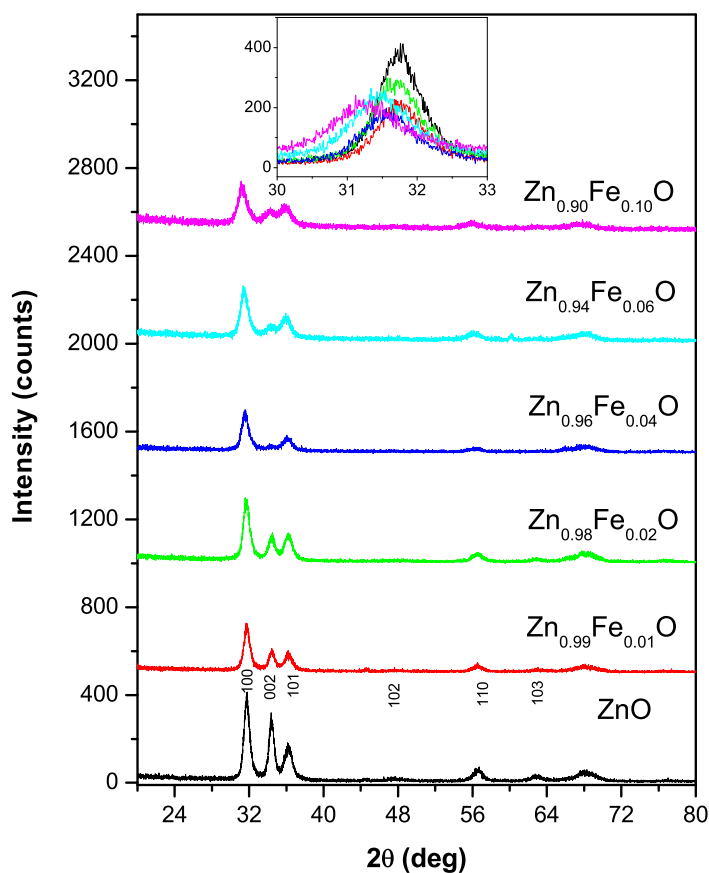


**Figure 4.1:** GIXRD plots of undoped ZnO and Fe doped ZnO thin films (1%, 2%, 4%, 6% and 10% doping). Inset: Variation of the (100) peak position with increase in Fe doping concentration.

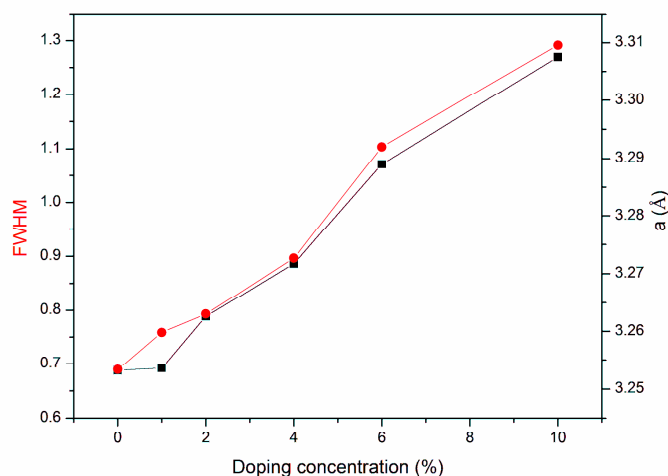


**Figure 4.2:** Variation of lattice constant (a) and FWHM of the diffraction peak (100) with Fe doping concentration.

The calculated lattice parameter and Full Width Half Maxima (FWHM) of the (100) diffraction peak are plotted with Fe doping concentration in Fig. 4.2, which shows that both the above quantities increase with Fe doping concentration. Chen et al.<sup>204</sup> also observed similar broadening in the FWHM and explained it on the basis of strain and disorder induced by difference in the ionic radii of Fe and Zn.

XANES spectra measured at Fe K edge for Fe doped ZnO films are shown in Fig. 4.3. Wei et al.<sup>73</sup> had calculated the full XANES spectra of Fe doped ZnO films using full multiple scattering ab initio calculations for two different configurations viz., Fe at the Zn site and Fe at the tetrahedral site in Fe<sub>3</sub>O<sub>4</sub>. The shallow shoulder feature obtained in case of our samples denoted by A in Fig. 4.3, is quite similar to the XANES spectra calculated with Fe at Zn site in ZnO as reported by Wei et al.<sup>73</sup> which confirms substitution of Zn atoms by Fe dopants in our samples.

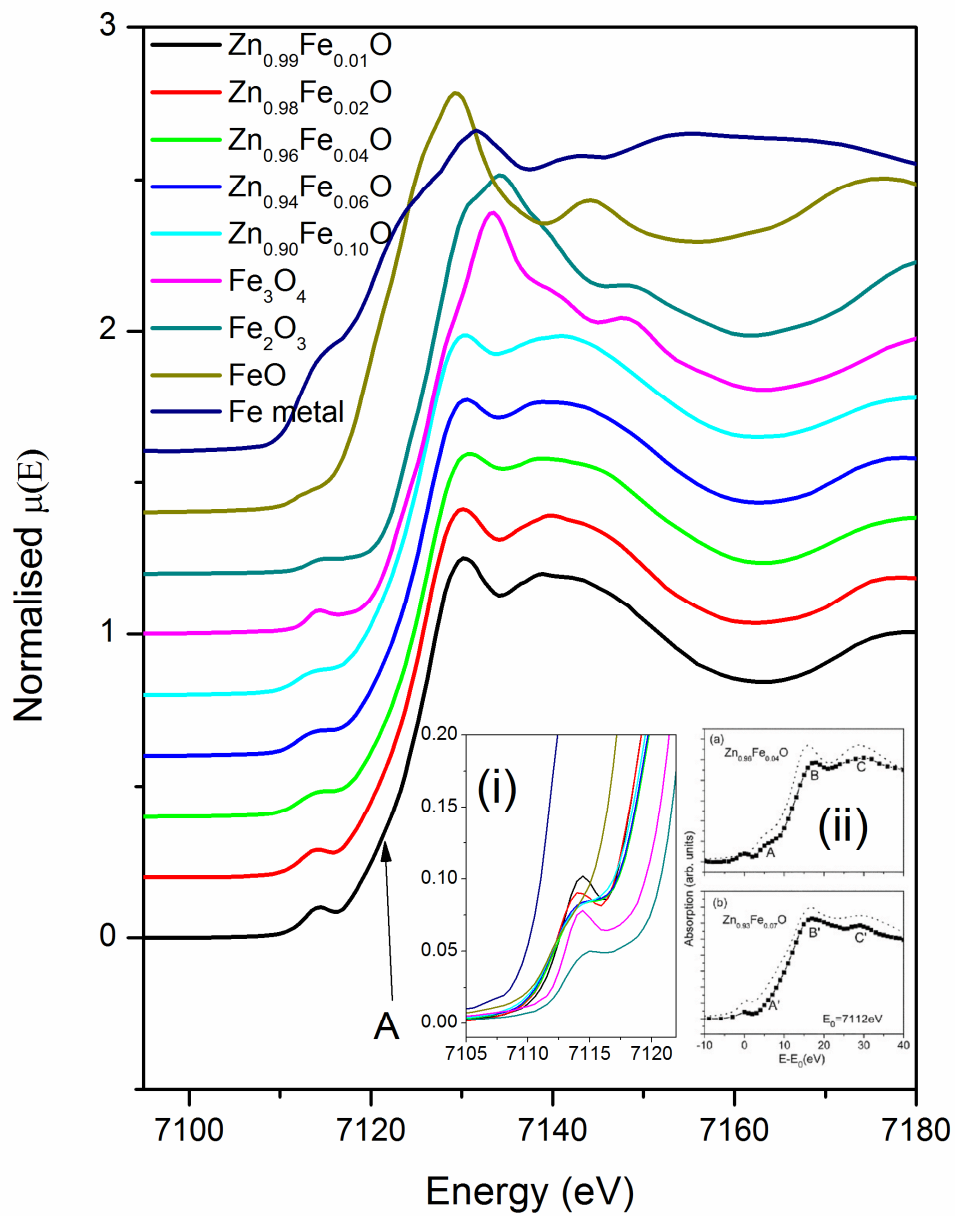


**Figure 4.3:** Normalised XANES spectra of undoped ZnO and Fe doped ZnO thin films (1%, 2%, 4%, 6% and 10% doping) at Fe K-edge. The reference spectra of Fe metal, FeO, Fe<sub>3</sub>O<sub>4</sub> and Fe<sub>2</sub>O<sub>3</sub> are given for comparison. The inset figure (i) shows the expanded part of the pre-edge region and (ii) shows the XANES spectra reported by Wei et al.<sup>73</sup>.

**Table 4.1:** Contribution of Fe<sup>+2</sup> and Fe<sup>+3</sup> oxidation states obtained from Linear Combination Fitting of XANES spectra.

Sample	Fe <sup>2+</sup>	Fe <sup>3+</sup>	<i>R</i> <sub>factor</sub>
Zn <sub>0.99</sub> Fe <sub>0.01</sub> O	29%	71%	0.0015
Zn <sub>0.98</sub> Fe <sub>0.02</sub> O	29%	71%	0.0020
Zn <sub>0.96</sub> Fe <sub>0.04</sub> O	32%	68%	0.0017
Zn <sub>0.94</sub> Fe <sub>0.06</sub> O	30%	70%	0.002
Zn <sub>0.90</sub> Fe <sub>0.10</sub> O	29%	71%	0.002

The XANES spectra of four standard samples with different oxidation states of Fe viz., Fe metal foil (+0), FeO (+2), Fe<sub>3</sub>O<sub>4</sub> (+2/ +3) and Fe<sub>2</sub>O<sub>3</sub> (+3) have also been shown in Fig. 4.3 along with the XANES spectra of the Fe doped ZnO films. It is well known that transition metals show the pre-edge features prior to the main absorption edge.<sup>210</sup> While the main absorption edge manifests transition of the core level electron to continuum, the pre-edge peak is mainly due to electric dipole transition of the core shell (1s) electron to the 3d–2p hybridized orbital, the pre-edge centroid position depends on the oxidation state of absorbing atom and the intensity of the pre-edge depends on the coordination geometry. In general, the pre-edge intensity of the tetrahedral geometry (non centro-symmetry) is higher than the intensity of the octahedral geometry (centro-symmetry). The intense pre-edge peak in the present Fe doped ZnO samples, as shown in Fig. 4.3, indicates the presence of tetrahedral coordination. Similar pre-edge peaks in the Fe K-edge XANES spectra have also been observed by Gautam et al.<sup>208</sup> for their Fe doped ZnO nanorods. The XANES spectra also indicate that Fe K-edges of the samples fall in-between that of FeO and Fe<sub>2</sub>O<sub>3</sub> standards, with more proximity to Fe<sub>2</sub>O<sub>3</sub>, indicating the presence of Fe in mixed oxidation states of +2 and +3 in our samples, with higher probability of +3 state. To determine the oxidation state of Fe quantitatively, we have performed linear combination fit (LCF) using the XANES spectra of all four standards. The best fitting can only be obtained after excluding the Fe metal

standard which indicates that there is no metal cluster present in our samples. This is in contrast to our earlier result<sup>211</sup> on Mn doped ZnO thin films which show signature of Mn clusters at higher doping concentrations. Signature of Fe clustering have not been observed for our sol-gel derived Fe doped ZnO nanoparticles also reported earlier<sup>201</sup>. The LCF results (Table 4.1) shows that Fe is present in 30:70 ratio in +2 and +3 oxidation state in the samples and the ratio does not vary significantly with the change in Fe doping concentration. Mixed oxidation state of Fe has been observed by Gautam et al.<sup>208</sup> also in polycrystalline Fe doped ZnO nanorods and they have also obtained similar ratio using LCF calculations. Seo et al.<sup>212</sup> have also observed a mixed oxidation state of Fe ions in ZnO thin films prepared by rf magnetron sputtering on sapphire substrate. However, many researchers<sup>13, 201, 213</sup> have also found that Fe exists in purely trivalent state in their Fe doped ZnO samples. The expected oxidation state of Fe is +2 if it replaces Zn atom in ZnO while the presence of Fe in +3 state may be due to the presence of nearby cationic vacancy (Zn vacancy) at the substitutional sites. The XANES spectra of the samples at Zn K edge are shown in Fig. 4.4 which completely resembles that of pure ZnO sample over the whole Fe doping concentration range. This indicates that Zn related impurity or defects around Zn sites are negligible in the films.

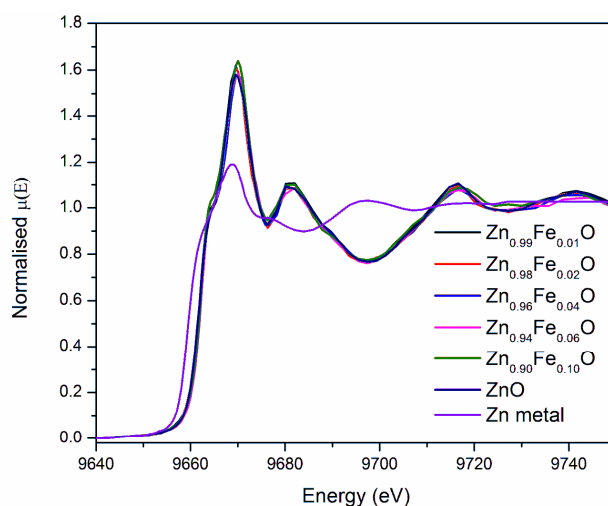


**Figure 4.4:** Normalised XANES spectra of undoped ZnO and Fe doped ZnO thin films (1%, 2%, 4%, 6% and 10% doping) measured at Zn K-edge along with Zn metal foil.

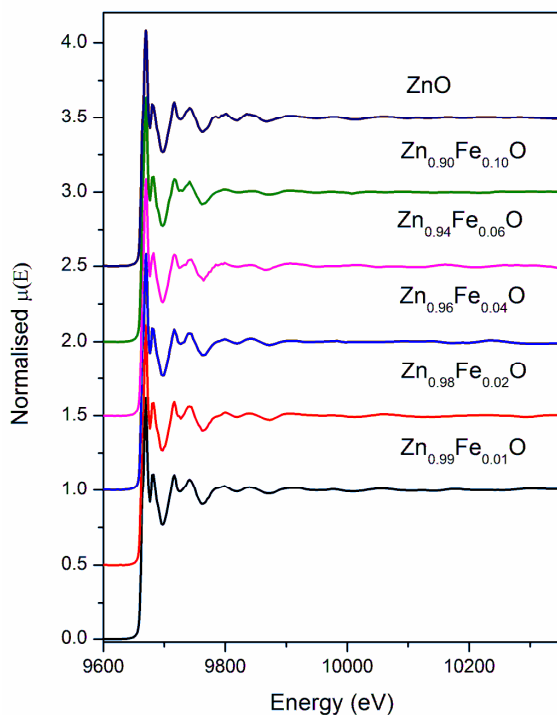


**Figure 4.5:** Normalised EXAFS spectra of undoped ZnO and Fe doped ZnO (1%, 2%, 4%, 6% and 10% doping) thin films measured at Zn K-edge.

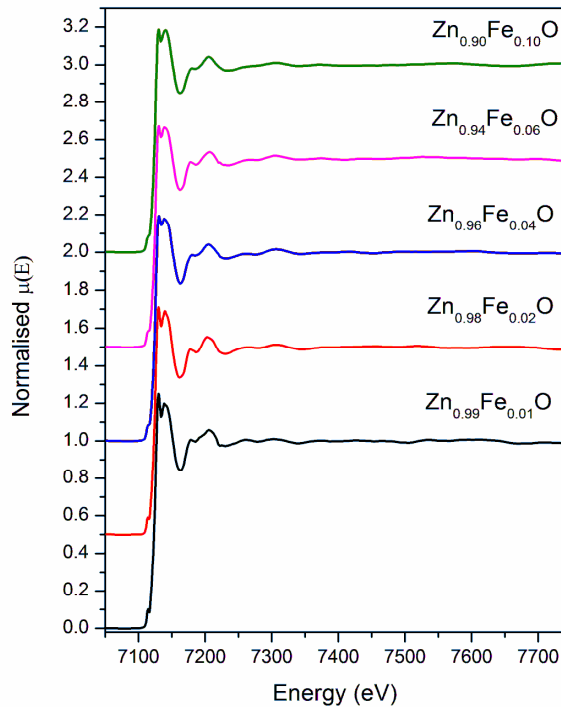


**Figure 4.6:** Normalised EXAFS spectra of Fe doped ZnO (1%, 2%, 4%, 6% and 10% doping) thin films measured at Fe K-edge.

The normalized EXAFS spectra of pure and Fe doped ZnO samples are shown in Fig. 4.5 and 4.6 at Zn and Fe K edges respectively. The Fourier transform EXAFS spectra or  $\chi(R)$  versus  $R$  plots have been generated for all the samples from the  $\mu(E)$  versus  $E$  spectra following the methodology described in Chapter-2 and are shown in Fig. 4.7 for the data measured at Zn K-edge. The structural parameters (atomic coordination and lattice parameters) of ZnO used for simulation of the theoretical EXAFS spectra of the samples have been obtained from ref. <sup>33</sup> and the best fit  $\chi(R)$  versus  $R$  plots (fitting range  $R = 1.0\text{--}3.5 \text{ \AA}$ ) of the samples have also been shown in Fig. 4.7 along with the experimental data. The bond distances, co-ordination numbers (including scattering amplitudes) and disorder (Debye-Waller) factors ( $\sigma^2$ ), which give the mean square fluctuations in the distances, have been used as fitting parameters and the best fit results are summarized in Table 4.2 and fig. 4.9 for Zn

K-edge measurements. It should be mentioned here that the amplitude reduction factors ( $S_0^2$ ) for the different paths have been obtained from fitting of FT-EXAFS spectrum of a commercial ZnO powder sample and have been kept constant during the fitting of the thin film data. The goodness of the fit in the above process is generally expressed by the  $R_{factor}$  (equation 2.20 in Chapter-2).

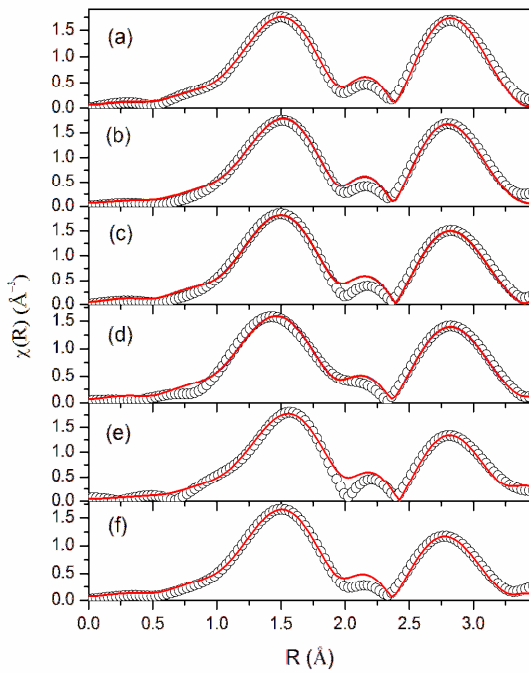


**Figure 4.7:** Fourier transformed EXAFS spectra of (a) ZnO (b) 1% Fe doped ZnO (c) 2% Fe doped ZnO (d) 4% Fe doped ZnO (e) 6% Fe doped ZnO and (f) 10% Fe doped ZnO (scatter points) at Zn K edge along with best fit theoretical plots (solid line).

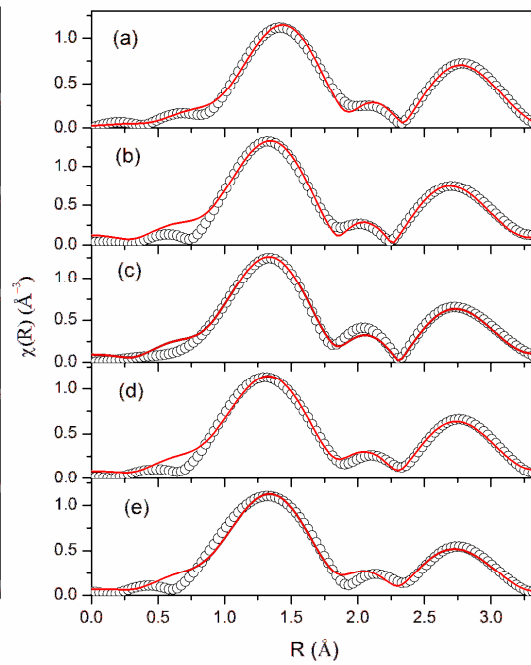


**Figure 4.8:** Fourier transformed EXAFS spectra of (a) 1% Fe doped ZnO (b) 2% Fe doped ZnO (c) 4% Fe doped ZnO (d) 6% Fe doped ZnO and (e) 10% Fe doped ZnO (scatter points) at Fe K edge along with best fit theoretical plots (solid line).

**Table 4.2:** Bond length, coordination number and disorder factor obtained by fitting of FT-EXAFS data measured at Zn K edge.

Path	Parameter	ZnO: Pure	ZnO: 1%Fe	ZnO: 2% Fe	ZnO: 4% Fe	ZnO: 6% Fe	ZnO: 10% Fe
Zn-O	R (Å)	1.94±0.01	1.95±0.01	1.94±0.01	1.94±0.02	1.96±0.01	1.96±0.01
	N	4	4	4	4	4	4
	$\sigma^2$	0.0060 ±0.0009	0.0063 ±0.0009	0.0060 ±0.0009	0.0074 ±0.0009	0.0073 ±0.0008	0.0072 ±0.0009
Zn-Zn	R (Å)	3.19±0.01	3.18±0.01	3.19±0.01	3.18±0.01	3.21±0.02	3.19±0.01
	N	12	12	12	12	12	12
	$\sigma^2$	0.0097 ±0.0007	0.0099 ±0.0008	0.0117 ±0.0009	0.0129 ±0.009	0.0123 ±0.0007	0.0146 ±0.0008

The first peak at 1.4 Å (phase uncorrected spectrum) in Zn Kedge FT-EXAFS spectrum (Fig. 4.7) of pure ZnO has contributions from four oxygen atoms at a bond length of 1.94 Å. The bond length obtained is in good agreement with other studies<sup>191</sup>. The second peak at 2.8 Å (phase uncorrected spectrum) is fitted with single Zn–Zn shell with coordination number of 12 and at a Zn– Zn distance of 3.19 Å. It can be seen from Table 4.2 that the Zn–O and Zn-Zn bond lengths do not change with increase in Fe doping concentration in the samples, however the Debye–Waller factor ( $\sigma^2$ ) increases which is due to the increase in disorder in ZnO lattice due to substitution of Zn atoms by Fe dopants. It should be noted here that in accordance to the shift of the XRD peaks of ZnO samples towards lower angles with Fe doping as discussed above, we expected to observe marginal increase in the Zn–O and Zn–Zn bond lengths by EXAFS measurements as has been observed by Gautam et al.<sup>208</sup>. However, we have not observed any such change possibly due to fact that it is beyond the detection limit of our measurement set-up. It should also be noted from Table 4.2 that there is no change in oxygen or Zn coordination around Zn sites with

increase in Fe doping concentration in the films. This result is quite different from what we have observed in case of Mn doped ZnO thin films,<sup>211</sup> which showed the presence of oxygen vacancy around Zn sites that increases with increase in Mn doping concentration.

**Table 4.3:** Bond length, coordination number and disorder factor obtained by fitting of FT-EXAFS data measured at Fe K edge.

Path	Parameter	ZnO: 1%Fe	ZnO: 2%Fe	ZnO: 4%Fe	ZnO: 6%Fe	ZnO: 10%Fe
Fe-O	R (Å)	1.92 ±0.02	1.88±0.01	1.87 ±0.01	1.87 ±0.01	1.88 ±0.01
	N	3.57 ±0.10	3.57±0.14	3.57 ±0.10	3.81 ±0.14	3.91 ±0.13
	$\sigma^2$	0.0047 ± 0.0009	0.0047 ±0.0009	0.0063 ±0.0008	0.0090 ±0.0009	0.0099 ±0.0009
Fe-Zn	R (Å)	3.21 ±0.02	3.20±0.01	3.19 ±0.01	3.20 ±0.02	3.20 ±0.02
	N	9.46 ±0.28	10.73±0.32	10.73 ±0.32	11.44 ±0.46	11.72 ±0.47
	$\sigma^2$	0.0196 ±0.002	0.0197 ±0.002	0.0194 ±0.001	0.0233 ±0.002	0.0256 ±0.002

The Fourier transform EXAFS spectra at Fe K edge are shown in Fig. 4.8. The first peak at 1.3 Å in the phase uncorrected spectra is a contribution of the nearest Fe–O shell and second peak at 2.7 Å is a contribution of next nearest Fe–Zn shell. To carry out the fitting theoretical FT-EXAFS spectrum has been generated by substituting Zn atoms in ZnO structure by Fe atoms. The bond distances, co-ordination numbers and disorder factors have been used as fitting parameters and best fit results of Fe K edge FT-EXAFS data are shown in Table 4.3 and fig. 4.9. The first peak in 1% Fe doped ZnO is a contribution of first oxygen

shell at distance of 1.92 Å. This bond length is found to be slightly lower than Zn–O bond lengths obtained in the samples from Zn K-edge EXAFS measurements.

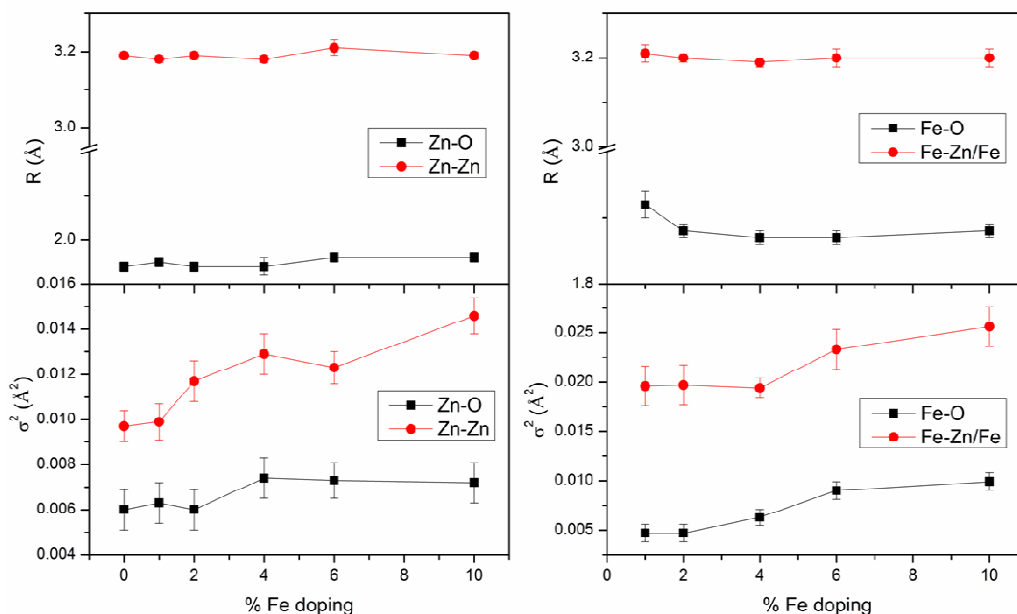


**Figure 4.9:** Variation of bond length ( $R$ ) and disorder factor ( $\sigma^2$ ) with doping concentration for Zn K-edge (left panel) and Fe K-edge (right panel).

This decrease in the bond length is expected since the ionic radii of tetrahedral coordinated  $\text{Fe}^{3+}$  (0.49 Å) is lower than the ionic radii of tetrahedral coordinated  $\text{Zn}^{2+}$  (0.60 Å)<sup>209</sup>. This result corroborates the presence of Fe primarily in  $\text{Fe}^{3+}$  state in the samples as obtained from the Fe K-edge XANES results described earlier. Similar decrease in the bond length is also observed by other researchers also<sup>13</sup>. The Fe–O bond length further decreases for 2% Fe doped sample and remains same for all the doping concentration. The second peak in the Fe K-edge FT-EXAFS spectra is a contribution of next nearest Fe–Zn shell at a distance of 3.20 Å. The Fe–Zn bond length is found to be comparable to the Zn–Zn bond length which suggests that Fe goes to Zn sites in the ZnO lattice. Zn coordination in this shell is however lower than the ideal value of 12 indicating the presence of Zn vacancies in the samples near the dopant sites. The presence of Zn vacancy and mixed oxidation state of the dopants, in case of Fe doped ZnO have been observed by many other researchers also<sup>214-217</sup>.

Karmakar et al.<sup>214</sup> have found that Fe is present in the +2 and +3 oxidation state and suggested that presence of the Fe in +3 state is due to the hole doping in the system by Zn vacancy, however no experimental evidence is provided on the presence of Zn vacancy. Our experimental results support the theoretical prediction of Debernardi et al.<sup>217</sup> by density functional theory which suggests that presence of Zn vacancies at the next nearest positions of Fe atoms is energetically more favourable than isolated Zn vacancies. In case of our samples also, the presence of Zn vacancies are not observed from Zn K-edge EXAFS measurements, however they are found in the neighbourhood of Fe atoms from the Fe K-edge EXAFS measurements.

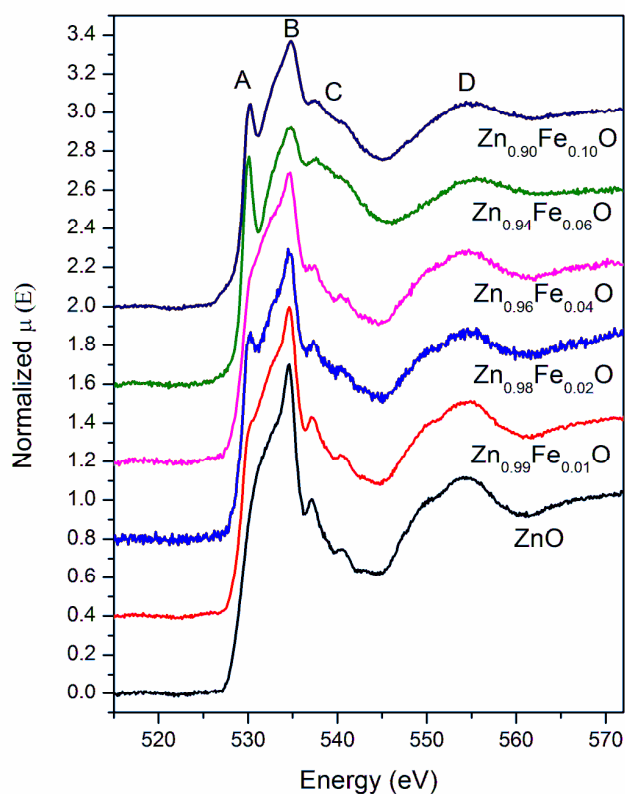


**Figure 4.10:** O K edge XANES spectra of undoped and Fe doped ZnO samples (1%, 2%, 4%, 6% and 10% doping).

As can be seen from Table 4.3, the variation in the bond length with Fe doping concentration is not significant, however the disorder factor ( $\sigma^2$ ) is found to increase with increase in Fe doping concentration manifesting again substitution of Zn atoms by Fe dopants. These results also corroborate with the results obtained from Zn K-edge EXAFS measurement and with the fact that FWHM of XRD peaks of the samples increase with increase in Fe doping concentration as discussed earlier.

Normalized XANES spectra at O K-edge for samples with different Fe concentrations are shown in Fig. 4.10. The spectral features are denoted by A, B, C and D in the figure. The main peak denoted by B at ~536 eV is due to the transition of 1s electron to O2p–Zn4sp hybridized state as stated by other workers also<sup>194, 218</sup>. The peak A at 530 eV, which is like a shallow shoulder for the undoped sample, shows significant enhancement with increase in Fe doping concentration. This feature at A is attributed to transitions from 1s core state of oxygen to 2p oxygen state hybridized with 3d state of Fe<sup>219</sup>. In case of undoped ZnO, the transition to oxygen 2p-Zn 3d hybridized state is not possible since the d orbital of Zn is fully occupied. As Fe atoms replace Zn atoms in ZnO lattice, the empty orbital of Fe 3d state are contributing to this transition and enhances this peak at position A. The peak at D is due to the O 2p hybridization with extended Fe 4sp orbital<sup>215</sup>. Thus O K-edge XANES measurements also support the above conjecture that Zn atoms are being substituted by Fe dopants in the samples.

The magnetization (M) versus field (H) curves for 2%, 4% and 10% Fe doped ZnO samples measured at RT are shown in Fig. 4.11. The diamagnetic contribution from the substrate as well as the host ZnO has been subtracted from each plot. The inset shows the enlarged view of low field region. All three samples exhibit RTFM ordering with significant and increasing saturation magnetization (MS) (0.14 emu g<sup>-1</sup> for 2%, 0.18 emu g<sup>-1</sup> for 4% and 0.63 emu g<sup>-1</sup> for 10% Fe doping at 5 kOe) with increase in Fe dopant concentration.

However, the coercive field ( $H_C$ ) is low ( $\sim 51$  Oe) for all samples and it indicates that all Fe doped ZnO thin film samples are ferromagnetically soft. The magnetization measurements by Kumar et al.<sup>219</sup> on 1% Fe doped ZnO sample shows soft ferromagnetic behaviour at room temperature with 27 Oe coercive field and  $\sim 0.125$  emu  $g^{-1}$  saturation magnetization. The saturation magnetization is found to increase with Fe doping concentration in the samples. Magnetic measurements on undoped ZnO and Fe doped ZnO nanocrystals by Inamdar et al.<sup>213</sup> showed similar coercivity and saturation magnetization.

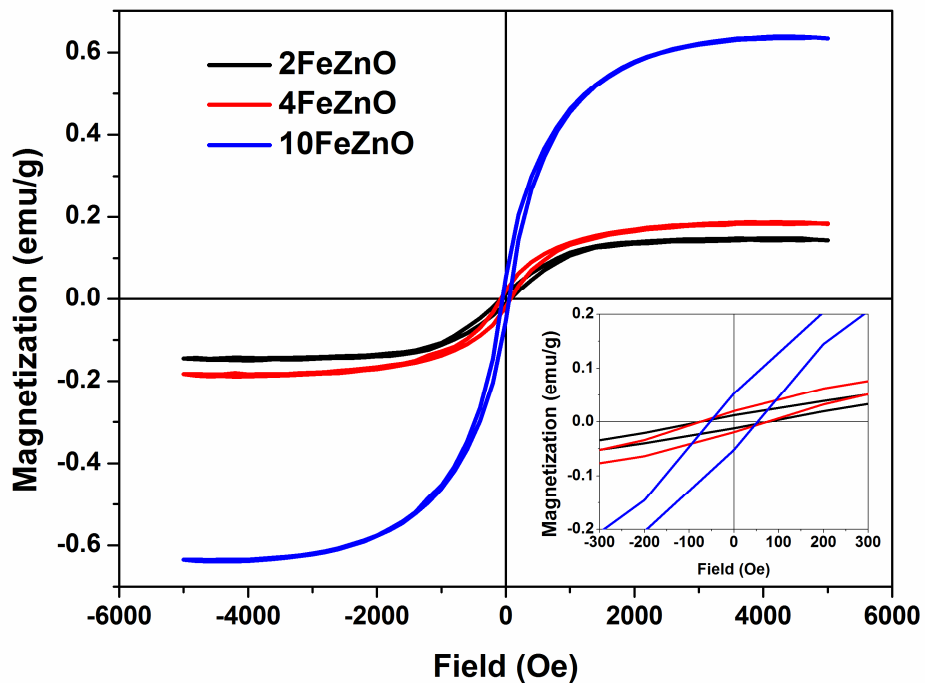


**Figure 4.11:** Room temperature M-H curve of Fe doped ZnO thin films (2%, 4% and 10% doping).

As has been explained in details in Chapter-1, the origin of room temperature ferromagnetism in TM doped DMS material is generally attributed to two major causes, intrinsic or extrinsic. The extrinsic origin is due to the possible presence of any secondary magnetic phase viz., metallic Fe cluster or Fe based oxide phases in case of the present set of samples. The intrinsic origin, on the other hand, is due to the substitution of host atoms by dopants or presence of defects and interstitials. For the present set of Fe doped ZnO thin film

samples, we have observed from GIXRD, XANES and EXAFS measurements that Fe gets incorporated into the Zn sites of ZnO lattice and no evidence of Fe metallic cluster or extra Fe related secondary oxide phases like FeO, Fe<sub>2</sub>O<sub>3</sub>, ZnFe<sub>2</sub>O<sub>4</sub> and Fe<sub>3</sub>O<sub>4</sub> is found upto the maximum Fe doping concentration. Thus it can be concluded that the origin of ferromagnetism in the present set of samples is intrinsic in nature and due to Fe substitution at Zn sites and subsequent creation of Zn vacancies near Fe sites. Wang et al.<sup>216</sup> have also suggested that p-type defects such as Zn vacancies play a crucial role in tuning and stabilization of ferromagnetism in Fe doped ZnO thin films.

## **4.2 Co doped ZnO thin films:**

Next, we present our studies on Co doped ZnO thin films which include the results on Zn and Co K-edge XANES and EXAFS measurements, O K-edge XANES measurements and Co L<sub>2,3</sub> edge XANES measurements on the samples to understand the change in local structure around the host and the dopant ions with varying Co doping concentration.

### **4.2.1 Experimental:**

Co doped ZnO thin films on Si substrate have been deposited with different doping concentration (1, 2, 4, and 10%) using the in-house built magnetron sputtering system<sup>142</sup>. Preliminary structural characterisations of the films were carried out by GIXRD measurements using a Bruker D8 Discover diffractometer with monochromatic Cu K $\alpha$  X-rays at a grazing angle of incidence angle and with a wavelength of 1.54 Å. The EXAFS measurements have been carried out at the Energy-Scanning EXAFS beamline (BL-9) and the X-ray absorption spectroscopy (XAS) measurements at the O K edges and L<sub>3,2</sub> edges of Co of Co doped ZnO samples were performed at room temperature in the total electron yield (TEY) mode at the soft X-ray absorption spectroscopy (SXAS) beamline (BL-01) of the Indus-2 synchrotron radiation source at RRCAT, Indore, India.

#### 4.2.2 Results and discussion:

GIXRD results given in fig.4.12 show no secondary phase other than wurzite hexagonal ZnO phase in the samples. However, we have observed preferential growth along (002) planes takes place for 1% and 2% Co doped samples.

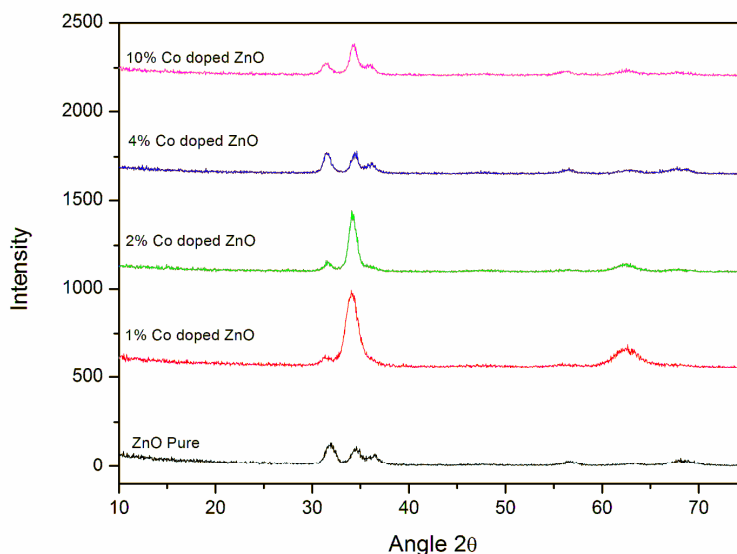


**Figure 4.12:** GIXRD spectra of the ZnO and Co doped ZnO thin films.

The XANES spectra at Co K edge and Zn K edge for Co doped ZnO films are shown in figure 4.13(a) and (b) respectively. The Co spectra are plotted with reference spectra of Co metal and CoO standards. The main edge (1s to 4p transition) position is sensitive to the oxidation state of probe atom and it shifts to higher energy side with increase in oxidation state. There is no significant shift observed for the XANES spectra with Co doping concentration and lies at the same position of CoO. This suggested that Co is present in +2 oxidation state for all doping concentration which ruled out metallic Co atom segregation. The pre edge peak appears due to the transition of Co 1s electron to 4p-3d hybridized state in tetrahedral symmetry. The pre edge intensity is same for all doping concentrations manifesting same coordination geometry in the samples. The XANES spectra at Zn edge is shown in figure 4.13 (b). It can be seen that Zn is present in 2+ oxidation state in all the samples as there is no chemical shift is observed with Co doping concentration.

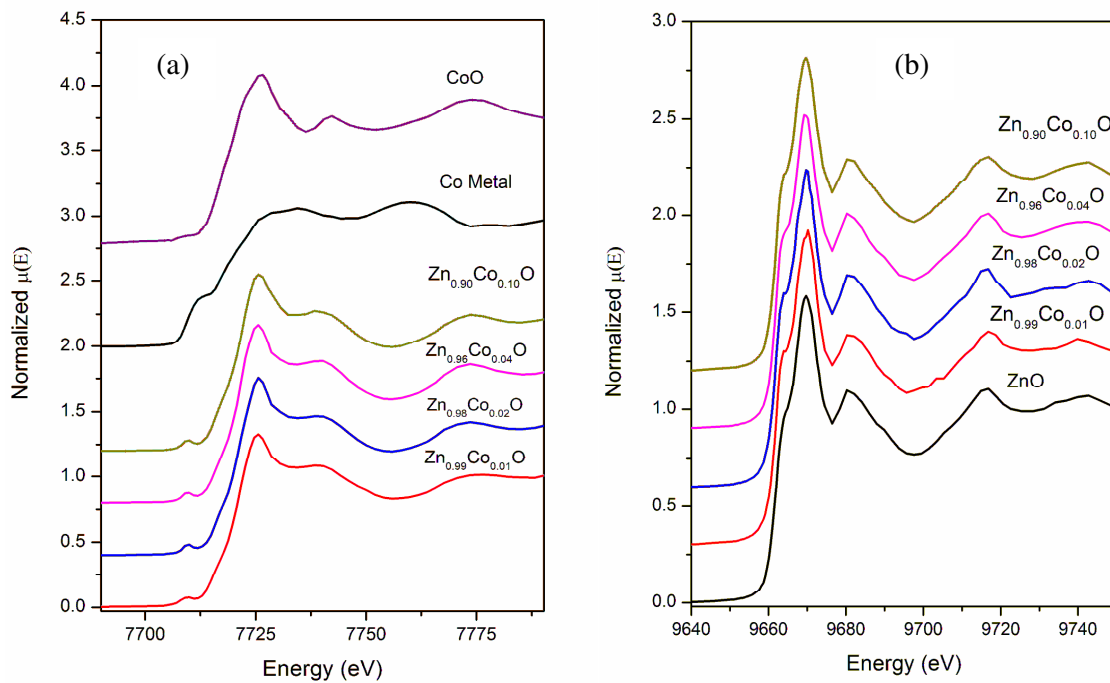


**Figure 4.13:** Normalised XANES spectra of pure ZnO and Co doped ZnO (1%, 2%, 4% and 10% doping) at (a) Co K-edge and (b) Zn K-edge.

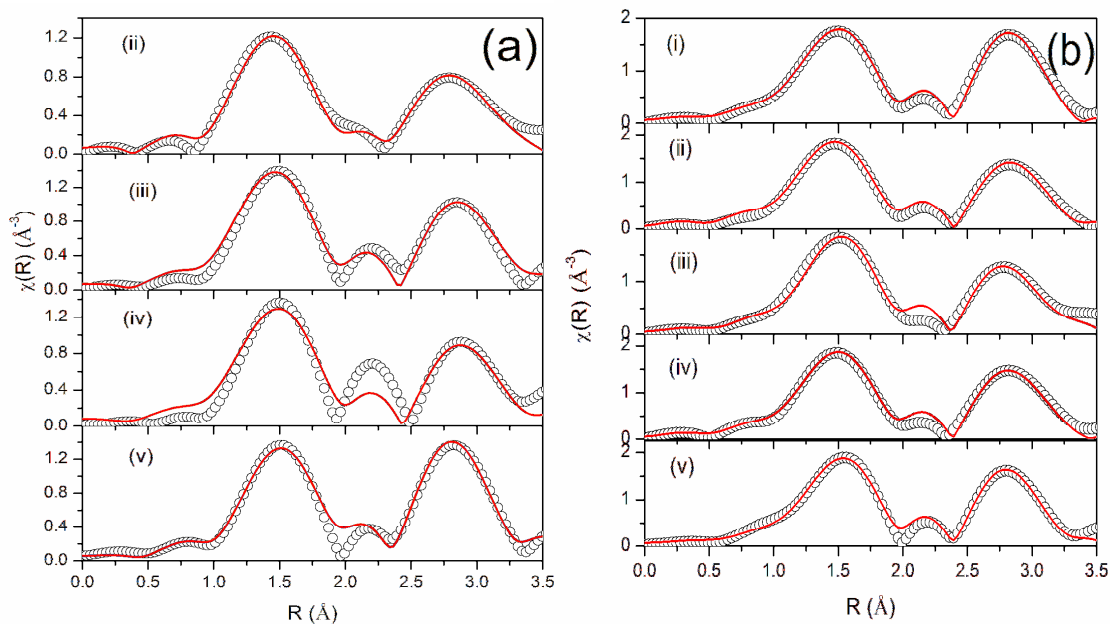


**Figure 4.14:** Fourier transformed EXAFS spectra (scatter points) of (i) ZnO, (ii) 1% Co doped ZnO (iii) 2% Co doped ZnO (iv) 4% Co doped ZnO and (v) 10% Co doped ZnO measured at (a) Co K edge and (b) Zn K edge and theoretical fits (Solid line)..

The  $\chi(R)$  versus  $R$  plots generated (Fourier transform range  $k = 3.0-11.0 \text{ \AA}^{-1}$ ) for all the samples from the  $\mu(E)$  versus  $E$  spectra following the methodology described in Chapter-2 are shown in figure 4.14 (a) and (b) for Co doped ZnO films measured at Co and Zn K edges. The structural parameters (atomic coordination and lattice parameters) of ZnO used for simulation of the theoretical EXAFS spectra of the samples have been obtained from reference<sup>33</sup> and the best fit  $\chi(R)$  versus  $R$  spectra (fitting range  $R = 1.0-3.5 \text{ \AA}$ ) of the samples have also been shown in figures 4.14 (a) and (b) along with the experimental data for the measurements carried out at Co and Zn K edges. The fitting results are tabulated in Tables 4.4 and 4.5 and in fig. 4.15. It can be seen that the first peak at  $1.5 \text{ \AA}$  (Phase uncorrected spectra) is due to 4 Zn-O bonds at  $1.94 \text{ \AA}$  and second peak at  $2.8 \text{ \AA}$  is due to 12 Zn-Zn paths. The fourier transform spectra at Co K edge is showing the peaks at same position as Zn edge spectra. This suggests that Co is going at Zn position in ZnO lattice and there is no secondary phase present as it is also observed by XANES spectra above.

**Table 4.4:** EXAFS parameters at Zn K edge of Co doped ZnO.

Path	Parameter	ZnO: Pure	ZnO: 1%Co	ZnO: 2%Co	ZnO: 4%Co	ZnO: 10%Co
Zn-O	R ( $\text{\AA}$ )	$1.94 \pm 0.01$	$1.93 \pm 0.01$	$1.95 \pm 0.01$	$1.94 \pm 0.01$	$1.95 \pm 0.01$
	N	3	3	3	3	3
	$\sigma^2$	$0.0060 \pm$ $0.0008$	$0.005 \pm$ $0.0009$	$0.0058 \pm$ $0.0006$	$0.0054 \pm$ $0.0009$	$0.0058 \pm$ $0.0010$
Zn-O	R ( $\text{\AA}$ )	$1.95 \pm 0.01$	$1.94 \pm 0.02$	$1.96 \pm 0.01$	$1.95 \pm 0.01$	$1.99 \pm 0.02$
	N	1.0	1.0	1.0	1.0	1.0
	$\sigma^2$	$0.0065 \pm$ $0.0012$	$0.0062 \pm$ $0.0009$	$0.0051 \pm$ $0.0006$	$0.0052 \pm$ $0.0013$	$0.0022 \pm$ $0.0003$
Zn-Zn	R ( $\text{\AA}$ )	$3.19 \pm 0.02$	$3.19 \pm 0.01$	$3.18 \pm 0.01$	$3.19 \pm 0.01$	$3.19 \pm 0.02$
	N	12.0	12	12	12	12
	$\sigma^2$	$0.0097 \pm$ $0.0009$	$0.0124 \pm$ $0.0014$	$0.0138 \pm$ $0.0009$	$0.0121 \pm$ $0.0022$	$0.0098 \pm$ $0.0012$

**Table 4.5:** EXAFS parameters at Co K edge of Co doped ZnO.

Path	Parameter	ZnO: 1%Mn	ZnO: 2%Mn	ZnO: 4%Mn	ZnO: 10%Mn
Co-O	R (Å)	1.95±0.01	1.96±0.01	1.99±0.01	2.02±0.02
	N	3.82±0.24	3.85±0.32	3.82±0.28	3.86±0.16
	$\sigma^2$	0.0026±0.0009	0.005±0.0010	0.005±0.0011	0.005±0.0016
Co-Zn	R (Å)	3.21±0.01	3.25±0.01	3.30±0.01	3.24±0.01
	N	12.0±0.72	12.0±0.96	12.0±0.81	12.0±0.48
	$\sigma^2$	0.017±0.0025	0.0130±0.0015	0.0150±0.0021	0.007±0.0016

Normalized XANES spectra at O K-edge for samples with different Co concentrations are shown in figure 4.16. The features are indicated by A, B, C, D and E in the figure 4.16.

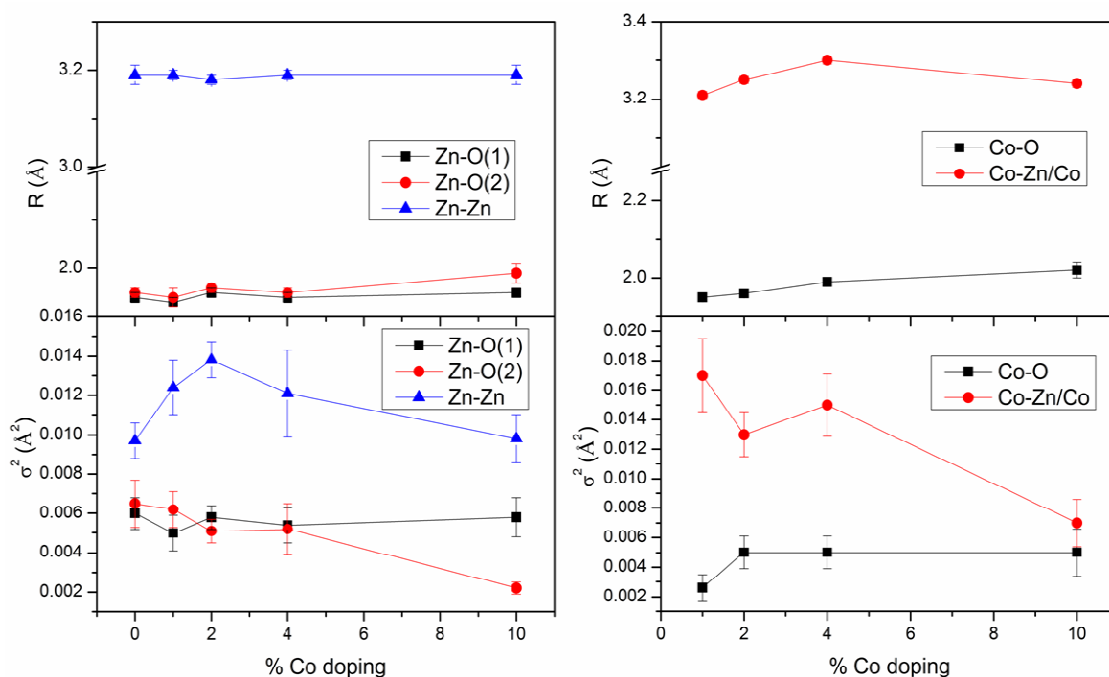


**Figure 4.15:** Variation of bond length ( $R$ ) and disorder factor ( $\sigma^2$ ) with doping concentration for Zn K-edge (left panel) and Co K-edge (right panel).

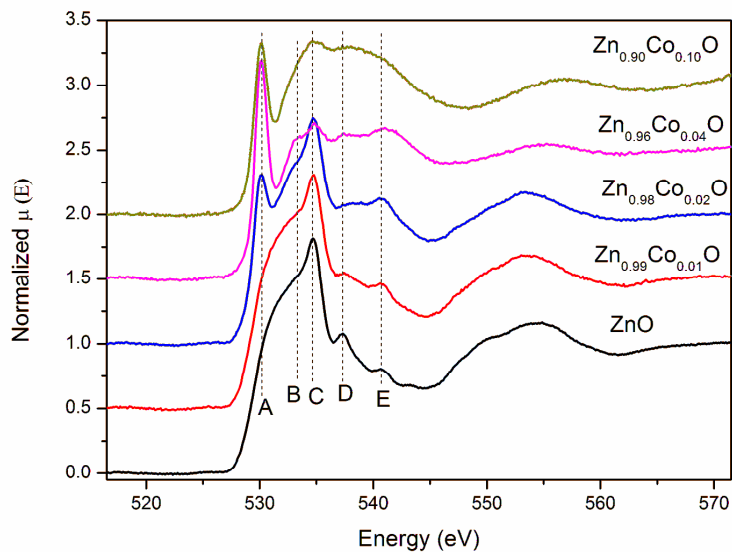


**Figure 4.16:** O K-edge XANES spectra of Co doped ZnO samples.

The O K edge spectra of ZnO obtained here matches well with earlier experimental results<sup>166</sup>. The five main structural features in the spectra are denoted by A, B, C, D and E. The structural feature between 528 and 536 is attributed mainly due to transition of K shell electron to O 2p hybridization with highly dispersive Zn3d4s/Co3d states which forms the bottom of the conduction band<sup>166</sup>. Undoped ZnO shows a shallow shoulder at position A in the spectra, however in case of 1% Co doped samples this shoulder increases and become a separate peak for 2% doping and above. The peak at A is attributed to transition to O2p-Co3d hybrid state with little contribution from fully occupied Zn 3d shell though it may have some contribution from Zn 4s states also as has been suggested by Guo et al.<sup>193</sup>. The other significant observation from O K edge XANES spectra is that at position D and E a small peak is present in case of undoped ZnO sample which becomes very weak for Co doped ZnO. The spectra are similar for all the samples in the energy region beyond D.

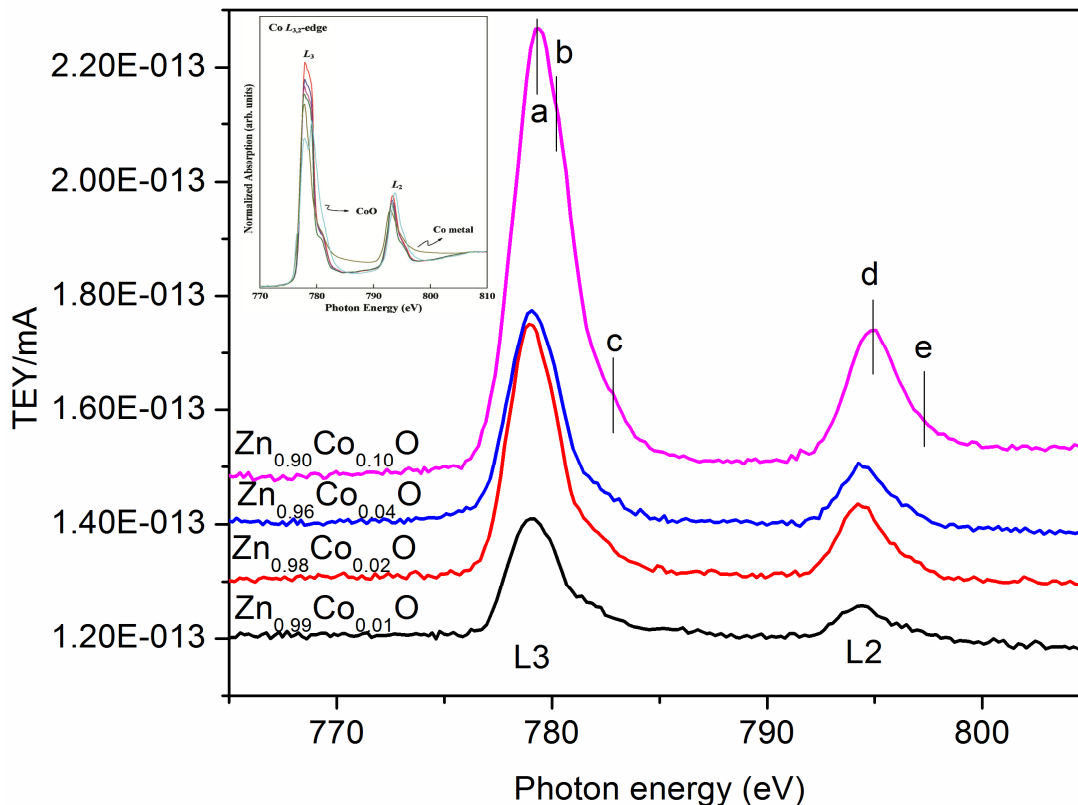


**Figure 4.17:** L<sub>2,3</sub> edge XANES spectra for Co K edge. The inset shows the spectra obtained by Chiou et al.<sup>220</sup>.

Fig 4.17 shows the Co L<sub>3,2</sub> edge absorption spectra for Co doped samples which results from 2p<sub>3/2</sub>—3d transition and 2p<sub>1/2</sub>—3d transition for L<sub>3</sub> and L<sub>2</sub> edge respectively. The separation between these peaks is ~15eV and this separation is due to spin orbit splitting of 2p core holes. The separations between the peaks agree well with the earlier studies<sup>221</sup> and confirms the 2+ oxidation state of Co atoms in the tetrahedral geometry. The features denoted by a,b,c, d and e is due to the coulomb and exchange interaction of 2p core holes with 3d electrons. It can be seen that there is no change in the spectral features over the full Co doping concentration range suggesting that Co is in +2 oxidation state and tetrahedral geometry. The comparison of XANES spectra given by Chiou et al. (inset of figure 4.17) with our spectra suggested that CoO and Co metal phases are not present in our samples<sup>220</sup>.

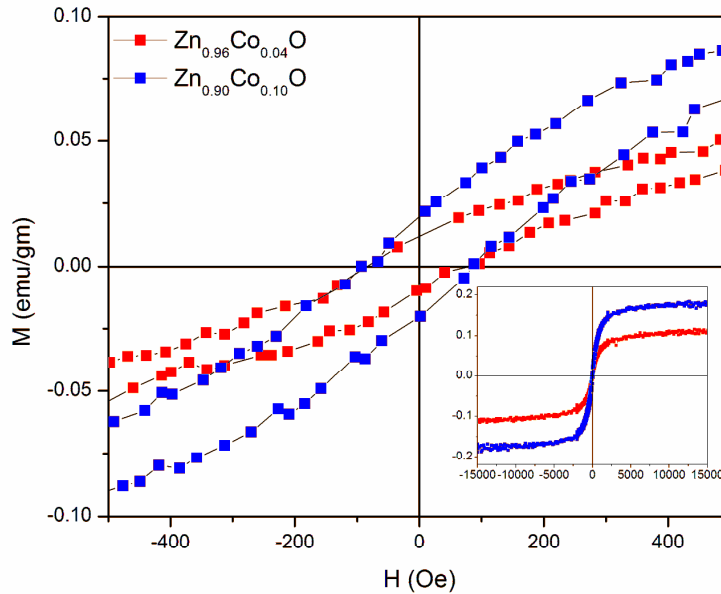


**Figure 4.18:** M-H curve of Co doped ZnO at room temperature.

The room temperature M-H curves of 4% and 10% Co doped ZnO are shown in figure 4.18. The diamagnetic contribution from the substrate as well as the host ZnO has been subtracted from each plot. The inset shows the full field region. The behavior of the M-H curve indicates ferromagnetic characteristic of the samples at room temperature. The saturation magnetization and coercivity is higher for 10% doped sample compared to the 4% Co doped sample. The obtained saturation magnetization and coercivity values agree with that reported by other researchers<sup>222, 223</sup>.

Similar results of increase in saturation magnetization with increase in Co-concentration have been observed by Kumar et al.<sup>224</sup> also for Co doped ZnO nanoparticles who have attributed this to the presence of grain boundaries and oxygen vacancies. Park et. al. showed that metallic clustering in Co doped ZnO thin films are responsible for RTFM for Co doping above 12%, however no such metal clustering has been observed in case of our films which has been confirmed by XAS measurements as discussed above<sup>98</sup>. Yang et al.

prepared Co doped ZnO thin films on sapphire (0001) substrates by PLD technique at various substrate temperatures under oxygen ambience where all the samples exhibited room-temperature ferromagnetism, However the average moment per Co atom was much smaller than moment of  $\text{Co}^{2+}$  ( $3d^7$ ), and this is attributed due to the different distribution of  $\text{Co}^{2+}$  ions, as well as the different defect concentrations in thin films<sup>110</sup>.

Patterson calculated the electronic structures of Co substituted for Zn in ZnO, for Zn and O vacancies and for interstitial Zn in ZnO using the hybrid density functional theory<sup>225</sup>. He reported that the oxygen vacancy is the only defect in Co-doped ZnO which can mediate ferromagnetic exchange coupling of Co ions at intermediate range (just beyond near neighbour distances) and this model is similar to the model proposed by Coey et al<sup>35</sup> in which the polarons bound to the oxygen vacancies mediate ferromagnetic coupling between Co ions.

However, our experimental results clearly indicate the intrinsic nature of ferromagnetism of the present Co doped ZnO samples. The XANES and EXAFS results at Zn and Co K edges show substitution of Co atoms at Zn site. This substitution is further confirmed by O K edge XANES measurements. The absence of any other metallic or oxide phase is ruled out from the results of EXAFS and Co K &  $L_{2,3}$  edge XANES measurements. Presence of oxygen vacancies have also not been observed from our EXAFS results. Hence, the observed ferromagnetism in Co doped ZnO thin films in this case might be due to the ferromagnetic coupling between nearby magnetic ions mediated by charge carriers. The ferromagnetic properties of Co doped ZnO thin films prepared by Seo et al. has also been attributed to the direct interaction between the magnetic ions or by the Co conduction-electron mediation<sup>226</sup>. Liu et al. have however, shown that Co doped ZnO thin film prepared with different oxygen partial pressure shows increasing oxygen vacancies<sup>227</sup>, where negligible change have been observed in oxygen coordination number. It may also be

possible that in our case that the number of oxygen vacancies produced are relatively low to be detected by EXAFS measurements at Co K edge.

### **4.3 Ni doped ZnO:**

In Chapter 3, Mn doped ZnO thin films<sup>211</sup>, we have shown that oxygen vacancies play crucial role in inducing ferromagnetism in the samples, while the presence of clusters destroys the RTFM. Further, for Fe doped ZnO thin films prepared by RF magnetron sputtering<sup>228</sup>, discussed in the beginning of this chapter, we have observed increasing magnetisation in the samples with increase in Fe concentration and have attributed the ferromagnetic ordering in the samples to substitution of Fe at Zn sites and subsequent creation of p-type Zn vacancies. In case of Co doped ZnO films however, we have not seen any clear signature of oxygen or Zn vacancies and have attributed the observed FM directly to ferromagnetic coupling between nearby magnetic ions mediated by charge carriers.

In the present section, we have carried out similar investigations on Ni doped ZnO thin films prepared by RF sputtering technique which also show weak ferromagnetism.

#### **4.3.1 Experimental:**

##### **4.3.1.1 Preparation of samples:**

The in-house built RF magnetron sputtering system described in Chapter-2 has been used to deposit pure and Ni (1, 2, 4, 6 and 10%) doped ZnO thin films used in this study<sup>142</sup>. High purity ZnO discs of 3 inch diameter and having requisite Ni doping have been used as sputtering targets. Substrates used for all the depositions are crystalline silicon (111) having dimension of 24mm x 12mm and all depositions have been carried out under high purity argon ambient, the argon flow rate being controlled by using a

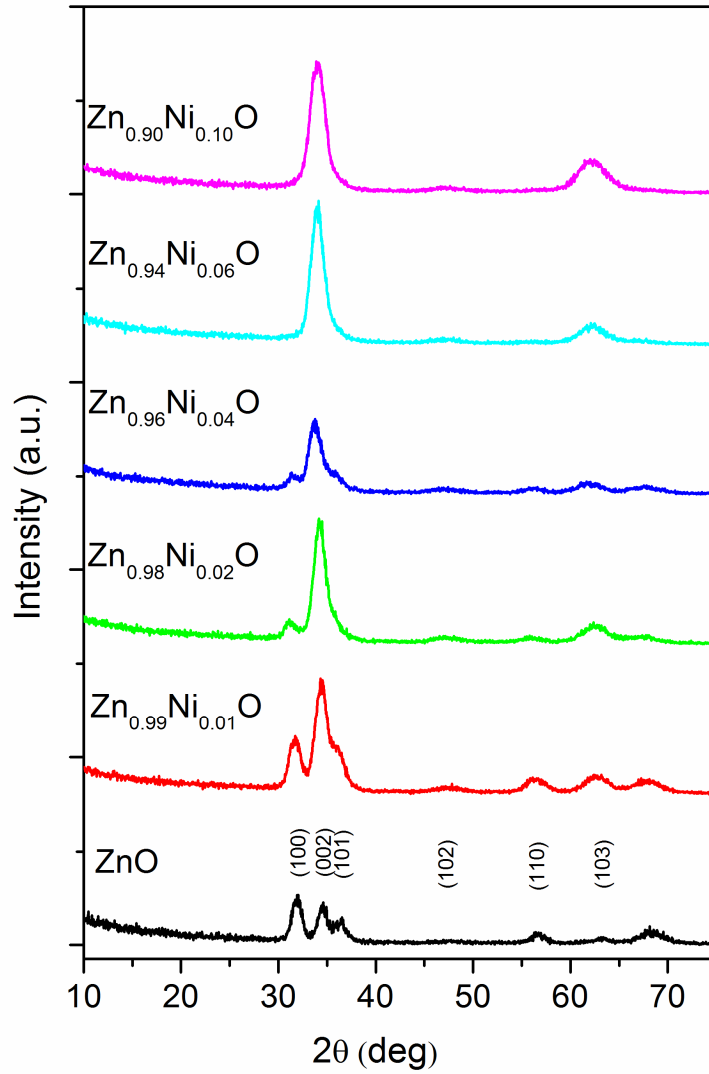
mass flow controller. The other deposition parameters used are sputtering pressure of 0.4 Pa, substrate to target distance of 4.5 cm, RF power of 100 W and all the films were deposited for 20 minutes. The spectroscopic ellipsometer has been used to measure the sample thickness accurately after deposition. The obtained film thickness was in the range of 200-230 nm range.

#### **4.3.1.2 Characterization of samples:**

Preliminary structural characterizations of the films were carried out by Grazing Incidence X-ray Diffraction (GIXRD) measurements using a Bruker D8 Discover diffractometer with monochromatic Cu  $K_{\alpha}$  X-rays at a grazing angle of incidence and with a wavelength of 1.54 Å. The XANES and EXAFS measurements at Zn and Ni K-edges have been carried out at the Energy Scanning EXAFS beamline (BL-09) while XANES measurements at the O K-edges of the Ni doped ZnO samples were performed at room temperature in the total electron yield mode at the soft X-ray absorption spectroscopy (SXAS) beamline (BL-01) at the Indus-2 Synchrotron Source as described in detail in Chapter-2. Optical characterization of all the films have been carried out by spectroscopic ellipsometry measurement using the rotating polarizer type spectroscopic ellipsometer (M/s. Semilab, model: GES5E) as described in Chapter-2. Ellipsometry spectra were measured for all the samples in the wavelength range of 200-900 nm at 70° angle of incidence. Photoluminescence (PL) spectra of the samples were recorded using an Edinburgh FL920 instrument. Magnetization measurements as functions of magnetic field were performed on the samples at room temperature by employing a commercial 7-Tesla SQUID-vibrating sample magnetometer (SVSM; Quantum Design Inc., USA).

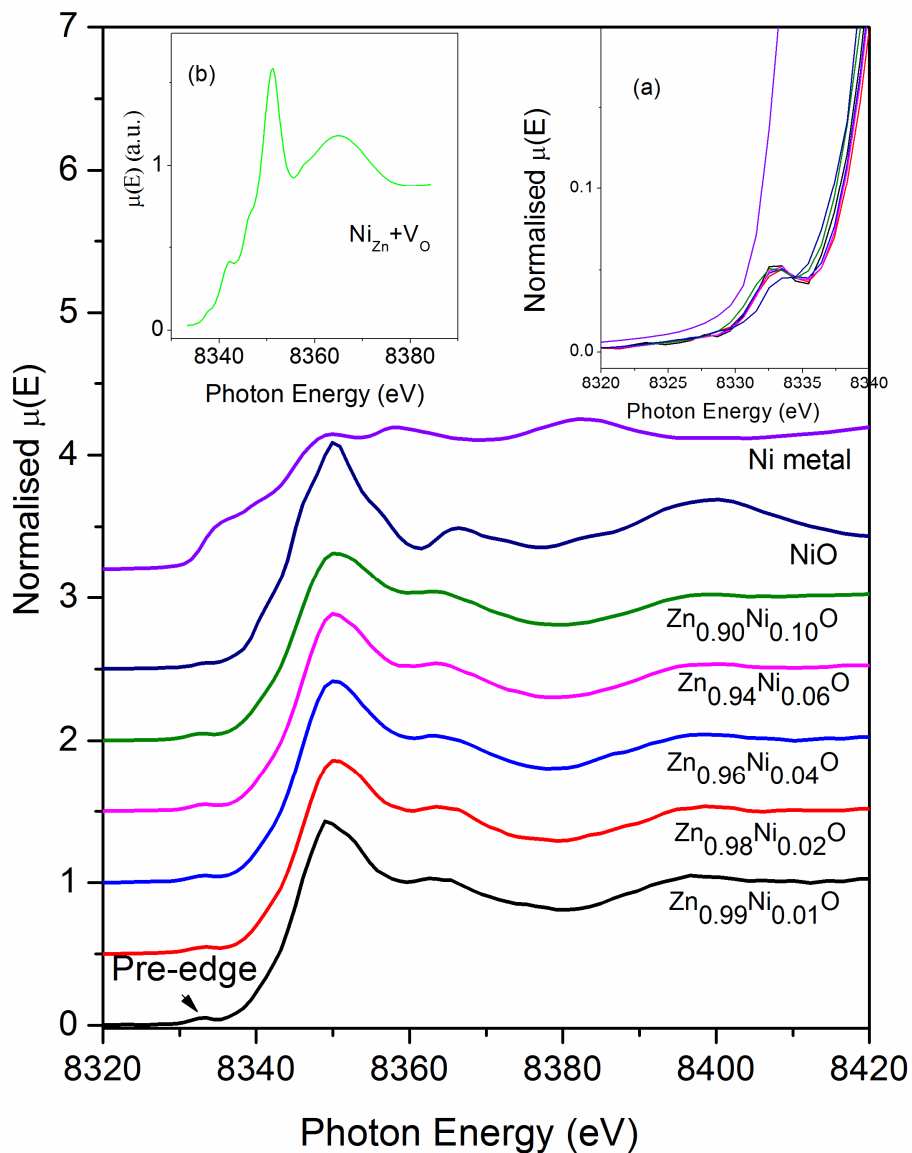
### 4.3.2 Results and discussion:

Fig.4.19 shows the GIXRD pattern of the undoped and Ni doped ZnO thin films. It can be seen that the films are polycrystalline with the positions of Bragg peaks agreeing with that of wurtzite hexagonal ZnO and even upto the highest Ni doping concentration of 10%, GIXRD measurements do not detect any additional secondary phase due to Ni segregation.



**Figure 4.19:** GIXRD plots of pure ZnO and Ni doped ZnO thin films (1%, 2%, 4%, 6% and 10% doping).

XANES spectra of Ni doped ZnO samples measured at Ni K-edge are shown in Fig. 4.20 along with that of Ni metal foil and NiO standard. The edge positions of Ni doped samples match with that of NiO standard manifesting that Ni is present in +2 oxidation state in the samples. However the difference observed between the intensity of the white line peaks and in the oscillation pattern just above the absorption edge suggests that environment of Ni in the doped ZnO samples is different from that of NiO. The pre-edge peak around 8333 eV is a result of the dipole-forbidden (quadrupole-allowed) transition of electrons from Ni(1s) state to Ni(3d) state. The intensity of such peak increases with an increase in Ni(3d)/O(2p) hybridization<sup>210</sup>, this hybridization being more efficient when Ni exhibits a tetrahedral-like geometry (non centro-symmetric) then when it experiences an octahedral-like geometry (centro-symmetric). The well defined pre-edge peaks (shown in enlarged scale in the inset (a) of Fig.4.20) in the present Ni doped ZnO samples indicate the presence of tetrahedral geometry around Ni atoms. The normalized XANES spectra at Zn K-edge is shown in Fig. 4.21. The main absorption jump at Zn K edge is the result of the transition of Zn1s electron to empty Zn4p states. No pre-edge peak is observed for Zn K-edge since the outer valance d shell is completely filled in case of Zn. No change is observed in the near edge structure at Zn K-edge XANES data with an increase in Ni doping concentration.



**Figure 4.20:** Normalised XANES spectra of Ni doped ZnO thin films (1%, 2%, 4%, 6% and 10% doping) at Ni K-edge. Reference spectra of Ni metal and NiO are also given for comparison. The inset (a) shows the extended part of the pre edge region. The inset (b) shows Ni K-edge XANES simulation with the defect model of substitutional Ni and oxygen vacancy ( $\text{Ni}_{\text{Zn}}+\text{V}_{\text{O}}$ ).

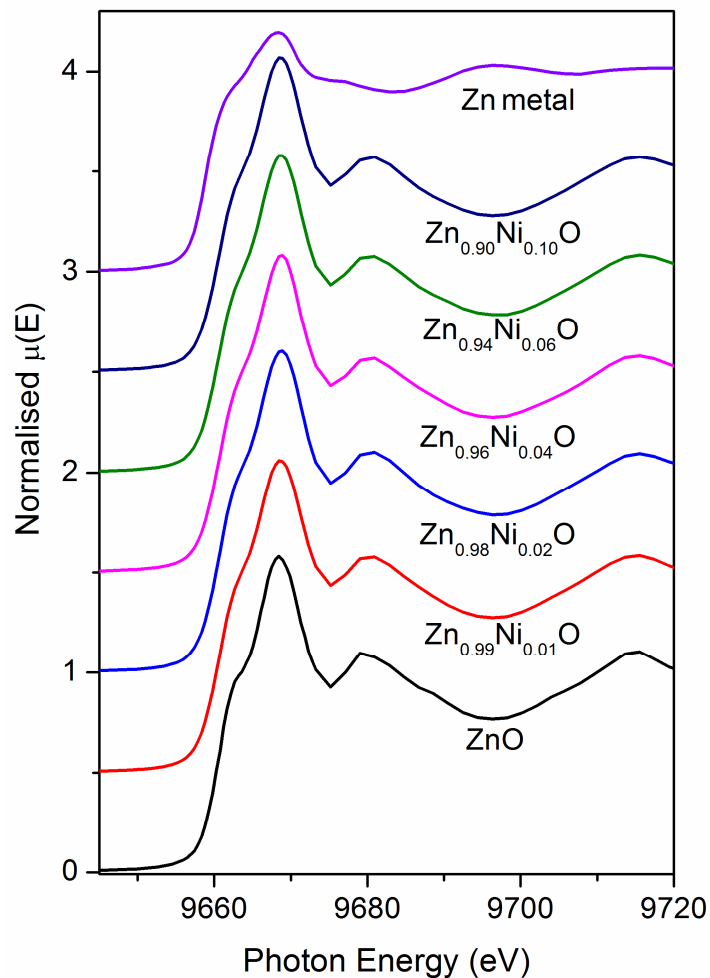


**Figure 4.21:** Normalised XANES spectra of pure ZnO and Ni doped ZnO thin films (1%, 2%, 4%, 6% and 10% doping) at Zn K-edge along with that of Zn metal foil.

The EXAFS ( $k^2\chi(k)$  versus  $k$ ) spectra of the samples derived from the absorption ( $\mu(E)$  versus  $E$ ) spectra (not shown here) and further the  $\chi(R)$  versus  $R$  plots obtained by Fourier transform of the ( $k^2\chi(k)$  versus  $k$ ) spectra have been generated following the standard procedure described in Chapter-2<sup>229</sup>. The  $k^2\chi(k)$  versus  $k$  spectra of the samples are shown in figures 4.22 and 4.23 at Zn and Ni K-edges respectively, while the corresponding  $\chi(R)$  versus  $R$  plots (fourier transform range is  $3.0-11.0 \text{ \AA}^{-1}$  in case of Zn K-edge data and is  $3.0-10.0 \text{ \AA}^{-1}$  in case of Ni K-edge data) have been shown in figures 4.24 and 4.25.

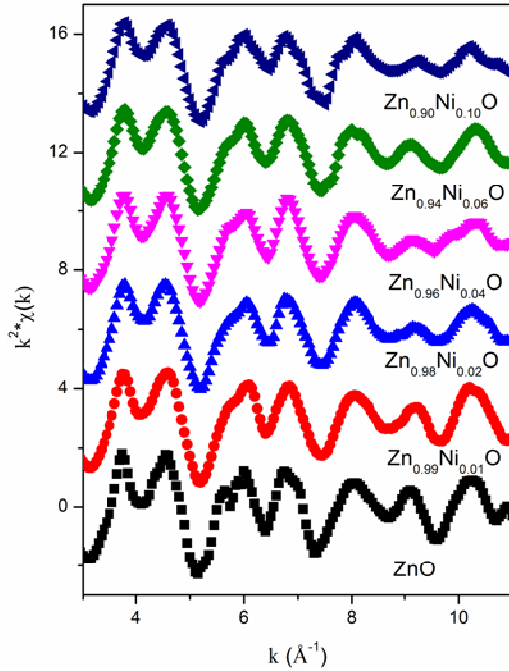


**Figure 4.22:** Normalised EXAFS spectra of pure ZnO and Ni doped ZnO (1%, 2%, 4%, 6% and 10% doping) at Zn K-edge.

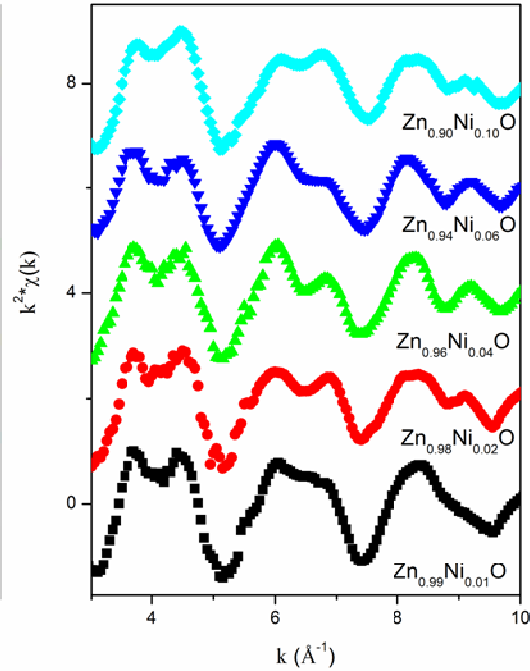


**Figure 4.23:** Normalised EXAFS spectra of Ni doped ZnO (1%, 2%, 4%, 6% and 10%).

The structural parameters (atomic coordination and lattice parameters) of ZnO used for simulation of the theoretical EXAFS spectra of the samples have been obtained from reference<sup>33</sup> and the best fit  $\chi(R)$  versus  $R$  plots (fitting range  $R=1.0-3.5$  Å) of the samples have also been shown in Fig. 4.24 along with the experimental data. The bond distances ( $R$ ), co-ordination numbers ( $N$ ) (including scattering amplitudes) and disorder (Debye-Waller) factors ( $\sigma^2$ ), which give the mean square fluctuations in the distances, have been used as fitting parameters and the best fit results are summarized in Table 4.6 and fig. 4.26 for Zn K-edge measurements. It should be noted that in the present work, during all EXAFS fitting process, the number of free variables ( $N_{\text{free}}$ ) were always kept below the upper limit set by Nyquist theorem ( $N_{\text{free}}=2\Delta k\Delta R/\pi$ )<sup>230</sup>, as mentioned in Chapter-2, where  $\Delta k$  is the range of  $k$  value used for Fourier transform and  $\Delta R$  is the range of  $R$  value used for fitting.

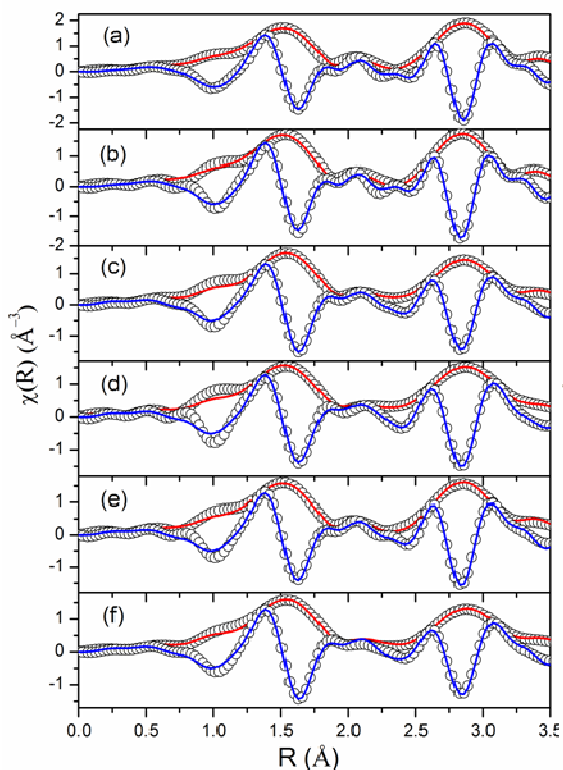


**Figure 4.24:** Fourier transformed EXAFS spectra (a) ZnO, (b) 1% Ni doped ZnO, (c) 2% Ni doped ZnO, (d) 4% Ni doped ZnO, (e) 6% Ni doped ZnO and (f) 10% Ni doped ZnO (scatter points) at Zn K edge along with best fit theoretical plots (solid line). Red line is for magnitude and blue line is imaginary part of  $\chi(R)$ .

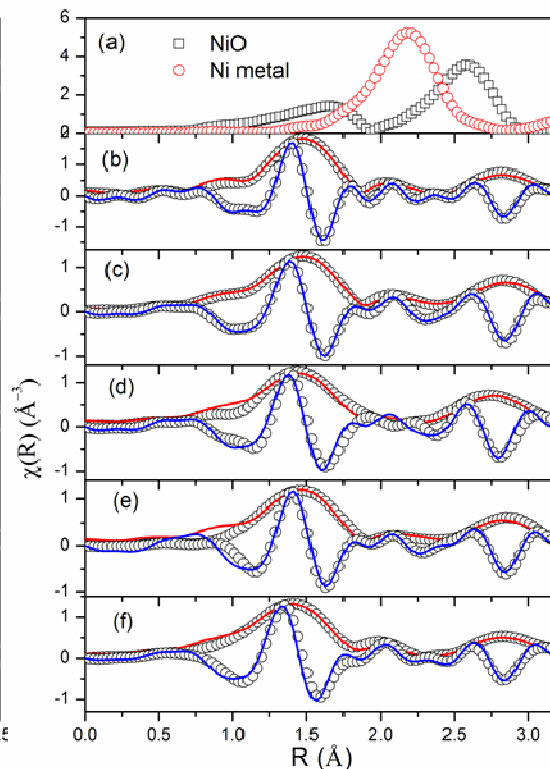


**Figure 4.25:** Fourier transformed EXAFS spectra of (a) Ni metal foil and NiO, (b) 1% Ni doped ZnO, (c) 2% Ni doped ZnO, (d) 4% Ni doped ZnO, (e) 6% Ni doped ZnO and (f) 10% Ni doped ZnO (scatter points) at Ni K edge along with best fit theoretical plots (solid line). Red line is for magnitude and blue line is imaginary part of  $\chi(R)$ .

For fitting of Zn K-edge data, we have assumed the crystallographic values of bond distance and coordination numbers and a reasonable value ( $\pm 0.003$ ) for Debye-Waller factors as initial guess values. The single energy shift parameter ( $\Delta E_0$ ) and amplitude reduction factor ( $S_0^2$ ) parameter have been decided for all the paths from the fitting of the undoped ZnO samples and have kept these constant for all other doped samples due to chemical transferability of amplitude reduction factor to similar systems. The goodness of the fit in the above process is generally expressed by the statistical parameter  $R_{factor}^{174}$  defined in Chapter-2.

The first peak at 1.5 Å in fourier transform spectrum (figure 4.24) is due to contributions from three oxygen atoms at the distance of 1.93 Å and one oxygen atom at the distance of 1.95 Å. The spectrum shown in Fig.4.24 is phase uncorrected, however the fitting results are shown for phase corrected data. The second peak at ~2.9 Å is due to contributions from two Zn-Zn coordination shells at distances of 3.12 Å and 3.19 Å with six coordinations each. The Zn-O and Zn-Zn bond lengths obtained for the present samples are in good agreement with other studies<sup>231</sup>.

**Table 4.6:** Bond length, coordination number and disorder factor obtained by EXAFS fitting at Zn K-edge. (Same values for the amplitude reduction factor ( $S_0^2$ ) and  $\Delta E_0$  have been used for all the coordination shells. The values of  $S_0^2$  and  $\Delta E_0$  obtained by fitting the FT-EXAFS spectrum of a pure ZnO sample are  $1.01 \pm 0.07$  and  $3.62 \pm 1.63$  eV, respectively. These values have been kept fixed for rest of the samples).

Path	Parameter	ZnO: Pure	ZnO: 1%Ni	ZnO: 2% Ni	ZnO: 4% Ni	ZnO: 6% Ni	ZnO: 10% Ni
Zn-O	$R$ (Å)	1.93±0.01	1.93±0.01	1.96±0.01	1.95±0.01	1.95±0.01	1.96±0.01
	N	3±0.42	3±0.48	3±0.21	3±0.30	3±0.42	3±0.33
	$\sigma^2$ (Å <sup>2</sup> )	0.004±0.001	0.004±0.001	0.004±0.001	0.005±0.001	0.004±0.001	0.004±0.001
Zn-O	$R$ (Å)	1.95±0.01	1.95±0.01	1.97±0.01	1.96±0.01	1.96±0.01	1.97±0.01
	N	1±0.14	1±0.16	1±0.07	1±0.10	1±0.14	1±0.11
	$\sigma^2$ (Å <sup>2</sup> )	0.002±0.001	0.002±0.001	0.002±0.001	0.002±0.001	0.004±0.001	0.003±0.001
Zn-Zn	$R$ (Å)	3.12±0.01	3.12±0.02	3.14±0.01	3.13±0.01	3.14±0.02	3.14±0.01
	N	6±0.84	6±0.96	6±0.42	6±0.60	6±0.84	6±0.66
	$\sigma^2$ (Å <sup>2</sup> )	0.021±0.001	0.021±0.001	0.005±0.001	0.004±0.001	0.006±0.001	0.006±0.001
Zn-Zn	$R$ (Å)	3.19±0.01	3.19±0.01	3.29±0.01	3.28±0.01	3.28±0.01	3.29±0.01
	N	6±0.84	6±0.96	6±0.42	6±0.60	6±0.84	6±0.66
	$\sigma^2$ (Å <sup>2</sup> )	0.006±0.001	0.006±0.001	0.005±0.001	0.003±0.001	0.007±0.001	0.006±0.001

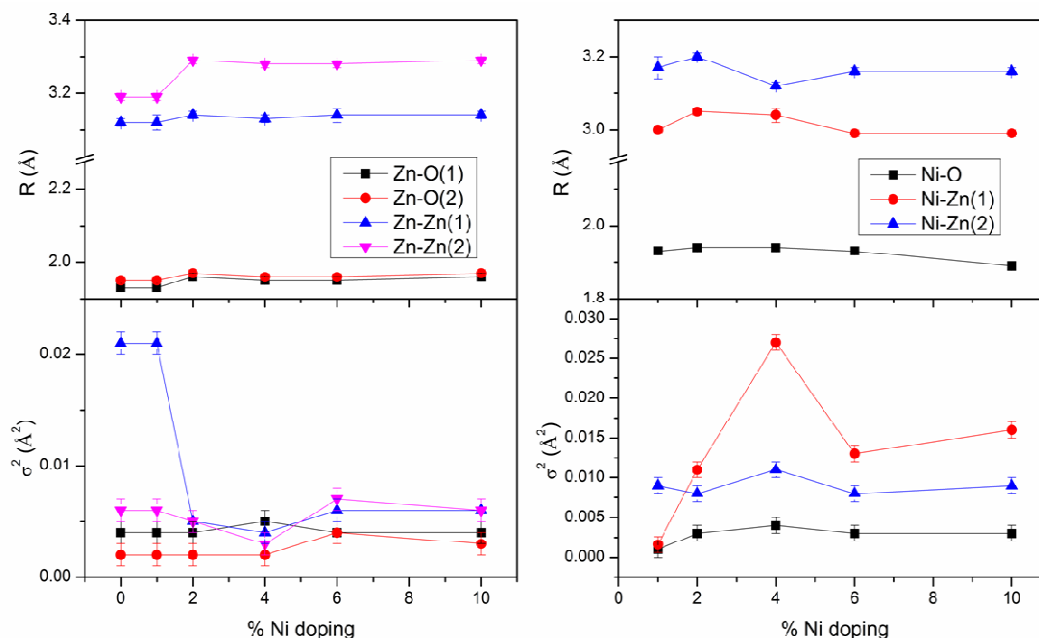


**Figure 4.26:** Variation of bond length ( $R$ ) and disorder factor ( $\sigma^2$ ) with doping concentration for Zn K-edge (left panel) and Fe K-edge (right panel).

The Fourier Transformed (FT)-EXAFS spectra or  $\chi(R)$  versus  $R$  plots of the Ni doped ZnO samples at Ni K-edge are also shown in Fig. 4.25 along with that of NiO and Ni metal standards. The first peak is a contribution from Ni-O coordination shells in Ni doped ZnO and NiO samples and Ni-Ni coordination shell in case of Ni metal foil. It can be seen from the figure 4.25 that the oxygen peak position is different for Ni doped ZnO and NiO samples, which clearly indicates that NiO phase is absent in the samples. The similarity in the experimental  $\chi(R)$  versus  $R$  plots at Zn K-edge (fig.4.24) and Ni K-edge (fig.4.25) show that Zn atoms are being substituted successfully by Ni atoms maintaining the ZnO crystal structure. Thus the structural parameters (atomic coordination and lattice parameters) of ZnO have been used for simulation of the theoretical EXAFS spectra of the samples by replacing the central Zn atom by Ni atoms and the best fit  $\chi(R)$  versus  $R$  plots of the samples obtained using the above theoretical model, have also been shown in Fig. 4.25 along with the experimental data and the best fit results are shown in Table 4.7 and fig. 4.26. The first peak

in the phase uncorrected spectrum shown in Fig. 4.25 at 1.5 Å is a contribution of oxygen atoms at a bond distance of 1.93 Å and the second peak around 2.9 Å is a contribution of two Ni-Zn coordination shells at distances of ~3.0 Å and ~3.17 Å. Similar Ni-O, Zn-O and Ni-Zn, Zn-Zn distances obtained here indicate that Ni is replacing Zn atoms in ZnO lattice. It should be noted here that we have obtained low  $\sigma^2$  values for the Ni-O coordination shell of the 1% Ni doped sample (Table-4.7), however it has also large uncertainty (~100%). This is because of slightly poor signal to noise ratio of the EXAFS data of this particular sample, due to low Ni concentration in the sample resulting in low detector counts.

**Table 4.7:** Bond length, coordination number and disorder factor obtain by EXAFS fitting at Ni K-edge. (Same values for the amplitude reduction factor ( $S_0^2$ ) and  $\Delta E_0$  have been used for all the coordination shells. The values of  $S_0^2$  and  $\Delta E_0$  obtained by fitting the FT-EXAFS spectrum of a pure NiO sample are  $0.77 \pm 0.08$  and  $-5.5 \pm 1.33\text{eV}$ , respectively. These values have been kept fixed for rest of the samples).

Path	Parameter	ZnO:1%Ni	ZnO:2% Ni	ZnO:4% Ni	ZnO:6% Ni	ZnO:10% Ni
Ni-O	$R$ (Å)	1.93±0.01	1.94±0.01	1.94±0.01	1.93±0.01	1.89±0.01
	N	3.57±0.26	3.62±0.40	3.62±0.54	3.62±0.34	3.62±0.54
	$\sigma^2$ (Å <sup>2</sup> )	0.001±0.001	0.003±0.001	0.004±0.001	0.003±0.001	0.003±0.001
Ni-Zn	$R$ (Å)	3.00±0.01	3.05±0.01	3.04±0.02	2.99±0.01	2.99±0.01
	N	5.36±0.37	5.36±0.54	6.0±1.08	6±0.78	6±1.14
	$\sigma^2$ (Å <sup>2</sup> )	0.016±0.001	0.011±0.001	0.027±0.001	0.013±0.001	0.016±0.001
Ni-Zn	$R$ (Å)	3.17±0.03	3.20±0.01	3.12±0.01	3.16±0.01	3.16±0.01
	N	5.36±0.37	6±0.54	6±1.08	6±0.78	6±1.14
	$\sigma^2$ (Å <sup>2</sup> )	0.009±0.001	0.008±0.001	0.011±0.001	0.008±0.001	0.009±0.001

The oxygen coordination number obtained here is slightly less than 4 indicating the presence of oxygen vacancy near the dopant site, though oxygen coordination does not significantly change with increase in Ni doping concentration. Ni-O and Ni-Ni coordination

shell distances however are found to decrease slightly with an increase in Ni doping concentration which is expected since the ionic radii of four coordinated Ni<sup>2+</sup> ions (0.55 Å) are smaller than the ionic radii of four coordinated Zn<sup>2+</sup> ions (0.60 Å)<sup>209</sup>. This has also led to an increase in disorder at the Ni sites compared to that at the Zn site as  $\sigma^2$  values are found to be higher at Ni-Ni(Zn) shells compared to that of Zn-Zn shells.

Normalized XANES spectra at O K-edge for samples with different Ni concentrations are shown in Fig. 4.27. O K-edge XAS spectra of Ni doped ZnO samples is though broadly similar to that of undoped ZnO, however small changes in the spectral features are observed<sup>194</sup>. This similarity is expected since the spectra are probes of the O atoms, and not directly of the Ni dopants, however small changes in the spectral features are related to the change in the electronic structure due to the doping of Ni at the Zn position<sup>232</sup>. The spectral features are denoted by A, B, C and D in Fig. 4.27. The spectral feature denoted by B is due to the transition of 1s electron to O2p-Zn4sp state as has been stated by Vaithianathan et al. and Guo et al.<sup>194, 218</sup>. The peak D arises due to transitions to O2p states hybridized with higher Zn/Ni orbitals<sup>211</sup>. The peak denoted by A at 532 eV, which is like a shallow shoulder for the undoped sample, shows significant enhancement with an increase in Ni doping concentration. The spectral features at A is attributed to transitions from 1s core state of oxygen to 2p oxygen state hybridized with 3d state of Ni<sup>219</sup>. In case of pure ZnO, the transition to oxygen 2p-Zn3d hybridized state is not possible since the d orbital of Zn is fully occupied. As Ni atoms replace Zn atoms in ZnO lattice, the empty orbital of Ni 3d state are contributing to this transition and enhances this peak at position A. The increase in the peak intensity at A confirms that Ni atoms are replacing Zn atoms in ZnO and corroborates the results obtained by EXAFS studies at Zn and Ni K-edges.

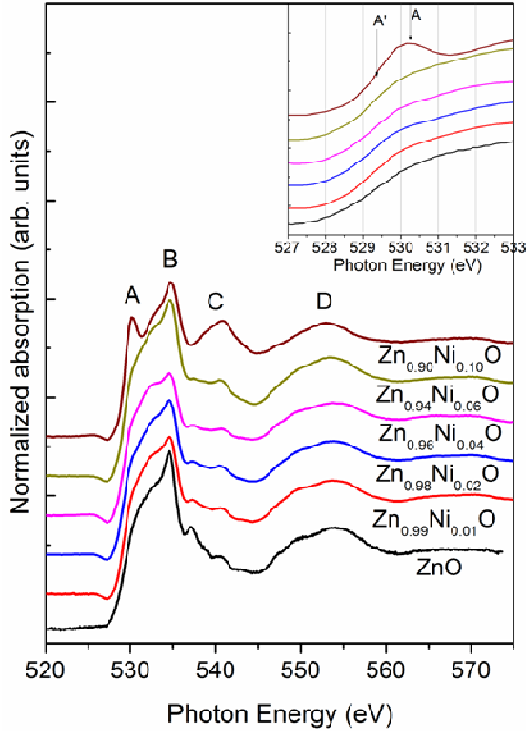


**Figure 4.27:** O K-edge XANES spectra of undoped and Ni doped ZnO samples (1%, 2%, 4%, 6% and 10% doping). (Inset shows extended part of the low energy region).

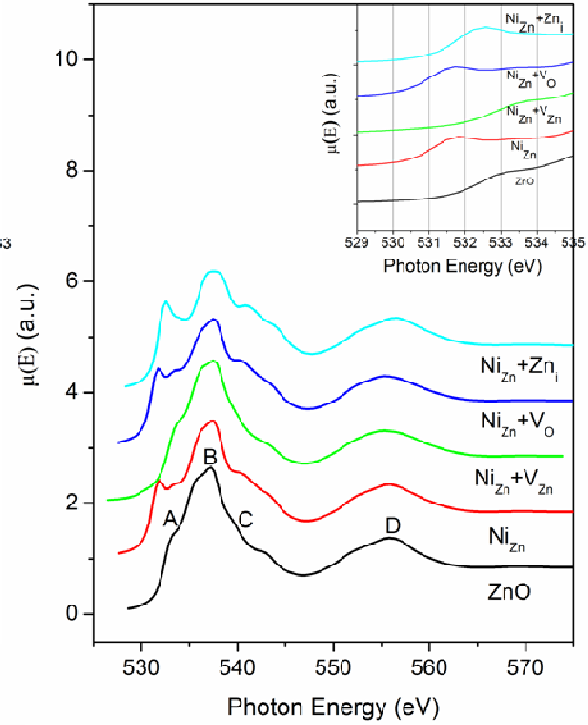


**Figure 4.28:** Simulated XANES spectra of ZnO at O K edge with different model clusters. (Inset shows extended part of the low energy region)

As has been discussed in the Introduction section, defects are the most reasonable explanation of the origin of the RTFM in TM doped ZnO DMS's. These defects include O vacancy, Zn Vacancy and Zn interstitials. We have performed the ab-initio first principle XANES calculations of ZnO using the FEFF9.6<sup>161</sup> code to study the influence of these defects. Different type of model clusters have been used for the above calculations i.e., substitutional Ni at Zn site ( $\text{Ni}_{\text{Zn}}$ ), substitutional Ni at Zn site with Zn vacancy ( $\text{Ni}_{\text{Zn}}+\text{V}_{\text{Zn}}$ ), substitutional Ni at Zn site with oxygen vacancy ( $\text{Ni}_{\text{Zn}}+\text{V}_{\text{O}}$ ) and substitutional Ni at Zn site with Zn interstitials ( $\text{Ni}_{\text{Zn}}+\text{Zn}_i$ ). The input parameters for these calculations are generated using the ATOMS code provided in ARTEMIS software of the IFEFFIT package. The convergence of the calculation is achieved for the cluster of 125 atoms for each model. The cluster radius is decided on the basis that adding the next coordination shells does not change

the fine structure<sup>233</sup>. The total scattering potentials including a fully relaxed core hole were obtained iteratively by successive calculations of the potential until self consistency was reached. Based on these scattering potential, the final state of the excited photoelectron were calculated. The closet match between the simulated and experimental spectra is obtained by using Hedin-Lundqvist model of exchange potential with 0.8 eV shift and additional broadening of 0.6 eV.

The simulated XANES spectra of ZnO at O K-edge generated with different model clusters along with that of pure ZnO are shown in fig.4.28, the validation of the calculation is confirmed as all the spectral features (A,B,C and D) are well produced in the calculated spectrum of ZnO at oxygen K-edge. Comparison of the simulated spectra with the experimental XANES spectra at oxygen K-edge (fig.4.27), clearly rules out the possibility of presence of Zn interstitial in the sample, though the simulated spectra of the other possibilities viz., ZnO with no defects, substitutional Ni at Zn site ( $\text{Ni}_{\text{Zn}}$ ), substitutional Ni at Zn site with Zn vacancy ( $\text{Ni}_{\text{Zn}}+\text{V}_{\text{Zn}}$ ), substitutional Ni at Zn site with oxygen vacancy ( $\text{Ni}_{\text{Zn}}+\text{V}_{\text{O}}$ ) resemble the XANES spectra given in fig.4.27.

To have a better interpretation of the O K-edge simulated data vis-à-vis the measured data at O K-edge, we have plotted the lower energy parts of both the spectra in expanded scale and have presented as insets of fig. 4.27 and 4.28 respectively. It can be observed from the above figures that the features A' & A of the experimental data (between 529 eV to 532 eV), which are not there in undoped ZnO sample, can be simulated by two defect models only viz., ZnO having substitutional Ni at Zn sites ( $\text{Ni}_{\text{Zn}}$ ) and substitutional Ni at Zn sites alongwith oxygen vacancy ( $\text{Ni}_{\text{Zn}}+\text{V}_{\text{O}}$ ). However, considering the result obtained from the Ni K-edge EXAFS data presented above, which indicates the possibility of presence of oxygen vacancies in the Ni doped samples, we can conclude that  $\text{Ni}_{\text{Zn}}+\text{V}_{\text{O}}$  is the most likely case scenario for the present samples. It should be noted here that Ni K-edge XANES spectrum

simulated with the above defect model can also describe the observed Ni K-edge XANES data as shown in the inset (b) of fig.4.20.

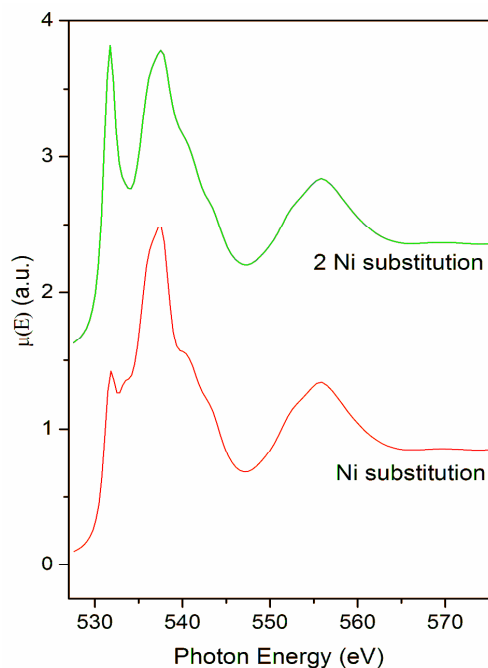


**Figure 4.29:** Simulated XANES spectra of ZnO at O K edge with Ni atoms replacing Zn atoms in first coordination shell.

It can also be seen from fig. 4.27 that the XANES features of the 10% Ni doped sample is quite different from the other samples with very sharp peak at A. Also from the Ni K-edge best fit results, as given in Table-4.7 it can be seen that Ni-O bond length is significantly low in this sample compared to the other samples. This indicates two possibilities (i) formation of Ni clustering or (ii) formation of NiO. However, it has been clearly shown in fig.4.25, that no peak corresponding to the Ni-Ni shell of Ni clusters appear in Ni K-edge FT-EXAFS spectra of the samples, which thus rules out the possibility of Ni clustering at least in the bulk of the samples. The formation of NiO is also ruled out since NiO has a higher band gap (~3.7 eV) than ZnO and ellipsometry measurements, discussed later, show significant reduction of the band gap in case of the 10% Ni doped ZnO sample. Also Ni K-edge XANES measurements (fig.4.20) show no resemblance with NiO for this sample. Thus the apparent changes in the O K-edge XANES spectra of the 10% Ni doped

samples should be due to surface effect, O K-edge measurements in total electron yield mode being more sensitive to the surface atoms. Thus the appearance of a strong peak at position A may be attributed to the formation of Ni clustering at the surface of the film. To probe it further, we have carried out XANES simulations at the O K-edge by replacing the Zn atoms one by one by Ni atoms which is shown in figure 4.29. It can be seen that there is significant enhancement of the peak at A if we replace two of the Zn atoms around one oxygen atom by two Ni atoms manifesting Ni clustering instead of one of the Zn atoms replaced by one Ni atom. This indicates that clustering of Ni atoms may take place at the surface of the 10% Ni doped sample, though it may not be significant to give a peak in the GIXRD spectrum of the sample.

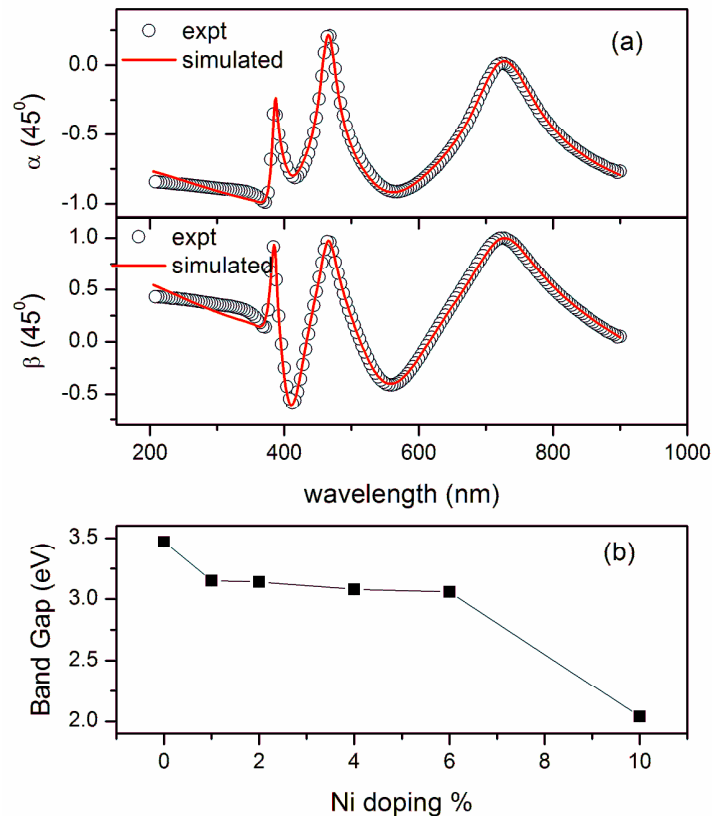


**Figure 4.30:** (a) Experimental Ellipsometry spectra (scatter points) alongwith best fit theoretical curves (solid line) over a wavelength range of 200-900 nm for a representative 1% Ni doped ZnO thin film deposited on Si substrate. (b) Variation of band gap of the films (obtained from ellipsometric measurements) as a function of Ni doping concentration.

The bandgap of the samples have been determined from spectroscopic ellipsometry measurements by using a rotating polarizer type spectroscopic ellipsometer. The ellipsometry measurements were performed at 70° angle of incidence and in the wavelength range of 200 to 900 nm. In ellipsometry, the variation of the amplitude and the phase difference between the parallel (p) and perpendicular (s) components of the reflected light polarized with respect to the plane of incidence are measured and its methodology is described in Chapter-2.

Fig. 4.30 (a) shows the experimental ellipsometry spectra ( $\alpha$  and  $\beta$ ) vs. wavelength over a wavelength range of 200-900 nm along with the best fit theoretical plot for a representative 1% Ni doped ZnO thin film deposited on Si substrate. The experimental ellipsometric spectra of the samples are fitted with appropriate models consisting of one single layer of pure/doped ZnO film on top of a silicon substrate having some amount of void. Optical constants of the bulk material (ZnO) are assumed to follow the Tauc-Lorentz dispersion model<sup>188</sup> which is common for such oxide dielectric films and the mixture of material and void has been treated under the Bruggeman Effective Medium Approximation<sup>189</sup>. The Tauc Lorentz model has been described briefly in the Appendix-A of the thesis, while the EMA model has been discussed in Appendix-B. The optical constants of silicon substrate have been estimated through a separate ellipsometric measurement and have been supplied in the above fitting process. The optical constants including band gap of the ZnO layers have been obtained for each sample from the best fit of the experimental and simulated ellispometric spectra.

The band gap values of the samples obtained from spectroscopic ellipsometry measurements discussed above are plotted in Fig. 4.30 (b). The optical bandgap obtained here for 1% Ni doped ZnO (3.15 eV) is similar to that obtained by other researchers also<sup>232</sup>. The optical bandgap for ZnO is 3.47 eV and it is observed that the presence of Ni greatly reduces the optical band gap of ZnO and increasing doping level leads to a continuous reduction<sup>232</sup>.

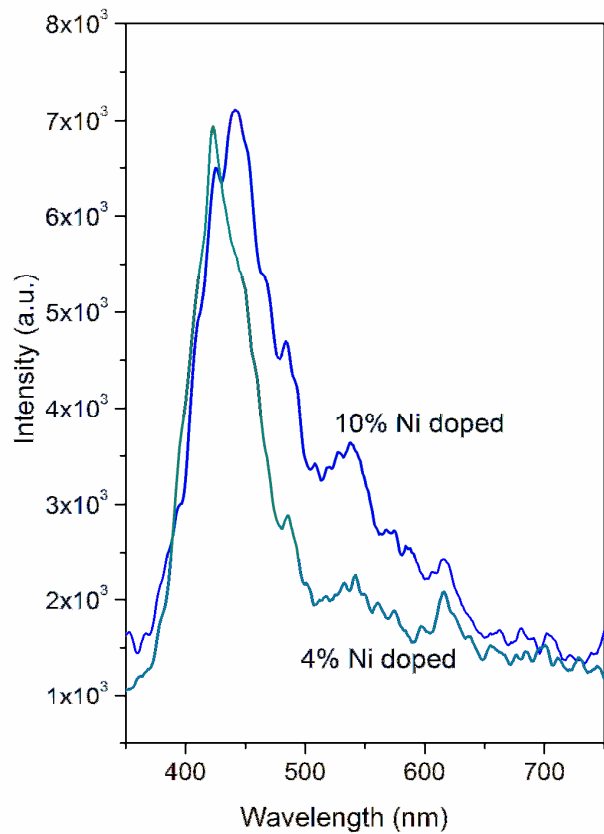
However, a large decrease in the band gap for the 10% Ni doped sample, as discussed above, is possibly due to the formation of Ni clusters at the surface of this sample. Since the bandgap of NiO is in the range of ~3.7-4.0 eV, therefore in this case doping is surely not tuning the bandgap of ZnO in the direction of NiO<sup>234</sup>. This observation corroborates the above mentioned results of GIXRD and XAS measurements. The band gap reduction with increased Ni concentration could be attributed to the introduction of Ni states at the top of the valance band of ZnO and suggests that the band gap of the nanocrystalline samples could be tuned for application in the various electronic and optical applications<sup>232</sup>.

Fig. 4.31 represents the PL emission spectra of 4% and 10% Ni doped ZnO thin films. The visible region emission is well known for the intrinsic defects in ZnO, such as zinc vacancy, oxygen vacancy, oxygen interstitial, zinc interstitial and antisite oxygen. As shown in the figure, at low concentration the emission spectrum is dominated by two emission spectral region; one at violet-blue region (400-480 nm) and another at greenish-yellow region (530-620 nm region). As has been reported by other workers<sup>235, 236</sup>, the violet-blue band is attributed to interstitial Zn atom while the greenish-yellow region is originated from oxygen vacancy related electronic states situated in the deep of the band gap.

This supports our earlier observation of oxygen vacancies in the samples from the EXAFS study, though the features related to Zn interstitial have not been observed in EXAFS study. Now in the present case, we have seen an increase in intensity of the greenish-yellow band while that of violet-blue region remains almost same when the dopant level is increased from 4% to 10% manifesting clearly an increase in oxygen vacancy related defects in the samples with the increase in Ni doping concentration.

The magnetization versus applied magnetic field curves (M-H curves) measured at room temperature for 4% and 10% Ni doped ZnO samples are shown in Fig.4.32 after subtracting the contribution of the Si substrate. Weak hysteresis loop has been observed in

the samples for both the concentrations, while saturation magnetization is found to decrease with increase in doping concentration, coercivity is found to increase. Srinet et. al. have observed RTFM behaviour in Ni doped ZnO nanoparticles which also showed a decrease in the saturation magnetization with increase in Ni doping concentration<sup>115</sup>. RTFM has also been observed by Liu et. al. in Ni doped ZnO nanocrystals where increased saturation magnetization is observed with increasing doping concentration up to 2% doping and decreasing saturation magnetization for further higher doping concentration<sup>237</sup>.



**Figure 4.31:** PL spectra of 4% and 10% Ni doped ZnO thin films

Coercivity values obtained in case of the present samples are also found to be comparable with that reported by other workers. For example, Lu et. al. have observed ferromagnetic character with similar small coercivity for Ni doped ZnO thin films with more than 6% Ni doping prepared by magnetron co-sputtering<sup>238</sup>. Perales-Perez et. al. have also

observed RTFM in Ni doped ZnO nanocrystals with coercivity of  $1.7 \times 10^3$  A/m<sup>239</sup>. Li et. al. have observed RTFM in Ni doped ZnO powder with coercive field of  $\sim 4.8-6.4 \times 10^3$  A m<sup>-1</sup> for 1% and 2% doping concentration<sup>240</sup>. Ni doped ZnO thin films deposited on sapphire substrate by Snure et al. showed RTFM with  $8-12 \times 10^3$  A m<sup>-1</sup> coercivity<sup>117</sup>.

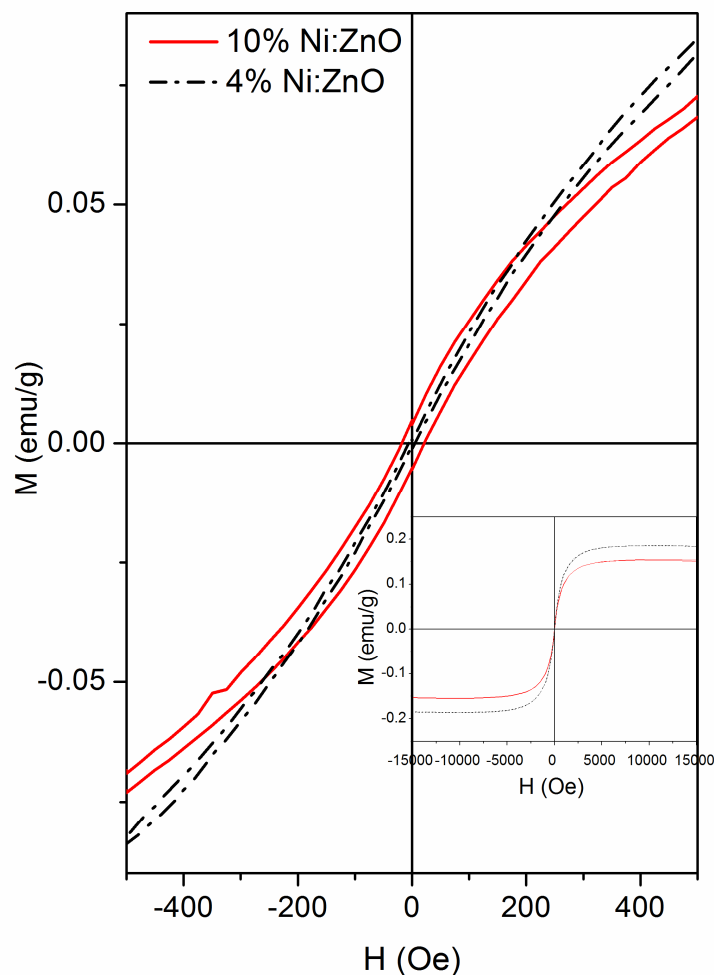


**Figure 4.32:** Room temperature M-H curves of 4% and 10% Ni doped ZnO thin films.

As has been discussed in detail in Chapter-1, the origin of RTFM in TM doped DMS materials is generally attributed to two major causes, intrinsic or extrinsic. The extrinsic origin is due to the possible presence of any secondary magnetic phase viz., metallic Ni cluster or Ni based oxides in case of the present set of samples. The intrinsic origin, on the other hand, is due to the replacement of host atoms by dopants or presence of defects and

interstitials. Liu et. al., for example, have attributed the ferromagnetic behaviour observed in their nanocrystalline ZnO samples with Ni doping upto 2% to the presence of oxygen vacancies<sup>237</sup>. The above authors have observed substitutional doping of Ni atoms at Zn sites upto 2% Ni concentration only, while doping at higher concentration resulted in precipitation of separate NiO phase. Lu et. al.<sup>238</sup>, on the other hand have explained the ferromagnetic behavior of their magnetron sputter deposited Ni doped ZnO thin films on the basis of bound-magnetic-polaron mediated exchange, because the charge valance made F-centre mediated exchange is reasonably unsuitable.

For the present Ni doped ZnO thin film samples, we have observed from GIXRD, XANES and EXAFS measurements that Ni gets incorporated into the Zn sites of ZnO lattice and no evidence of Ni metallic cluster (ferromagnetic) or extra Ni related secondary oxide phases like NiO (anti-ferromagnetic) is found upto the maximum Ni doping concentration. Thus it can be concluded that the origin of ferromagnetism in the present set of samples is intrinsic in nature. PL study confirms the presence of oxygen vacancy in the samples, which also helps to explain the observed features in the O and Ni K-edge XANES simulation and Ni K-edge EXAFS measurements of the samples. Thus we can say that oxygen vacancies may play a major role in the origin of magnetic properties of these RF sputter deposited Ni doped ZnO thin films as the electrons associated with these defects (oxygen vacancies) are responsible for exchange interaction between magnetic ions and form bound magnetic polarons (BMP's)<sup>35</sup>.

It should be noted here that we have seen such correlation between oxygen vacancies and ferromagnetism in ZnO samples in our earlier studies also. For example, in case of polyvinylpyrrolidone (PVP) capped ZnO nanocrystals synthesized in isopropanol at room temperature through a wet chemical route with zinc acetate as precursors, no oxygen vacancies are observed<sup>241</sup>. This has been reflected in their magnetic properties, where weak

ferromagnetic order is observed for undoped ZnO and for ZnO with low Ni doping concentration (upto 1.5% Ni doping) only. However, for higher Ni doping concentration, with the absence of oxygen vacancies and hence BMPs, anti-ferromagnetic correlation in the samples increases resulting in a decrease in ferromagnetism. Whereas, in case of  $Zn_{1-x}Ni_xO$  ( $0 < x < 0.125$ ) samples prepared by low temperature wet chemical method, we have found RTFM up to 12.5% Ni doping concentration<sup>242</sup>, accompanied by modification of the morphology of the samples from nanorods to nanoflakes. XAS analysis shows evidence of oxygen vacancies in the samples, which has also been supported by Raman spectroscopy and photoluminescence measurements. Thus the above studies also corroborate the fact that presence of oxygen vacancy related BMP's has direct implications on the ferromagnetism observed in these Ni doped ZnO samples.

## Chapter 5

### **TM (Mn, Co AND Ni)-DOPED NANOCRYSTALLINE-ZnO/PVDF COMPOSITE THIN FILMS**

As has been mentioned in Chapter-1, though ZnO based DMS materials show encouraging potential as spintronic material, there exists a challenge for synthesizing these materials in freestanding flexible form by a cost effective, scalable and reproducible process. Polymer-based composites with high dielectric constant<sup>77-82</sup> or high permeability<sup>83-86</sup> are treated as a possible candidate for the above due to their flexible nature. In this regard, polyvinylidene fluoride (PVDF) has become one of the most suitable and potential materials for advanced applications due to the extraordinary electroactive properties among other polymer systems. In this chapter we have described the preparation of transition metal doped (Ni, Co doped and Ni/Co co-doped and Mn doped) ZnO nanocrystallites embedded PVDF composite films and their structural characterisation primarily by XAS measurements at Zn and dopant edges. XPS has also been used as a complementary technique to ascertain the oxidation state of the metal ions in the composite films.

#### **5.1 Ni doped ZnO/PVDF:**

In the following we describe the synthesis and characterisation of Ni-ZnO/PVDF composite free-standing flexible films. Zuo et al.<sup>243</sup> reported the synthesis of  $Zn_{1-x}Ni_xO$  by a hydrothermal method and studied morphology, optical, and magnetic properties. They observed that no metallic Ni clusters or NiO phases existed in their  $Zn_{1-x}Ni_xO$  samples. Ni doped ZnO nanocrystals were synthesized by a wet chemical reaction by Wang et al.<sup>244</sup>. X-ray photoelectron spectroscopy and Raman studies indicated that  $Ni^{2+}$  was incorporated into the ZnO lattice at  $Zn^{2+}$  site. Mohapatra et al.<sup>245</sup> reported the synthesis of  $Zn_{1-x}Ni_xO$  systems using a solid state reaction technique and observed that the binding-energy difference of Ni

$2p_{3/2}$  and Ni  $2p_{1/2}$  indicated that Ni present in the ZnO matrix was in the form of NiO rather than metallic Ni. Venkataiah et al.<sup>246</sup> utilized hydrothermal method to prepare Ni/ZnO nanorod and Zn/NiO nanowall composites and studied microstructural and magnetic behavior. A significant ferromagnetic and antiferromagnetic coupling was observed.

Regarding probing local structures in Ni-ZnO systems, reports are not very many till today. Ni doped ZnO polycrystalline powders were subjected to EXFAS studies by Li et al.<sup>247</sup>. From the Ni-K-edge result, it was observed that the Ni atoms belonged to the substitutional positions in the ZnO lattice. Venkataiah et al.<sup>246</sup> reported from EXAFS and XANES studies that substitutional Ni is doped in ZnO nanorods. Pulsed laser deposition technique was utilized by Mino et al.<sup>231</sup> for depositing Ni doped, Li doped, and (Li, Ni) co-doped ZnO thin films. These films were subjected to investigation by EXAFS and XANES studies. Doped ZnO thin films were found to contain more than 50% of substitutional Ni. Presence of Ni clusters was confirmed from EXAFS signal. Kuzmin et al.<sup>248</sup> described the present state of the art for the interpretation of EXAFS, including an advanced approach based on the use of classical molecular dynamics and its application to nickel oxide nanoparticles (NPs). In the area of Ni doped ZnO embedded in polymer matrix, the only study reported is by Trofimova et al.<sup>249</sup> who used two types of polymer matrices: (i) cross linked polymethacrylate (PMA) and (ii) products of thermal polymerization of low molecular acrylamide complexes. Synchrotron XAFS and EXAFS spectroscopy measurements at the K edges of Ni and Co were performed by them.

### **5.1.1 Experimental:**

Synthesis protocol for obtaining the requisite sol for the deposition of Ni-ZnO/PVDF or  $Zn_{1-x}Ni_xO$ /PVDF films is described in Chapter-2. The chemicals used in the synthesis process are Zinc acetate dihydrate (Merck Specialities Private Limited, 98%), nickel acetate tetrahydrate (Merck Specialities Private Limited, 98%), N-N dimethyl

formamide (Merck Specialities Private Limited, 99.9%), diethanolamine (Merck Specialities Private Limited, 98%), and PVDF (Alpha aesar) were used. In brief, appropriate amount of Zinc acetate dihydrate was taken to obtain a sol with 4 ml dimethyl formamide (DMF). The above sol was refluxed for 1 h with constant stirring at 30°C for complete dissolution of the solute. Three such stock solutions were obtained and three different amounts of Ni-acetate were added to the above flasks for getting three different doping molar concentrations of Ni ( $x = 0.01, 0.04, 0.09$  in  $Zn_{1-x}Ni_xO$ ). These mixtures were refluxed for 3 h with constant stirring at 150°C for complete dissolution of the solute with resultant formation of intermediate products of  $Zn(OH)_2 + Ni(OH)_2$ . Appropriate amount of dimethyl amine, acting as a reducing agent, was added to the above sol while heating and stirring for another 30 min. A fixed amount of PVDF (15 wt%) was then added to the above sols which were cooled down to 60°C. Stirring was continued for another 2 h. A semi-gel liquid with a brownish tinge was obtained. The above sol was spin-casted uniformly on glass substrates at room temperature at a low spin (60 rpm) for depositing the Ni doped nano-ZnO/PVDF composite films. A microwave oven was used to heat the as-coated films at 100 W for 3 min. The films so obtained could be easily peeled out from the glass substrate. These films were used for characterizations.

The films deposited as above were polled in vacuum ( $\sim 10^{-6}$  Torr) at a field of 5 MV/m for 2 h. The poling creates H terminated surface at one side of the films, while F-terminated surface at the other end as explained in detail in Chapter-2. The poling unit<sup>250</sup>, used for this purpose has also been described in Chapter-2. XAS measurements have been carried out at the Energy-Scanning EXAFS beamline (BL-9) at the Indus-2 Synchrotron Source as described in details in Chapter-2. In the present case, EXAFS measurements at Zn K-edge (9659 eV) have been performed in transmission mode and while that at Ni K-edge (8333 eV) have been carried out in fluorescence mode.  $Ni_xZn_{1-x}O/PVDF$  ( $x = 0.01, 0.04,$

0.09) films of appropriate numbers have been stacked to one another to obtain a reasonable edge jump at Zn K edge. XPS (X-ray photoelectron spectroscopy) measurements were carried out in a SPECS (Germany) spectrometer with delay line detector at 300 W power and measurements were carried out at a chamber pressure of  $\sim 4 \times 10^{-10}$  Torr with Al K $\alpha$  line source of 1486.74 eV.

## **5.1.2 Results and discussion:**

### **5.1.2.1 Microstructural studies:**

FESEM micrographs of unpoled and poled representative  $Zn_{1-x}Ni_xO$  ( $x = 0.01, 0.04, 0.09$ ) embedded PVDF films are shown in Fig.5.1. FESEM micrographs of the poled Ni doped nano-ZnO/PVDF (henceforth referred as  $Zn_{1-x}Ni_xO/PVDF$ ) composite films with three different Ni doping levels are shown in panels a–c of Fig.5.1 while the corresponding micrographs of the unpoled samples are shown in the insets of the above figures. Change in morphology of the PVDF films after inclusion of ZnO nanocrystallites doped with different amount of Ni is apparent from Fig.5.1a–c. The surface is covered with Ni doped ZnO nanocrystallites. Localized segregation of Ni-ZnO nanocrystallites could be seen in the unpoled samples (insets of Fig.5.1a–c), and upon poling, the Ni-ZnO nanocrystallites could be seen dispersed quite uniformly (Fig.5.1a–c). It may be observed that increase in Ni doped ZnO nanocrystallites in PVDF matrix culminated in increase in sizes of the nanocrystallites. The surfaces became compact and their surface roughness increased with increase in Ni content in the ZnO nanocrystallites.

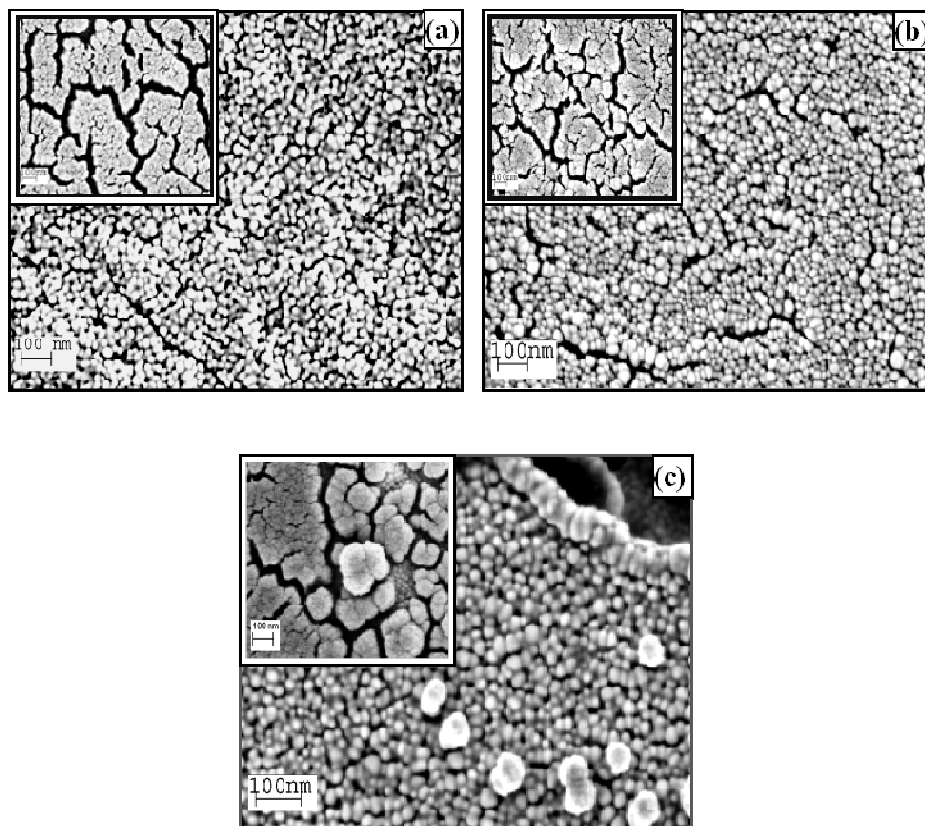


**Figure 5.1:** FESEM pictures of poled: (a)  $Zn_{1-x}Ni_xO/PVDF$  ( $x=0.01$ ) sample, (b)  $Zn_{1-x}Ni_xO/PVDF$  ( $x=0.04$ ) and (c)  $Zn_{1-x}Ni_xO/PVDF$  ( $x=0.09$ ) sample, Insets show the corresponding FESEM pictures of unpoled films.

### 5.1.2.2 XPS studies:

XPS studies were carried out on unpoled and poled samples of flexible free-standing  $Zn_{1-x}Ni_xO/PVDF$  films with three different Ni doping concentrations ( $x = 0.01, 0.04, 0.09$ ) to derive information on the bonding environment of the constituent elements. The calibration of the all peaks was done with respect to the peak for C1s (284.5 eV). It may be mentioned here that all the spectra recorded for the films with different Ni doping concentrations were very nearly similar to one another regarding the peak positions of the individual core level peaks. We present here the detailed discussion of the XPS spectra using the ones related to  $Zn_{1-x}Ni_xO/PVDF$  film containing  $x = 0.04$  Ni as the representative one.

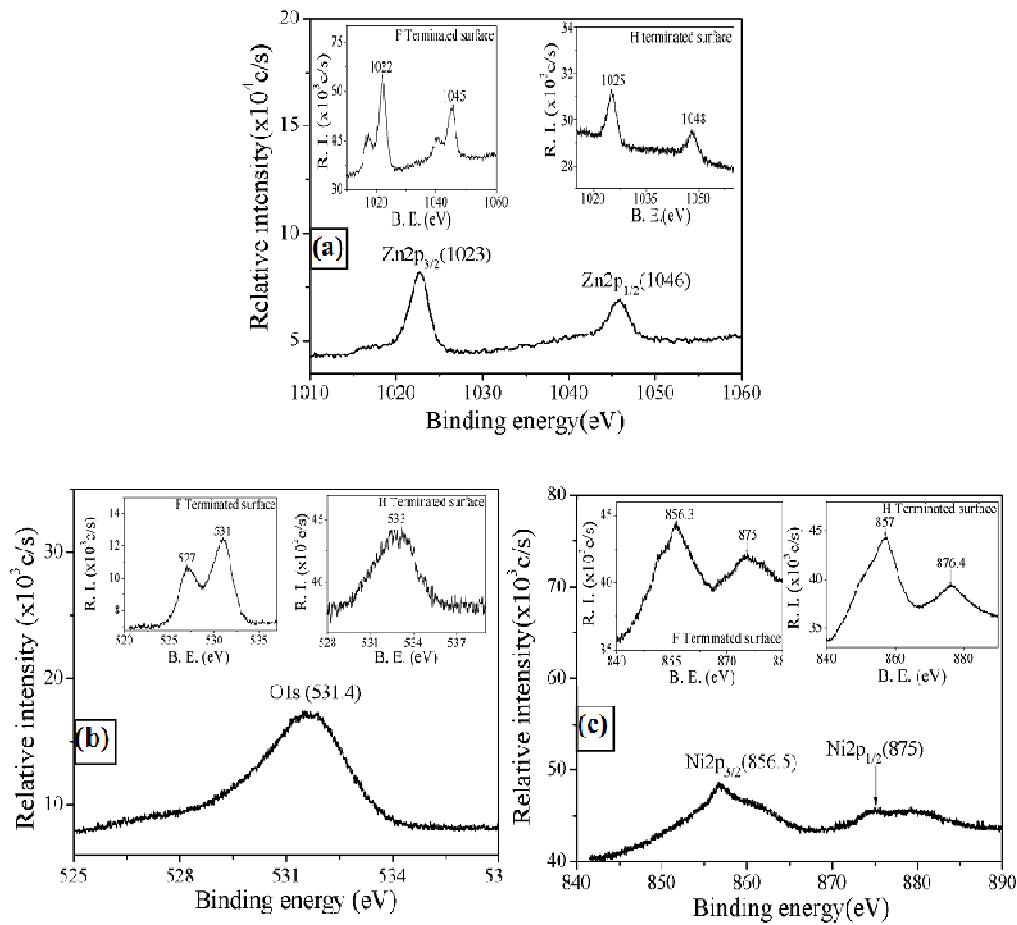


**Figure 5.2** (a) Core level XPS spectra for Zn2p peak of a representative unpoled  $Zn_{1-x}Ni_xO/PVDF$  ( $x=0.04$ ) sample, (b) O1s peak and (c) Core level spectra of Ni2p peak. Corresponding insets show the same for poled samples recorded from H-terminated (right hand insets) and F-terminated (left hand insets) surfaces

Figure 5.2a–c shows the core level spectra for Zn2p, O1s, and Ni2p levels respectively. The core level XPS spectra for Zn2p for the unpoled (Fig.5.2a) and poled  $Zn_{1-x}Ni_xO/PVDF$  films recorded from the hydrogen and fluorine terminated sides are shown in the right and left insets of Fig.5.2a, respectively. It may be observed that the spectra for Zn2p contain a doublet structure whose binding energies are located at  $\sim 1023$  and  $1046$  eV and can be assigned to Zn2p<sub>3/2</sub> and Zn2p<sub>1/2</sub> lines, respectively. The binding-energy difference between these lines is 23.0 eV and this difference was consistent for the spectra recorded from hydrogen terminated side (right hand inset of Fig.5.2a) and fluorine terminated side (left

hand inset of Fig.5.2a) for the poled films too. This value is well within the standard reference value of ZnO and matches well with that (23.2 eV) reported by Mohapatra et al.<sup>245</sup>. Zn atoms are in the Zn<sup>2+</sup> state<sup>251</sup> which are indicated by the binding energies and the binding-energy difference value. This observation is also in conformity with that for Zn<sub>1-x</sub>Ni<sub>x</sub>O system studied by Mohaparta et al.<sup>245</sup>. Asymmetry in the lower binding energy range for both the peaks related to Zn2p<sub>3/2</sub> and Zn2p<sub>1/2</sub> was observed. The above asymmetry became predominant for the poled samples (left hand inset) when the spectra were recorded from fluorine terminated side. Two distinct shoulders (inset of Fig.5.2a) located at ~1016 and 1039 eV could be observed. Here again the energy difference was ~23 eV. Appearance of these shoulders may be due to the modulation of binding energies arising out of fluorine ambience of the Zn atoms. It is well known that ZnO is a polar crystal and produces positively Zn<sup>2+</sup> terminated and negatively O<sup>2-</sup> terminated polar surfaces, which induces a net dipole moment along the c axis. Polar planes have higher surface energies than those of nonpolar planes. Thus, preferential growth along the c axis direction would be energetically favorable. Thus, when such polar molecule in nano form is incorporated in PVDF matrix, the binding energies of Zn and Ni might be modulated due to the presence of induced electric field upon poling.

The core level spectra for O1s for the unpoled and poled (insets of Fig.5.2b) are shown in Fig.5.2b. Variation of oxidation number of oxygen ions is indicated by the asymmetry in the higher binding and lower binding energy regions. Here again, the asymmetry was prominent when the spectra was recorded from the fluorine terminated side. The presence of the peaks related to both Zn and O at appropriate binding energies is in agreement with the reported values, which indicates +2 state of Zn in the films.

The Ni2p spectrum shown in Fig.5.2c contains a doublet structure whose binding energies are ~856.5 and ~875 eV, which can be assigned to Ni2p<sub>3/2</sub> and Ni2p<sub>1/2</sub> lines, respectively. The observed binding-energy difference between the lines is ~ 18.5 eV. The

spin-orbital splitting energy difference is different from that in metallic nickel<sup>237</sup>. As per the reference spectrum<sup>252</sup>, the binding energy separation is 17.4 eV for metallic nickel and 18.4 eV for NiO. The experimental observation on the present sample indicates the binding-energy separation above 18.5 eV manifesting that Ni is present in the matrix replacing Zn in ZnO lattice and not as metallic Ni cluster<sup>237, 244</sup>. Ni2p spectrum contained prominent satellite peaks which confirm the presence of NiO. These satellite peaks are very much weaker in metallic Ni. One main emission line at ~856.5 eV due to Ni2p ion (Fig.5.2c) is observed in unpoled film. This peak was present in poled samples also (insets of Fig.5.2c). The peak at ~856.5 eV for Ni2p<sub>3/2</sub> is asymmetric in nature and could be deconvoluted (not shown here) into two peaks located at ~853.5 and 856.7 eV. The observed binding energy of the Ni2p<sub>3/2</sub> peak (~853.5 eV) matches well with Ni<sup>+2</sup> in NiO (~853.5 eV). However, the other peak located at ~856.7 eV for Ni2p<sub>3/2</sub> peak is nearer to the binding energy of Ni<sup>+3</sup> as in Ni<sub>2</sub>O<sub>3</sub> (857.3 eV)<sup>253</sup>. The core spectra for Ni for poled samples (insets of Fig.5.2c) show similar behavior with the exception that of the Ni2p<sub>3/2</sub> peak, which when deconvoluted (not shown here) indicated a shift towards metallic Ni2p<sub>3/2</sub> peak ~852.7 eV for the peak at lower binding energy, especially for the hydrogen terminated side. The area covered under the peak located at ~857 eV decreased indicating decrease of Ni atoms in the Ni<sup>+3</sup> states. Thus, it may be concluded that majority of nickel in Ni doped ZnO in PVDF matrix is in +2 valence state while some of them are in Ni<sup>+3</sup> state. Therefore, it is likely that there is a replacement of Zn<sup>+2</sup> by Ni<sup>+2</sup> in the ZnO lattice. The increase of intensity of peaks with increased Ni concentration was observed. Core level XPS studies of Ni2p ions (Fig.5.2c) supports the observation obtained from XANES spectra for unpoled PVDF ZnO films measured at Ni K edge as discussed below.

### 5.1.2.3 XAS studies:

Normalized XANES spectra of pure and Zn<sub>1-x</sub>Ni<sub>x</sub>O/PVDF (x = 0.01(S<sub>1</sub>), 0.04(S<sub>2</sub>), 0.09(S<sub>3</sub>)) films measured at Zn K edge have been shown in Fig. 5.3a along with that of ZnO

commercial powder sample and Zn metal foil. It can be seen that XANES spectra of the PVDF-ZnO films resemble that of commercial ZnO, however, with some distinct differences. The small shoulder appearing in the main edge of bulk ZnO (denoted by A) and immediate oscillation after the white line (denoted by B) in Fig. 5.3a are absent in case of PVDF-ZnO thin film samples. Similar difference in XANES spectra of bulk ZnO and PVDF-ZnO has also been observed in our recent studies<sup>250</sup> and has been attributed to the fact that local band structure around Zn site is different in nanostructured samples compared to their bulk counterparts due to size effect, structural distortion and disorder. XANES spectra of the poled samples have been plotted over the respective unpoled samples in Fig.5.3a; however, no significant change has been observed between the poled and unpoled samples.

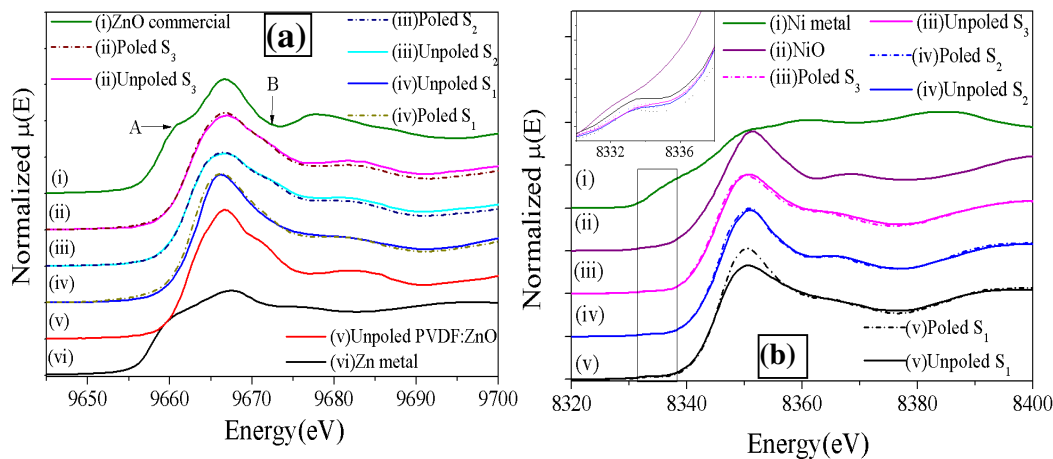


**Figure 5.3** (a) Normalised XANES spectra of unpoled and poled  $Zn_{1-x}Ni_xO/PVDF$  ( $x=0.01(S_1)$ ,  $0.04(S_2)$  and  $0.09(S_3)$ ) at measured Zn K-edge with along with the spectra for reference Zn metal and commercial ZnO powder sample. (b) Normalised XANES spectra of unpoled and poled  $Zn_{1-x}Ni_xO/PVDF$  ( $x=0.01(S_1)$ ,  $0.04(S_2)$  and  $0.09(S_3)$ ) measured at Ni K-edge along with the reference Ni metal and NiO sample.

The XANES spectra for unpoled PVDF ZnO films measured at Ni K edge are shown in Fig. 5.3b along with that of Ni metal foil and commercial NiO powder. The maxima of the first derivative is taken as the edge energy and it has been observed that Ni K edge of PVDF

ZnO films, which corresponds to transitions from Ni 1s to Ni 4p states, matches with that in the NiO sample, suggesting the fact that Ni is present 2+ oxidation state in the Ni doped ZnO/PVDF films. This observation is in conformity with that reported by Ventakataya et al.<sup>246</sup> for the Ni-ZnO nanowall structure prepared by hydrothermal technique. The Ni K edge XANES spectra of the samples also have resemblance with ZnO spectra measured at Zn K edge and shown in Fig.5.3a.

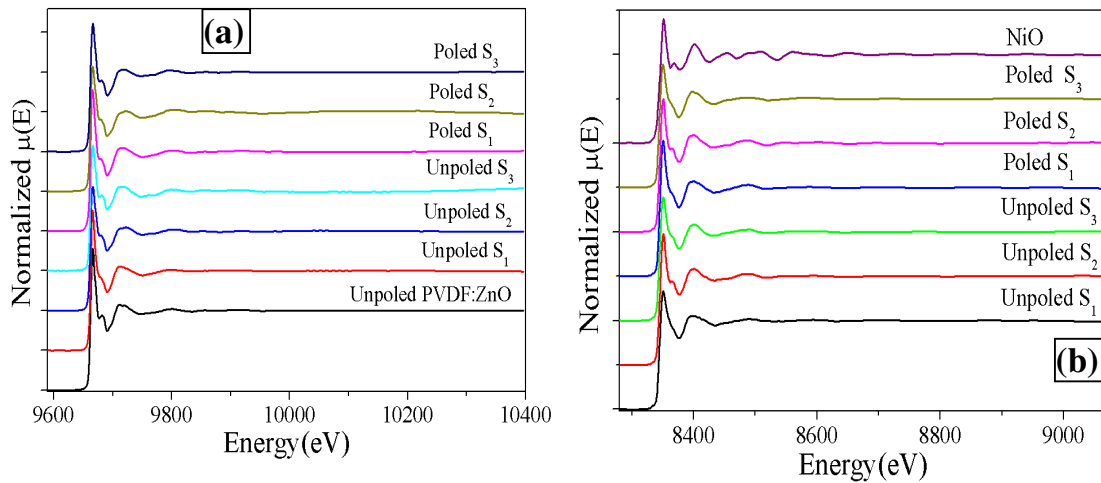


**Figure 5.4** (a) Normalised EXAFS spectra of unpoled and poled  $Zn_{1-x}Ni_xO/PVDF$  ( $x=0.01(S_1)$ ,  $0.04(S_2)$  and  $0.09(S_3)$ ) at Zn K-edge. (b) Normalised EXAFS spectra of unpoled and poled  $Zn_{1-x}Ni_xO/PVDF$  ( $x=0.01(S_1)$ ,  $0.04(S_2)$  and  $0.09(S_3)$ ) at Ni K-edge with along with reference NiO sample

The enlarged portion of pre-edge features below the main Ni K edge is shown in the inset of the Fig.5.3b. This pre-edge feature is a characteristic of the tetrahedral coordination of  $Ni^{190}$  in ZnO. It has been observed that the intensity of the pre edge peak is highest for  $x = 0.01$  Ni doped unpoled sample and its intensity is less for  $x = 0.04$  and  $0.09$  Ni doped unpoled sample. The spectra of the poled samples are also plotted along with the unpoled samples and it has been observed that for the  $x = 0.01$  Ni doped sample, the pre-edge is lower in case of the poled sample compared to that of the unpoled sample, whereas for the other doping concentrations there is no significant difference in the intensity of the pre-edge between the

poled and unpoled samples. It should also be noted that the intensity of the white line, which gives a qualitative estimation of unoccupied d states, is higher for  $x = 0.01$  Ni doped poled sample compared to that of the unpoled sample and samples with other doping concentrations.

Figures 5.4a, b show the normalized EXAFS spectra of Ni doped ( $x = 0.01, 0.04,$  and  $0.09$ ) PVDF-ZnO films measured at Zn and Ni K-edges, respectively, for both unpoled and poled samples. It may be observed that the near-edge profiles did not differ in basic characteristics with Ni concentration. For EXAFS data analysis, program available within IFEFFIT software package has been utilized and procedure of data analysis is described in Chapter-2.

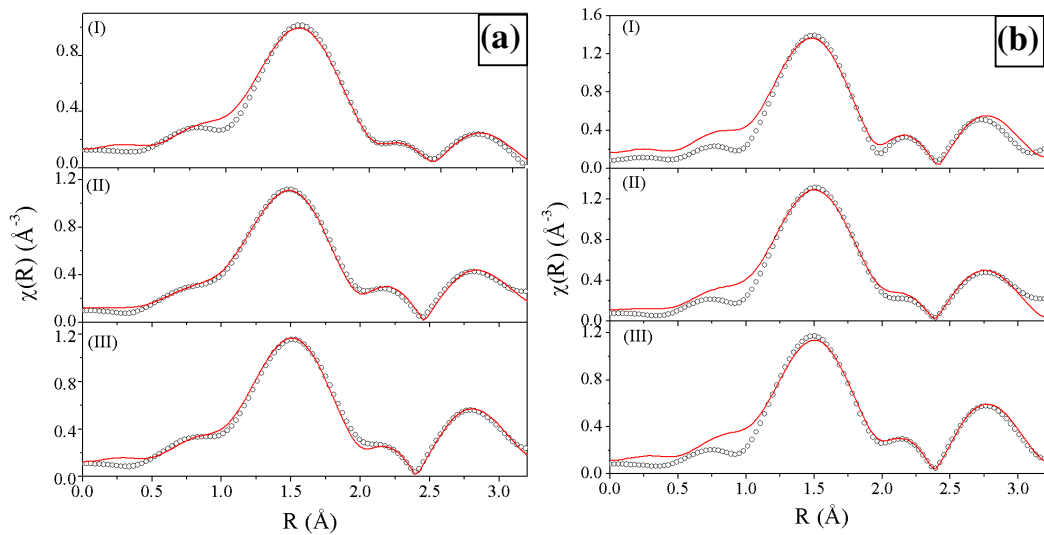


**Figure 5.5** (a) Fourier transformed EXAFS spectra of unpoled  $Zn_{1-x}Ni_xO/PVDF$  at Zn K-edge (Scatter points) and theoretical fit (Solid line): (I)  $x=0.01$  (II)  $x=0.04$  and (III)  $x=0.09$ . (b) Fourier transformed EXAFS spectra of Poled  $Zn_{1-x}Ni_xO/PVDF$  at Zn K-edge (Scatter points) and theoretical fit (Solid line): (I)  $x=0.01$  (II)  $x=0.04$  and (III)  $x=0.09$

**Table 5.1:** Bond length, coordination number and disorder factor obtain by EXAFS fitting for unpoled  $Zn_{1-x}Ni_xO/PVDF$  at Zn K edge.

Paths	Parameters	ZnO-PVDF	$Zn_{1-x}Ni_xO/PVDF$ (x=0.01)	$Zn_{1-x}Ni_xO/PVDF$ (x=0.04)	$Zn_{1-x}Ni_xO/PVDF$ (x=0.09)
Zn-O	R(Å)	2.00±0.01	2.00±0.01	1.96±0.01	1.97±0.01
	N	2.7±0.21	2.7±0.24	2.7±0.15	2.7±0.18
	$\sigma^2$	0.0063±0.0006	0.0099±0.0010	0.0053±0.0008	0.0053±0.0007
Zn-O	R(Å)	2.08±0.02	2.03±0.01	2.04±0.01	2.05±0.01
	N	1.12±0.07	1.1±0.08	1.1±0.05	1.1±0.06
	$\sigma^2$	0.0045±0.0008	0.0018±0.0009	0.002±0.001	0.002±0.0007
Zn-Zn	R(Å)	2.88±0.02	2.76±0.02	2.88±0.01	2.89±0.02
	N	5.1±0.36	5.1±0.48	5.1±0.30	5.1±0.36
	$\sigma^2$	0.0247±0.0010	0.0267±0.0008	0.0270±0.0016	0.0318±0.0010
Zn-Zn	R(Å)	3.08±0.01	3.0±0.02	3.14±0.01	3.12±0.01
	N	4.98±0.36	4.98±0.48	4.98±0.30	4.98±0.36
	$\sigma^2$	0.0119±0.0002	0.0184±0.0015	0.0121±0.0011	0.0111±0.0010

**Table-5.2:** Bond length, coordination number and disorder factor obtain by EXAFS fitting for Poled  $Zn_{1-x}Ni_xO/PVDF$  at Zn K edge.

Paths	Parameters	$Zn_{1-x}Ni_xO/PVDF$ (x=0.01)	$Zn_{1-x}Ni_xO/PVDF$ (x=0.04)	$Zn_{1-x}Ni_xO/PVDF$ (x=0.09)
Zn-O	R(Å)	1.99±0.01	1.99±0.01	2.00±0.01
	N	4.0±0.24	4.0±0.28	4.0±0.36
	$\sigma^2$	0.0041±0.0007	0.0057±0.0009	0.0073±0.0005
Zn-Zn	R(Å)	2.80±0.02	2.79±0.01	2.84±0.02
	N	5.1±0.36	5.1±0.42	5.1±0.54
	$\sigma^2$	0.0190±0.0008	0.0284±0.0009	0.0226±0.0010
Zn-Zn	R(Å)	3.05±0.02	3.04±0.01	3.06±0.01
	N	4.98±0.36	4.98±0.42	4.98±0.54
	$\sigma^2$	0.0097±0.0011	0.0119±0.0016	0.0095±0.0015

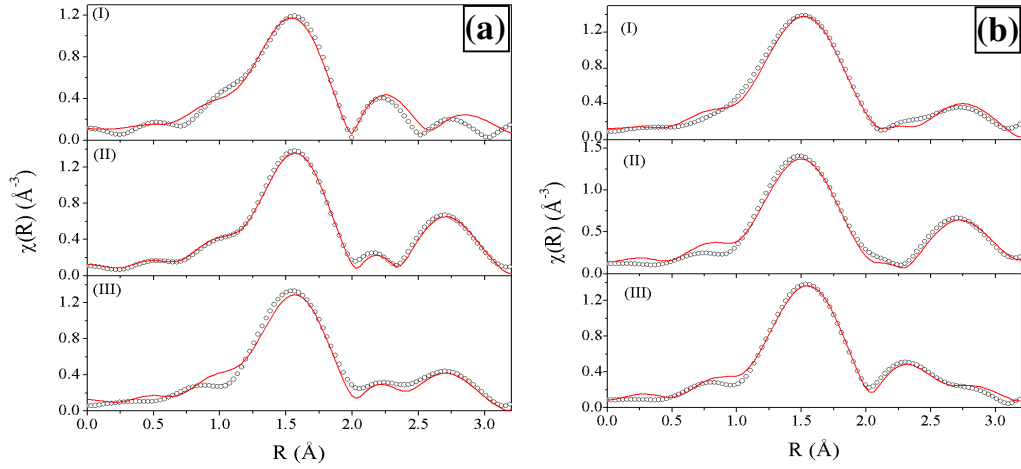


**Figure 5.6:** (a) Fourier transformed EXAFS spectra of unpoled  $Zn_{1-x}Ni_xO/PVDF$  at Ni K-edge (Scatter points) and theoretical fit (Solid line): (I)  $x=0.01$  (II)  $x=0.04$  and (III)  $x=0.09$ . (b) Fourier transformed EXAFS spectra of Poled  $Zn_{1-x}Ni_xO/PVDF$  at Ni K-edge (Scatter points) and theoretical fit (Solid line): (I)  $x=0.01$  (II)  $x=0.04$  and (III)  $x=0.09$

**Table 5.3:** Bond length, coordination number and disorder factor obtain by EXAFS fitting for unpoled  $Zn_{1-x}Ni_xO/PVDF$  at Ni K edge.

Paths	Parameters	$Zn_{1-x}Ni_xO/PVDF$ ( $x=0.01$ )	$Zn_{1-x}Ni_xO/PVDF$ ( $x=0.04$ )	$Zn_{1-x}Ni_xO/PVDF$ ( $x=0.09$ )
Ni-O	R(Å)	$1.99 \pm 0.01$	$2.04 \pm 0.01$	$2.04 \pm 0.01$
	N	$2.7 \pm 0.18$	$2.85 \pm 0.27$	$3.0 \pm 0.21$
	$\sigma^2$	$0.0049 \pm 0.0008$	$0.0033 \pm 0.0007$	$0.0045 \pm 0.0011$
Ni-O	R(Å)	$2.04 \pm 0.01$	$2.04 \pm 0.02$	$2.04 \pm 0.01$
	N	$0.9 \pm 0.06$	$0.95 \pm 0.09$	$1.0 \pm 0.07$
	$\sigma^2$	$0.001 \pm 0.001$	$0.0037 \pm 0.0013$	$0.0045 \pm 0.0015$
Ni-Zn	R(Å)	$2.90 \pm 0.02$	$2.95 \pm 0.03$	$2.91 \pm 0.01$
	N	$5.1 \pm 0.36$	$5.1 \pm 0.54$	$5.1 \pm 0.42$
	$\sigma^2$	$0.0162 \pm 0.0021$	$0.0304 \pm 0.0017$	$0.0279 \pm 0.0012$
Ni-Zn	R(Å)	$3.13 \pm 0.01$	$3.08 \pm 0.02$	$3.08 \pm 0.01$
	N	$4.08 \pm 0.36$	$4.98 \pm 0.54$	$4.98 \pm 0.42$
	$\sigma^2$	$0.0119 \pm 0.0018$	$0.0135 \pm 0.0022$	$0.0179 \pm 0.0015$

**Table 5.4:** Bond length, coordination number and disorder factor obtain by EXAFS fitting for Poled Zn<sub>1-x</sub>Ni<sub>x</sub>O/PVDF at Ni K edge.

Paths	Parameters	Zn <sub>1-x</sub> Ni <sub>x</sub> O/PVDF (x=0.01)	Zn <sub>1-x</sub> Ni <sub>x</sub> O/PVDF (x=0.04)	Zn <sub>1-x</sub> Ni <sub>x</sub> O/PVDF (x=0.09)
Ni-O	R(Å)	2.02±0.01	2.02±0.01	2.04±0.01
	N	4.0±0.22	4.0±0.26	4.0±0.23
	σ <sup>2</sup>	0.0032±0.0008	0.0025±0.001	0.003±0.0007
Ni-Zn	R(Å)	2.84±0.02	2.84±0.02	2.85±0.02
	N	5.1±0.46	5.1±0.78	5.1±0.52
	σ <sup>2</sup>	0.0292±0.0009	0.0270±0.0011	0.0154±0.0012
Ni-Zn	R(Å)	3.22±0.03	3.06±0.01	3.06±0.02
	N	4.98±0.43	4.98±0.77	4.98±0.50
	σ <sup>2</sup>	0.0217±0.0015	0.0096±0.001	0.0133±0.001

The  $\chi(R)$  versus  $R$  plots generated (Fourier transform range  $k = 3.0\text{--}10.0 \text{ \AA}^{-1}$ ) for all the samples from the  $\mu(E)$  versus  $E$  spectra following the methodology described above are shown for Ni doped ( $x = 0.01, 0.04, \text{ and } 0.09$ ) in Zn<sub>1-x</sub>Ni<sub>x</sub>O/PVDF films measured at Zn K edge in Figs. 5.5a, b for unpoled and poled films, respectively. Atomic coordination and lattice parameters of ZnO used for simulation of theoretical EXAFS spectra of the samples have been obtained from ref.<sup>33</sup>. Figures 5.5a, b shows the best fit  $\chi(R)$  versus  $R$  plots (fitting range  $R = 1.0\text{--}3.5 \text{ \AA}$ ) of the samples along with the experimental data for all the samples. Bond distances, co-ordination numbers (including scattering amplitudes), and disorder (Debye Waller) factors ( $\sigma^2$ ) were utilized to derive mean square fluctuations in the distances. These were used as fitting parameters. The quality of fit has been determined by the value of the  $R_{\text{factor}}$ .

The best fit results of the above Zn K edge data are summarized in Tables 5.1 and 5.2, for the unpoled and poled films, respectively. The first peak in the  $\chi(R)$  versus  $R$  plots at Zn edge has contributions from two Zn-O paths at 2.00 and 2.08 Å. These values are nearly similar to those reported (1.90–1.98 Å) by Jeong et al.<sup>254</sup> for ZnO NPs, nanorods, and powder produced by solution method. The second peak in Fourier transform spectrum has

contributions from two Zn-Zn coordination shells. Venkatayah et al.<sup>246</sup> also observed similar first and second major peaks in the radial distribution function (RDF) of Ni-ZnO nanowire samples when recorded at the Ni or Zn K edge. They observed that the two major peaks in the RDF of the as-grown sample resembled those of ZnO as viewed from a specific Zn atom. This implied that most of the Ni atoms substituted Zn ions in the ZnO matrix. This observation is in commensurate with our observation in our Ni ZnO/PVDF composites.

It can be found from Table 5.1 that the bond lengths of Zn-O shells are comparable to their theoretical values though bond lengths of the Zn-Zn shells are less. Similar difference in the bond lengths between ZnO bulk and nanostructures has also been reported by other researchers<sup>254</sup>. The coordination numbers of Zn shells are also found to be less compared to their bulk values which are due to nanocrystalline nature of the samples as has been observed by other researchers<sup>191, 254</sup>. Jeong et al.<sup>254</sup> reported the local structural properties of ZnO NPs, nanorods, and powder by using EXAFS. They obtained the values of Zn-Zn bond length as 3.10 compared to 3.21 Å. This value agrees well with those reported by us (3.08–3.14 Å) for Ni- ZnO/PVDF composites studied here. It can also be seen that the Debye-Waller factor ( $\sigma^2$ ) is significantly high for Zn-Zn shells as expected in case of nanocrystalline samples<sup>191</sup>. The Debye-Waller factors ( $\sigma^2$ ) for Zn-O paths are found to increase from undoped ZnO/PVDF film to Zn<sub>1-x</sub>Ni<sub>x</sub>O/PVDF (x = 0.01) film; however, it is found to decrease with increase in the Ni doping concentration. This shows enhanced distortion in the Ni doped (x = 0.01) unpoled samples compared to other samples, which resulted in an intense pre-edge peak in the Ni K edge XANES spectrum of this sample as mentioned before. From Tables 5.1 and 5.2, it can be seen that the only salient difference between the unpoled and poled samples is that in the former case the two oxygen shells are close enough for the shell to be represented by one oxygen shell only with average bond length and total oxygen coordination close to the bulk values. This would imply that the Ni atoms are substituted in the Zn sites for all the Ni

concentrations under this study. This observation is in conformity with those reported by Li et al.<sup>240</sup>.

$\chi(R)$  versus  $R$  plots for the Ni K edge data have been shown in panels a and b of Fig. 5.6, respectively, for the unpoled and poled samples along with their best fit theoretical plots, and the values of the best fit parameters are shown in Tables 5.3 and 5.4. The theoretical fitting has been carried out assuming Ni substitution in wurtzite ZnO structure. It has been observed that for  $x = 0.04$  Ni doped unpoled sample, oxygen coordination is smaller than that for the  $x = 0.01$  and  $x = 0.09$  Ni doped unpoled samples. In the Ni K-edge XANES spectra shown in fig. 5.3(b), we have observed that the intensity of the pre-edge peak is highest for  $x = 0.01$  Ni doped unpoled sample and its intensity is less for  $x = 0.04$  and  $x = 0.09$  Ni doped unpoled samples. The intensity of the pre edge increases as metal site is distorted (greater p-d mixing due to symmetry reduction) and therefore can be used as a probe of the coordination number or the site symmetry of the absorbing atom<sup>255</sup>. The increased intensity of  $x = 0.01$  Ni unpoled sample suggests lower coordination number than  $x = 0.04$  and  $x = 0.09$  samples. In case of  $x = 0.04$  and  $x = 0.09$  Ni doped samples, Ni-O bond length ( $\sim 2.02$ – $2.04$  Å) obtained here both for unpoled and poled samples (Tables 5.3 and 5.4) is slightly longer than the theoretical Zn-O bond length (Table 5.1). However, the above values for our Ni-ZnO/PVDF composites agree well with those reported by Trofimova et al. ( $2.04$ – $2.08$  Å)<sup>249</sup> and match very well with that reported by Li et al. ( $2.01$ – $2.05$  Å)<sup>247</sup>. Table 5.4 also indicated that Ni-Zn distances are quite similar to the Zn-Zn distance ( $\sim 3.222$  Å) in ZnO. Mino et al.<sup>231</sup> also made a similar observation from their EXAFS studies on Ni doped ZnO thin films prepared by laser ablation technique. The increase in the Ni-O bond length in Ni doped ZnO thin films contradicts the expected change by considering the smaller ionic radii of Ni<sup>2+</sup> ( $0.55$  Å) compared to Zn<sup>2+</sup> ( $0.60$  Å); however, similar results have also been observed by other researchers<sup>231, 238, 240</sup>.

Thus in brief, XPS results indicate the existence of  $\text{Ni}^{2+}$  and  $\text{Ni}^{3+}$  species in the samples, though Ni K edge XANES studies manifest the presence of Ni in  $\text{Ni}^{2+}$  states for all the films studied here, the difference is attributed to the fact that XPS is surface sensitive while XANES gives the bulk information. EXAFS analysis recorded from Zn edge suggests that there is no significant change in the local structure surrounding Zn due to Ni doping since both ions are in +2 oxidation state and are being of similar size.

## **5.2 Co doped ZnO/PVDF:**

Next we describe the results of our study on sol-gel derived free standing flexible films of Co-doped nanocrystalline ZnO/PVDF ( $\text{Co}_x\text{Zn}_{1-x}\text{O}/\text{PVDF}$ ) composites. Three different Co doping concentrations ( $x=0.01, 0.04, 0.07$ ) were used in the composite films. Surface morphology of the films has been studied by Field Emission Scanning Electron Microscopy (FESEM) measurements. Local structure surrounding the Zn and Co sites was probed by XAS (combined techniques of X-ray absorption near edge structure (XANES) and EXAFS). Both the unpoled and poled samples were subjected to the above measurements.

### **5.2.1 Experimental:**

The synthesis protocol followed for the deposition of  $\sim 50$   $\mu\text{m}$  thick (surface area  $\sim 5$  mm  $\times$  5 mm) free standing Co-ZnO/PVDF or  $\text{Co}_x\text{Zn}_{1-x}\text{O}/\text{PVDF}$  films has been explained in Chapter-2, where Co-acetate tetrahydrate has been used for Co doping. In brief, appropriate amount of Zinc acetate dihydrate was taken to obtain a sol with 4 ml dimethyl formamide (DMF). The above sol was refluxed for 1 h with constant stirring at  $30^\circ\text{C}$  for complete dissolution of the solute. Three such stock solutions were obtained and three different amounts of Ni-acetate were added to the above solutions for getting three different doping molar concentrations of Co ( $x = 0.01, 0.04, 0.07$  in  $\text{Zn}_{1-x}\text{Co}_x\text{O}$ ). These mixtures were refluxed for 3 h with constant stirring at  $150^\circ\text{C}$  for complete dissolution of the solute with

resultant formation of intermediate products of  $\text{Zn(OH)}_2 + \text{Co(OH)}_2$ . Appropriate amount of dimethyl amine, acting as a reducing agent, was added to the above sol while heating and stirring for another 30 min. A fixed amount of PVDF (15 wt%) was then added to the above sols which were cooled down to 60 °C. Stirring was continued for another 2 h. A semi-gel liquid with a brownish tinge was obtained. The above sol was spin-casted uniformly on glass substrates at room temperature at a low spin (60 rpm) for depositing the Co doped nano-ZnO/PVDF composite films. A microwave oven was used to heat the as-coated films at 100 W for 3 min. The films so obtained could be easily peeled out from the glass substrate.

A field of 5 MV/m was applied across the films surfaces for 2 h for poling the composite films. The poling creates H terminated surface at one side of the films, while F-terminated surface at the other end as explained in detail in Chapter-2. The poling unit<sup>250</sup>, used for this purpose has also been described in Chapter-2. The surface morphology of the films was recorded by FESEM (Carl Zeiss AURIGA). XPS (X-ray photoelectron spectroscopy) measurements were carried out in a SPECS (Germany) spectrometer with delay line detector at 300 W power and measurements were carried out at a chamber pressure of  $\sim 4 \times 10^{-10}$  Torr with Al K $\alpha$  line source of 1486.74 eV. XAS measurements were carried out at the Energy-Scanning EXAFS beamline (BL-9) at the Indus-2 Synchrotron Source as described in Chapter-2. In the present case, XAS measurements at the Zn K-edge (9659 eV) have been performed in transmission mode while measurements at the Co K edge (8333 eV) have been carried out in fluorescence mode.

## **5.2.2 Results and discussion:**

### **5.2.2.1 Microstructural studies:**

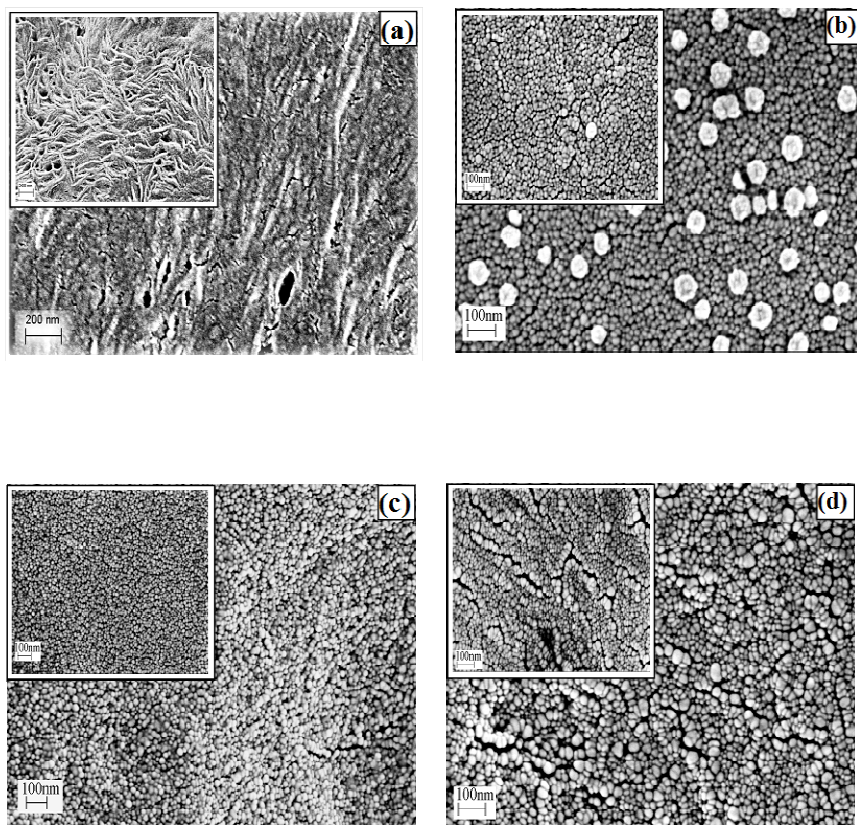


**Figure 5.7:** FESEM pictures of poled: (a) pristine PVDF film, (b)  $\text{Co}_x\text{Zn}_{1-x}\text{O}/\text{PVDF}$  ( $x = 0.01$ ) sample, (c)  $\text{Co}_x\text{Zn}_{1-x}\text{O}/\text{PVDF}$  ( $x = 0.04$ ) and (d)  $\text{Co}_x\text{Zn}_{1-x}\text{O}/\text{PVDF}$  ( $x = 0.07$ ) sample. Insets show the corresponding FESEM pictures of unpoled films.

FESEM picture of poled and unpoled representative pristine PVDF and Co-doped ( $x = 0.01, 0.04, 0.07$  in  $\text{Co}_x\text{Zn}_{1-x}\text{O}$ ) nano-ZnO/PVDF films are shown in Fig.5.7. The texture of the un-poled film of pristine PVDF film (inset of Fig.5.7a) indicates randomly oriented fibrous structure. The FESEM pictures of the same film when poled showed that the fibrous structure was oriented in one direction (Fig. 5.7a). Change in morphology of the PVDF films after inclusion of Co-doped ZnO nanocrystallites is apparent from Fig. 5.7b, c and d. The FESEM pictures of poled Co-ZnO/PVDF composite films recorded from hydrogen terminated surface with three different Co doping levels of 0.01, 0.04, 0.07 are shown in Fig. 5.7b, c and d, respectively. The micrographs recorded from fluorine terminated side were nearly similar to those shown in Fig. 5.7b–d. The corresponding pictures of unpoled samples

are shown in the insets of the above figures. One may observe that the film surfaces do not show the fibrous structure of the pristine PVDF film. The surface now is covered with Co-doped ZnO nanocrystallites. Localized segregation of Co-ZnO nanocrystallites could be seen in the unpoled samples (insets of Fig.5.7b,c,d) and upon poling the Co-ZnO nanocrystallites are dispersed quite uniformly (Fig.5.7b,c,d). The surfaces became compact and their surface roughness increased with increase in Co content in the ZnO nanocrystallites. ZnO films having maximum Co ( $x=0.07$ ) in PVDF matrix showed a maximum surface roughness of 2 nm.

### 5.2.2.2 XPS and XANES studies:

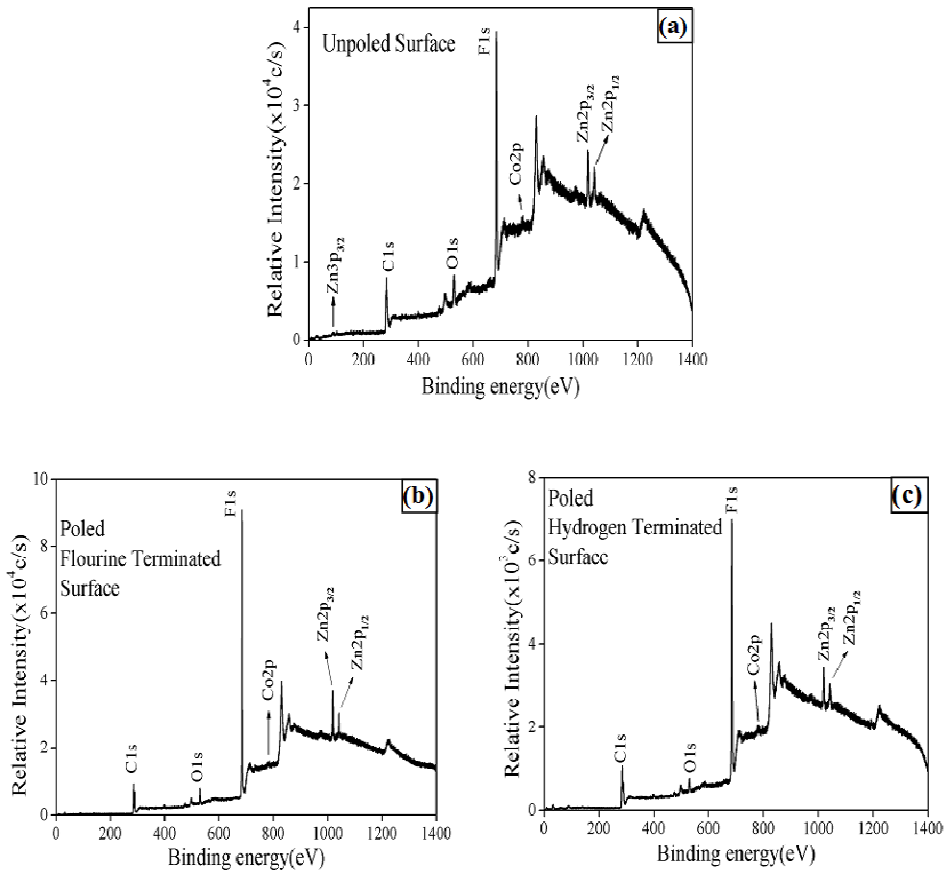


**Figure 5.8:** General survey XPS spectra of  $\text{Co}_x\text{Zn}_{1-x}\text{O}/\text{PVDF}(x=0.07)$  for (a) unpoled Surface, (b) poled sample of the same film when recorded from fluorine terminated surface and (c) shows the same when recorded from hydrogen terminated surface.

XPS studies were carried out on unpoled and poled samples of flexible free-standing Co doped ZnO/PVDF films with different Co-doping concentrations ( $x=0.01, 0.04, 0.07$ ) to derive information on the bonding environment of the constituent elements. The calibration of all the peaks was done with respect to the peak for C1s (284.5 eV) as well as Au4f<sub>7/2</sub> (84 eV). It may be mentioned here that all the general survey spectra recorded for the films with different Co-doping concentrations were similar to one another regarding the peak positions of the individual core level peaks. In Fig. 5.8a–c, we present the general survey XPS spectra of unpoled and poled samples of a representative Co<sub>x</sub>Zn<sub>1-x</sub>O/ PVDF film ( $x=0.07$ ). The spectra of the above Co doped ZnO/PVDF film for unpoled samples are shown in Fig.5.8a, while that recorded from fluorine terminated and hydrogen terminated sides of these films are shown in Fig.5.8b and c, respectively. Peaks related to Zn, O and Co present in the films are found in all the spectra in addition to peaks for C and fluorine.

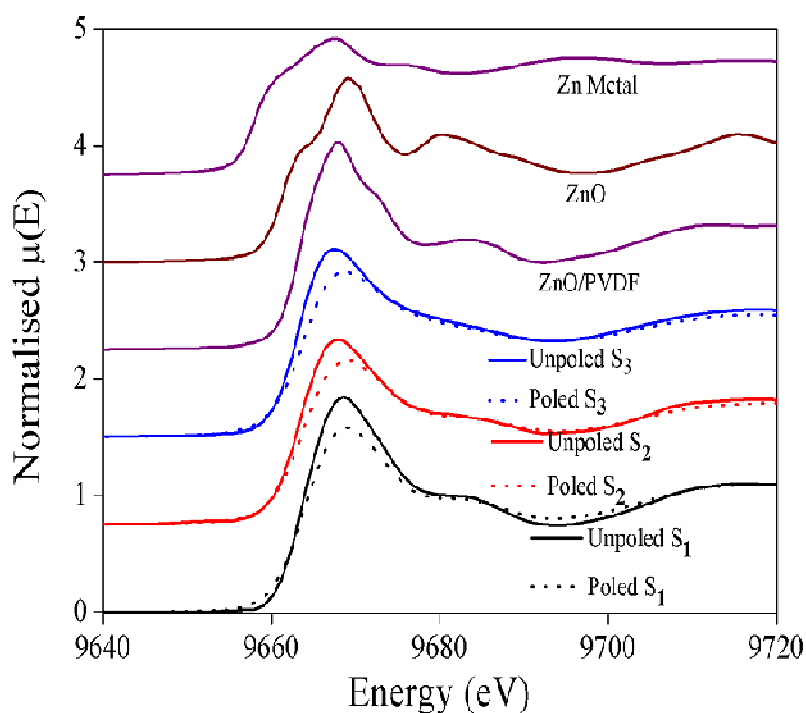


**Figure 5.9:** Normalised XANES spectra of unpoled and poled Co<sub>x</sub>Zn<sub>1-x</sub>O/PVDF films (with  $x=0.01$ (S<sub>1</sub>),  $x =0.04$ (S<sub>2</sub>) and  $x= 0.07$ (S<sub>3</sub>)) measured at Zn K-edge with along with the spectra for reference Zn metal and commercial ZnO powder sample.

Normalized XANES spectra of pure ZnO/PVDF and  $\text{Co}_x\text{Zn}_{1-x}\text{O}/\text{PVDF}$  films ( $x = 0.01, 0.04, 0.07$ ) measured at Zn K-edge are shown in Fig. 5.9 along with that of ZnO commercial powder and Zn metal foil. The Zn K-edge position of the samples agree with that in ZnO powder sample, manifesting that Zn is present in  $\text{Zn}^{+2}$  oxidation state in all the samples. For unpoled samples, we have observed a decrease in the intensity of the white line peak with increase in Co doping concentration which is suggestive of decrease in unoccupied d levels where the 1s-4p transition takes place at the main absorption edge. In case of the poled samples the decrease in the intensity of white line with Co doping is also accompanied by a shift towards higher energy side. Since Zn does not acquire any higher oxidation state than +2, it might be due to increase in effective positive charge at Zn sites due to poling effect. Similar change in absorption edge position due to change in effective charge at cationic site has been observed by us in several other cases also <sup>256-258</sup>. This has been reflected in the Zn core level XPS spectra also as discussed below.

The core level XPS spectra for Zn2p for representative unpoled  $\text{Co}_x\text{Zn}_{1-x}\text{O}/\text{PVDF}$  films ( $x = 0.01, 0.04, 0.07$ ) and poled ( $x=0.07$ ) samples are shown in Fig.5.10a and b, respectively. It may be observed that the spectra of the Zn2p state for the unpoled samples contain a doublet structure whose binding energies are located at ~1018.5 eV and 1041.5 eV with shake-up resonance transitions (satellite) of these two peaks at higher binding energies. The above two peaks can be assigned to Zn2p<sub>3/2</sub> and Zn2p<sub>1/2</sub> states respectively and they show distinct asymmetry in the higher binding energy range for films containing lower Co doping concentration (insets of Fig. 5.10a) for both unpoled and poled samples. Further to the above, one may note that with increased incorporation of Co in the ZnO matrix, the position of the Zn2p<sub>3/2</sub> peak moves to higher binding energy (Fig. 5.10a). The binding energy and the binding energy difference values calculated from the XPS study show that Zn atoms are in +2 oxidation state. It is interesting to note that the binding energies for both the Zn2p<sub>3/2</sub> and

Zn2p<sub>1/2</sub> states get shifted to higher energies for poled samples recorded from both the fluorine and hydrogen terminated surface (Fig. 5.10b). This may be due to a change in local environment of Zn in case of the poled samples as has been indicated from the Zn K-edge XANES measurements also (discussed earlier).

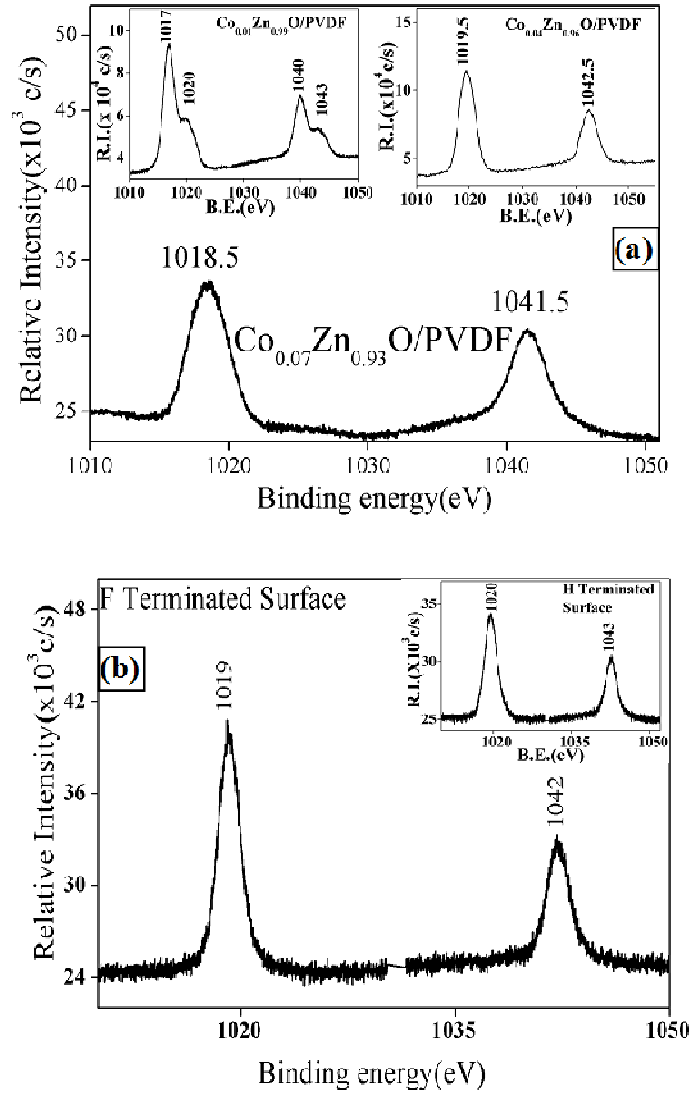


**Figure 5.10:** Core level XPS spectra for Zn2p peaks showing doublet structure for: (a) unpoled  $\text{Co}_x\text{Zn}_{1-x}\text{O}/\text{PVDF}$  ( $x=0.07$ ) films. Insets show the core level spectra of  $\text{Co}_x\text{Zn}_{1-x}\text{O}/\text{PVDF}$  film for  $x=0.01$ (left hand side) and  $x=0.04$ (right hand side), (b) poled  $\text{Co}_x\text{Zn}_{1-x}\text{O}/\text{PVDF}$  ( $x=0.07$ ) film when recorded from fluorine terminated side and Inset shows the same film from hydrogen terminated side.

The normalized XANES spectra of Co doped ZnO/PVDF films measured at Co K edge are shown in Fig.5.11 along with that of Co metal foil and commercial CoO powder sample. The edge positions of most of the samples are very close to CoO which suggests that Co is present in +2 oxidation state in the samples. Only for low Co doped sample( $x = 0.01$ ), Co edge lies at a relatively higher energy which suggests the presence of  $\text{Co}^{+3}$  phase too in this sample.

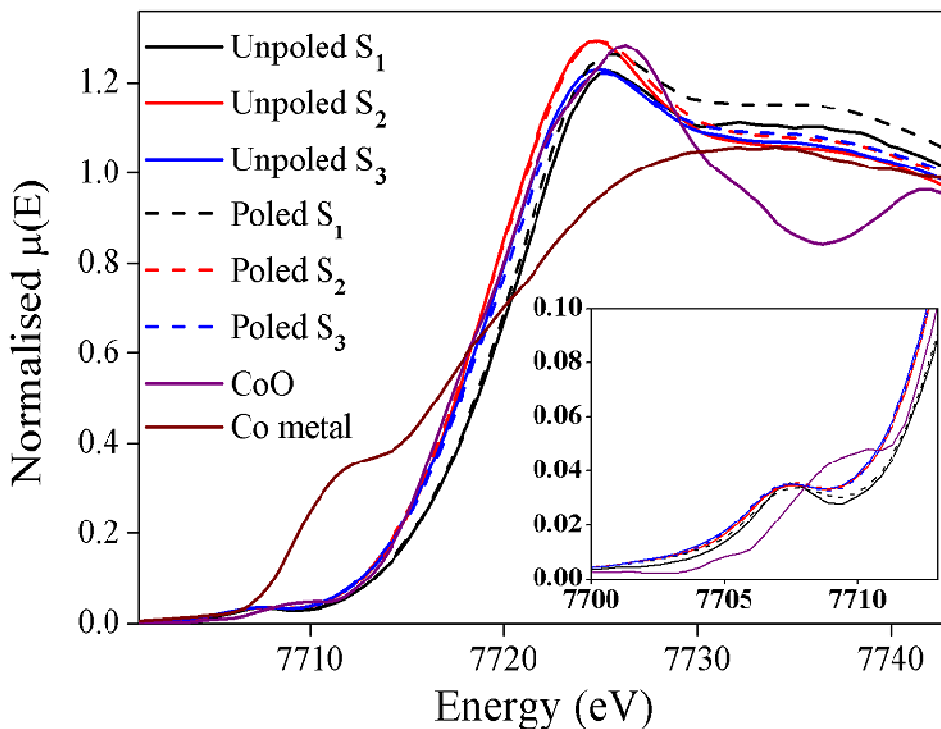


**Figure 5.11:** Normalised XANES spectra of unpoled and poled  $\text{Co}_x\text{Zn}_{1-x}\text{O}/\text{PVDF}$  films (with  $x = 0.01(S_1)$ ,  $x = 0.04(S_2)$  and  $x = 0.07(S_3)$ ) measured at Co K-edge along with the reference Co metal and CoO sample.

The enlarged portion of the pre-edge features is shown in the inset of the Fig. 5.11. Tetrahedral coordination is characterized by the presence of pre-edge features<sup>190</sup>. They originate due to Co 1s transition into unoccupied O 2p-Co 3d (or Co 3d/4p) hybridized states.

These hybridized states have p components projected at the Co site and have been observed in many transition metal oxides. The pre-edge positions observed in all the samples are at lower energies and of less intensity compared to that of CoO. This pre-edge peak positions at lower energy give the indication of presence of some amount of metallic Co in all the doped samples. Presence of Co metallic cluster has also been observed by Co doped ZnO films prepared by sol-gel route for Co doping of more than 12%<sup>98</sup>.

Core level Co2p XPS spectra for a representative unpoled  $\text{Co}_x\text{Zn}_{1-x}\text{O}/\text{PVDF}$  film ( $x = 0.01, 0.04, 0.07$ ) and poled ( $x = 0.07$ ) samples are shown in Fig.5.12a and b, respectively. All the spectra show two main peaks corresponding to  $\text{Co}2p_{3/2}$  and  $\text{Co}2p_{1/2}$  states. Two shake up satellites at higher binding energies can also be found to exist. This means that high-spin  $\text{Co}^{2+}$  ions were surrounded by O ions. The  $\text{Co}2p_{3/2}$  core levels for Co-O bonding are 779 eV, and the energy difference between  $\text{Co}2p_{3/2}$  and  $\text{Co}2p_{1/2}$  is 15.5 eV (Fig.5.12b), which matches with that of Co2p spectrum of standard CoO sample. This is consistent with the divalent state of cobalt homogeneously surrounded by the oxygen tetrahedral<sup>259</sup>. If Co would have existed largely in the form of metal cluster in these samples, the energy difference of these peaks would have been 15.05 eV<sup>72</sup>. Thus the above findings confirm successful incorporation of Co atoms in tetrahedral sites of the wurtzite host matrix of ZnO. They were incorporated as substitutional impurities without forming any detectable impurity phase or Co clusters<sup>29</sup>. It is known that the  $\text{Co}2p_{3/2}$  peak corresponding to Co-Co bonding is located at 778 eV and the peak corresponding to Co-O bonding is located around 779 eV<sup>54</sup>. Thus, looking at the Co spectra, one may clearly appreciate that the peak ~778-779 eV contain both the peaks related to Co-O and Co-Co bonding. However, deconvolution of these peaks (not shown here) indicated that presence of Co-Co binding energy is comparatively much less even in films containing highest amount of Co ( $x=0.07$ ).

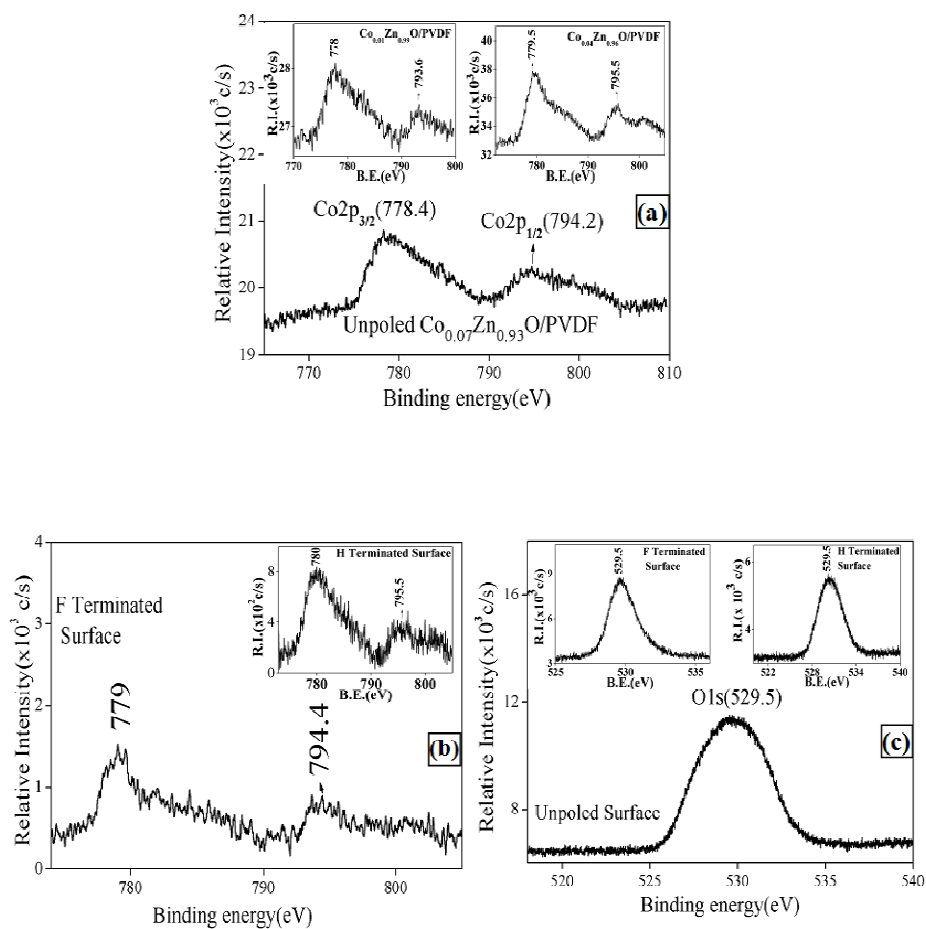


**Figure 5.12:** Core level Co2p peaks showing doublet structure for (a) unpoled  $\text{Co}_x\text{Zn}_{1-x}\text{O}/\text{PVDF}$  ( $x=0.07$ ) films, Insets show the core level spectra of  $\text{Co}_x\text{Zn}_{1-x}\text{O}/\text{PVDF}$  film for  $x=0.01$ (left hand side) and  $x=0.04$ (right hand side), (b) poled  $\text{Co}_x\text{Zn}_{1-x}\text{O}/\text{PVDF}$  ( $x=0.07$ ) film when recorded from fluorine terminated side and Inset shows the same film from hydrogen terminated side.(c) Core level O1s peaks for unpoled  $\text{Co}_x\text{Zn}_{1-x}\text{O}/\text{PVDF}$  ( $x=0.07$ ) films and Insets show same films recorded from fluorine terminated side(left hand side) and hydrogen terminated side(right hand side).

Thus, it is apparent from the above discussion that though XPS measurements indicates that there is negligible possibility of the presence of metallic Co phase in the samples, XANES results clearly show that though Co is primarily present as  $\text{Co}^{+2}$  states, small amount of Co metallic phase is also present in the samples. Such small differences between the XANES and XPS results have also been observed in case of Mn doped ZnO/PVDF films<sup>250</sup>. This is due to the fact that XANES gives bulk information of the sample whereas XPS is primarily a surface sensitive probe

The oxygen environment surrounding Zn and Co sites can also be probed by oxygen XPS spectra of the samples. The core level spectra for O1s for  $\text{Co}_x\text{Zn}_{1-x}\text{O}/\text{PVDF}$  (with  $x=0.07$ ) unpoled and poled samples (recorded from hydrogen terminated side and fluorine terminated side) are shown in Fig. 5.12c. For our samples, the position of the peak did not show any significant shift of binding energy with increasing Co concentration as observed by Moulder et al.<sup>260</sup>. The high-resolution spectra of oxygen were deconvoluted (not shown here) to study the oxygen states present in the films. The low-energy peak located at 529.5 eV in the O 1s spectrum is generally attributed to  $\text{O}^{2-}$  ions in the Zn-O bonding of the wurtzite hexagonal ZnO structure, while the high-energy peak located at 531.0 eV is attributed to O-H bonds due to exposure to air<sup>261</sup>. It may be observed from the spectra for poled samples (insets of Fig. 5.12c) recorded from the fluorine terminated surface that the low-energy peak at 529.5 eV related to the intrinsic binding energy of O ion in ZnO is the predominant peak for films signifying that oxygen is present in Zn-O bonding state.

### 5.2.2.3 EXAFS studies:

The  $\chi(R)$  versus  $R$  plots or radial structure functions generated (Fourier transform range  $k=3-10 \text{ \AA}^{-1}$ ) from the  $\mu(E)$  versus  $E$  spectra measured at Zn K-edge are shown in Fig. 5.13a and b for unpoled and poled films, respectively. Atomic coordination and lattice parameters of ZnO used for simulation of theoretical EXAFS spectra of the samples were obtained from ref.<sup>33</sup> and the best fit radial distribution functions (fitting range  $R=1.0-3.5 \text{ \AA}$ ) of the samples have been shown in the above figures along with the experimental data. It should be noted that the first peak with its shoulder (between 1.0 and 2.5  $\text{ \AA}$ ) in the radial distribution functions at Zn K-edge has contributions from two Zn-O paths at their nominal values of 1.98  $\text{ \AA}$  and 1.99  $\text{ \AA}$ . The second peak in the Fourier transform spectrum (between 2.75 and 3.0  $\text{ \AA}$ ) has contributions from two Zn-Zn coordination shells with their nominal values at 3.21  $\text{ \AA}$  and 3.25  $\text{ \AA}$ .

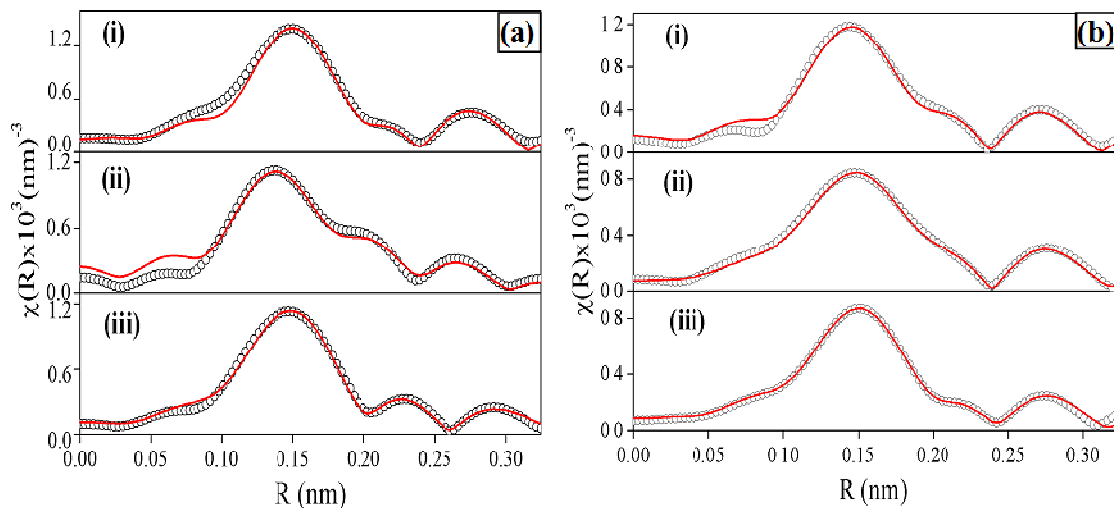


**Figure 5.13:** Radial structure functions of  $\text{Co}_x\text{Zn}_{1-x}\text{O}/\text{PVDF}$  films with: (i)  $x=0.01$ , (ii)  $x=0.04$  and (iii)  $x=0.07$  measured at Zn K-edge (scatter points) and theoretical fit (solid line) for (a) unpoled surface and (b) poled surface.

The values of the best fit parameters of bond distances, co-ordination numbers (including scattering amplitudes) and disorder (Debye-Waller) factors ( $\sigma^2$ ) are given in Table 5.5. As expected, a gradual decrease in oxygen coordination in the first two shells and Zn coordinations in the next two shells with increase in Co doping concentration in case of the poled samples was observed. This was accompanied by a gradual increase in the Debye-Waller factor which is due to perturbation at the Zn sites due to Co doping. However, we have not observed any such systematic change in case of unpoled samples (Table 5.5) apart from the fact that the Zn-O bond length and Zn-Zn distances for the 4% Co doped sample is significantly lower than the other samples. It should also be noted that the Zn-Zn distance of the fourth coordination shell for the highest Co doped unpoled ZnO sample is significantly higher than that of the other samples.

**Table 5.5:** Bond length, coordination number and disorder factor obtained by EXAFS fitting of unpoled and poled Co doped PVDF-ZnO films at Zn K edge.

Paths	Parameters	Unpoled films			Poled films		
		Co <sub>x</sub> Zn <sub>1-x</sub> O/PVDF (x = 0.01)	Co <sub>x</sub> Zn <sub>1-x</sub> O/PVDF (x = 0.04)	Co <sub>x</sub> Zn <sub>1-x</sub> O/PVDF (x = 0.07)	Co <sub>x</sub> Zn <sub>1-x</sub> O/PVDF (x = 0.01)	Co <sub>x</sub> Zn <sub>1-x</sub> O/PVDF (x = 0.04)	Co <sub>x</sub> Zn <sub>1-x</sub> O/PVDF (x = 0.07)
Zn-O	R(Å)	1.98±0.01	1.94±0.02	0.1.96±0.03	0.1.96±0.01	0.1.95±0.02	0.1.97±0.01
	N	3±0.24	3±0.63	3±0.35	3±0.18	2.85±0.12	2.4±0.15
	σ <sup>2</sup>	0.0021±0.001	0.0018±0.001	0.0035±0.001	0.0020±0.001	0.0087±0.0009	0.0098±0.001
Zn-O	R(Å)	2.08±0.02	2.12±0.06	2.11±0.04	2.08±0.02	2.07±0.03	2.02±0.02
	N	1±0.25	1±0.33	1±0.30	1±0.1	0.95±0.05	0.8±0.06
	σ <sup>2</sup>	0.0018±0.0009	0.0018±0.0007	0.0018±0.0009	0.0018±0.001	0.0018±0.001	0.0018±0.001
Zn-Zn	R(Å)	2.89±0.03	2.62±0.07	2.88±0.04	2.74±0.02	2.73±0.03	2.74±0.02
	N	6±0.24	6±0.42	6±0.60	6±0.30	5.7±0.30	4.8±0.36
	σ <sup>2</sup>	0.0323±0.002	0.0170±0.003	0.0249±0.003	0.0249±0.003	0.0280±0.003	0.0279±0.002
Zn-Zn	R(Å)	3.06±0.02	2.90±0.08	3.15±0.03	3.00±0.04	3.0±0.03	3.0±0.03
	N	6±0.30	6±0.25	6±0.25	6±0.30	5.7±0.30	4.8±0.30
	σ <sup>2</sup>	0.0183±0.003	0.0225±0.005	0.0192±0.003	0.0153±0.002	0.0182±0.003	0.0193±0.002

The radial distribution functions obtained for unpoled and poled Co doped ZnO/PVDF films at Co K edge are shown in Fig. 5.14a and b, respectively while the best fit results are shown in Table 5.6. The FT-EXAFS spectra of the samples obtained from the Zn K-edge data and Co K edge data resemble each other which suggest that Co atoms primarily substitute Zn atoms in the ZnO lattice<sup>262</sup> and thus EXAFS fitting at Co K edge has been carried out assuming Co substitution at Zn sites. The first peak in Fourier transform spectrum is a contribution of first coordination shell having 4 oxygen atoms and the second and third peaks at ~2.25 Å and 2.75 Å (phase uncorrected spectra) respectively have contributions of two Co-Zn coordination shells. The simulated radial distribution functions for a Co metal foil have also been shown in Fig. 5.14a (iv) which shows a large peak at 2.0 Å which is absent in our sample showing no significant metallic Co phase in our samples<sup>98, 261</sup>. Thus the above results suggest successful uniform doping of Co at Zn sites throughout the Co concentration

range of  $x = 0.01$  to  $0.07$  which is in contrast to our results obtained in case of Mn doped ZnO/ PVDF films<sup>250</sup> discussed later, where the 1% Mn doped film was more like a composite of ZnO and Mn acetate and not Mn doped ZnO film.

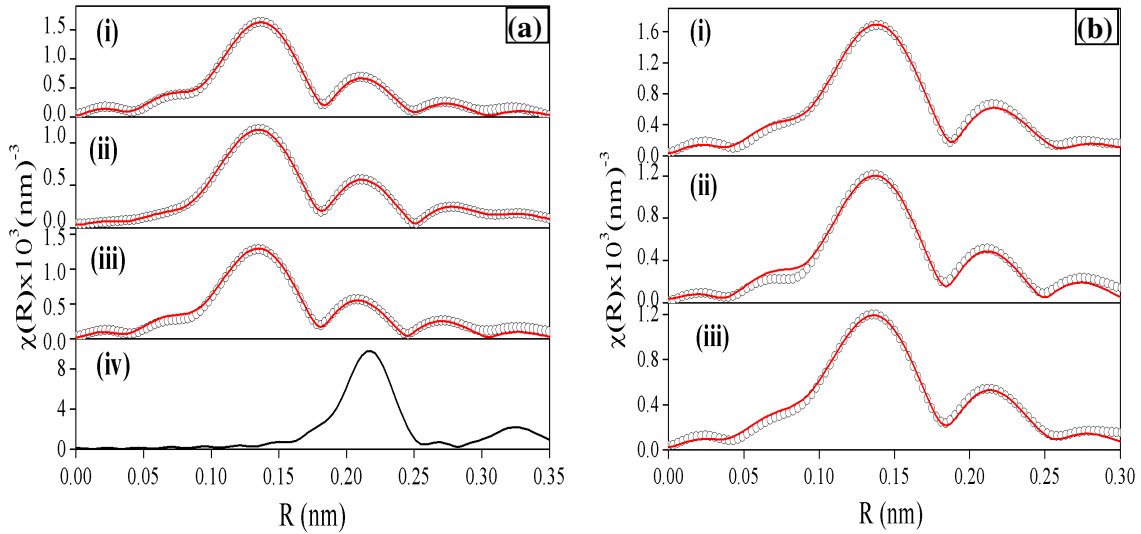


**Figure 5.14:** Radial structure functions of  $\text{Co}_x\text{Zn}_{1-x}\text{O}/\text{PVDF}$  films with: (i)  $x=0.01$ , (ii)  $x=0.04$ , (iii)  $x=0.07$  and (iv) Co metal measured at Co K-edge (scatter points) and theoretical fit (solid line) for (a) unpoled surface (b) poled Surface.

For both the unpoled and poled samples the Co-O ( $\sim 1.88 \text{ \AA}$ ) the bond lengths obtained from the best fit are found to be lower than Zn-O bond lengths which is expected since ionic radii of 4-coordinated  $\text{Co}^{2+}$  ( $0.58 \text{ \AA}$ ) is lower than 4-coordinated  $\text{Zn}^{2+}$  ( $0.6 \text{ \AA}$ ). We have also observed a decrease in the distance of Co-Zn coordination sphere as compared to Zn-Zn distance which is as expected. In this case, contrary to the result obtained from Zn K-edge data, for the unpoled samples, the coordination numbers are found to decrease gradually with Co doping for Co-O coordination shell as well as Co-Zn coordination shells while in case of the poled samples, there is no systematic variation found and the 4% Co doped sample shows lower oxygen coordination as compared to other two doping concentrations.

**Table 5.6:** Bond length, coordination number and disorder factor obtain by EXAFS fitting for unpoled and poled Co doped PVDF-ZnO films at Co K edge

Paths	Parameters	Unpoled films			Poled films		
		Co <sub>x</sub> Zn <sub>1-x</sub> O/PVDF (x = 0.01)	Co <sub>x</sub> Zn <sub>1-x</sub> O/PVDF (x = 0.04)	Co <sub>x</sub> Zn <sub>1-x</sub> O/PVDF (x = 0.07)	Co <sub>x</sub> Zn <sub>1-x</sub> O/PVDF (x = 0.01)	Co <sub>x</sub> Zn <sub>1-x</sub> O/PVDF (x = 0.04)	Co <sub>x</sub> Zn <sub>1-x</sub> O/PVDF (x = 0.07)
Co-O	R(Å)	1.87±0.01	1.88±0.01	1.87±0.03	1.88±0.02	1.89±0.01	1.88±0.02
	N	4±0.20	3.64±0.1	3.36±0.12	4.4±0.08	3.28±0.18	4±0.20
	σ <sup>2</sup>	0.0034±0.001	0.0061±0.0009	0.0041±0.001	0.0045±0.001	0.0042±0.002	0.0075±0.001
Co-Zn	R(Å)	2.66±0.02	2.68±0.02	2.65±0.03	2.75±0.03	2.68±0.02	2.69±0.03
	N	6±0.30	5.46±0.18	5.04±0.15	6.6±0.18	4.92±0.32	6±0.30
	σ <sup>2</sup>	0.0173±0.003	0.0174±0.003	0.0153±0.002	0.0211±0.003	0.0173±0.001	0.0202±0.002
Co-Zn	R(Å)	2.89±0.04	2.93±0.02	2.89±0.02	3.0±0.02	2.92±0.04	2.92±0.04
	N	6±0.30	5.46±0.18	5.04±0.15	6.6±0.18	4.92±0.32	6±0.30
	σ <sup>2</sup>	0.0215±0.002	0.0226±0.002	0.0171±0.003	0.0280±0.002	0.0204±0.002	0.0267±0.003

Thus to summarise, XPS measurements reveal negligible possibility of the presence of metallic Co phase in the samples. However, XANES measurements clearly show that though Co is primarily present as Co<sup>+2</sup>, small amount of Co metallic phase can also be present in the samples. However, EXAFS measurements both Zn and Co edges confirm that Co atoms primarily substitute Zn atoms in the ZnO lattice and there is no significant presence of Co metallic clusters in the samples. Thus the study describes successful preparation of Co-doped free standing flexible ZnO/PVDF films up to 7% Co doping.

### 5.3 (Ni,Co) co-doped PVDF-ZnO thin films:

X-ray absorption spectroscopy (XAS) measurements, comprising of both EXAFS and XANES, have been carried out on the unpoled and poled Ni/Co co-doped PVDF\_ZnO flexible polymer films to probe the local structure surrounding the Zn, Co and Ni sites.

### 5.3.1 Experimental:

The measurements have been carried out at the Energy-Scanning EXAFS beamline (BL-9) at the Indus-2 Synchrotron Source at RRCAT, Indore, India<sup>171, 172</sup> as described in Chapter-2. In the present case, XAS measurements have been performed in transmission mode. PVDF\_ZnO\_Ni/Co films of appropriate numbers have been stacked to one another to obtain a reasonable edge jump.

### 5.3.2 Results and Discussion:

The name code used for different samples is given in Table 5.7.

**Table 5.7:** Sample name code for Ni and Co codoped ZnO/PVDF.

Sr. No.	Sample	Name Code
1.	ZnO/PVDF	ZnO_PVDF
2.	$Zn_{0.92}Ni_{0.07}Co_{0.01}O/PVDF$	Ni07Co01
3.	$Zn_{0.92}Ni_{0.01}Co_{0.07}O/PVDF$	Ni01Co07
4.	$Zn_{0.95}Ni_{0.04}Co_{0.01}O/PVDF$	Ni04Co01
5.	$Zn_{0.95}Ni_{0.01}Co_{0.04}O/PVDF$	Ni01Co04
6.	$Zn_{0.98}Ni_{0.01}Co_{0.01}O/PVDF$	Ni01Co01

The normalized XANES spectra at Zn K edge are shown for all the co-doped samples in figure 5.15 along that of the Zn metal foil and pure ZnO\_PVDF film and commercial ZnO powder. The spectral features denoted by A and B are quite different in undoped and co-doped PVDF\_ZnO sample compared to ZnO commercial sample and the origin of this difference is explained in our earlier reports on similar systems and attributed to the modification of local band structure around Zn site for nanostructured sample due to size effect, structural distortion and disorder<sup>250</sup>. The absorption edge position is found to be the same for films with all doping concentrations and shifted towards higher energy compared to

the Zn foil, suggesting that Zn is present in +2 oxidation state. The XANES spectra of poled samples are also plotted along with that of unpoled samples which are similar, indicating similar coordination geometry and oxidation state of Zn in both sets of samples.

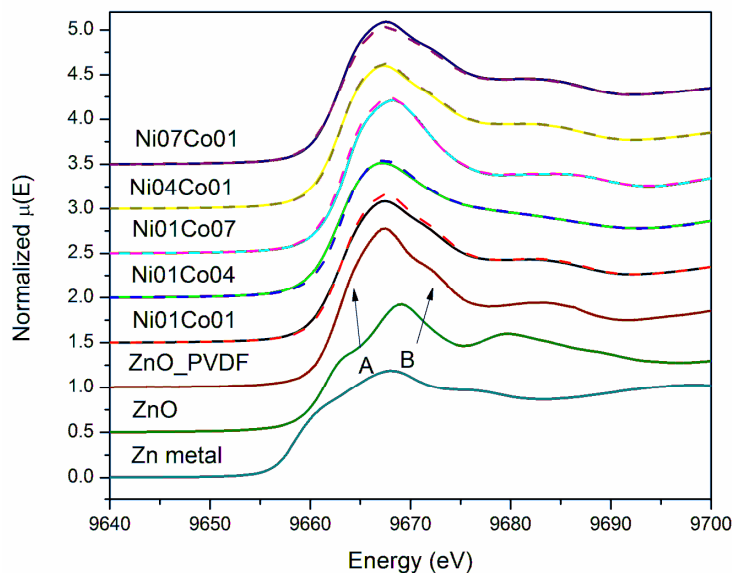


**Figure 5.15:** Normalised XANES spectra of Co/Ni codoped PVDF\_ZnO at measured Zn K-edge with along with the spectra for reference Zn metal and commercial ZnO powder sample (solid line). Dash line is for poled samples.

The normalized XANES spectra of the samples measured at Co K edge are shown in figure 5.16 along with that of CoO commercial powder sample. The transition metal oxide shows the pre-edge just before the main absorption edge (7704-7714 eV). The enlarged portion of the pre-edge region is shown in the inset of the figure 5.16. This pre edge peak is attributed as the transition of 1s electron of cobalt in the Co 3d/O2p hybridized state<sup>210</sup>. The intensity of pre-edge peak depends on the coordination geometry and disorder in the system. In perfect octahedral coordination the above transition is forbidden, it appears weakly in case of distorted octahedral coordination, while in a perfect tetrahedral coordination it is very strong. In can be seen from fig.5.16 that the pre-edge peak intensity is minimum for the

sample Ni01Co07 and maximum for Ni04Co01 sample, manifesting that for Co-rich samples, Co is having octahedral-like coordination while for Ni-rich samples Co is having tetrahedral-like coordinations. The absorption edge position is an indication of oxidation state of the absorbing atom. The absorption edge of the Co-rich Ni01Co07 sample, is at the same position of CoO indicating +2 oxidation state of Co, however for all other samples the edge position is shifted towards higher oxidation state. However, the spectral features of the XANES spectra of the doped samples above Co K absorption edge are quite different from that of CoO indicating that Co is not present as CoO but substituting the Zn atoms in the ZnO matrix. The pre-edge intensity and absorption edge positions of the poled samples match with that of the respective unpoled samples.

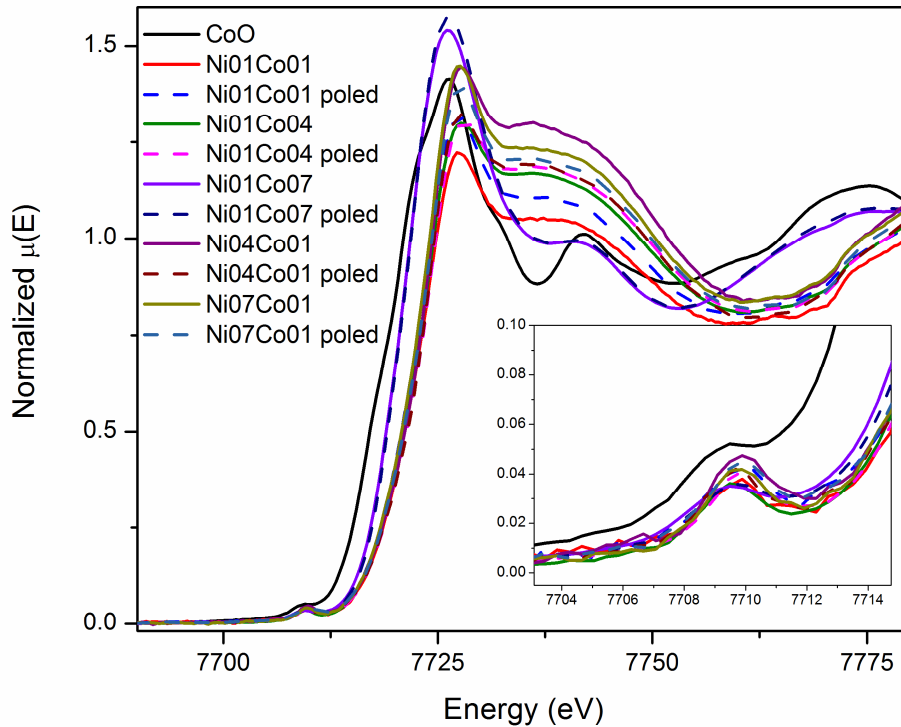


**Figure 5.16:** Normalised XANES spectra of Ni/Co codoped PVDF\_ZnO measured at Co K-edge along with the reference CoO sample (solid line). Dash line is for poled samples. Inset shows the extended portion of pre edge.

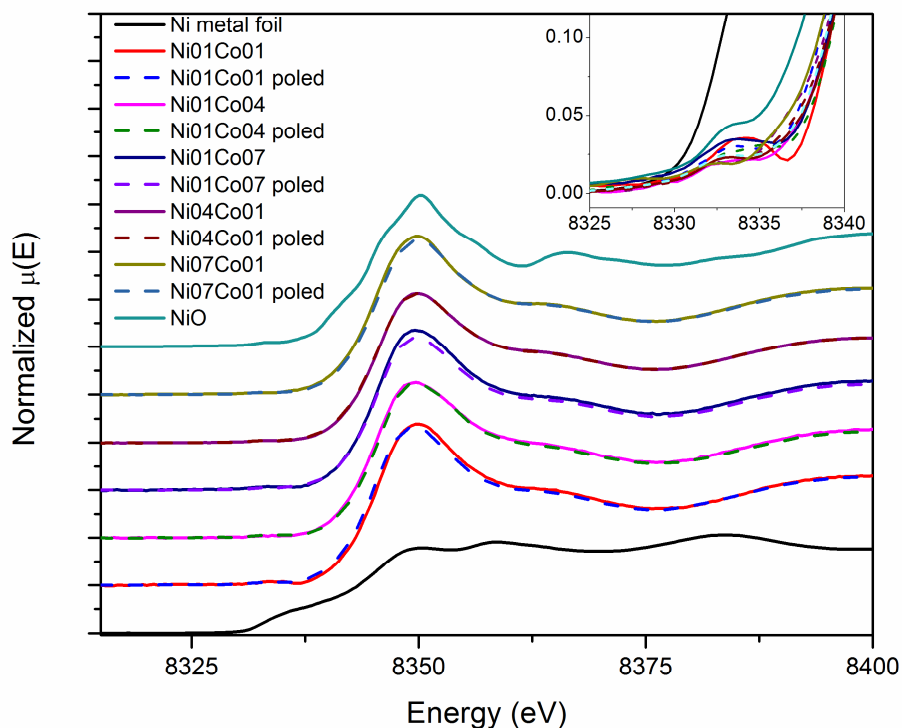


**Figure 5.17:** Normalised XANES spectra of Ni/Co codoped PVDF\_ZnO measured at Ni K-edge along with the reference NiO sample (solid line). Dash line is for poled samples. Inset shows the extended portion of pre edge.

The normalized XANES spectra at Ni K edge is shown in figure 5.17 alongwith that of commercial NiO powder and Ni metal foil. The absorption edge positions of the samples coincide with that of NiO, confirming +2 oxidation state of Ni ions in all the samples. Similar to Co K edge, Ni K edge XANES spectra also show the presence of pre-edge peaks related to transition from 1s to Ni3d/O2p state. The pre-edge intensity is maximum for the Co-rich Ni01Co07 sample and minimum for the Ni-rich Ni07Co01 samples, manifesting tetrahedral – like coordination around Ni atoms in the former and octahedral-like coordination in the later sample. This is opposite to the case observed in case of Co K-edge data discussed above.

Thus combining the trends observed in the XANES data of both Co and Ni K-edges, it can be concluded that for Co-rich samples, Co atoms are in octahedral coordination and Ni atoms are having tetrahedral oxygen coordination, while for Ni-rich samples Ni atoms are in octahedral coordination while Co atoms are having tetrahedral coordination. This is expected since at lower doping concentrations the TM ions are supposed to replace the Zn atoms efficiently in the tetrahedral ZnO lattice while at higher doping concentration there is a possibility of having another phase in the samples related to the TM ions. It can be further seen from fig.5.17 that, the absorption edge positions and pre-edge peaks of poled and unpoled samples match with each other.

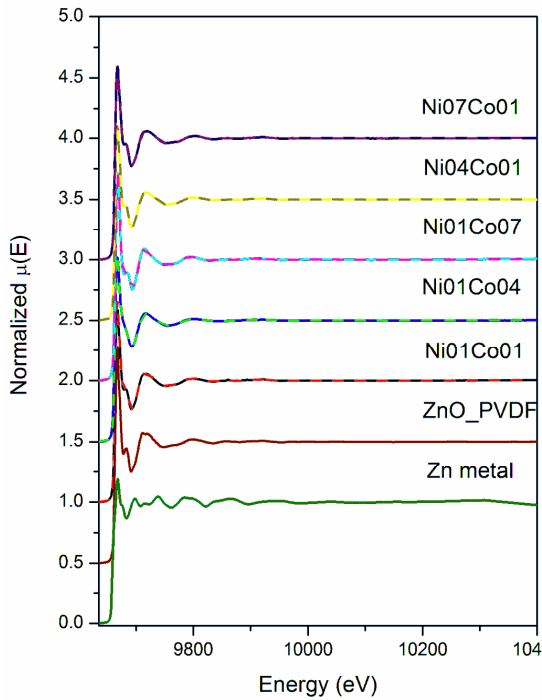


**Figure 5.18:** Normalised EXAFS spectra of Co/Ni codoped PVDF\_ZnO at Zn K-edge (solid line). Dash line is for poled samples.

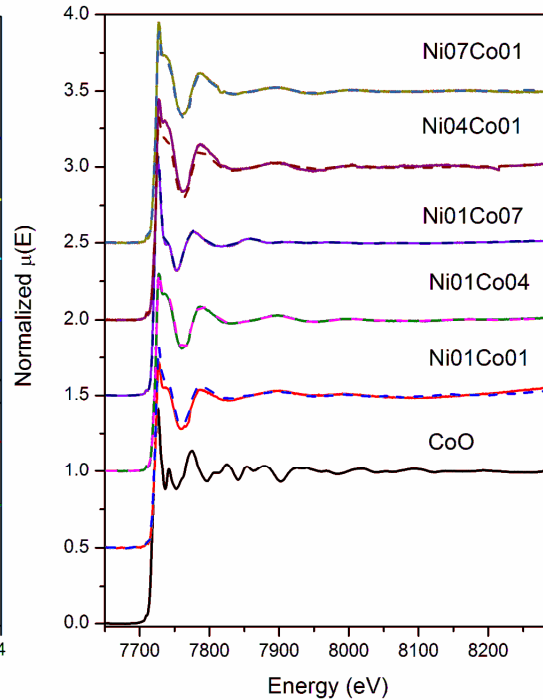


**Figure 5.19:** Normalised EXAFS spectra of Co/Ni codoped PVDF\_ZnO at Co K-edge (solid line). Dash line is for poled samples.

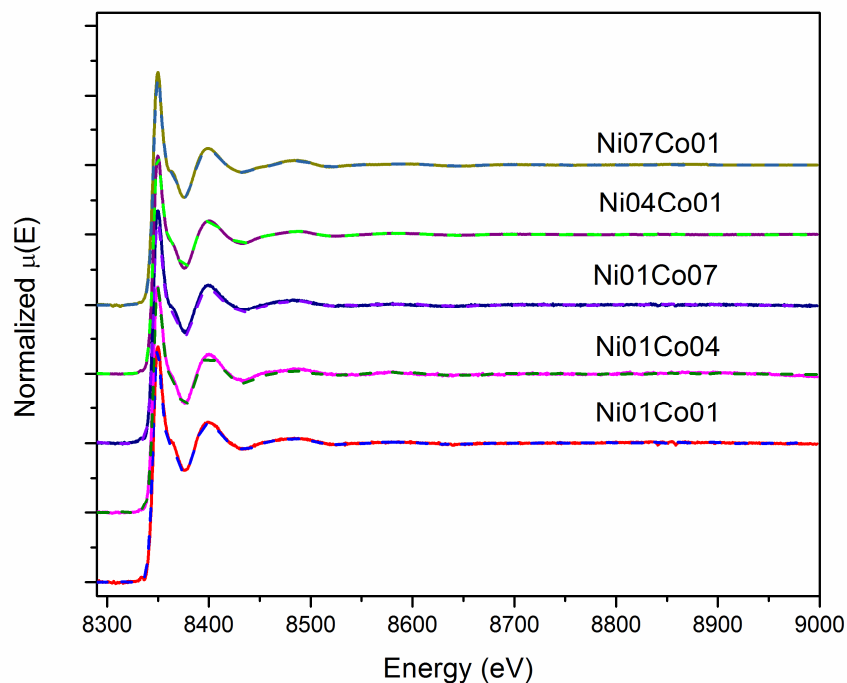


**Figure 5.20:** Normalised EXAFS spectra of Co/Ni codoped PVDF\_ZnO at Ni K-edge (solid line). Dash line is for poled samples.

Figs. 5.18-5.20 show the normalised EXAFS spectra of Ni/Co co-doped PVDF ZnO films measured at Zn, Co and Ni K-edges respectively for unpoled and poled samples. In order to take care of the oscillations in the absorption spectra  $\mu(E)$  has been converted to absorption function  $\chi(E)$  and detailed analysis procedure is described in chapter 2.  $\chi(R)$  versus  $R$  plots are generated at Zn K edge using fourier transform range  $k = 3.0-11.0 \text{ \AA}^{-1}$  from the  $\mu(E)$  versus  $E$  spectra following the methodology described in chapter-2 are shown in fig. 5.21 for poled & unpoled films respectively. The structural parameters (atomic coordination and lattice parameters) of ZnO are used for simulation of theoretical EXAFS spectra of the samples have been obtained from ref.<sup>33</sup> and the best fit  $\chi(R)$  versus  $R$  plots (fitting range  $R = 1.0-3.5 \text{ \AA}$ ) of the samples have been shown in fig.5.21 along with the experimental data. During the fitting, bond distances, co-ordination numbers (including

scattering amplitudes) and disorder (Debye-Waller) factors ( $\sigma^2$ ), which give the mean square fluctuations in the distances, have been used as fitting parameters. The goodness of fit has been determined by the value of the  $R_{factor}$  defined in Chapter-2.

**Table 5.8:** Bond length, coordination number and disorder factor obtain by EXAFS fitting for unpoled Co/Ni codoped PVDF-ZnO at Zn K edge.

Paths	Parameters	Ni01Co01	Ni01Co04	Ni01Co07	Ni04Co01	Ni07Co01
Zn-O	R(Å)	2.00±0.01	1.98±0.01	2.02±0.01	1.99±0.01	1.99±0.01
	N	4	4	4	4	4
	$\sigma^2$	0.011± 0.002	0.0116± 0.001	0.0087± 0.001	0.0109± 0.001	0.0110± 0.001
Zn-Zn	R(Å)	3.10±0.01	3.11±0.02	3.14±0.02	3.10±0.01	3.08±0.01
	N	6	6	6	6	6
	$\sigma^2$	0.0145± 0.002	0.0223± 0.001	0.0135± 0.002	0.0156± 0.001	0.0133± 0.002

**Table 5.9:** Bond length, coordination number and disorder factor obtain by EXAFS fitting for poled Co/Ni codoped PVDF-ZnO at Zn K edge.

Paths	Parameters	Ni01Co01	Ni01Co04	Ni01Co07	Ni04Co01	Ni07Co01
Zn-O	R(Å)	2.00±0.01	1.98±0.01	2.02±0.01	1.99±0.01	1.99±0.01
	N	4	4	4	4	4
	$\sigma^2$	0.0114± 0.001	0.0117± 0.002	0.0089± 0.001	0.0108± 0.002	0.0112± 0.001
Zn-Zn	R(Å)	3.10±0.01	3.12±0.01	3.14±0.02	3.10±0.02	3.09±0.01
	N	6	6	6	6	6
	$\sigma^2$	0.0149± 0.001	0.0244± 0.002	0.0147± 0.001	0.0163± 0.001	0.0142± 0.001

The fitting results are tabulated in Table 5.8 for unpoled samples and Table 5.9 for poled samples at Zn K-edge. The first peak at 1.5 Å in fourier transform spectra (fig 5.21) has contributions of four oxygen atoms shells at 1.96 Å and 1.97Å with 1 and 3 oxygens and the second peak at ~2.75 Å has contributions from two Zn-Zn coordination shells at distances of 3.12 Å and 3.19 Å with six coordination each. However, for Ni/Co co-doped ZnO\_PVDF

samples, the first peak is fitted with single oxygen coordination shell with four oxygen atoms with an average Zn-O bond distance. The second coordination shell Zn-Zn also was fitted with an average Zn-Zn distance, however the Zn coordination has taken to be 6, significantly less than its bulk value of 12. This is possibly due to the fact that for nanocrystals, the Zn-Zn shell generally has a lower coordination than its bulk value which decreases with decrease in particle size<sup>263</sup>. It can be seen from Tables 5.8 & 5.9 that the best fit values of the parameters obtained for the poled and unpoled samples are similar. It can also be seen from the above tables that the Debye-Waller factor ( $\sigma^2$ ), which gives the mean square fluctuations in the distances, in both poled and unpoled cases, is minimum for the Co-rich sample Ni01Co07, in which Co is in octahedral coordination and Ni is in tetrahedral coordination.

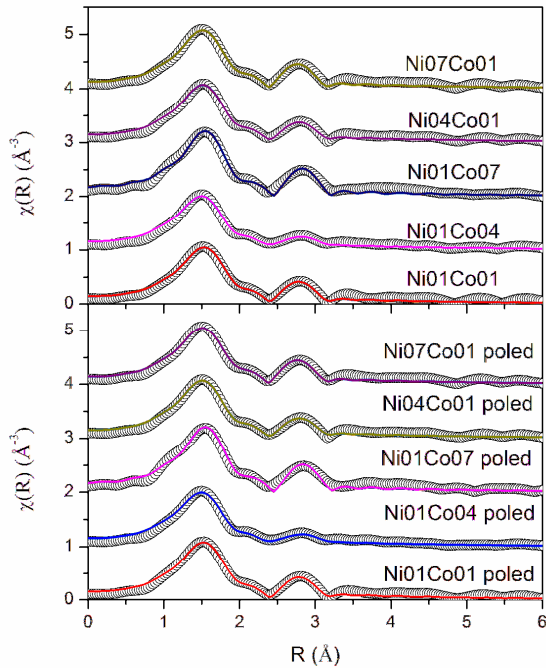


**Figure 5.21:** Fourier transformed EXAFS spectra of Co/Ni codoped PVDF\_ZnO at Zn K-edge (Scatter points) and theoretical fit (Solid line).

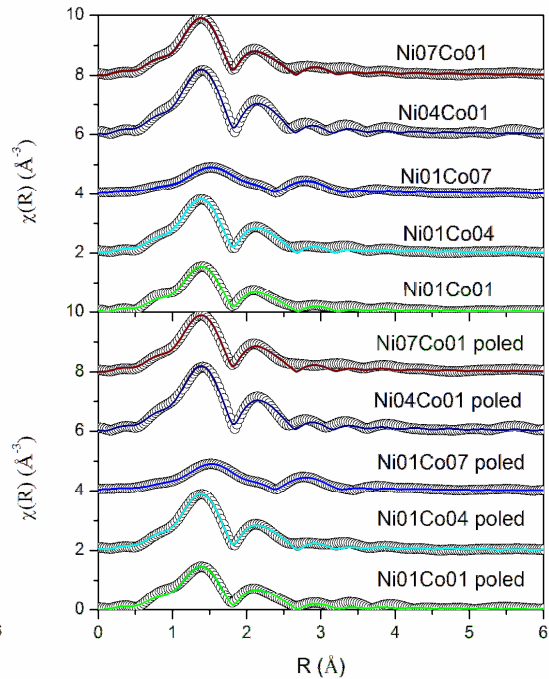


**Figure 5.22:** Fourier transformed EXAFS spectra of Co/Ni codoped PVDF\_ZnO at Co K-edge (Scatter points) and theoretical fit (Solid line).

**Table 5.10:** Bond length, coordination number and disorder factor obtain by EXAFS fitting for unpoled Co/Ni codoped PVDF-ZnO at Co K edge.

Paths	Parameters	Ni01Co01	Ni01Co04	Ni01Co07	Ni04Co01	Ni07Co01
Co-O	R(Å)	1.88±0.01	1.87±0.02	2.03±0.02	1.88±0.01	1.87±0.01
	N	4.28±0.16	5.35±0.13	4.28±0.16	6.42±0.18	5.35±0.15
	$\sigma^2$	0.0043± 0.0007	0.005± 0.001	0.0083± 0.001	0.0047± 0.0009	0.0042± 0.001
Co-O	R(Å)			2.13±0.02		
	N			1.07±0.04		
	$\sigma^2$			0.0014± 0.0006		
Co-Zn	R(Å)	2.73±0.01	2.71±0.01		2.71±0.01	2.71±0.01
	N	6.42±0.24	6.42±0.15		5.35±0.15	6.42±0.18
	$\sigma^2$	0.020± 0.0009	0.0184± 0.001		0.0128± 0.0008	0.0192± 0.0007
Co-Zn	R(Å)	3.49±0.01	3.45±0.02	3.15±0.01	3.41±0.02	3.49±0.01
	N	6.42±0.24	6.42±0.15	6.42±0.24	6.42±0.18	6.42±0.18
	$\sigma^2$	0.0309± 0.001	0.0309± 0.002	0.0196± 0.001	0.0207± 0.001	0.0280± 0.002

**Table 5.11:** Bond length, coordination number and disorder factor obtain by EXAFS fitting for poled Co/Ni codoped PVDF-ZnO at Co K edge.

Paths	Parameters	Ni01Co01	Ni01Co04	Ni01Co07	Ni04Co01	Ni07Co01
Co-O	R(Å)	1.88±0.01	1.87±0.01	2.03±0.01	1.88±0.01	1.88±0.01
	N	4.28±0.12	5.35±0.10	4.28±0.16	6.42±0.36	5.35±0.10
	$\sigma^2$	0.0047± 0.001	0.0046± 0.001	0.0080± 0.001	0.0048± 0.001	0.0043± 0.001
Co-O	R(Å)			2.20±0.02		
	N			1.07±0.04		
	$\sigma^2$			0.0019± 0.001		
Co-Zn	R(Å)	2.72±0.01	2.72±0.01		2.72±0.01	2.71±0.01
	N	6.42±0.18	6.42±0.12		5.35±0.30	6.42±0.12
	$\sigma^2$	0.0204± 0.001	0.0187± 0.0009		0.0146± 0.002	0.0188± 0.001
Co-Zn	R(Å)	3.51±0.01	3.48±0.01	3.15±0.01	3.42±0.01	3.47±0.01
	N	6.42±0.18	6.42±0.12	6.42±0.24	6.42±0.36	6.42±0.12
	$\sigma^2$	0.0325± 0.001	0.0328± 0.001	0.0192± 0.0007	0.0208± 0.001	0.0325± 0.001

The  $\chi(R)$  vs.  $R$  plots obtained after fourier transformation of  $k$  space spectra at Co K-edge are shown in figure 5.22 for both poled and unpoled samples. It can be seen from figures 5.21&5.22 that except from the sample Ni01Co07, the Zn K-edge and Co K-edge plots of the samples are different, where in the Co K-edge plots the peak at 2.7 Å, which is characteristic of the Zn-Zn (or dopant) coordination of the wurtzite ZnO structure is absent and instead there is a peak at 2.2 Å. We have explored the possibility of the presence of CoO phase in the samples, however it has been seen that this peak does not also arise from CoO phase also. The best fit results are of the Co K-edge data are shown in Tables 5.10 &5.11 for the unpoled and poled samples respectively. It can be seen that for all the samples except Ni01Co07, the first peak at 1.5 Å is fitted using oxygen coordination shell at ~1.88 Å and the second peak at 2.2 Å is fitted using Co-Zn path at ~2.73 Å. This Co-O and Co-Zn bond distances are much lower than Zn-O and Zn-Zn distances and hence might be due to Co interstitials or significant distortion of the ZnO lattice.

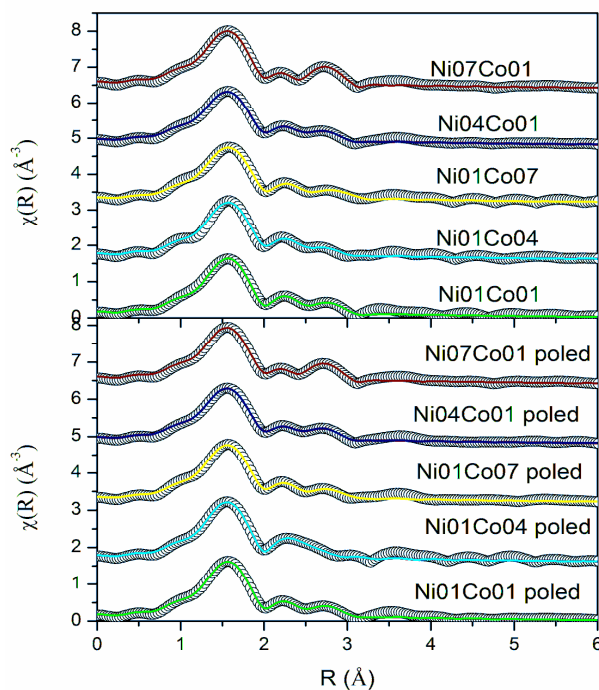


**Figure 5.23:** Fourier transformed EXAFS spectra of Co/Ni codoped PVDF\_ZnO at Ni K-edge (Scatter points) and theoretical fit (Solid line).

The presence of Co interstitial can be ruled out since we have not seen any Co metallic phase in the samples from XANES measurements. On the other hand, XANES measurements reveal that oxidation states of Co in these samples are higher than +2 and they show strong pre-edge peaks manifesting tetrahedral coordination. These all suggest Co substitution in wurtzite ZnO lattice with significant distortion of the lattice or presence of a different structure with higher oxidation state of Co and tetrahedral oxygen coordination, the absence of any extra phase in GIXRD data of the samples, though rules out the second option. However, in case of the sample Ni01Co07, the first peak is slightly shifted to higher bond distance compared to other doping concentration and fitted with two different oxygen coordination shells at 2.03 Å and 2.13 Å. The second peak appeared at 2.7 Å for Ni01Co07 is fitted with Co-Zn coordination shell at ~3.15 Å. The obtained Co-Zn bond length in this sample is similar to Zn-Zn bond length of ZnO. Thus we can say that for this sample there is proper substitution of Zn atoms by Co atoms in ZnO lattice with least distortion and XANES measurement reveals that Co is present in Co<sup>+2</sup> state in this sample.

**Table 5.12:** Bond length, coordination number and disorder factor obtain by EXAFS fitting for unpoled Co/Ni codoped PVDF-ZnO at Ni K edge.

Paths	Parameters	Ni01Co01	Ni01Co04	Ni01Co07	Ni04Co01	Ni07Co01
Ni-O	R(Å)	2.05±0.01	2.05±0.01	2.05±0.01	2.04±0.01	2.04±0.01
	N	5.76±0.24	5.76±0.18	5.76±0.24	5.76±0.12	5.76±0.30
	$\sigma^2$	0.0067± 0.0005	0.0070± 0.001	0.0076± 0.0005	0.0077± 0.002	0.0068± 0.001
Ni-Ni	R(Å)	2.87±0.01	2.86±0.01	2.91±0.02	2.86±0.01	2.88±0.01
	N	5.76±0.24	5.76±0.18	5.76±0.24	5.76±0.12	5.76±0.30
	$\sigma^2$	0.0201± 0.001	0.023± 0.002	0.0220± 0.001	0.0234± 0.0008	0.0249± 0.001
Ni-Zn	R(Å)	3.09±0.02	3.07±0.01	3.14±0.01	3.07±0.01	3.08±0.01
	N	5.76±0.24	5.76±0.18	5.76±0.24	5.76±0.12	5.76±0.30
	$\sigma^2$	0.0172± 0.001	0.0225± 0.001	0.0191± 0.001	0.0202± 0.001	0.0148± 0.001

**Table 5.13:** Bond length, coordination number and disorder factor obtain by EXAFS fitting for poled Co/Ni codoped PVDF-ZnO at Ni K edge.

Paths	Parameters	Ni01Co01	Ni01Co04	Ni01Co07	Ni04Co01	Ni07Co01
Ni-O	R(Å)	2.04±0.01	2.04±0.01	2.04±0.01	2.04±0.01	2.04±0.01
	N	5.76±0.15	5.76±0.21	5.76±0.24	5.76±0.18	5.76±0.15
	$\sigma^2$	0.0069± 0.0004	0.0067± 0.0005	0.0075± 0.0005	0.0078± 0.0006	0.0073± 0.0004
Ni-Ni	R(Å)	2.88±0.01	2.89±0.02	2.87±0.01	2.87±0.02	2.88±0.01
	N	5.76±0.15	5.76±0.21	5.76±0.24	5.76±0.18	5.76±0.15
	$\sigma^2$	0.0234± 0.001	0.0197± 0.001	0.0244± 0.001	0.0256± 0.001	0.0266± 0.001
Ni-Zn	R(Å)	3.09±0.01	3.10±0.01	3.10±0.01	3.07±0.02	3.07±0.02
	N	5.76±0.15	5.76±0.21	5.76±0.24	5.76±0.18	5.76±0.15
	$\sigma^2$	0.0197± 0.001	0.0259± 0.002	0.0210± 0.001	0.0207± 0.001	0.0166± 0.002

The Ni K-edge FT-EXAFS spectra in  $R$  space is shown in figure 5.23 alongwith the fitted results for poled and unpoled samples and the best fit results of the parameters have been shown in Tables 5.12 & 5.13 for the unpoled and ppoled samples. Comparing figures 5.21 and 5.23 it can be seen that the FT-EXAFS spectra of the samples at Zn K edge and Ni K-edge are almost similar, except for the presence of a well-resolved reasonably significant peak at  $\sim 2.25 \text{ \AA}$  for Ni K-edge data in most of the samples which is not present in Zn K-edge data. The first peak at  $1.5 \text{ \AA}$  is fitted with the contributions of six oxygen atoms at the bond distance of  $\sim 2.05 \text{ \AA}$ . Though this Ni-O distance is close to the Zn-O bond lengths, however, the values are closer to Ni-O bond lengths in NiO, moreover the best fit can be obtained with oxygen coordination of 6 instead of 4 (which is a characteristic of ZnO structure), manifesting the presence of NiO phase also in the samples. The next peak at  $\sim 2.25 \text{ \AA}$  is fitted using Ni-Zn/Ni coordination shell at  $\sim 2.87 \text{ \AA}$  with six coordination number. The third coordination peak at  $\sim 2.7 \text{ \AA}$  is fitted using Ni-Zn coordination shell with six coordination at the distance of  $\sim 3.09 \text{ \AA}$ . These Ni-Zn bond distances confirm the presence Ni substituting Zn site as well alongwith that of a separate NiO phase in the samples.

Thus Ni atoms apart from substituting Zn atoms in ZnO lattice in a tetrahedral coordination are also forming a separate NiO phase having octahedral oxygen coordination. Samples having lower Ni concentration will have lesser probability of having NiO phase, while Ni-rich samples will have higher fraction of NiO phase. This is consistent with the XANES results also discussed above where Ni-rich samples like Ni07Co01 have lower pre-edge peak compared to Co-rich samples like Ni01Co07 which have higher intensity of pre-edge peak.

#### **5.4 Mn doped ZnO/PVDF:**

Finally, we present local structural studies on Mn-doped nanocrystalline ZnO/PVDF composite free standing flexible films (Mn-ZnO/PVDF) by XANES and EXAFS measurements.

##### **5.4.1 Experimental:**

Protocol for obtaining the requisite sol for the deposition of Mn doped nano-ZnO/PVDF films is described in Chapter-2. In brief, appropriate amount of Zn-acetate was used to obtain a 10 wt% (0.275 M) sol with 4 ml dimethyl formamide (DMF). The above sol was refluxed for 1 h with constant stirring at 30 °C for complete dissolution of the solute. Three such stock solutions were obtained and three different amounts of Mn-acetate were added to these solutions to form  $Zn_{1-x}Mn_xO$  ( $x = 0, 0.03, 0.05, 0.07$ ). These mixtures were refluxed for 3 h with constant stirring at 150 °C for complete dissolution of the solute with resultant formation of intermediate products of  $Zn(OH)_2$  and  $Mn(OH)_2$ . Appropriate amount of dimethyl amine is used acting as a reducing agent to the above sol while keeping the heating and stirring for another 30 min. A fixed amount of PVDF (15 wt%) was then added to the above sols which was cooled down to 60 °C keeping stirring constant for another 2 h. A semi-gel sol with a brownish tinge was obtained. The above sol was spin-casted uniformly on

glass substrates at room temperature at a low spin (60 rpm) for depositing the Mn-doped nano-ZnO/PVDF composite films. A microwave oven was used to heat the as-coated films at 100 W for 3 min. The films so obtained could be easily peeled out from the glass substrate. The films deposited as above were poled in vacuum ( $\sim 10^{-6}$  Torr) at a field of 5 MV/m for 2 h. The poling creates H terminated surface at one side of the films, while F-terminated surface at the other end as explained in detail in Chapter-2. The poling unit<sup>250</sup>, used for this purpose has also been described in Chapter-2.

XANES and EXAFS measurements have been carried out at the Energy-Scanning EXAFS beamline (BL-9) in transmission mode at the Indus-2 Synchrotron Source as described in Chapter-2. Mn-ZnO/PVDF (different Mn doping:  $x = 0.01, 0.03$  and  $0.05$ ) films of appropriate numbers have been stacked on one another to obtain a reasonable edge jump at Zn K edge. The Mn K edge measurements have been carried out in fluorescence mode.

#### **5.4.2 Results and discussion:**

Normalized XANES spectra of ZnO/PVDF and Mn-ZnO/PVDF (different Mn doping:  $x = 0.01, 0.03$  and  $0.05$ ) films, (both poled and unpoled) measured at Zn K edge and Mn K edge are shown in Fig.5.24a and Fig.5.24b respectively. XANES spectrum of a bulk ZnO sample (commercial powder, Aldrich make, purity 99.99%) is also plotted along with that of the thin film samples for comparison in Fig.5.24a. The Zn K edge positions of the samples agree well with that of the ZnO bulk sample depicting Zn to be present only in Zn<sup>2+</sup> state in the samples. However, it may be noted that the features denoted by A and B in Fig. 5.24a present in case of the ZnO bulk sample are absent in case of PVDF-ZnO thin film samples which may be due to slightly different band structure in nano-ZnO. Jeong et al.<sup>254</sup> have observed such dissimilarity in XANES spectra of nanostructured and bulk ZnO and explained that the band structure is different in nanostructured samples as compared to that in bulk due to size effect, structural distortion and disorder. However, as can be seen from Fig.

5.24a, there is no significant difference in XANES spectra of the poled and unpoled samples which might be due to the fact that XANES is not a surface sensitive technique and Zn K-edge measurements have been done in transmission mode.

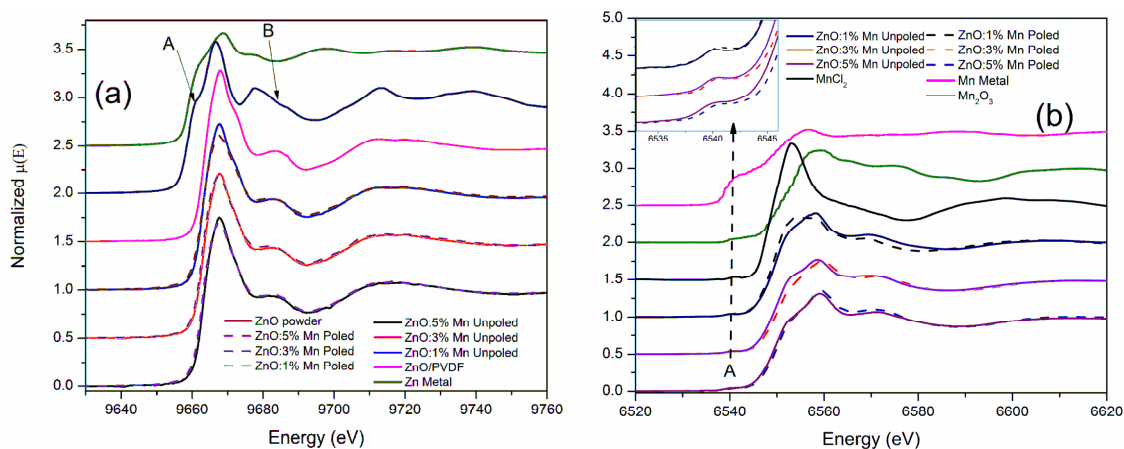


**Figure 5.24:** (a) XANES spectra of unpoled and poled  $Mn_xZn_{1-x}O/PVDF$  with  $x = 0.01, 0.03$  and  $0.05$  Mn doping measured at Zn K-edge along with spectra for reference Zn metal and ZnO/ PVDF film; (b) Normalised XANES spectra for unpoled and poled  $Mn_xZn_{1-x}O/PVDF$  with  $x=0.01, 0.03$  and  $0.05$  Mn doping measured at Mn K-edge along with the reference Mn metal,  $MnCl_2$  and  $Mn_2O_3$  samples. (Inset of (b) shows extended pre-edge part).

The XANES spectra for normal PVDF/ZnO films measured at Mn K edge, along with that of three standards viz., Mn metal foil,  $MnCl_2$  and  $Mn_2O_3$  with 0, +2 and +3 oxidation state respectively, are shown in Fig.5.24b. The Mn K edge XANES spectra (Fig.5.24b) have resemblance with ZnO spectra measured at Zn K edge (Fig.5.24a). The pre-edge features in Fig.5.24b (marked as A) below the main edge, which are characteristics of tetrahedral coordination<sup>190</sup> like ZnO, are due to transitions from Mn 1s into unoccupied O2p-Mn 3d (or Mn3d/4p) hybridized states, which have p components projected at the Mn site and as observed in many transition-metal oxides. The main edge at the Mn K-edge corresponds to the high-energy Mn4p states. It is found that maxima of the first derivative of  $\mu$  vs. E spectra, which give the edge energies quantitatively; in PVDF/ZnO films are slightly higher than

MnCl<sub>2</sub> but much lower than Mn<sub>2</sub>O<sub>3</sub> suggesting that Mn is present in 2<sup>+</sup> oxidation state in all the thin film samples.

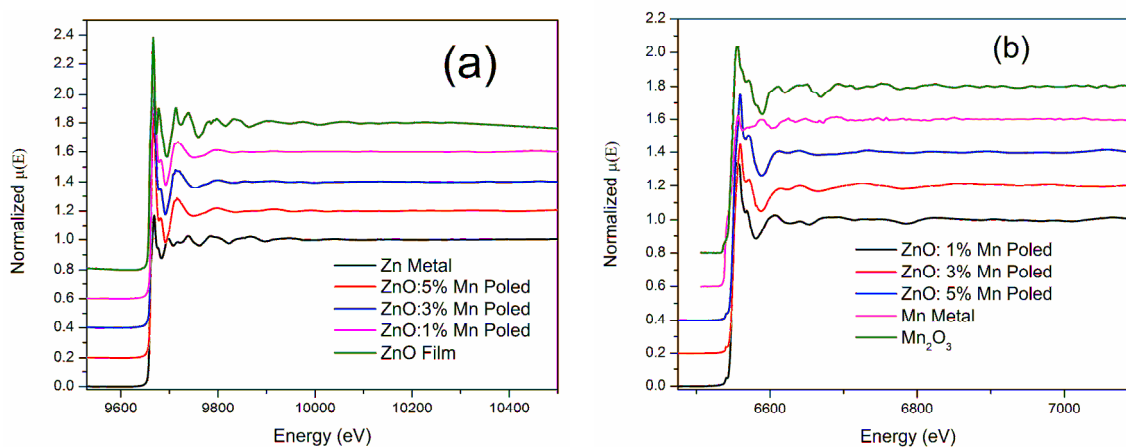


**Figure 5.25:** (a) Normalised EXAFS spectra of poled Mn<sub>x</sub>Zn<sub>1-x</sub>O/PVDF samples with x = 0.01, 0.03 and 0.05 Mn doping measured at Zn K-edge along with the spectra for poled ZnO/PVDF film and reference Zn metal. (b) Normalised EXAFS spectra for poled Mn<sub>x</sub>Zn<sub>1-x</sub>O/PVDF samples with x = 0.01, 0.03 and 0.05 Mn doping measured at Mn K-edge along with the reference Mn metal and Mn<sub>2</sub>O<sub>3</sub> sample.

The normalised EXAFS spectra of Mn doped (Mn doping concentration; x = 0.01, 0.03 and 0.05) PVDF-ZnO films measured at Zn K-edge and Mn K-edge (as shown in Fig. 5.24a and Fig. 5.24b respectively) have been further analyzed following the methodology presented in Chapter-2. The  $\chi(R)$  versus  $R$  plots generated (Fourier transform range k = 3.0-10.0 Å<sup>-1</sup>) for all the samples (unpoled and poled) from the  $\mu(E)$  versus  $E$  spectra following the methodology described above are shown for Mn doped (Mn doping concentration; x = 0.01, 0.03 and 0.05) PVDF-ZnO films measured at Zn K edge and Mn K edges in Fig.5.26I-IV. The structural parameters (atomic coordination and lattice parameters) of ZnO used for simulation of theoretical EXAFS spectra of the samples have been obtained from Ref. <sup>33</sup> and the best fit  $\chi(R)$  versus  $R$  plots (fitting range  $R = 1.0-3.5$  Å) of the Mn-ZnO/PVDF (Mn doping concentration; x = 0.01, 0.03 and 0.05) unpoled PVDF-ZnO films samples have been shown in Fig. 5.26(I) along with the experimental data for the measurements carried out at Zn K edge. The bond distances, co-ordination numbers (including scattering amplitudes) and

disorder (Debye-Waller) factors ( $\sigma^2$ ), which give the mean square fluctuations in the distances, have been used as fitting parameters and the best fit results are summarized in Table 5.14.

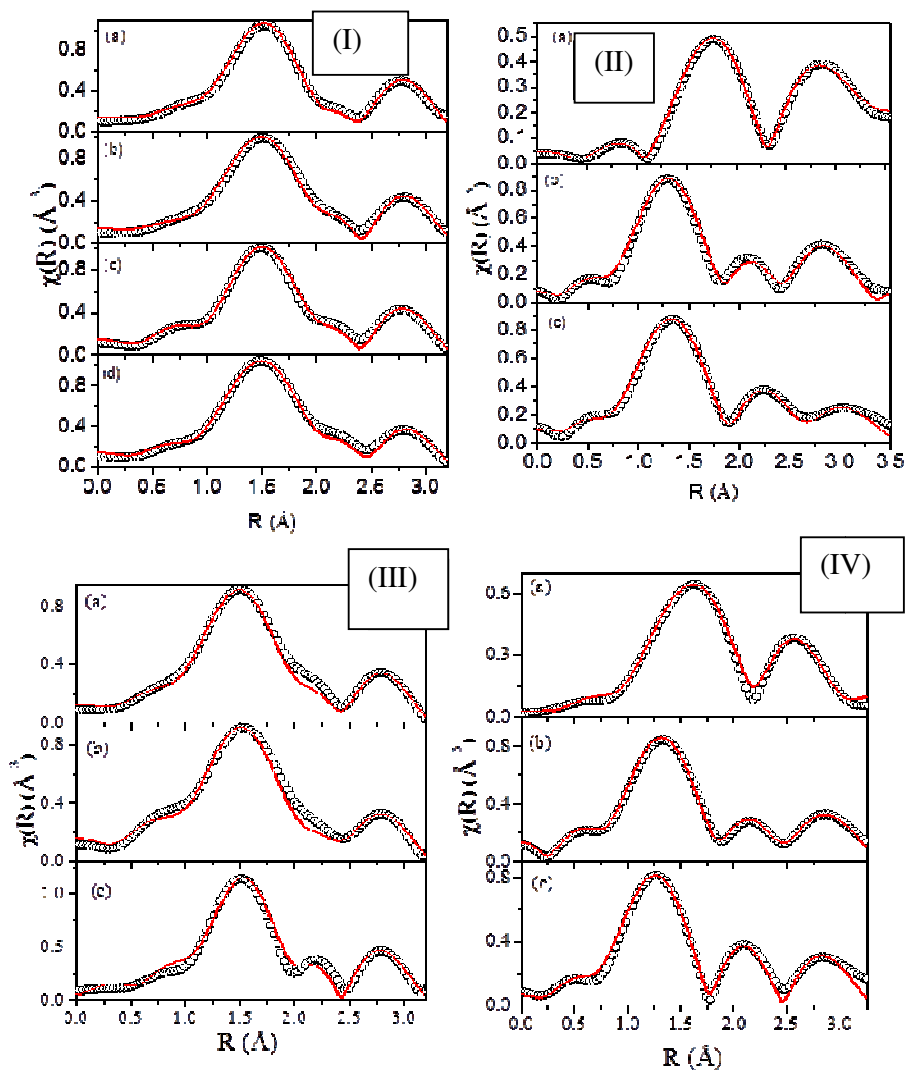


**Figure 5.26:** (I) Fourier transformed EXAFS spectra of unpoled Mn doped ZnO/PVDF samples measured at Zn K-edge (Scatter points) and theoretical fit (Solid line): (a)  $x = 0$  Mn, (b)  $x = 0.01$  Mn; (c)  $x = 0.03$  Mn and (d)  $x = 0.05$  Mn. (II) Fourier transformed EXAFS spectra of unpoled Mn ZnO/PVDF samples measured at Mn K-edge (Scatter points) and theoretical fit (Solid line): (a)  $x = 0.01$  Mn, (b)  $x = 0.03$  Mn and (c)  $x = 0.05$  Mn. (III) Fourier transformed EXAFS spectra of poled Mn ZnO/PVDF measured at Zn K-edge (Scatter points) and theoretical fit (Solid line): (a)  $x = 0.01$  Mn, (b)  $x = 0.03$  Mn and (c)  $x = 0.05$  Mn. (IV) Fourier transformed EXAFS spectra of poled Mn ZnO/PVDF measured at Mn K-edge (Scatter points) and theoretical fit (Solid line): (a)  $x = 0.01$  Mn, (b)  $x = 0.03$  Mn and (c)  $x = 0.05$  Mn.

From Table 5.14 it can be seen that the bond lengths of Zn-O shells are comparable to the theoretical values though the bond length of the Zn-Zn shells are less than the bulk values. Similar difference in the bond lengths between Zn-O bulk and nanostructures have also been reported by other workers <sup>254</sup>. However, no significant change in the bonds length values have been observed due to Mn doping because of similar ionic radii of Zn and Mn. The coordination numbers for both the oxygen and zinc shells are also found to be less compared to their bulk values which is due to nanocrystalline nature of the samples as has been observed by other workers also <sup>191, 254</sup>. It can also be seen from the fact that the Debye Waller factor ( $\sigma^2$ ) is significantly high for Zn-Zn shells as expected in case of nanocrystalline samples <sup>264</sup> and it increases further on Mn doping due to enhancement of disorder in the lattice.

**Table 5.14:** Bond length, coordination number and disorder factor obtained by EXAFS fitting for unpoled samples at Zn K edge.

Paths	Parameters	ZnO	ZnO:1%Mn	ZnO:3%Mn	ZnO:5%Mn
Zn-O	R(Å)	2.00±0.01	2.00±0.01	2.00±0.01	1.99±0.01
	N	2.7±0.24	2.79±0.63	2.79±0.35	2.91±0.18
	$\sigma^2$	0.0063±0.001	0.0065±0.001	0.0063±0.001	0.0062±0.001
Zn-O	R(Å)	2.08±0.02	2.10±0.01	2.11±0.01	2.10±0.01
	N	1.12±0.08	1.12±0.33	1.2±0.30	1.2±0.10
	$\sigma^2$	0.0045±0.0009	0.0093±0.0007	0.009±0.001	0.0093±0.002
Zn-Zn	R(Å)	2.88±0.02	2.84±0.01	2.85±0.02	2.83±0.01
	N	5.1±0.48	5.1±0.42	5.1±0.60	5.1±0.33
	$\sigma^2$	0.0247±0.002	0.0272±0.003	0.0287±0.003	0.0296±0.002
Zn-Zn	R(Å)	3.08±0.01	3.08±0.01	3.08±0.01	3.08±0.01
	N	4.98±0.48	5.1±0.42	4.98±0.60	5.34±0.33
	$\sigma^2$	0.0119±0.003	0.0135±0.002	0.0139±0.002	0.0171±0.001

**Table 5.15:** Bond length, coordination number and disorder factor obtained by EXAFS fitting for unpoled samples at Mn K edge.

Paths	Parameters	ZnO:1%Mn	ZnO:3%Mn	ZnO:5%Mn
Mn-O	R(Å)	2.21±0.01	1.84±0.02	1.87±0.01
	N	2.88±0.24	3.93±0.36	4.0±0.32
	$\sigma^2$	0.0042±0.001	0.0021±0.001	0.002±0.001
Mn-Mn/Zn	R(Å)	2.93±0.01	2.84±0.01	2.97±0.02
	N	6.0±0.36	6.0±0.54	6.0±0.48
	$\sigma^2$	0.0487±0.003	0.0175±0.001	0.0162±0.003
Mn-Mn/Zn	R(Å)	3.48±0.01	3.10±0.01	3.22±0.01
	N	6.0±0.36	6.0±0.54	6.0±0.48
	$\sigma^2$	0.0232±0.002	0.0118±0.003	0.0148±0.003

$\chi(R)$  versus  $R$  plots of unpoled Mn-ZnO/PVDF (Mn doping concentration;  $x = 0.01$ , 0.03 and 0.05) and PVDF-ZnO films measured at Mn K-edge along with the best theoretically fit plots are shown in Fig.5.26(II) and the values of the best fit parameters are shown in Table 5.15. The theoretical fitting has been carried out assuming Mn substitution in wurtzite ZnO structure. It can be seen from Fig.5.26(II) that the spectrum of the Mn ( $x = 0.01$ ) doped sample is significantly different from that of the  $x = 0.03$  and 0.05 doped samples. Best fit results also show that Mn-O bond length in this sample is 2.21 Å which is significantly higher than Zn-O bond length (1.99 Å) and is comparable to Mn-O bond length (2.22 Å) in Mn acetate tetrahydrate which is used as the precursor for the preparation of the Mn doped samples. Significantly low coordination number and high Debye Waller factor observed for Mn ( $x = 0.01$ ) doped sample suggested that the structure is highly disordered. The third shell Mn-Mn/Zn bond length is also found to be significantly higher in case of the Mn ( $x = 0.01$ ) doped sample compared to Zn-Zn bond length in ZnO and is comparable to Mn-Mn bond length in Mn acetate tetrahydrate. Thus from the above observations it can be concluded that the Mn ( $x = 0.01$ ) doped sample is more like a composite of ZnO and Mn acetate tetrahydrate where proper Mn substitution at Zn sites has not taken place. However, in case of other samples doped with Mn ( $x = 0.03$  and 0.05), the Mn-O bond lengths are 1.84 Å

and 1.87 Å which are comparable with Zn-O bond length (1.99 Å). Though the values of the Mn-O bond lengths agree more closely with theoretical Mn-O bond in MnO<sub>2</sub>, XANES results suggested the presence of Mn in 2<sup>+</sup> oxidation state in the samples and ruled out the presence of MnO<sub>2</sub>.

The corresponding Fourier transformed plots for poled sample recorded at Zn K-edge are shown in Fig.5.26(III) while the  $\chi(R)$  versus  $R$  plots for the poled samples at Mn K-edge are shown in Fig. 5.26(IV) and the best fit results are shown in Tables 5.16 and 5.17 respectively. It can be seen from Table 5.16 that for the Mn doped ( $x = 0.01, 0.03$  and  $0.05$ ) poled samples the coordination number and bond lengths of Zn-O shells are comparable with the values obtained for the unpoled samples while Debye Waller factors are found to be slightly higher in case of the poled samples suggesting increased disorder in the system. It has also been seen that coordination numbers of Zn-Zn(Mn) shells are lower in case of all the poled samples. From the Mn edge data (Fig. 5.26(IV)) it can be seen that the  $\chi(R)$  versus  $R$  plot of the Mn doped ( $x = 0.01$ ) sample is significantly different from that of the Mn doped ( $x = 0.03$  and  $0.05$ ) samples as have also been observed in case on the unpoled samples. Also the  $\sigma^2$  values for the first Mn-O shell are found to be higher in case of poled samples compared to unpoled samples while they are lower in case of Mn-Mn shells.

Thus for this set of samples, Mn edge EXAFS data suggest that the 1% Mn doped sample is more likely a composite of ZnO and Mn acetate tetrahydrate where proper Mn substitution at Zn sites has not been taken place, though 3% and 5% Mn doped samples show signature of proper Mn substitution at Zn sites in ZnO lattice.

**Table 5.16:** Bond length, coordination number and disorder factor obtained by EXAFS fitting for poled samples at Zn K edge.

Paths	Parameters	ZnO:1%Mn	ZnO:3%Mn	ZnO:5%Mn
Zn-O	R(Å)	1.99±0.01	2.00±0.01	1.99±0.01
	N	3.0±0.24	2.7±0.15	3.0±0.33
	$\sigma^2$	0.0099±0.001	0.009±0.002	0.0057±0.0012
Zn-O	R(Å)	2.11±0.2	2.09±0.01	2.11±0.02
	N	1.2±0.08	1.2±0.05	1.27±0.11
	$\sigma^2$	0.009±0.0011	0.009±0.0008	0.009±0.0015
Zn-Zn	R(Å)	2.85±0.02	2.88±0.03	2.83±0.01
	N	6.0±0.48	4.8±0.30	4.08±0.44
	$\sigma^2$	0.0324±0.0031	0.0297±0.0032	0.0297±0.0027
Zn-Zn	R(Å)	3.08±0.03	3.08±0.02	3.08±0.01
	N	3.72±0.32	3.6±0.20	3.96±0.66
	$\sigma^2$	0.0140±0.0023	0.0149±0.0016	0.0120±0.0018

**Table 5.17** Bond length, coordination number and disorder factor obtained by EXAFS fitting for poled samples at Mn K edge.

Paths	Parameters	ZnO:1%Mn	ZnO:3%Mn	ZnO:5%Mn
Mn-O	R(Å)	2.12±0.01	1.87±0.01	1.84±0.01
	N	3.57±0.28	4.0±0.24	3.88±0.44
	$\sigma^2$	0.0074±0.0013	0.005±0.001	0.0046±0.0009
Mn-Mn/Zn	R(Å)	2.80±0.01	2.88±0.01	2.78±0.01
	N	6.0±0.42	6.0±0.36	6.0±0.66
	$\sigma^2$	0.0146±0.0031	0.0166±0.0011	0.0158±0.0017
Mn-Mn/Zn	R(Å)	3.05±0.01	3.12±0.01	3.04±0.01
	N	6.0±0.42	6.0±0.36	6.0±0.66
	$\sigma^2$	0.010±0.0030	0.0135±0.0023	0.0137±0.0018

# Chapter 6

## **Mn AND Co DOPED TiO<sub>2</sub> THIN FILMS**

### **6.1 Introduction:**

As has been discussed in detail in Chapter-1, like in case of doped ZnO samples, the explanation of RTFM in transition metal doped TiO<sub>2</sub> samples also is not unique and has been attributed to a variety of intrinsic and extrinsic reasons. Thus origin of FM in TM doped TiO<sub>2</sub> is still a fairly unresolved question and further experimental and theoretical studies are required in this area. In this chapter we present our work on the preparation of Mn and Co doped TiO<sub>2</sub> thin films by magnetron sputtering on c-Si substrates and their thorough analysis by XAS technique, comprising of both EXAFS and XANES measurements, to explore the local environment around the host and the dopant cations carefully. XAS measurements on the samples have been carried out at host (Ti), dopant (Co and Mn) K and L<sub>3</sub>-edges and oxygen K-edges to have an overall information on the short range order in the samples. Apart from XAS, long range structural characterization of the samples have also been carried out by synchrotron based Grazing Incidence X-ray Diffraction (GIXRD) measurements. The structural information have finally been used to explain the magnetic properties of the samples.

### **6.2 Experimental:**

#### **6.2.1 Preparation of samples:**

Thin films of Mn doped TiO<sub>2</sub> and Co doped TiO<sub>2</sub> have been prepared by radio-frequency (RF) magnetron sputtering technique on c-Si substrates using the in-house built deposition system described in chapter 2. Commercial high purity TiO<sub>2</sub> sputtering targets of 3 inch diameter size and having requisite Mn and Co doping concentrations, verified by Energy

Dispersive X-ray (EDX) spectroscopy results provided by the supplier, were used for the depositions. Depositions have been carried out under high purity argon ambient, the Ar flow rate (13 sccm) being controlled by using a mass flow controller. *In-situ* quartz crystal thickness monitor has been used for thickness control, which is initially calibrated by depositing few test samples and measuring their thickness *ex-situ* by spectroscopic ellipsometry. The substrates have not been heated during deposition intentionally though the temperatures of the substrates are found to remain at ~50-80°C during deposition due to heating effect of the magnetron plasma. The other deposition parameters used are sputtering pressure of  $3 \times 10^{-3}$  Torr, substrate to target distance of 4.5 cm, RF power of 100 W and all the films were deposited for 20 minutes. The film thicknesses measured using spectroscopic ellipsometry are found to be in the range of 76-80 nm. Atomic compositions of the films have been checked prior to EXAFS measurements using X-ray Fluorescence (XRF) technique in the same set up and the atomic composition of the films have been found to agree with that of the targets.

### **6.2.2 Characterisation of samples:**

Preliminary structural characterizations of the films were carried out by Grazing Incidence X-ray Diffraction (GIXRD) measurements at BL-11 of Indus-2 synchrotron facility at Raja Ramanna Centre for Advanced Technology (RRCAT), Indore, India and its brief introduction is given in Chapter-2. A monochromatic X-ray energy of 16.4 keV was selected for the measurements with Si(111) channel cut monochromator and the diffracted rays were collected in a Mar 345 Image Plate detector. The XANES and EXAFS measurements have been carried out at the Energy-Scanning EXAFS beamline (BL-9) at the Indus-2 Synchrotron Source at RRCAT, Indore, India (details are given in Chapter-2). In case of the present thin film samples, Si drift detector (Vortex detector) is used for the measurement in fluorescence mode in 45° geometry. Rejection of the higher harmonic content in the X-ray beam is

performed by detuning the second crystal of DCM. XANES measurements at the O K-edges and TM (TM=Ti, Mn and Co) L<sub>2,3</sub> edges of the Mn and Co doped TiO<sub>2</sub> samples were performed at room temperature in the total electron yield (TEY) mode at the SXAS beamline (BL-01) of the Indus-2 synchrotron radiation source at RRCAT, Indore, India. M-H measurements at room temperature (RT) were performed with a Superconducting Quantum Interference Device Vibrating Sample Magnetometer (SQUID-VSM-050 MPMS), Quantum Design, USA.

### **6.3 Results and discussion:**

#### **6.3.1 Grazing Incidence X-ray Diffraction:**

The as-prepared films are found to be amorphous in nature. Annealing of the samples under vacuum ( $6 \times 10^{-8}$  Torr) was subsequently carried out with different temperatures viz., 350, 450, 550 and 600°C for 2 hrs. The ramping time is kept slow (3°C/min) to avoid the peeling out of the film. These annealed samples are checked for crystallization and the TiO<sub>2</sub> film annealed at 600°C is found to attain the anatase phase. The GIXRD data measured at BL-11 are shown in figure 6.1 for different doping concentrations of Mn and Co doped TiO<sub>2</sub> thin films alongwith that of undoped TiO<sub>2</sub>. The diffraction peaks of undoped TiO<sub>2</sub> coincide with anatase phase with space group of I4<sub>1</sub>amd.<sup>265</sup> Though rutile phase is more likely to be formed in TiO<sub>2</sub> at high temperature, however there are many reports suggesting relatively higher transition temperature for anatase to rutile phase transition and presence of Anatase phase at 600°C<sup>266, 267</sup>. The XRD patterns of standard anatase as well as rutile TiO<sub>2</sub> are also presented in figure 6.1 for comparison alongwith the sample. For the 1% Mn doped TiO<sub>2</sub> sample, GIXRD peaks match with the anatase phase of TiO<sub>2</sub>. As the doping concentration is further increased to 4%, both anatase as well as the rutile phases start appearing. For the 10% Mn doped samples, we have also observed an extra peak at ~15° (marked by asterisk) which can be attributed to MnTiO<sub>3</sub> phase.

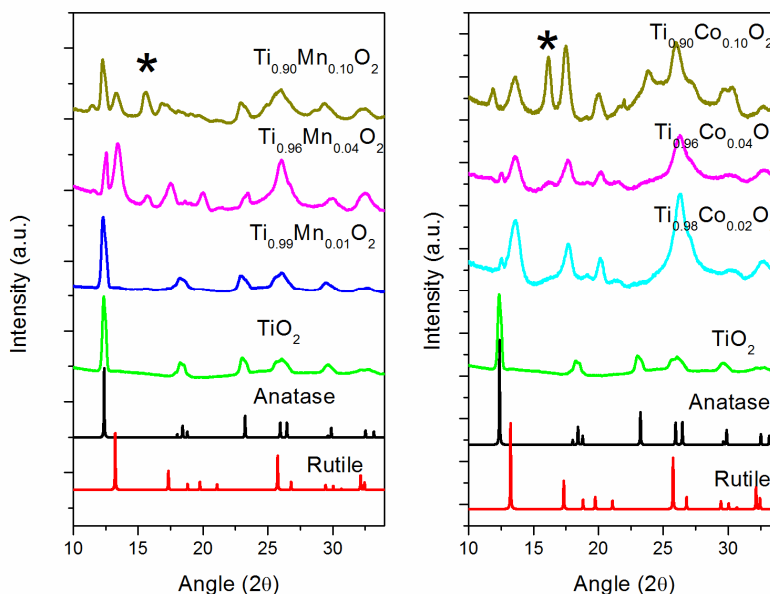


**Figure 6.1:** GIXRD plots of Mn doped  $\text{TiO}_2$  and Co doped  $\text{TiO}_2$  thin films. The XRD spectra of pure anatase and rutile phase are also plotted for reference.

However, in case of Co doped sample, the GIXRD data shows mixture of anatase as well as the rutile phase for even 2% Co doped  $\text{TiO}_2$ . The anatase and rutile phases are still present for 4% sample however for 10% sample, extra peaks appear due to the  $\text{CoTiO}_3$  phase (marked by asterisk). Similar impurity phases are also observed by other researchers for Co and Mn doped  $\text{TiO}_2$  samples for higher doping concentrations.<sup>118, 120, 268</sup>

### 6.3.2 X-ray Absorption Spectroscopy:

#### 6.3.2.1 XANES results of Mn doped $\text{TiO}_2$ :

The normalised XANES spectra of the Mn doped  $\text{TiO}_2$  thin films measured at Ti K-edge are shown in figure 6.2. The absorption edge position clearly indicates that Ti is present in +4 oxidation state and the XANES spectral features for undoped  $\text{TiO}_2$  sample exactly resemble that of anatase  $\text{TiO}_2$ .<sup>269</sup> The white line observed for  $\text{TiO}_2$  is transition of 1s electron to the vacant np orbital of Ti or the anti bonding orbital of Ti-O. Transition metal shows pre-edge features due to weak dipole forbidden transition of 1s electron to 3d orbitals. This transition is made allowed by hybridization of 3d orbitals with O 2p orbitals. Anatase

has distorted  $\text{TiO}_6$  octahedrons, hence three peaks in pre-edge region are seen in the spectra. The pre-edge peaks  $A_2$  and  $A_3$  are attributed to the  $1s-2t_{2g}$  and  $1s-3e_g$  transitions in octahedral field respectively.<sup>267</sup> The pre-edge peak  $A_1$  is attributed to exciton band or  $1s-1t_{1g}$  transition from possible perturbation due to shake-up and shake-off processes.<sup>270</sup>

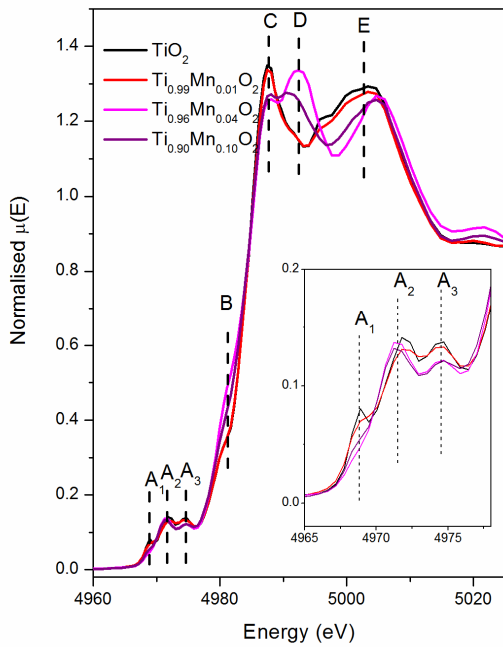


**Figure 6.2:** Normalised XANES spectra of  $\text{TiO}_2$  and Mn doped  $\text{TiO}_2$  thin films at Ti K-edge. The inset figure shows the extended part of the pre-edge region.

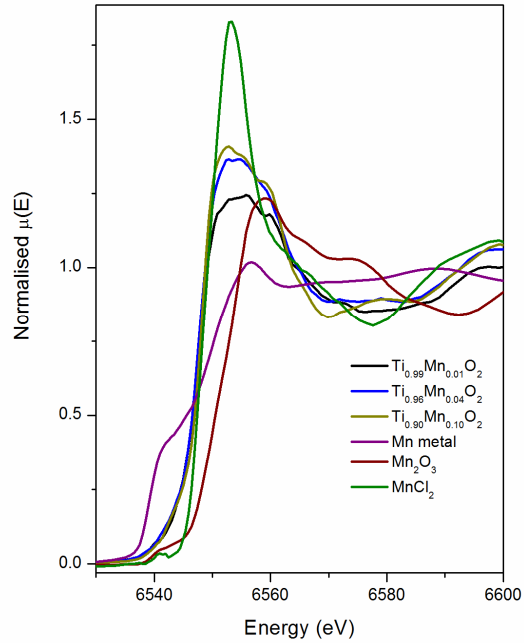


**Figure 6.3:** Normalised XANES spectra of  $\text{TiO}_2$  and Mn doped  $\text{TiO}_2$  thin films at Mn K-edge. The reference spectrum of Mn metal, Spectra of  $\text{MnCl}_2$  and  $\text{Mn}_2\text{O}_3$  are given for comparison.

The peak intensities of  $A_1$ ,  $A_2$  and  $A_3$  are quite sharp in case of the undoped  $\text{TiO}_2$  sample and their sharpness are diminished for the 1% Mn doped sample, however all three peaks are clearly visible. On the other hand in case of Mn doped samples with doping concentration of 4% or higher, the intensity of the peak  $A_1$  becomes very small, though the intensities of the peaks  $A_2$  and  $A_3$  remain the same. This is a characteristic of rutile phase formation. The significant changes in the spectra can also be seen at the positions B, C, D and E which are quite different for  $\text{TiO}_2$  and 4% Mn doped  $\text{TiO}_2$ . The XANES spectrum of the

10% Mn doped sample appears to be in between that of undoped and 4% Mn doped TiO<sub>2</sub>. The white line spectra of TiO<sub>2</sub> and 1% doped samples show pure anatase phase however for samples with Mn doping of 4% or higher the crystal structure changes to more rutile-like phase. This observation of anatase to rutile phase change with increase in Mn doping concentration corroborates with the GIXRD results reported above. Similar phase change (anatase to rutile) with doping concentration of Co and Ni have been observed by Gole et al.<sup>271</sup> in case of ZnO nanocolloids. Recently Khatun et al. have also demonstrated a decrease in transition temperature from anatase to rutile in TiO<sub>2</sub> by vanadium doping<sup>272</sup>.

The normalised XANES spectra of the samples at Mn K-edge are shown in figure 6.3 alongwith that of Mn metal, MnCl<sub>2</sub> and Mn<sub>2</sub>O<sub>3</sub> standards. The edge positions of Mn in the samples clearly indicate that Mn is present in +2 oxidation state in the samples throughout doping concentration, though the white-line intensity is found to increase with Mn doping concentration possibly due to creation of oxygen vacancies as has been discussed in details later<sup>273</sup>. Deng et al. explored the oxidation state of the Mn by XPS in Mn doped TiO<sub>2</sub> and found mixed oxidation state for Mn in +3 and +4, however, in our case single oxidation state of Mn is found.<sup>274</sup>

### **6.3.2.2 XANES results of Co doped TiO<sub>2</sub>:**

The normalized XANES spectra at Ti K-edge of Co doped TiO<sub>2</sub> samples are shown in figure 6.4. Similar to Mn doped sample, the pre-edge peaks are denoted by A<sub>1</sub>, A<sub>2</sub> and A<sub>3</sub> and the pre-edge region is shown in expanded scale in the inset of the figure. The anatase phase of TiO<sub>2</sub> have three separate peaks and these are clearly visible for the undoped TiO<sub>2</sub> sample, however first pre-edge peak A<sub>1</sub> is generally very weak in the case of rutile phase. This weak A<sub>1</sub> peak in the doped samples thus indicates that in these samples rutile is the majority phase. The reduction in intensity of peak C and appearance of extra peak at the

position D are also characteristics of rutile phase and thus confirm that the doped samples are of rutile structure.

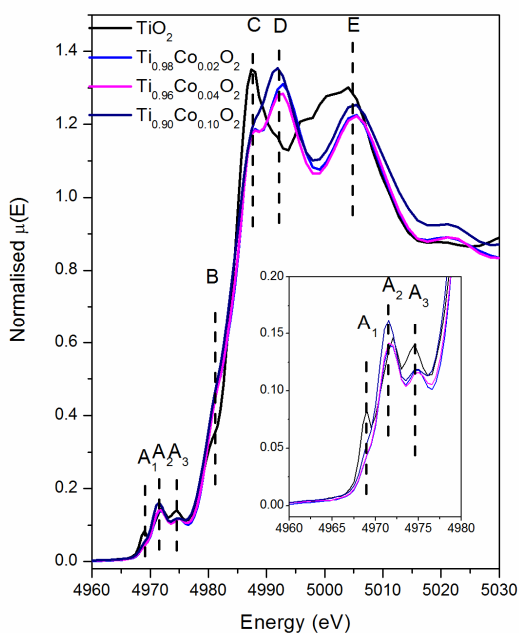


**Figure 6.4:** Normalised XANES spectra of  $\text{TiO}_2$  and Co doped  $\text{TiO}_2$  thin films at Ti K-edge. The inset figure shows the extended part of the pre edge region.

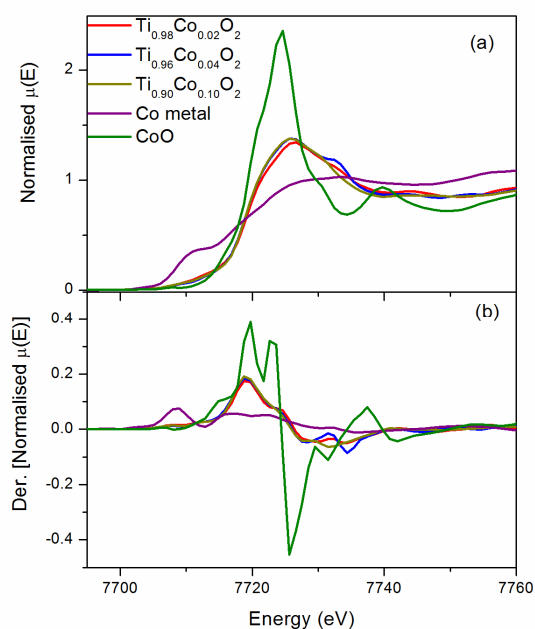


**Figure 6.5:** (Upper) Normalised XANES spectra of  $\text{TiO}_2$  and Co doped  $\text{TiO}_2$  thin films at Co K-edge. The reference spectrum of Co metal and CoO are given for comparison. (Lower) The derivative of XANES spectra.

The normalized XANES spectra at Co K-edge of Co doped  $\text{TiO}_2$  thin films are shown in figure 6.5 along with that of Co metal foil and standard CoO powder. For more clarity the derivative spectra are plotted in the lower panel of figure 6.5. The absorption edge position, as it is clearly visible in derivative spectra matches with that of CoO. This indicates the presence of  $\text{Co}^{+2}$  oxidation state, however the overall XANES spectra of Co doped  $\text{TiO}_2$  samples are quite different from that of CoO. This rules out the presence of CoO or metallic Co in the sample. This corroborates with XRD results also where no extra peaks for the above phases are observed for 2% Co doped  $\text{TiO}_2$  sample.

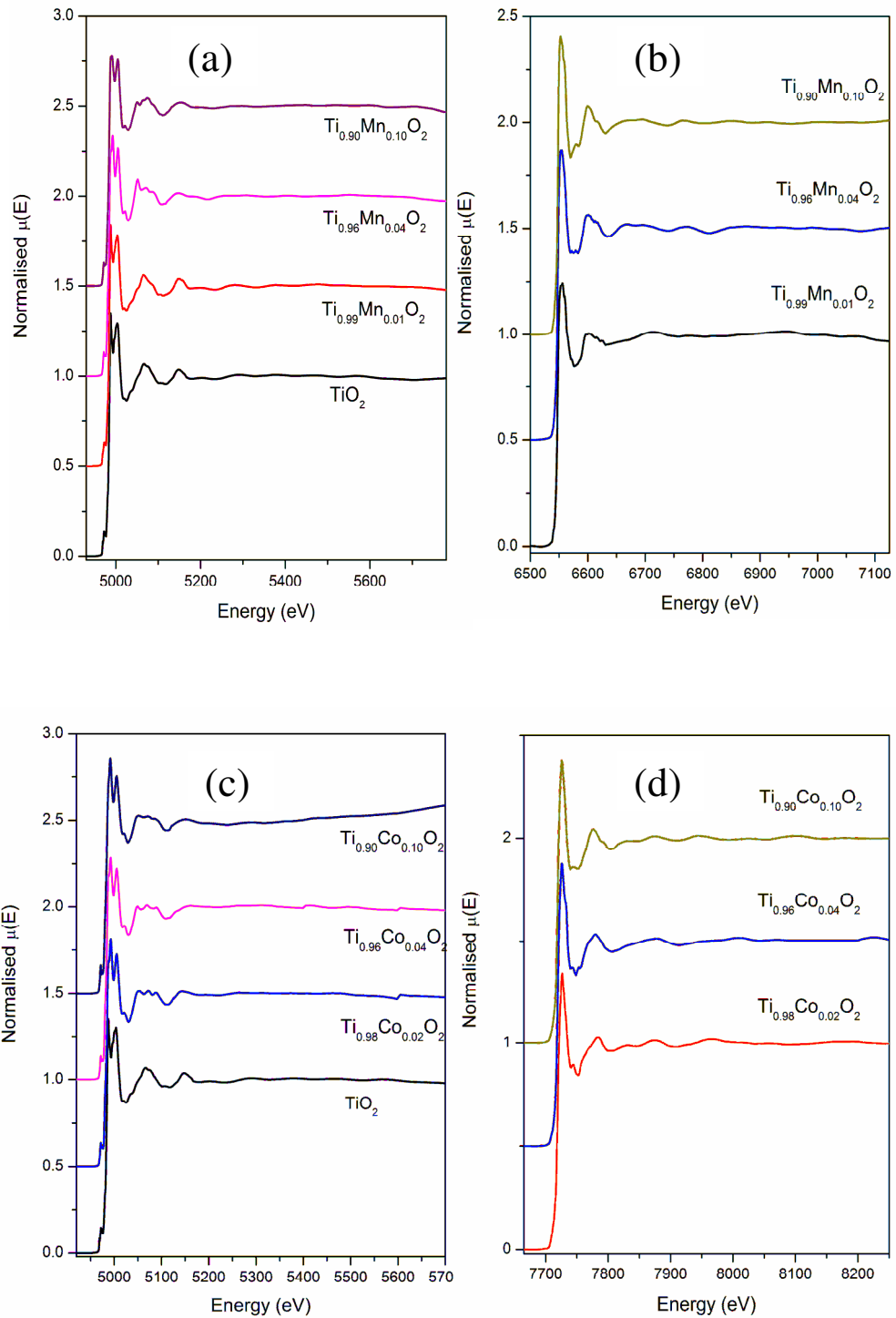


**Figure 6.6:** Normalised EXAFS spectra of (a)  $\text{TiO}_2$  and Mn doped  $\text{TiO}_2$  at Ti K-edge (b) Mn doped  $\text{TiO}_2$  at Mn K-edge (c)  $\text{TiO}_2$  and Co doped  $\text{TiO}_2$  at Ti K-edge and (d) Co doped  $\text{TiO}_2$  at Co K-edge.

Since the ionic radii of  $\text{Co}^{2+}$  (0.65 Å) is comparable to ionic radii of  $\text{Ti}^{+4}$  (0.61 Å), it is most likely that Co atoms replace Ti atoms in  $\text{TiO}_2$  matrix. However to confirm this we have carried out analysis of the EXAFS data measured at both host and dopant edges. The XANES spectra obtained here is quite different from that reported by Mukrakami et al.,<sup>124</sup> who have found small amount of metallic phase alongwith the  $\text{Co}^{2+}$ , however the XANES spectra observed in the present case are quite similar to that obtained by Kim et al..<sup>275</sup>

### **6.3.2.3 EXAFS results of Mn and Co doped $\text{TiO}_2$ :**

The normalized EXAFS spectra of undoped  $\text{TiO}_2$ , Mn doped  $\text{TiO}_2$  and Co doped  $\text{TiO}_2$  samples are shown in figures 6.6a-d at Ti, Mn and Co K edges. In order to take care of the oscillations in the absorption spectra,  $\mu(E)$  has been converted to absorption function  $\chi(E)$  following the methodology described in Chapter-2. The Demeter software package (EXAFS data analysis software) have been used for EXAFS data analysis.<sup>276</sup>

### **6.3.2.4 EXAFS results of Mn doped $\text{TiO}_2$ :**

The  $\chi(R)$  versus  $R$  plots of the Mn doped  $\text{TiO}_2$  films are shown in figures 6.7 and 6.8 for Ti and Mn K-edges respectively. The plots shown in the above figures are phase uncorrected plots which show the coordination peaks at slightly lower distances than the real bond lengths. To obtain the real physical parameters like bond length, coordination number and Debye-Waller (disorder) factor, theoretical plots are generated and fitted with experimental data. For undoped and 1% Mn doped  $\text{TiO}_2$  film, anatase structure has been assumed while for rest of the samples scattering paths from both anatase and rutile phases have been taken into account.

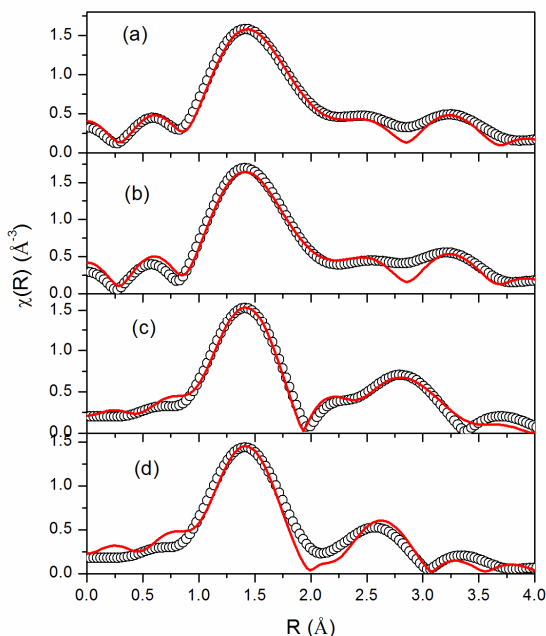


**Figure 6.7:** Fourier transformed EXAFS spectra of (a)  $\text{TiO}_2$  (b) 1% Mn doped  $\text{TiO}_2$  (c) 4% Mn doped  $\text{TiO}_2$  and (d) 10% Mn doped  $\text{TiO}_2$  (scatter points) at Ti K-edge along with best fit theoretical plots (solid line).

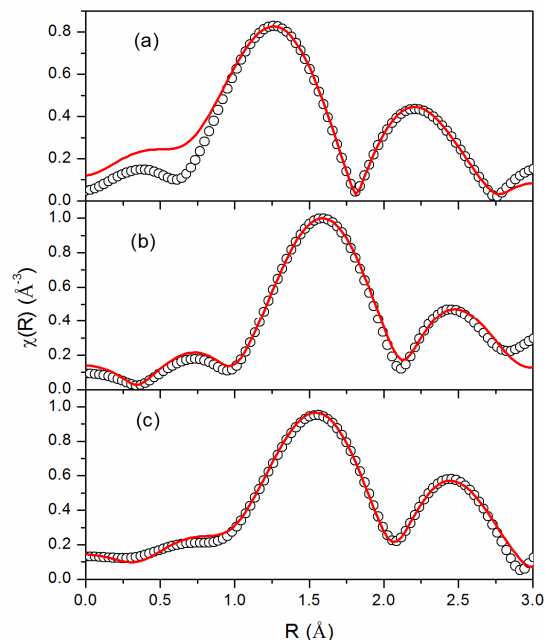


**Figure 6.8:** Fourier transformed EXAFS spectra of (a) 1% Mn doped  $\text{TiO}_2$  (b) 4% Mn doped  $\text{TiO}_2$  and (c) 10% Mn doped  $\text{TiO}_2$  (scatter points) at Mn K-edge along with best fit theoretical plots (solid line).

The crystal structures of anatase and rutile phases of  $\text{TiO}_2$  have been taken from refs. 32<sup>265</sup> and 45<sup>277</sup> respectively. The fitted plot is shown in figure 6.7 as solid red line and the fitting results are given in Table 6.1 for the Ti K-edge data. It should be noted that the phase correction is included during the fitting and the distances shown in Table 6.1 are the real distances. The anatase polymorph of  $\text{TiO}_2$  have six oxygen atoms in octahedral geometry with the Ti-O bond distance of 1.94 Å. However the rutile polymorph of  $\text{TiO}_2$  have distorted octahedra with four planar Ti-O bonds at 1.95 Å and 2 apical Ti-O bond at 1.98 Å. The first peak in undoped  $\text{TiO}_2$  (figure 6.7 (a)) at 1.5 Å has contributions of six Ti-O bonds at a distance of 1.96 Å. The second doublet peak between 2.0 Å-3.5 Å has contributions of two Ti-Ti coordination shells with five and four coordinations at bond distances of 3.00 Å and 3.75 Å respectively.

**Table 6.1:** Bond length, coordination number and disorder factor obtain by EXAFS fitting at Ti K edge.

Path	Parameter	TiO <sub>2</sub> : Undoped	TiO <sub>2</sub> : 1%Mn	TiO <sub>2</sub> : 4%Mn	TiO <sub>2</sub> : 10%Mn
Ti-O	R (Å)	1.96±0.01	1.96±0.01	1.92±0.01	1.93±0.01
	N	6.0	5.88±0.48	3.79±0.19	3.92±0.26
	σ <sup>2</sup>	0.0012±0.0008	0.0012±0.001	0.0017±0.0007	0.0030±0.0009
Ti-O	R (Å)			1.95±0.01	1.96±0.01
	N			1.80±0.10	1.99±0.13
	σ <sup>2</sup>			0.0017±0.0007	0.0030±0.0009
Ti-Ti	R (Å)	3.00±0.01	3.01±0.02	2.96±0.01	3.05±0.02
	N	4.0	4.18±0.40	2.15±0.10	5.20±0.13
	σ <sup>2</sup>	0.0021±0.0011	0.0020±0.001	0.0087±0.0016	0.0097±0.0023
Ti-Ti	R (Å)	3.75±0.01	3.76±0.02	3.57±0.01	
	N	4.0	3.34±0.32	6.44±0.29	
	σ <sup>2</sup>	0.0021±0.0011	0.0020±0.001	0.0087±0.0016	

These Ti-O and Ti-Ti bond distances agree with anatase polymorph of TiO<sub>2</sub>. Similar to undoped TiO<sub>2</sub>, for 1% Mn doped TiO<sub>2</sub>, the first peak has contributions of single oxygen coordination shells, however two oxygen coordination shells are required for 4% and 10% doping concentrations with first Ti-O path between 1.92-1.94 Å and the second Ti-O path at 1.95-1.96 Å which are characteristics of rutile phase.

**Table 6.2:** Bond length, coordination number and disorder factor obtain by EXAFS fitting at Mn K edge.

Path	Parameter	TiO <sub>2</sub> : 1%Mn	TiO <sub>2</sub> : 4%Mn	TiO <sub>2</sub> : 10%Mn
Mn-O	R (Å)	1.92±0.01	2.12±0.01	2.10±0.01
	N	4.86±0.27	3.98±0.30	4.76±0.37
	σ <sup>2</sup>	0.0093±0.0007	0.002±0.001	0.0082±0.0008
Mn-Ti	R (Å)	2.78±0.01	2.96±0.01	2.97±0.01
	N	7.70±0.36	6.30±0.40	7.01±0.5
	σ <sup>2</sup>	0.0162±0.0015	0.0019±0.0009	0.0089±0.0013

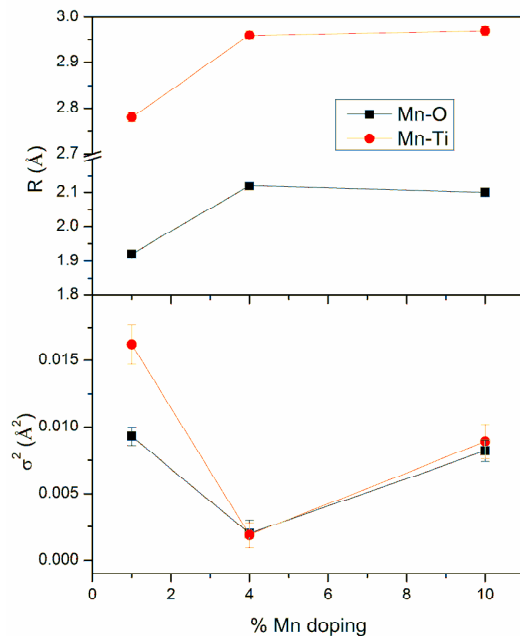


**Figure 6.9:** Variation of bond length ( $R$ ) and disorder factor ( $\sigma^2$ ) with doping concentration at Mn K-edge.

Fourier transformed EXAFS spectra or  $\chi(R)$  versus  $R$  plots of Mn doped  $\text{TiO}_2$  samples at the dopant site (Mn) are shown in figure 6.8. The first peak at 1.5 Å has contributions of Mn-O coordination shells and the second peak at 2.5 Å has contributions of Mn-Ti scattering paths. The theoretical plots are generated using the  $\text{TiO}_2$  structure, where the central Ti atoms are replaced by Mn atoms and the fitting results are shown in Table 6.2 and fig. 6.9. The first peak at 1.5 Å has contributions of oxygen atoms at the bond distance of 1.92 Å for 1% Mn doped  $\text{TiO}_2$ . From Table 6.2 it can be seen that the Mn-O bond length increases with an increase in Mn doping concentration. The larger Mn-O bond length for higher doping concentration is due to the presence of  $\text{MnTiO}_3$  (Mn-O bond length 2.11 Å for  $\text{MnTiO}_3$ ) phase in samples with higher doping concentration as has been observed in XRD measurement also. Oxygen coordination number obtained here is less than six, which suggests the presence of oxygen vacancies near Mn ions. Oxygen vacancies are expected since in the present samples  $\text{Ti}^{4+}$  ions are replaced by  $\text{Mn}^{2+}$  ions (confirmed by XANES) and

the charge neutrality condition requires creation of oxygen vacancies. Similar oxygen deficiencies are observed in Mn doped TiO<sub>2</sub> nanostructures by Zhang et al.<sup>278</sup> The second metal-metal peak appeared in the  $\chi(R)$  versus  $R$  plots at 2.5 Å has contributions of ~6-7 Ti atoms around Mn atoms.

### 6.3.2.5 EXAFS results of Co doped TiO<sub>2</sub>:

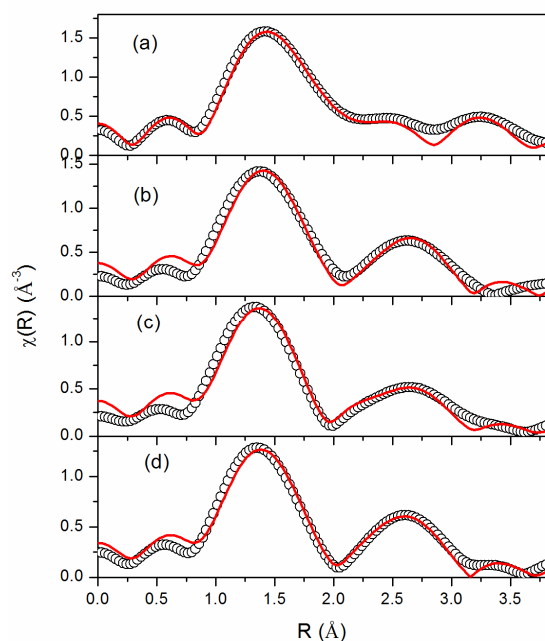


**Figure 6.10:** Fourier transformed EXAFS spectra of (a) TiO<sub>2</sub> (b) 2% Co doped TiO<sub>2</sub> (c) 4% Co doped TiO<sub>2</sub> and (d) 10% Co doped TiO<sub>2</sub> (scatter points) at Ti K-edge along with best fit theoretical plots (solid line).

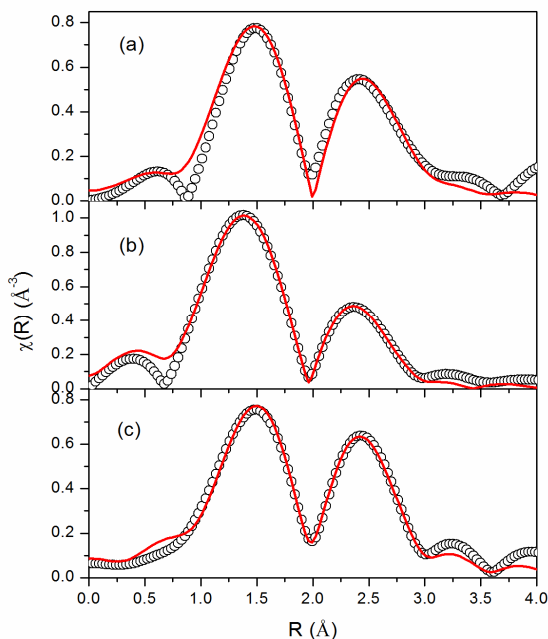


**Figure 6.11:** Fourier transformed EXAFS spectra of (a) 2% Co doped TiO<sub>2</sub> (b) 4% Co doped TiO<sub>2</sub> and (c) 10% Co doped TiO<sub>2</sub> (scatter points) at Co K-edge along with best fit theoretical plots (solid line).

The Fourier transformed EXAFS spectra in  $R$  space is shown in figure 6.10 for Co doped TiO<sub>2</sub> thin films at Ti K-edge. Based on the XANES results shown above the EXAFS spectra are fitted using the rutile phase as the initial guess structure and the best fit results are given in Table-6.3. The FT-EXAFS spectra shown here is in phase uncorrected  $R$  space which is showing the coordination peaks at slightly lower  $R$  values than the actual distances,

however the fitting results are obtained after including the phase part. The first peak appearing at 1.5 Å in figure 6.10 has contributions from Ti-O coordination shells at 1.94 Å and 1.97 Å with total six oxygen atoms. The second peak is fitted with single Ti-Ti scattering path. The obtained Ti-Ti bond length is quite similar to that of rutile phase. The EXAFS measurements of Co doped TiO<sub>2</sub> are done at Co K-edge and the experimental  $\chi(R)$  versus  $R$  data alongwith best fit theoretical plots are shown in figure 6.11. Initial guess structure of rutile TiO<sub>2</sub> is used to generate theoretical spectra, where replacement of central Ti atoms is done with Co atoms. The fitted plots are shown in figure 6.11 in solid red line and the fitting results are given in Table 6.4 and fig. 6.12.

**Table 6.3:** Bond length, coordination number and disorder factor obtain by EXAFS fitting at Ti K edge.

Path	Parameter	TiO <sub>2</sub> : Undoped	TiO <sub>2</sub> : 2%Co	TiO <sub>2</sub> : 4%Co	TiO <sub>2</sub> : 10%Co
Ti-O	R (Å)	1.96±0.01	1.94±0.01	1.92±0.01	1.93±0.01
	N	6.0	3.66±0.24	3.73±0.15	3.98±0.12
	$\sigma^2$	0.0012± 0.0008	0.0014± 0.0005	0.0016± 0.0006	0.0032± 0.0007
Ti-O	R (Å)		1.97±0.01	1.95±0.01	1.96±0.01
	N		1.83±0.12	1.86±0.07	1.99±0.06
	$\sigma^2$		0.0014± 0.0005	0.0016± 0.0006	0.0032± 0.0007
Ti-Ti	R (Å)	3.00±0.01	3.06±0.02	3.06±0.02	3.05±0.02
	N	4.0	6.22±0.48	6.22±0.30	5.61±0.24
	$\sigma^2$	0.0021± 0.0011	0.0217± 0.0009	0.0217± 0.0017	0.0084± 0.0013
Ti-Ti	R (Å)	3.75±0.01			
	N	4.0			
	$\sigma^2$	0.0021± 0.0011			

The first peak at Co K-edge EXAFS spectra shown at 1.5 Å has contributions of Co-O paths at the distance of 1.94-2.02 Å. The Co-O bond length obtained here is larger than the Ti-O bond length and this is due to the larger ionic radii of Co<sup>2+</sup> (0.75 Å) compared to Ti<sup>4+</sup> (0.61Å).<sup>209</sup> The Co-O bond length obtained here are in good agreement with other

researchers.<sup>118, 122, 279, 280</sup> The large Co-O bond length of 2.07 Å for 10% doped sample is due to the presence of extra phase of CoTiO<sub>3</sub>.<sup>118</sup> It is found that the disorder factor ( $\sigma^2$ ) of Co-O path increases with an increase in Co doping concentrations. Similar to the Mn doped case Co doped TiO<sub>2</sub> samples also show the presence of oxygen vacancies as coordination number of oxygen is lower than 6, which is expected since Co is present in the samples in +2 oxidation state as observed from the XANES spectra. The second peak at 2.5 Å is the Co-Ti coordination peak at a distance of ~3.00 Å.

**Table 6.4:** Bond length, coordination number and disorder factor obtain by EXAFS fitting at Co K edge.

Path	Parameter	TiO <sub>2</sub> : 2%Co	TiO <sub>2</sub> : 4%Co	TiO <sub>2</sub> : 10%Co
Co-O	R (Å)	1.93±0.01	1.94±0.01	2.02±0.01
	N	3.84±0.21	3.84±0.11	4.08±0.14
	$\sigma^2$	0.0065±0.0008	0.0012±0.0004	0.0072±0.0005
Co-Ti	R (Å)	3.02±0.02	2.99±0.01	2.97±0.02
	N	6.40±0.27	6.72±0.15	7.36±0.11
	$\sigma^2$	0.0032±0.0011	0.0083±0.0011	0.0036±0.0006

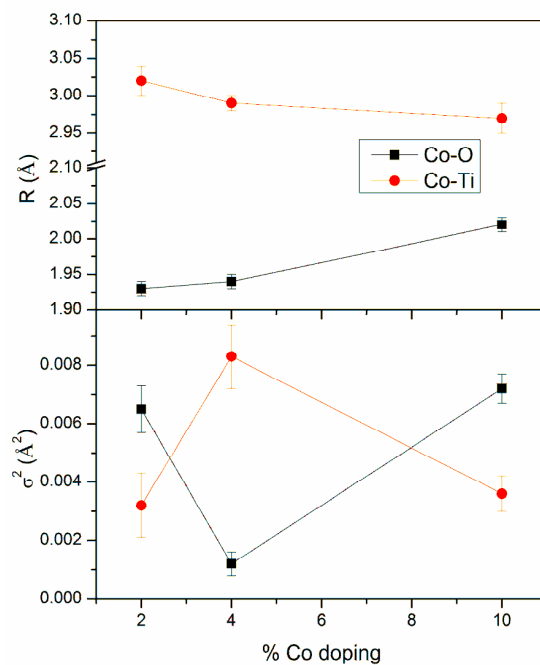


**Figure 6.12:** Variation of bond length ( $R$ ) and disorder factor ( $\sigma^2$ ) with doping concentration at Co K-edge.

### 6.3.2.6 XANES results at Ti L-edge:

Ti L<sub>2</sub> and L<sub>3</sub>-edge XANES spectra of the samples are shown in fig. 6.13. In transition metal oxides, the 2*p* X-ray absorption spectra are completely dominated by the strong 2*p*→3*d* dipole allowed transitions and the fine structural signature can be clearly seen. The spectral features are identified using the previously reported literatures<sup>281-284</sup> based on theoretical simulations or experimental observations for two common crystal structures of TiO<sub>2</sub>. TiO<sub>2</sub> shows multiple peaks for L<sub>2</sub> and L<sub>3</sub> edges.

The resonance peaks denoted by A<sub>1</sub> and A<sub>2</sub> (consist of A<sub>2</sub>' , A<sub>2</sub>" ) are for L<sub>3</sub> edge and the resonance peaks B<sub>1</sub> and B<sub>2</sub> are for L<sub>2</sub> edge. Zhou et al.<sup>285</sup> suggested that transition from 2*p*<sub>3/2</sub> and 2*p*<sub>1/2</sub> to the final state Ti 3*d*<sub>5/2,3/2</sub> are modified by the combined spin-orbit and crystal field interactions and forms low energy *t*<sub>2*g*</sub> and high energy *e*<sub>g</sub> orbital. This signifies that L<sub>3</sub> and L<sub>2</sub> are not simply interpreted using dipole selection rules but have to follow collective effect of spin-orbit interactions and crystal field splitting since the eigen states are no longer truly atomic in nature. Zhou et al. further suggested that the distortion in the symmetry will further split peak A<sub>2</sub> in to A<sub>2</sub>' and A<sub>2</sub>". This splitting or asymmetry has been attributed to distortion from *O<sub>h</sub>* symmetry.<sup>282</sup> The changes in the local symmetry from anatase to rutile phase can be identified through relative intensities of the peaks A<sub>2</sub>' and A<sub>2</sub>". A<sub>2</sub>'>A<sub>2</sub>" is a signature of anatase phase, while A<sub>2</sub>'<A<sub>2</sub>" is a characteristic of rutile phase. These characteristic features can be used to identify the dominant structures. The small pre-edge peak S at 457 eV is related to a transition which is forbidden in L-S coupling, but become allowed because of the multipole *p-d* transitions.

The XANES spectra at Ti L<sub>2,3</sub>-edge for Mn doped TiO<sub>2</sub> are shown in figure 6.13. The peaks are denoted by A<sub>1</sub>, A<sub>2</sub> for L<sub>3</sub>-edge and B<sub>1</sub> and B<sub>2</sub> for L<sub>2</sub>-edge. The peak A<sub>2</sub> is further splitted to A<sub>2</sub>' and A<sub>2</sub>" for TiO<sub>2</sub>. In case of undoped TiO<sub>2</sub> film, the intensity of A<sub>2</sub>' is higher than A<sub>2</sub>" indicating the presence of anatase phase, as explained above. Similar intensity ratio

of peak  $A_2'$  and  $A_2''$  is also found for 1% Mn doped sample, however almost equal peak intensities are found for 4% and 10% Mn doped samples manifesting the presence of rutile phase in higher doping concentrations. Similar change in the phase structure from anatase to rutile phase after incorporation of Li in  $\text{TiO}_2$  matrix is observed by Zhou et al.<sup>285</sup> The change in the oxidation state  $\text{Ti}^{+4}$  to  $\text{Ti}^{+3}$  will shift the peak at the lower energy side. The position of resonance peaks are at the same energy indicating that Ti is present in the samples in +4 oxidation state only.

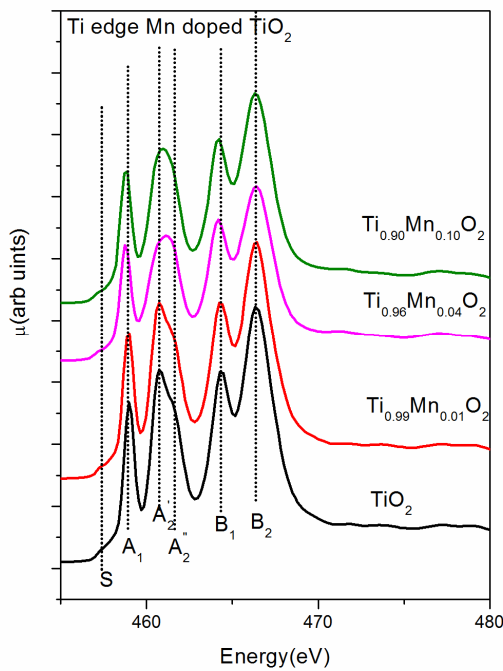


**Figure 6.13:** Soft X-ray absorption spectra of  $\text{TiO}_2$  and Mn doped  $\text{TiO}_2$  at Ti  $L_{2,3}$  edge.

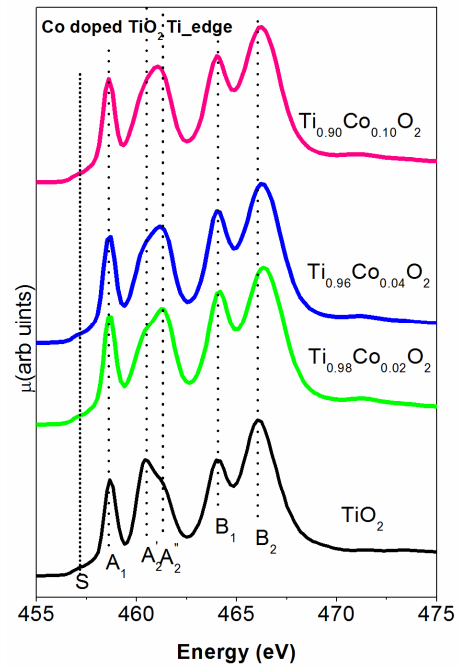


**Figure 6.14:** Soft X-ray absorption spectra of  $\text{TiO}_2$  and Co doped  $\text{TiO}_2$  at Ti  $L_{2,3}$  edge.

The Ti  $L_{2,3}$ -edge XANES spectra of Co doped  $\text{TiO}_2$  samples are shown in figure 6.14. As has been explained above in case of Mn doped samples, peaks  $A_1$  and  $A_2$  are for  $L_3$ -edge and peaks  $B_1$  and  $B_2$  are for  $L_2$ -edge. The pre-edge peak (denoted by S in figure 6.14) is also observed for Co doped  $\text{TiO}_2$  samples. As it is mentioned above, the peak  $A_2$  is quite sensitive

to the anatase and rutile polymorphs, undoped TiO<sub>2</sub> sample shows pure anatase phase, however Co doped TiO<sub>2</sub> samples show the signature of rutile phase for all doping concentrations. The significant difference in the peak shift is also observed at B<sub>2</sub> peak position compared to undoped TiO<sub>2</sub>, however all the other peaks remain at the same position.

#### **6.3.2.7 XANES results at O K-edge and theoretical simulation:**

The oxygen K-edge XANES spectra originated from the transition of O 1s electron to higher orbital of Mn doped TiO<sub>2</sub> are shown in figure 6.15. Since as has been discussed in the context of Ti K-edge XANES spectra, the O 2p orbital are hybridized with Ti 3d and 4sp states, it will give the crucial information regarding local structure of the host site in these doped samples. The peaks denoted by A and B are associated with transition of O1s electron to the O2p-Ti3d state.<sup>281</sup> The two peaks A and B are due to the splitting of Ti 3d state into *t<sub>2g</sub>* and *e<sub>g</sub>* states. The spectral features C at ~540 eV is due to transition of O1s electron into O2p anti-bonding state and feature E at ~545 eV is due to transition to O(2p)-Ti(4sp) band. The spectral peaks between 537 eV and 550 eV for anatase and rutile phase TiO<sub>2</sub> have been presented in the works of Zhou et al. and Ruus et al.<sup>285, 286</sup>

The rutile phase shows three low resolved peaks in this region and anatase phase will give two well resolved peaks. The comparison of our XANES spectra with the above reports shows that undoped TiO<sub>2</sub> and 1% Mn doped TiO<sub>2</sub> are in anatase phase as only two peaks are observed in between 537 to 550 eV. However for higher doping concentrations three weak features are clearly visible which is a signature of rutile phase. This observation confirms the metal K-edge XANES and EXAFS results and the findings from XRD results also as discussed above. The XANES spectra at O K-edge of Co doped TiO<sub>2</sub> samples are shown in figure 6.16. The peaks A, B, C, D and E clearly resemble that of rutile phase. The region between 537 to 550 eV is quite different for Co doped and undoped TiO<sub>2</sub> samples. While the

undoped  $\text{TiO}_2$  samples show the features related to pure anatase phase, the doped samples show the presence of rutile phase.

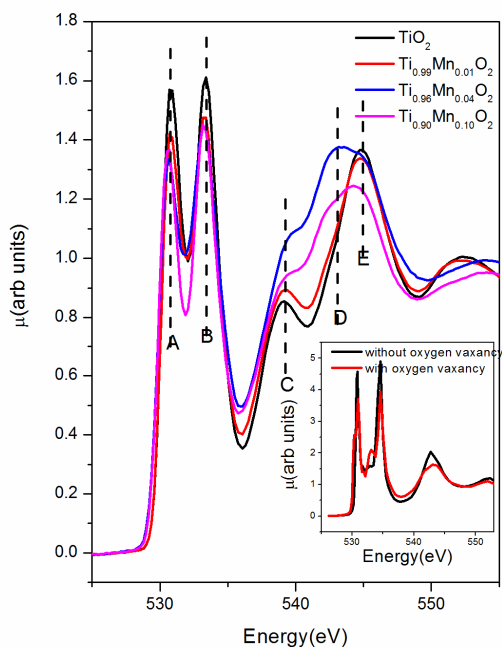


**Figure 6.15:** Soft X-ray absorption spectra of  $\text{TiO}_2$  and Mn doped  $\text{TiO}_2$  at Oxygen K-edge. The inset shows the theoretically calculated XANES spectra using FEFF9.

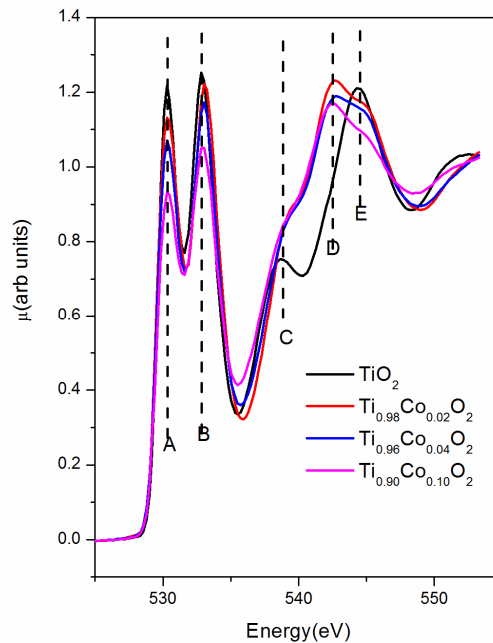


**Figure 6.16:** Soft X-ray absorption spectra of  $\text{TiO}_2$  and Co doped  $\text{TiO}_2$  at Oxygen K-edge.

It has been observed that the intensities of the peaks A and B are reduced in case of both Co and Mn doped  $\text{TiO}_2$  samples compared to that in undoped  $\text{TiO}_2$ . Such reduction of these peaks are also observed by Souza et al.<sup>279</sup> for Co doped  $\text{TiO}_2$ . To investigate the origin of this peak intensity, theoretical calculations are done using FEFF9 software at O K-edge. The cluster of 6.0 Å is used for XANES calculations. The simulated spectra generated for anatase  $\text{TiO}_2$  and oxygen deficient  $\text{TiO}_2$  are shown in the inset of the figure 6.15. The theoretical spectra reproduce the experimental spectra satisfactorily for undoped  $\text{TiO}_2$  except the fact that peak C is not very weak. The intensities of peaks A and B are found to be less for the oxygen deficient case indicating the presence of oxygen vacancies in the doped systems. The above results are expected since the peaks A and B are due to the transition of O 1s

electron to hybridized Ti 3d-O 2p band and hence the reduction of the peak intensities are associated with the reduction of the transition probability from oxygen 1s orbital or in other words with the presence of oxygen vacancies in the samples.

### 6.3.2.8 XANES results at (Mn,Co) L<sub>3</sub>-edges:

The Mn L<sub>2,3</sub>-edge XANES spectra of Mn doped TiO<sub>2</sub> are shown in figure 6.17. The L<sub>3</sub> edge originates from the transition of Mn2p<sub>3/2</sub> → Mn 3d states and the L<sub>2</sub>-edge is due to Mn2p<sub>1/2</sub> → Mn3d. Since these transitions involve outer shells of Mn, the change in the oxidation state is more pronounced for L<sub>2,3</sub> edges than for Mn K-edge. The position and lineshape of peaks are changed when the charge state and crystal field on Mn changes. Comparing the spectra of the present samples with that reported by Thakur et al.<sup>192</sup> it is confirmed that Mn is present in +2 oxidation state for all the doping concentrations.

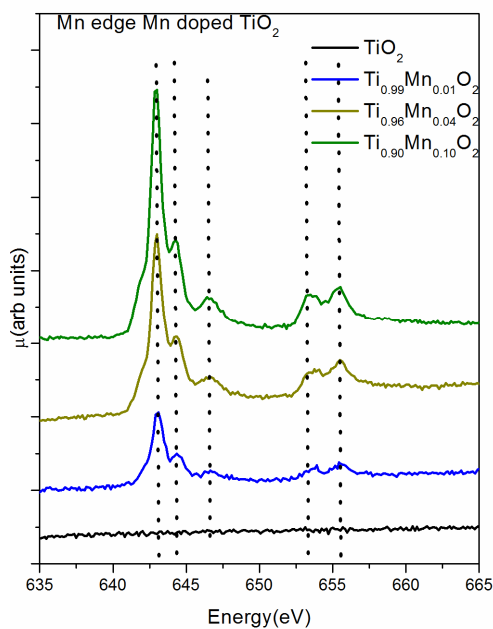


**Figure 6.17:** Soft X-ray absorption spectra of TiO<sub>2</sub> and Mn doped TiO<sub>2</sub> at Mn L<sub>2,3</sub> edge.

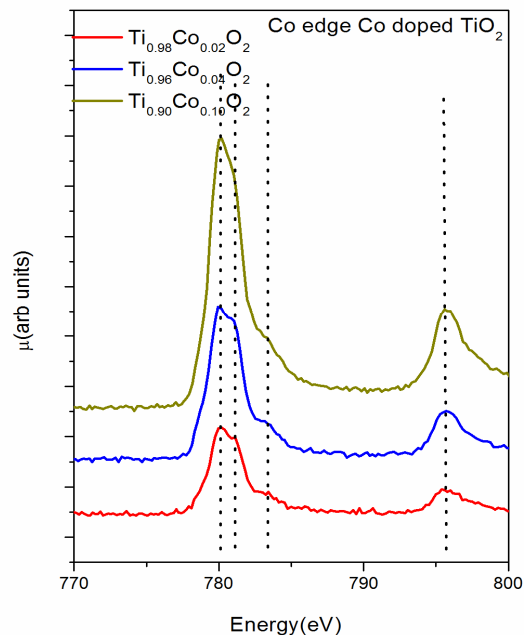


**Figure 6.18:** Soft X-ray absorption spectra of TiO<sub>2</sub> and Co doped TiO<sub>2</sub> at Co L<sub>2,3</sub> edge.

Figure 6.18 shows the Co L<sub>2,3</sub> X-ray absorption spectra for Co doped TiO<sub>2</sub> samples. The spectral features of L<sub>3</sub>-edge between 640-650 eV are quite similar to other reports.<sup>287, 288</sup> The spectra matches with that reported by Ohtsuki et al. suggesting that Co is present in +2 oxidation state in Co doped TiO<sub>2</sub> samples.

### 6.3.3 Magnetization studies on Mn and Co doped TiO<sub>2</sub> samples:

The magnetization verses applied magnetic field curve (M-H) measured at room temperature are shown in figure 6.19 for 1, 4 and 10% Mn doped TiO<sub>2</sub> thin films and figure 6.20 for 2%, 4% and 10% Co doped TiO<sub>2</sub> thin films after subtracting the contributions of the c-Si substrate. The undoped TiO<sub>2</sub> is diamagnetic in nature (not shown here). The saturation magnetization is found to increase here with an increase in the dopant concentration for Mn doped TiO<sub>2</sub>.

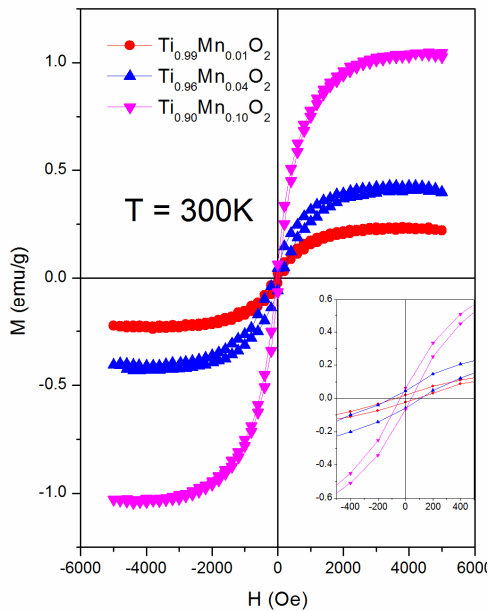


**Figure 6.19:** M Vs H plot for Mn doped TiO<sub>2</sub> at room temperature.

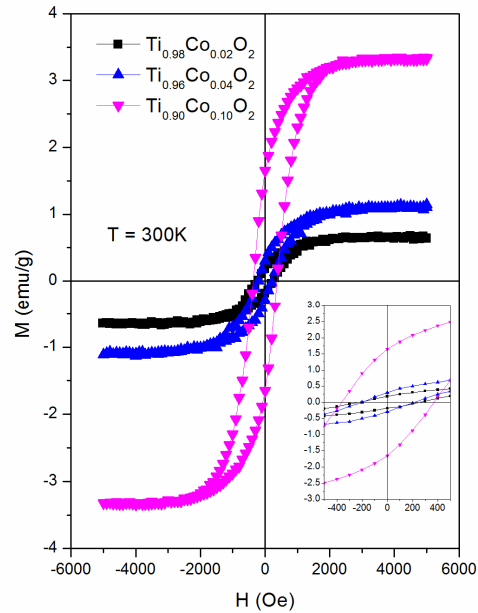


**Figure 6.20:** M Vs H plot for Co doped TiO<sub>2</sub> at room temperature.

RTFM shown by Patel et al. on Mn doped TiO<sub>2</sub> nanorods shows increasing saturation magnetization with dopant concentration.<sup>289</sup> However, Tian et al. shown that Mn doped TiO<sub>2</sub> exhibits RTFM up to 8% of Mn doping with coercive field of 60Oe and saturation magnetization of 0.026 emu/g<sup>268</sup> and similarly Wang et al. have observed that the magnetic moment per Mn increases initially with the Mn concentration in Mn doped TiO<sub>2</sub> films. It peaks at x=0.08 and decreases upon further increase of the Mn doping level<sup>132</sup> and this decrease in the saturation magnetization for higher doping concentration is explained due to reduced incorporation of Mn ions. Sharma et al. have shown that RTFM in Mn doped TiO<sub>2</sub> films for 10% and 15% doping concentration, however at lower doping concentration below 10% the films are diamagnetic in nature. The obtained coercivity was 85-140 Oe.<sup>131</sup> Since the extra phase i.e. MnTiO<sub>3</sub> observed from XRD and EXAFS measurements on these samples is antiferromagnetic in nature<sup>290</sup>, the observed ferromagnetism in the present samples is due to the presence of Mn ions at the Ti sites. However, due to the presence of MnTiO<sub>3</sub> phase in the samples, the saturation magnetisation of the samples does not increase in proportion to an increase in doping concentration of Mn in the samples. For example, from 1% Mn doped TiO<sub>2</sub> to 4% Mn doped TiO<sub>2</sub>, saturation magnetisation increases only by two times.

Similar to Mn doped TiO<sub>2</sub> case increase in the saturation magnetization with increase in the doping concentration of Co for Co doped TiO<sub>2</sub> is also observed (figure 6.20). In case of Co doped TiO<sub>2</sub> saturation magnetisation of 2%, 4% and 10% Co doped TiO<sub>2</sub> is 0.649 emu/gm, 1.10 emu/gm and 3.33 emu/gm, respectively. Thus though ~50% of CoTiO<sub>3</sub> phase is obtained in 10% Co doped TiO<sub>2</sub>, which is antiferromagnetic in nature with Neel temperature around 38 K<sup>123</sup>, unlike the Mn doped films discussed above, room temperature saturation magnetisation of Co doped ZnO films increases almost proportionally with increase in Co doping concentration. Similar increase in saturation magnetization with

increase in doping concentration is also reported by other researchers<sup>291-293</sup> for Co doped TiO<sub>2</sub> systems.

As has been discussed in detail in Chapter-1, the origin of ferromagnetism present in these systems have been attributed by different authors to different reasons from extrinsic reasons like presence of metallic clusters or completely separate secondary phase to intrinsic reasons like substitution of transition metal dopants at the host site, creation of defects in the form of oxygen vacancies or dopant interstitials. In case of the present samples presence of no secondary metallic or oxide ferromagnetic phase was observed in XRD as well as the metal K-edge XANES and EXAFS results other than CoTiO<sub>3</sub> and MnTiO<sub>3</sub> which are antiferromagnetic in nature.<sup>118, 123, 290</sup> Thus for present TM doped thin film TiO<sub>2</sub> samples, the source of ferromagnetism is intrinsic in nature and is most probably due to the interaction of Co<sup>2+</sup> and Mn<sup>2+</sup> ions mediated by oxygen vacancies. These oxygen vacancies are detected in the metal K-edge EXAFS as well as O K-edge XANES results presented above. These oxygen vacancies play crucial roles for origin of ferromagnetism as the electrons associated with these defects (oxygen vacancies) are responsible for exchange interaction between magnetic ions and form Bound Magnetic Polarons (BMP)<sup>35</sup>. As the doping concentration is increased, number of dopant ions are also increased in the samples besides the extra antiferromagnetic phase and more defects and hence BMP's are created to promote the ferromagnetic interaction leading to enhancement of ferromagnetic order in the samples.

# Chapter 7

## **SUMMARY, CONCLUSION AND FUTURE WORK**

### **7.1 Summary and conclusion:**

The present thesis delineates experimental results on three different Dilute Magnetic Semiconductor (DMS) thin film systems, transition metal (TM) doped ZnO thin films, TM doped ZnO/PVDF composite flexible polymer films and TM doped TiO<sub>2</sub> thin films. The samples have primarily been characterised by synchrotron radiation based X-ray absorption spectroscopy technique comprising of EXAFS and XANES measurements to probe detailed local structural information around dopant and host sites. GIXRD, FESEM and XPS techniques have also been used wherever is required to complement the above studies. The obtained structural information has finally been used to explain the origin of ferromagnetism in each system. The brief summary and conclusion for the individual chapters are given below.

#### **7.1.1 TM doped ZnO thin films:**

Chapter-3 elucidates experimental results on thin films of ZnO with different Mn doping concentrations which are deposited by rf. sputtering technique. GIXRD measurements show pure phase of the samples with preferential growth along [001] direction. XANES and EXAFS measurements have been performed at Zn, Mn and O K edges and Mn L<sub>2,3</sub> edges for detail local structure investigations at the host and dopant sites. XANES results at Mn site confirm the presence of Mn in +2 oxidation state while EXAFS results at Zn and Mn sites confirm that Mn substitutes Zn in ZnO lattice with indication of Mn clustering at relatively higher Mn doping concentration. Mn K edge XANES measurements show that oxygen vacancies in the sample increase with increase in Mn doping concentration which is also

supported by O K edge XANES measurements. Magnetic measurements show room temperature ferromagnetism in the samples at lower Mn doping concentration which is destroyed at higher Mn doping concentration of ~10% possibly due to Mn clustering. The results have been explained using the model that magnetisation in Mn doped ZnO is defined by two competitive processes viz., ferromagnetic ordering (FM) by oxygen vacancy mediated interaction between Mn ions and anti-ferromagnetic ordering (AFM) in Mn clusters and the above proposition has been corroborated by the findings of the EXAFS and XANES measurements.

Chapter-4 describes the experimental results of inclusion of three magnetic dopants i.e. Fe, Co and Ni in ZnO thin films. Fe doped ZnO thin films with varying Fe doping concentrations have been deposited with rf magnetron sputtering technique on c-Si substrates. GIXRD measurements show pure wurtzite structure of all the samples. XANES measurements show that Fe is present in the samples with mixed oxidation states of  $\text{Fe}^{2+}$  and  $\text{Fe}^{3+}$  and quantitative ratio of the two contributions have been obtained using linear combination fitting of the XANES spectra. GIXRD and XANES measurements also rule out the presence of any metallic phase or other Fe based impurity phase in the sample. EXAFS measurements at Zn and Fe K edges show that Zn atoms are being substituted by Fe dopants and Zn vacancies are created near to Fe substituting sites. EXAFS results support the presence of mixed oxidation states of  $\text{Fe}^{2+}$  and  $\text{Fe}^{3+}$  in the samples as observed also by XANES measurements. Oxygen K edge XANES results also support that Fe is going to Zn sites in the ZnO lattice. Magnetization measurement shows the room temperature ferromagnetic behaviour of the samples with increasing saturation magnetization as Fe doping concentration increases in the samples. Magnetic behaviour of the Fe doped ZnO thin film samples is thus found to be due to substitution of host Zn atoms by Fe dopants and

subsequent creation of Zn vacancies near Fe sites and not due to any extrinsic effect such as presence of Fe metallic cluster or Fe related secondary oxide phases in the samples.

GIXRD results show that Co doped ZnO thin films prepared by rf magnetron sputtering technique with varying Co doping concentration also have pure wurzite structure. The short range orders in the samples have been investigated with Zn, Co and Oxygen K edge X-ray absorption spectroscopy. The XANES and EXAFS results at Zn and Co K edge show that Co is going at Zn site in ZnO matrix and no other phase is present. The substitution of Co at Zn site is also confirmed with Oxygen K edge XANES and Co L<sub>2,3</sub> XANES spectra. The Zn and Co K-edge EXAFS data also do not conclusively show the criterion of oxygen vacancies in the samples due to Co doping. The obtained room temperature ferromagnetism in Co doped ZnO thin films is thus found to be intrinsic in nature due to interaction among the transition metal ions mediated by charge carriers.

RF magnetron sputtering technique has been used to prepare Ni doped ZnO thin films also with varying Ni doping concentration of upto 10 at.%. GIXRD results show wurzite structure of the samples throughout the whole Ni concentration range. XANES and EXAFS results at Zn and Ni K-edges show that Ni is substituting Zn in ZnO lattice and no other extra phase is present in the samples. Substitution of Zn by Ni is further confirmed by O K-edge XANES measurements. Presence of oxygen vacancies in the samples is confirmed experimentally by PL study and Ni K-edge EXAFS measurements of the samples and XANES simulations carried out assuming the presence of oxygen vacancies also help to explain the observed features in the experimental O and Ni K-edge XANES spectra. Weak ferromagnetism observed in the samples is thus believed to be originated from intrinsic origin of interaction between Ni ions with possible mediation by oxygen vacancies.

The above experimental results on TM doped ZnO thin films indicated room temperature ferromagnetism for all transition metal dopants of Mn, Fe, Co and Ni arises from

the intrinsic origin of interaction between the TM ions mediated by charge carriers or defects and not due to the presence of metallic clusters or any other impurity magnetic phase in the samples.

### **7.1.2 TM doped nanocrystalline-ZnO/PVDF composite thin films:**

Chapter-5 describes the experimental results on TM (Co and Ni) doped, (Co,Ni) co-doped and Mn doped free standing and flexible nano-ZnO/PVDF composite films. Preparation of these samples with proper TM doping has immense technological importance in production of DMS materials in a freestanding flexible form by a cost effective, scalable and reproducible process. In the present study, the films have been prepared by sol-gel technique and a field of 5 MV/m was applied across the films surfaces for 2 h for poling the composite films. The poling creates H terminated surface at one side of the films, while F-terminated surface at the other end.

In case of Ni doped ZnO/PVDF the poled and unpoled films (with Ni doping concentration of 1%, 4% and 9%) have been subjected to FESEM, XPS and XANES/EXAFS studies. FESEM micrographs showed highly oriented nanocrystals of ZnO embedded in free standing PVDF matrix in the poled samples. A strong peak of F1s at ~695 eV arising due to C-F bonds was observed in the XPS spectra recorded from the fluorine terminated surface of the poled samples. This peak was of very low intensity for the reversed surface (hydrogen terminated surface). XANES measurements show that Zn K edge positions of the samples agree well with that of ZnO bulk sample manifesting that Zn is present only in Zn<sup>2+</sup> state in the samples and which is also supported by core level XPS spectra of the samples. Difference in core level XPS peaks of Zn2p<sub>3/2</sub> and Zn2p<sub>1/2</sub> on fluorine-terminated and hydrogen terminated surfaces of the poled samples further suggests presence of highly aligned ZnO nanocrystallites in the poled PVDF matrix which would effectively modulate the piezoelectric behavior of the composite. Core level XPS peaks of Ni2p<sub>3/2</sub> and Ni2p<sub>1/2</sub> are

attributed to the existence of  $\text{Ni}^{2+}$  and  $\text{Ni}^{3+}$  species in the samples, though Ni K edge XANES studies indicate the presence of Ni in  $\text{Ni}^{2+}$  states for all the films studied here, the difference is attributed to the fact that XPS is surface sensitive while XANES gives the bulk information. EXAFS analysis recorded from Zn edge suggests that there is no significant change in the local structure surrounding Zn due to Ni doping since both ions are in +2 oxidation state and are being of similar size.

In case of Co doped ZnO/PVDF films (with Co doping concentration of 1%, 4% and 7%), FESEM studies show that doped samples do not show the fibrous structure of the pristine PVDF film and upon poling the Co-ZnO nanocrystallites get dispersed quite uniformly in the samples. Zn K edge XANES studies show that Zn is present in the samples in  $\text{Zn}^{+2}$  oxidation state though poled samples show the position of Zn K absorption edge at higher energies than that corresponding to  $\text{Zn}^{+2}$  state possibly due to increase in effective positive charge at Zn sites due to poling effect. Similar effect has also been observed in core level XPS spectra of Zn in the poled samples. The energy difference between  $\text{Co}2p_{3/2}$  and  $\text{Co}2p_{1/2}$  states obtained from the Co core level XPS measurements agrees well with that of  $\text{Co}2p$  spectrum of standard CoO sample. This is consistent with the assumption of divalent state cobalt homogeneously surrounded by the oxygen tetrahedral with negligible possibility of the presence of metallic Co phase in the samples. However, XANES measurements clearly show that though Co is primarily present as  $\text{Co}^{+2}$ , small amount of Co metallic phase can also be present in the samples. The FT-EXAFS spectra of the samples obtained from the Zn K-edge data and the Co K-edge data resemble each other and also the observation that there is no peak corresponding to the Co-Co distance of metallic Co in the Co K-edge spectra of the samples, confirm that Co atoms primarily substitute Zn atoms in the ZnO lattice and there is no significant presence of Co metallic clusters in the samples. Thus the study describes successful preparation of Co-doped free standing flexible ZnO/PVDF films up to 7% Co

doping. In case of Ni/Co co-doped ZnO/PVDF composite flexible and free-standing films, it was observed from EXAFS studies that Ni atoms apart from substituting Zn atoms in ZnO lattice in a tetrahedral coordination formed a separate NiO phase having octahedral oxygen coordination. Samples having lower Ni concentration had lesser probability of having NiO phase, while Ni-rich samples had higher fraction of NiO phase. XANES results are also in conformity with the above observation which show that Ni-rich samples had lower pre-edge peak, manifesting lower probability of tetrahedral coordination compared to Co-rich samples which had higher intensity of pre-edge peak.

In case of Mn doped ZnO/PVDF films (with Mn doping concentration of 1%, 3% and 5%), XANES measurements show that Zn K edge positions of the samples agree well with that of ZnO bulk sample which shows that Zn is present only in  $Zn^{2+}$  state in the samples, though Mn K edge XANES studies indicate the presence of Mn in 2+ states for all the films studied here. Zn K edge EXAFS analysis suggests that there is no significant change in the local structure surrounding Zn due to Mn doping since both ions are in +2 oxidation state and are of similar size. However, Mn edge EXAFS data suggest that the 1% Mn doped sample is more likely a composite of ZnO and Mn acetate tetrahydrate where proper Mn substitution at Zn sites has not been taken place, though 3% and 5% Mn doped samples show signature of proper Mn substitution at Zn sites in ZnO lattice.

In conclusion, free standing and flexible TM doped and co-doped nano-ZnO/PVDF composite films were prepared successfully by sol gel technique though it should be mentioned that these samples are relatively less clean DMS material compared to TM doped ZnO thin films prepared by rf sputtering technique, however much promising piezoelectric properties can be obtained from these systems<sup>294</sup>..

### 7.1.3 TM doped TiO<sub>2</sub> thin films:

Chapter-6 delineate the experimental results on Mn and Co doped TiO<sub>2</sub> thin films prepared by rf magnetron sputtering technique on c-Si substrates. GIXRD measurements show anatase phase for undoped TiO<sub>2</sub> and Mn doped TiO<sub>2</sub> films at lower Mn doping concentration and mixed anatase and rutile phases for Co doped TiO<sub>2</sub>. The above structural results have also been corroborated by EXAFS measurements at host (Ti) and dopant (Mn,Co) K-edges. EXAFS measurements at the dopant edges further indicate creation of oxygen vacancies in the samples due to TM doping, which is also confirmed by XANES measurements at O K-edge and by FEFF calculations. The oxidation states of the dopants in the host matrix have been confirmed by K and L-edge XANES measurements of dopant edges which rules out the presence of any other metal cluster or ferromagnetic oxide phases in the samples. Ferromagnetism observed in the doped samples has thus been attributed to the defect (oxygen vacancy) mediated interaction between the TM ions.

### 7.2 Future work:

The obtained room temperature ferromagnetism in TM doped ZnO and TiO<sub>2</sub> seems to be promising, however the magnetic moment obtained from such systems are comparatively low for device applications. To get further in-depth understanding of the ferromagnetism observed in these materials, the contribution of magnetic moment of the dopant transition metal ions in the magnetism of the samples should be found out. One such technique for studying magnetic property of individual elements in a material is X-ray Magnetic Circular Dichroism (XMCD), where X-ray absorption spectra of the sample are taken at the absorption edge of a particular element under positive and negative magnetic fields and using polarised synchrotron radiation, the difference of which allows to estimate the magnetic moment of that particular element in that material. There are few reports on XMCD of TM doped ZnO<sup>295-297</sup> and TiO<sub>2</sub><sup>298</sup>, however in depth understanding is still missing compared to

III-V DMS<sup>299, 300</sup>. Recently, a X-ray magnetic circular dichroism facility has been set up at the Energy Dispersive EXAFS beamline (BL-08) at Indus-2 SRS using a 2T electromagnet. The present studies will be extended by carrying out XMCD measurements of the samples at BL-08 at various TM absorption edges.

## References

1. G. E. Moore, *Electronics*, 1965, **38**.
2. Samsung Press Release, Samsung Starts Industry's First Mass Production of System-on-Chip with 10-Nanometer FinFET Technology, *Journal*, Oct 2016.
3. S. A. Wolf, D. D. Awschalom, R. A. Buhrman, J. M. Daughton, S. von Molnár, M. L. Roukes, A. Y. Chtchelkanova and D. M. Treger, *Science*, 2001, **294**, 1488-1495.
4. I. Žutić, J. Fabian and S. Das Sarma, *Reviews of Modern Physics*, 2004, **76**, 323-410.
5. S. A. Wolf, A. Y. Chtchelkanova and D. M. Treger, *IBM Journal of Research and Development*, 2006, **50**, 101-110.
6. M. N. Baibich, J. M. Broto, A. Fert, F. N. Van Dau, F. Petroff, P. Etienne, G. Creuzet, A. Friederich and J. Chazelas, *Physical Review Letters*, 1988, **61**, 2472-2475.
7. G. Binasch, P. Grünberg, F. Saurenbach and W. Zinn, *Physical Review B*, 1989, **39**, 4828-4830.
8. H. Ohno, *Science*, 1998, **281**, 951-956.
9. T. Dietl, H. Ohno, F. Matsukura, J. Cibert and D. Ferrand, *Science*, 2000, **287**, 1019-1022.
10. T. Dietl, *Nature Materials*, 2010, **9**, 965.
11. H. Ohno, A. Shen, F. Matsukura, A. Oiwa, A. Endo, S. Katsumoto and Y. Iye, *Applied Physics Letters*, 1996, **69**, 363-365.
12. Y. Matsumoto, M. Murakami, T. Shono, T. Hasegawa, T. Fukumura, M. Kawasaki, P. Ahmet, T. Chikyow, S.-y. Koshihara and H. Koinuma, *Science*, 2001, **291**, 854.
13. K. Sato and H. Katayama-Yoshida, *Physica E: Low-dimensional Systems and Nanostructures*, 2001, **10**, 251-255.
14. F. Pan, C. Song, X. J. Liu, Y. C. Yang and F. Zeng, *Materials Science and Engineering: R: Reports*, 2008, **62**, 1-35.
15. J. Rebecca, G. Priya and A. S. Nicola, *Journal of Physics: Condensed Matter*, 2005, **17**, R657.
16. M. Oestreich, *Nature*, 1999, **402**, 735.
17. H. Ohno, D. Chiba, F. Matsukura, T. Omiya, E. Abe, T. Dietl, Y. Ohno and K. Ohtani, *Nature*, 2000, **408**, 944.
18. M. Ciorga, A. Einwanger, U. Wurstbauer, D. Schuh, W. Wegscheider and D. Weiss, *Physical Review B*, 2009, **79**, 165321.
19. S. Ohya, I. Muneta and M. Tanaka, *Applied Physics Letters*, 2010, **96**, 052505.
20. K. Olejník, M. H. S. Owen, V. Novák, J. Mašek, A. C. Irvine, J. Wunderlich and T. Jungwirth, *Physical Review B*, 2008, **78**, 054403.
21. M. Wang, R. P. Campion, A. W. Rushforth, K. W. Edmonds, C. T. Foxon and B. L. Gallagher, *Applied Physics Letters*, 2008, **93**, 132103.
22. E. Abe, F. Matsukura, H. Yasuda, Y. Ohno and H. Ohno, *Physica E: Low-dimensional Systems and Nanostructures*, 2000, **7**, 981-985.
23. T. Wojtowicz, G. Cywiński, W. L. Lim, X. Liu, M. Dobrowolska, J. K. Furdyna, K. M. Yu, W. Walukiewicz, G. B. Kim, M. Cheon, X. Chen, S. M. Wang and H. Luo, *Applied Physics Letters*, 2003, **82**, 4310-4312.
24. T. Dietl, H. Ohno and F. Matsukura, *Physical Review B*, 2001, **63**, 195205.
25. T. Fukumura, Z. Jin, A. Ohtomo, H. Koinuma and M. Kawasaki, *Applied Physics Letters*, 1999, **75**, 3366-3368.
26. Ü. Özgür, Y. I. Alivov, C. Liu, A. Teke, M. A. Reshchikov, S. Doğan, V. Avrutin, S. J. Cho and H. Morkoç, *Journal of Applied Physics*, 2005, **98**, 041301.

27. A. Janotti and C. G. Van de Walle, *Physical Review B*, 2007, **76**, 165202.
28. L. Sang, Y. Zhao and C. Burda, *Chemical Reviews*, 2014, **114**, 9283-9318.
29. M. Naeem, S. K. Hasanain, M. Kobayashi, Y. Ishida, A. Fujimori, B. Scott and S. I. Shah, *Nanotechnology*, 2006, **17**, 2675.
30. G. Martínez-Criado, A. Segura, J. A. Sans, A. Homs, J. Pellicer-Porres and J. Susini, *Applied Physics Letters*, 2006, **89**, 061906.
31. R. Knut, J. M. Wikberg, K. Lashgari, V. A. Coleman, G. Westin, P. Svedlindh and O. Karis, *Physical Review B*, 2010, **82**, 094438.
32. J. Anderson and G. V. d. W. Chris, *Reports on Progress in Physics*, 2009, **72**, 126501.
33. E. H. Kisi and M. M. Elcombe, *Acta Crystallographica Section C*, 1989, **45**, 1867-1870.
34. K. J. Kim and Y. R. Park, *Applied Physics Letters*, 2002, **81**, 1420-1422.
35. J. M. D. Coey, M. Venkatesan and C. B. Fitzgerald, *Nature Materials*, 2005, **4**, 173.
36. Z. Yang, *Applied Physics A*, 2013, **112**, 241-254.
37. G. Giuli, A. Trapananti, F. Mueller, D. Bresser, F. d'Acapito and S. Passerini, *Inorganic Chemistry*, 2015, **54**, 9393-9400.
38. X. L. Wang, Z. X. Dai and Z. Zeng, *Journal of Physics: Condensed Matter*, 2008, **20**, 045214.
39. K. Gopinadhan, D. K. Pandya, S. C. Kashyap and S. Chaudhary, *Journal of Applied Physics*, 2006, **99**, 126106.
40. K. Gopinadhan, S. C. Kashyap, D. K. Pandya and S. Chaudhary, *Journal of Applied Physics*, 2007, **102**, 113513.
41. H. Zhang, T. Ji, L. Li, X. Qi, Y. Liu, J. Cai, H. Du and J. Sun, *Acta Physico-Chimica Sinica*, 2008, **24**, 607-611.
42. N. Akdogan, B. Z. Rameev, L. Dorosinsky, H. Sozeri, R. I. Khaibullin, B. Aktaş, L. R. Tagirov, A. Westphalen and H. Zabel, *Journal of Physics: Condensed Matter*, 2005, **17**, L359.
43. Z. Wang, J. Tang, H. Zhang, V. Golub, L. Spinu and L. D. Tung, *Journal of Applied Physics*, 2004, **95**, 7381-7383.
44. S. Sudesh, C. Sujeet and C. K. Subhash, *Journal of Physics D: Applied Physics*, 2010, **43**, 015007.
45. S. Sharma, S. Chaudhary and S. C. Kashyap, *Journal of Superconductivity and Novel Magnetism*, 2011, **24**, 839-843.
46. M. S. Ramachandra Rao, D. C. Kundaliya, S. B. Ogale, L. F. Fu, S. J. Welz, N. D. Browning, V. Zaitsev, B. Varughese, C. A. Cardoso, A. Curtin, S. Dhar, S. R. Shinde, T. Venkatesan, S. E. Lofland and S. A. Schwarz, *Applied Physics Letters*, 2006, **88**, 142505.
47. N. H. Hong, J. Sakai, W. Prellier, A. Hassini, A. Ruyter and F. Gervais, *Physical Review B*, 2004, **70**, 195204.
48. K. Ando, H. Saito, Z. Jin, T. Fukumura, M. Kawasaki, Y. Matsumoto and H. Koinuma, *Journal of Applied Physics*, 2001, **89**, 7284-7286.
49. K. Takamura, F. Matsukura, D. Chiba and H. Ohno, *Applied Physics Letters*, 2002, **81**, 2590-2592.
50. S. A. Chambers, *Today 34-39*, (April 2002).
51. F. Matsukura, Y. Ohno, H. Ohno, *JSAP Int.*, 2002, **5**.
52. J.-W. Yoo, C.-Y. Chen, H. W. Jang, C. W. Bark, V. N. Prigodin, C. B. Eom and A. J. Epstein, *Nature Materials*, 2010, **9**, 638.
53. Y. Ohno, D. K. Young, B. Beschoten, F. Matsukura, H. Ohno and D. D. Awschalom, *Nature*, 1999, **402**, 790.

54. R. Fiederling, M. Keim, G. Reuscher, W. Ossau, G. Schmidt, A. Waag and L. W. Molenkamp, *Nature*, 1999, **402**, 787.
55. S. Datta and B. Das, *Applied Physics Letters*, 1990, **56**, 665-667.
56. B. Huang, D. J. Monsma and I. Appelbaum, *Applied Physics Letters*, 2007, **91**, 072501.
57. M. Endo, D. Chiba, H. Shimotani, F. Matsukura, Y. Iwasa and H. Ohno, *Applied Physics Letters*, 2010, **96**, 022515.
58. S. J. Pearton, D. P. Norton, M. P. Ivill, A. F. Hebard, J. M. Zavada, W. M. Chen and I. A. Buyanova, *IEEE Transactions on Electron Devices*, 2007, **54**, 1040-1048.
59. T. Fukumura, Y. Yamada, H. Toyosaki, T. Hasegawa, H. Koinuma and M. Kawasaki, *Applied Surface Science*, 2004, **223**, 62-67.
60. K. Ueda, H. Tabata and T. Kawai, *Applied Physics Letters*, 2001, **79**, 988-990.
61. M. A. Ruderman and C. Kittel, *Physical Review*, 1954, **96**, 99-102.
62. K. Yosida, *Physical Review*, 1957, **106**, 893-898.
63. P. A. Cox, *Transition Metal Oxides*, Clarendon Press, Oxford, 1992.
64. M. v. Schilfhaarde and O. N. Mryasov, *Physical Review B*, 2001, **63**, 233205.
65. S. J. Pearton, W. H. Heo, M. Ivill, D. P. Norton and T. Steiner, *Semiconductor Science and Technology*, 2004, **19**, R59.
66. M. Diaconu, H. Schmidt, A. Pöpl, R. Böttcher, J. Hoentsch, A. Rahm, H. Hochmuth, M. Lorenz and M. Grundmann, *Superlattices and Microstructures*, 2005, **38**, 413-420.
67. Y. Belghazi, G. Schmerber, S. Colis, J. L. Rehspringer, A. Dinia and A. Berrada, *Applied Physics Letters*, 2006, **89**, 122504.
68. D. C. Kundaliya, S. B. Ogale, S. E. Lofland, S. Dhar, C. J. Metting, S. R. Shinde, Z. Ma, B. Varughese, K. V. Ramanujachary, L. Salamanca-Riba and T. Venkatesan, *Nature Materials*, 2004, **3**, 709.
69. X. Z. Li, J. Zhang and D. J. Sellmyer, *Solid State Communications*, 2007, **141**, 398-401.
70. D. Wang, Z. Q. Chen, D. D. Wang, J. Gong, C. Y. Cao, Z. Tang and L. R. Huang, *Journal of Magnetism and Magnetic Materials*, 2010, **322**, 3642-3647.
71. Y. M. Cho, W. K. Choo, H. Kim, D. Kim and Y. Ihm, *Applied Physics Letters*, 2002, **80**, 3358-3360.
72. H.-J. Lee, S.-Y. Jeong, C. R. Cho and C. H. Park, *Applied Physics Letters*, 2002, **81**, 4020-4022.
73. X. X. Wei, C. Song, K. W. Geng, F. Zeng, B. He and F. Pan, *Journal of Physics: Condensed Matter*, 2006, **18**, 7471.
74. S. Jiansirisomboon, K. Songsiri, A. Watcharapasorn and T. Tunkasiri, *Current Applied Physics*, 2006, **6**, 299-302.
75. H. Gleskova, I. C. Cheng, S. Wagner, J. C. Sturm and Z. Suo, *Solar Energy*, 2006, **80**, 687-693.
76. K. J. Loh and D. Chang, *Journal of Materials Science*, 2011, **46**, 228-237.
77. Y. Bai, Z. Y. Cheng, V. Bharti, H. S. Xu and Q. M. Zhang, *Applied Physics Letters*, 2000, **76**, 3804-3806.
78. C. Huang and Q. Zhang, *Advanced Functional Materials*, 2004, **14**, 501-506.
79. J. Y. Li, C. Huang and Q. Zhang, *Applied Physics Letters*, 2004, **84**, 3124-3126.
80. Z. M. Dang, Y. Shen and C. W. Nan, *Applied Physics Letters*, 2002, **81**, 4814-4816.
81. Z. M. Dang, Y. H. Lin and C. W. Nan, *Advanced Materials*, 2003, **15**, 1625-1629.
82. Y. Shen, C.-W. Nan and M. Li, *Chemical Physics Letters*, 2004, **396**, 420-423.
83. J. Sláma, R. Dosoudil, R. Vícen, A. Grusková, V. Olah, I. Hudec and E. Ušák, *Journal of Magnetism and Magnetic Materials*, 2003, **254-255**, 195-197.

84. R. Lebourgeois, S. Bérenguer, C. Ramiarinjaona and T. Waeckerlé, *Journal of Magnetism and Magnetic Materials*, 2003, **254-255**, 191-194.
85. J. H. Paterson, R. Devine and A. D. R. Phelps, *Journal of Magnetism and Magnetic Materials*, 1999, **196-197**, 394-396.
86. T. Tsutaoka, *Journal of Applied Physics*, 2003, **93**, 2789-2796.
87. V. F. Cardoso, G. Minas, C. M. Costa, C. J. Tavares and S. Lanceros-Mendez, *Smart Materials and Structures*, 2011, **20**, 087002.
88. V. Sencadas, R. Gregorio Filho and S. Lanceros-Mendez, *Journal of Non-Crystalline Solids*, 2006, **352**, 2226-2229.
89. A.J. Lovinger and D. C. Basset, *Developments in Crystalline Polymers*, Elsevier Applied Science, London, 1982.
90. H. S. Nalwa, *Ferroelectric Polymers: Chemistry, Physics, and Applications*, Dekker, New York, 1982.
91. W. Yan, Z. Sun, Q. Liu, Z. Li, Z. Pan, J. Wang, S. Wei, D. Wang, Y. Zhou and X. Zhang, *Applied Physics Letters*, 2007, **91**, 062113.
92. X. M. Cheng and C. L. Chien, *Journal of Applied Physics*, 2003, **93**, 7876-7878.
93. A. Tiwari, C. Jin, A. Kvit, D. Kumar, J. F. Muth and J. Narayan, *Solid State Communications*, 2002, **121**, 371-374.
94. S. S. Kim, J. H. Moon, B.-T. Lee, O. S. Song and J. H. Je, *Journal of Applied Physics*, 2003, **95**, 454-459.
95. A. Ali Fatima, S. Devadason and T. Mahalingam, *Journal of Materials Science: Materials in Electronics*, 2014, **25**, 3466-3472.
96. G. Vijayaprasath, R. Murugan, G. Ravi, T. Mahalingam and Y. Hayakawa, *Applied Surface Science*, 2014, **313**, 870-876.
97. V. R. Shinde, T. P. Gujar, C. D. Lokhande, R. S. Mane and S.-H. Han, *Materials Chemistry and Physics*, 2006, **96**, 326-330.
98. J. H. Park, M. G. Kim, H. M. Jang, S. Ryu and Y. M. Kim, *Applied Physics Letters*, 2004, **84**, 1338-1340.
99. J. H. Kim, H. Kim, D. Kim, Y. E. Ihm and W. K. Choo, *Journal of Applied Physics*, 2002, **92**, 6066-6071.
100. A. J. Behan, A. Mokhtari, H. J. Blythe, D. Score, X. H. Xu, J. R. Neal, A. M. Fox and G. A. Gehring, *Physical Review Letters*, 2008, **100**, 047206.
101. Z. L. Lu, H. S. Hsu, Y. H. Tzeng, F. M. Zhang, Y. W. Du and J. C. A. Huang, *Applied Physics Letters*, 2009, **95**, 102501.
102. M. H. Kane, K. Shalini, C. J. Summers, R. Varatharajan, J. Nause, C. R. Vestal, Z. J. Zhang and I. T. Ferguson, *Journal of Applied Physics*, 2004, **97**, 023906.
103. N. Jedrecy, H. J. von Bardeleben, Y. Zheng and J. L. Cantin, *Physical Review B*, 2004, **69**, 041308.
104. G. Lawes, A. S. Risbud, A. P. Ramirez and R. Seshadri, *Physical Review B*, 2005, **71**, 045201.
105. M. S. Moreno, T. Kasama, R. E. Dunin-Borkowski, D. Cooper, P. A. Midgley, L. B. Steren, S. Duhalde and M. F. Vignolo, *Journal of Physics D: Applied Physics*, 2006, **39**, 1739.
106. R. Podila, W. Queen, A. Nath, J. T. Arantes, A. L. Schoenhalz, A. Fazzio, G. M. Dalpian, J. He, S. J. Hwu, M. J. Skove and A. M. Rao, *Nano Letters*, 2010, **10**, 1383-1386.
107. J. Coey and S. Chambers, *MRS bulletin*, 2008, **33**, 1053-1058.
108. X. Han, G. Wang, J. Jie, X. Zhu and J. G. Hou, *Thin Solid Films*, 2005, **491**, 249-252.
109. C. N. R. Rao and F. L. Deepak, *Journal of Materials Chemistry*, 2005, **15**, 573-578.

110. S. Yang, R. Lv, C. Wang, Y. Liu and Z. Song, *Journal of Alloys and Compounds*, 2013, **579**, 628-632.
111. L. Li, Y. Guo, X. Y. Cui, R. Zheng, K. Ohtani, C. Kong, A. V. Ceguerra, M. P. Moody, J. D. Ye, H. H. Tan, C. Jagadish, H. Liu, C. Stampfl, H. Ohno, S. P. Ringer and F. Matsukura, *Physical Review B*, 2012, **85**, 174430.
112. X. Liu, F. Lin, L. Sun, W. Cheng, X. Ma and W. Shi, *Applied Physics Letters*, 2006, **88**, 062508.
113. T. Wakano, N. Fujimura, Y. Morinaga, N. Abe, A. Ashida and T. Ito, *Physica E: Low-dimensional Systems and Nanostructures*, 2001, **10**, 260-264.
114. X. J. Liu, X. Y. Zhu, C. Song, F. Zeng and F. Pan, *Journal of Physics D: Applied Physics*, 2009, **42**, 035004.
115. G. Srinet, R. Kumar and V. Sajal, *Journal of Applied Physics*, 2013, **114**, 033912.
116. Z. Yin, N. Chen, F. Yang, S. Song, C. Chai, J. Zhong, H. Qian and K. Ibrahim, *Solid State Communications*, 2005, **135**, 430-433.
117. M. Snure, D. Kumar and A. Tiwari, *Applied Physics Letters*, 2009, **94**, 012510.
118. I. Nakai, M. Sasano, K. Inui, T. Korekawa, H. Ishijima, H. Katoh, Y. J. Li and M. Kurisu, *Journal of the Korean Physical Society*, 2013, **63**, 532-537.
119. K. A. Griffin, A. B. Pakhomov, C. M. Wang, S. M. Heald and K. M. Krishnan, *Physical Review Letters*, 2005, **94**, 157204.
120. J. Y. Kim, J. H. Park, B. G. Park, H. J. Noh, S. J. Oh, J. S. Yang, D. H. Kim, S. D. Bu, T. W. Noh, H. J. Lin, H. H. Hsieh and C. T. Chen, *Physical Review Letters*, 2003, **90**, 017401.
121. W. Hu, K. Hayashi, T. Fukumura, K. Akagi, M. Tsukada, N. Hapoo, S. Hosokawa, K. Ohwada, M. Takahashi, M. Suzuki and M. Kawasaki, *Applied Physics Letters*, 2015, **106**, 222403.
122. S. A. Chambers, S. M. Heald and T. Droubay, *Physical Review B*, 2003, **67**, 100401.
123. B. Z. Jiang, T. L. Phan, D. S. Yang, K. W. Lee and S. C. Yu, *Solid State Communications*, 2010, **150**, 1932-1935.
124. M. Murakami, Y. Matsumoto, T. Hasegawa, P. Ahmet, K. Nakajima, T. Chikyow, H. Ofuchi, I. Nakai and H. Koinuma, *Journal of Applied Physics*, 2004, **95**, 5330-5333.
125. V. I. Anisimov, M. A. Korotin, I. A. Nekrasov, A. S. Mylnikova, A. V. Lukoyanov, J. L. Wang and Z. Zeng, *Journal of Physics: Condensed Matter*, 2006, **18**, 1695.
126. H. Wang, H. Wang, Q. He, X. Wang and J. Zhang, *Journal of the American Ceramic Society*, 2012, **95**, 2266-2271.
127. H. Wang, Q. He, H. Wang, X. Wang, J. Zhang, Y. Jiang and Q. Li, *Thin Solid Films*, 2011, **519**, 3312-3317.
128. K. Griffin Roberts, M. Varela, S. Rashkeev, S. T. Pantelides, S. J. Pennycook and K. M. Krishnan, *Physical Review B*, 2008, **78**, 014409.
129. W. T. Geng and K. S. Kim, *Physical Review B*, 2003, **68**, 125203.
130. J. P. Xu, J. F. Wang, Y. B. Lin, X. C. Liu, Z. L. Lu, Z. H. Lu, L. Y. Lv, F. M. Zhang and Y. W. Du, *Journal of Physics D: Applied Physics*, 2007, **40**, 4757.
131. S. Sharma, S. Chaudhary, S. C. Kashyap and S. K. Sharma, *Journal of Applied Physics*, 2011, **109**, 083905.
132. Z. Wang, J. Tang, Y. Chen, L. Spinu, W. Zhou and L. D. Tung, *Journal of Applied Physics*, 2004, **95**, 7384-7386.
133. K. J. Kim, Y. Ran Park, J. Han Lee, S.-L. Choi, H. Jung Lee, C. Sung Kim and J. Yun Park, *Journal of Magnetism and Magnetic Materials*, 2007, **316**, e215-e218.
134. L. M. Xu, Y. P. Yu, X. J. Xing, X. Y. Wu and S. W. Li, *Applied Physics A*, 2008, **92**, 361-365.

135. J. A. Wibowo, N. F. Djaja and R. Saleh, *Advances in Materials Physics and Chemistry*, 2013, **3**, 48.
136. M. H. N. Assadi, Y. B. Zhang, P. Photongkam and S. Li, *Journal of Applied Physics*, 2011, **109**, 013909.
137. H. Huang, Y. Ou, S. Xu, G. Fang, M. Li and X. Z. Zhao, *Applied Surface Science*, 2008, **254**, 2013-2016.
138. N. Tiwari, S. Kumar, A. K. Ghosh, S. Chatterjee, S. N. Jha and D. Bhattacharyya, *RSC Advances*, 2017, **7**, 56662-56675.
139. L. Properzi, A. Di Cicco, L. Nataf, F. Baudelet and T. Irifune, *Scientific Reports*, 2015, **5**, 10188.
140. N. C. Das, N. K. Sahoo, D. Bhattacharyya, S. Thakur, N. M. Kamble, D. Nanda, S. Hazra, J. K. Bal, J. F. Lee, Y. L. Tai and C. A. Hsieh, *Journal of Applied Physics*, 2010, **108**, 023515.
141. N. C. Das, N. K. Sahoo, D. Bhattacharyya, S. Thakur, D. Nanda, S. Hazra, J. K. Bal, J. F. Lee, Y. L. Tai and C. A. Hsieh, *Journal of Applied Physics*, 2011, **110**, 063527.
142. S. Maidul Haque, A. Biswas, D. Bhattacharya, R. B. Tokas, D. Bhattacharyya and N. K. Sahoo, *Journal of Applied Physics*, 2013, **114**, 103508.
143. K. Seshan, *Deposition Processes and Techniques*, Noyes Publications, Norwich, New York, U.S.A., 2002.
144. E. Alfonso, J. Olaya and G. Cubillos, in *Crystallization-Science and Technology*, InTech, 2012.
145. J. George, *Preparation of Thin Films*, Marcel Dekker, NY, 1992.
146. R. Bhunia, D. Ghosh, B. Ghosh, S. Hussain, R. Bhar and A. K. Pal, *Polymer International*, 2015, **64**, 924-934.
147. G. Nusinovich, R. Pu, O. Sinitsyn, A. Kesar, T. Antonsen Jr, Y. Dimant and V. Granatstein, *Development of sub-THz gyrotrons for detecting concealed radioactive materials*, 2010.
148. G. Bunker, *Introduction to XAFS A Practical Guide to X-ray Absorption Fine Structure Spectroscopy*, Cambridge University Press, New York, 2010.
149. D. C. Koningsberger, R. Prince, *X-Ray Absorption: Principles Applications Techniques of EXAFS SEXAFS and XANES*, Wiley, New York 1988.
150. Jeroen A. van Bokhoven and C. Lamberti, *X-Ray Absorption and X-Ray Emission Spectroscopy: Theory and Applications*, John Wiley & Sons, Ltd, West Sussex, 2016.
151. S. Calvin, *XAFS for Everyone*, CRC Press, New York, 2013.
152. M. R. Claudia S. Schnohr, *X-Ray Absorption Spectroscopy of Semiconductors*, Springer-Verlag Berlin Heidelberg, 2015.
153. H. Fricke, *Physical Review*, 1920, **16**, 202-215.
154. G. Hertz, *Zeitschrift für Physik*, 1920, **3**, 19-25.
155. D. E. Sayers, E. A. Stern and F. W. Lytle, *Physical Review Letters*, 1971, **27**, 1204-1207.
156. P. A. Lee and J. B. Pendry, *Physical Review B*, 1975, **11**, 2795-2811.
157. J. J. Rehr and R. C. Albers, *Physical Review B*, 1990, **41**, 8139-8149.
158. T. Fujikawa and N. Yiwata, *Surface Science*, 1996, **357-358**, 60-64.
159. A. L. Ankudinov, B. Ravel, J. J. Rehr and S. D. Conradson, *Physical Review B*, 1998, **58**, 7565-7576.
160. N. Binsted, *EXCURV98: CCLRC Daresbury Laboratory computer program*; <http://srs.dl.ac.uk/XRS/Computing/Programs/excurv97/intro.html>, 1998.
161. J. J. Rehr, J. J. Kas, F. D. Vila, M. P. Prange and K. Jorissen, *Physical Chemistry Chemical Physics*, 2010, **12**, 5503-5513.

162. A. Filipponi, A. Di Cicco and C. R. Natoli, *Physical Review B*, 1995, **52**, 15122-15134.
163. P. Blaha, K. Schwarz, G. Madsen, D. Kvasnicka, J. Luitz, *Wien2k An Augmented Plane Wave Plus Local Orbital Program for Calculating the Crystal Properties*, Vienna University of Technology, Austria, 2001.
164. W. Zhong, B. He, Z. Li and S. Wei, *Journal of China University of Science and Technology*, 2001, **31**, 328-333.
165. P. Willmott, *An Introduction to Synchrotron Radiation: Techniques and Applications*, John Wiley & Sons, Ltd, West Sussex, 2011.
166. Z. Sun, W. Yan, T. Yao, Q. Liu, Y. Xie and S. Wei, *Dalton Transactions*, 2013, **42**, 13779-13801.
167. S. Kelly, D. Hesterberg and B. Ravel, *Methods of soil analysis. Part*, 2008, **5**, 387-463.
168. P. Willmott, *An Introduction to Synchrotron Radiation*, John Wiley & Sons, Ltd, 2011, ch3, pp. 39-86.
169. <http://www.rrcat.gov.in/technology/accel/indus2.html>.
170. <http://www.rrcat.gov.in/technology/accel/srul/beamlines/index.html>.
171. S. Basu, C. Nayak, A. K. Yadav, A. Agrawal, A. K. Poswal, D. Bhattacharyya, S. N. Jha and N. K. Sahoo, *J. Phys.: Conf. Ser.*, 2014, **493**.
172. A. K. Poswal, A. Agrawal, A. K. Yadav, C. Nayak, S. Basu, S. R. Kane, C. K. Garg, D. Bhattacharyya, S. N. Jha and N. K. Sahoo, *AIP Conference Proceedings*, 2014, **1591**, 649-651.
173. [http://www.cat.ernet.in/technology/accel/srul/beamlines/mcd\\_pes.html](http://www.cat.ernet.in/technology/accel/srul/beamlines/mcd_pes.html).
174. B. Ravel and M. Newville, *Journal of Synchrotron Radiation*, 2005, **12**, 537-541.
175. M. Newville, *Journal of Synchrotron Radiation*, 2001, **8**, 322-324.
176. S. I. Zabinsky, J. J. Rehr, A. Ankudinov, R. C. Albers and M. J. Eller, *Physical Review B*, 1995, **52**, 2995-3009.
177. M. Newville, P. Livinš, Y. Yacoby, J. J. Rehr and E. A. Stern, *Physical Review B*, 1993, **47**, 14126-14131.
178. E. A. Stern, *Physical Review B*, 1993, **48**, 9825-9827.
179. P.R. Bevington, D. K. Robinson, *data reduction and error analysis for the physical science*, McGraw-Hill, New York, 2nd edn., 1992.
180. A. I. Frenkel, O. Kleifeld, S. R. Wasserman and I. Sagi, *The Journal of Chemical Physics*, 2002, **116**, 9449-9456.
181. Q. Wang, J. C. Hanson and A. I. Frenkel, *The Journal of Chemical Physics*, 2008, **129**, 234502.
182. J. Kas, *Toward Quantitative Calculation and Analysis of X-Ray Absorption Near Edge Spectra*, University of Washington, Seattle, WA, 2009.
183. M. Benfatto, P. D'Angelo, S. Della Longa and N. V. Pavel, *Physical Review B*, 2002, **65**, 174205.
184. Y. Joly, *Physical Review B*, 2001, **63**, 125120.
185. <http://www.rrcat.gov.in/technology/accel/srul/beamlines/edxrd.html>.
186. R. M. A. Azzam and N. M. Bashara, *Ellipsometry and Polarized Light*, North-Holland, Amsterdam, 1977.
187. H. Fujiwara, *Spectroscopic Ellipsometry: Principles and Applications*, John Wiley & Sons Ltd, West Sussex, 2003.
188. G. E. Jellison and F. A. Modine, *Applied Physics Letters*, 1996, **69**, 371-373.
189. M. H. Francombe, K. Vedam, J. L. Vossen, *Optical Characterization of real surfaces and films*, Academic, San Diego, 1994.

190. T. C. Droubay, D. J. Keavney, T. C. Kaspar, S. M. Heald, C. M. Wang, C. A. Johnson, K. M. Whitaker, D. R. Gamelin and S. A. Chambers, *Physical Review B*, 2009, **79**, 155203.
191. S. Basu, D. Y. Inamdar, S. Mahamuni, A. Chakrabarti, C. Kamal, G. R. Kumar, S. N. Jha and D. Bhattacharyya, *The Journal of Physical Chemistry C*, 2014, **118**, 9154-9164.
192. P. Thakur, K. H. Chae, J. Y. Kim, M. Subramanian, R. Jayavel and K. Asokan, *Applied Physics Letters*, 2007, **91**, 162503.
193. J. H. Guo, G. Amita, S. Parmanand, K. V. Rao, M. A. Marcus, C. L. Dong, J. M. O. Guillen, S. M. Butorin, M. Mattesini, P. A. Glans, K. E. Smith, C. L. Chang and R. Ahuja, *Journal of Physics: Condensed Matter*, 2007, **19**, 172202.
194. V. Vaithianathan, B.-T. Lee, C.-H. Chang, K. Asokan and S. S. Kim, *Applied Physics Letters*, 2006, **88**, 112103.
195. F. Bondino, K. B. Garg, E. Magnano, E. Carleschi, M. Heinonen, R. K. Singhal, S. K. Gaur and F. Parmigiani, *Journal of Physics: Condensed Matter*, 2008, **20**, 275205.
196. A. A. Guda, N. Smolentsev, J. Verbeeck, E. M. Kaidashev, Y. Zubavichus, A. N. Kravtsova, O. E. Polozhentsev and A. V. Soldatov, *Solid State Communications*, 2011, **151**, 1314-1317.
197. B. Zhang, M. Li, J. Z. Wang, L. Q. Shi and H. S. Cheng, *Materials Sciences and Applications*, 2013, **Vol.04No.05**, 5.
198. L.-T. Chang, C.-Y. Wang, J. Tang, T. Nie, W. Jiang, C.-P. Chu, S. Arafim, L. He, M. Afsal, L.-J. Chen and K. L. Wang, *Nano Letters*, 2014, **14**, 1823-1829.
199. J. J. Liu, M. H. Yu and W. L. Zhou, *Journal of Applied Physics*, 2006, **99**, 08M119.
200. L. Huilian, Y. Jinghai, Z. Yongjun, Y. Lili, W. Maobin and D. Xue, *Journal of Physics: Condensed Matter*, 2009, **21**, 145803.
201. S. Kumar, N. Tiwari, S. N. Jha, S. Chatterjee, D. Bhattacharyya, N. K. Sahoo and A. K. Ghosh, *RSC Advances*, 2015, **5**, 94658-94669.
202. T.-X. Chen, L. Cao, W. Zhang, Y.-Y. Han, Z.-Y. Zheng, F.-Q. Xu, K. Ibrahim, H.-J. Qian and J.-O. Wang, *Chinese Physics B*, 2013, **22**, 026101.
203. S. D. Yoon, Y. Chen, D. Heiman, A. Yang, N. Sun, C. Vittoria and V. G. Harris, *Journal of Applied Physics*, 2006, **99**, 08M109.
204. A. J. Chen, X. M. Wu, Z. D. Sha, L. J. Zhuge and Y. D. Meng, *Journal of Physics D: Applied Physics*, 2006, **39**, 4762.
205. A. Biswas, R. Sampathkumar, A. Kumar, D. Bhattacharyya, N. K. Sahoo, K. D. Lagoo, R. D. Veerapur, M. Padmanabhan, R. K. Puri, D. Bhattacharya, S. Singh and S. Basu, *Review of Scientific Instruments*, 2014, **85**, 123103.
206. Z. C. Chen, L. J. Zhuge, X. M. Wu and Y. D. Meng, *Thin Solid Films*, 2007, **515**, 5462-5465.
207. C. Wang, Z. Chen, Y. He, L. Li and D. Zhang, *Applied Surface Science*, 2009, **255**, 6881-6887.
208. G. Sanjeev, K. Shalendra, P. Thakur, K. H. Chae, K. Ravi, B. H. Koo and C. G. Lee, *Journal of Physics D: Applied Physics*, 2009, **42**, 175406.
209. R. D. Shannon, *Acta Crystallographica A* 1976, **32**.
210. T. Yamamoto, *X-Ray Spectrometry*, 2008, **37**, 572-584.
211. A. K. Yadav, S. M. Haque, D. Shukla, R. J. Choudhary, S. N. Jha and D. Bhattacharyya, *AIP Advances*, 2015, **5**, 117138.
212. S. Y. Seo, C. H. Kwak, S. H. Kim, B. H. Kim, C. I. Park, S. H. Park and S. W. Han, *Journal of Crystal Growth*, 2010, **312**, 2093-2097.
213. D. Y. Inamdar, A. K. Pathak, I. Dubenko, N. Ali and S. Mahamuni, *The Journal of Physical Chemistry C*, 2011, **115**, 23671-23676.

214. D. Karmakar, S. K. Mandal, R. M. Kadam, P. L. Paulose, A. K. Rajarajan, T. K. Nath, A. K. Das, I. Dasgupta and G. P. Das, *Physical Review B*, 2007, **75**, 144404.
215. W.-G. Zhang, B. Lu, L.-Q. Zhang, J.-G. Lu, M. Fang, K.-W. Wu, B.-H. Zhao and Z.-Z. Ye, *Thin Solid Films*, 2011, **519**, 6624-6628.
216. Q. Wang, Q. Sun, P. Jena and Y. Kawazoe, *Physical Review B*, 2009, **79**, 115407.
217. A. Debernardi and M. Fanciulli, *Applied Physics Letters*, 2007, **90**, 212510.
218. J. H. Guo, L. Vayssieres, C. Persson, R. Ahuja, B. Johansson and J. Nordgren, *Journal of Physics: Condensed Matter*, 2002, **14**, 6969.
219. S. Kumar, Y. J. Kim, B. H. Koo, S. K. Sharma, J. M. Vargas, M. Knobel, S. Gautam, K. H. Chae, D. K. Kim, Y. K. Kim and C. G. Lee, *Journal of Applied Physics*, 2009, **105**, 07C520.
220. J. W. Chiou, H. M. Tsai, C. W. Pao, K. P. Krishna Kumar, J. H. Chen, D. C. Ling, F. Z. Chien, W. F. Pong, M. H. Tsai, J. J. Wu, M. H. Yang, S. C. Liu, I. H. Hong, C. H. Chen, H. J. Lin and J. F. Lee, *Applied Physics Letters*, 2007, **90**, 062103.
221. S. Gautam, P. Thakur, K. H. Chae, G. S. Chang, M. Subramanain, R. Jayavel, K. Asokan, *Jou. Korean Phy. Soc.*, 2009, **55**.
222. H. Gu, W. Zhang, Y. Xu and M. Yan, *Applied Physics Letters*, 2012, **100**, 202401.
223. S. Kumar, S. Basu, B. Rana, A. Barman, S. Chatterjee, S. N. Jha, D. Bhattacharyya, N. K. Sahoo and A. K. Ghosh, *Journal of Materials Chemistry C*, 2014, **2**, 481-495.
224. S. Kumar, K. Asokan, R. K. Singh, S. Chatterjee, D. Kanjilal and A. K. Ghosh, *RSC Advances*, 2014, **4**, 62123-62131.
225. C. H. Patterson, *Physical Review B*, 2006, **74**, 144432.
226. S. Y. Seo, E. S. Jeong, C. H. Kwak, C. I. Park, J. Zhenlan, S. H. Kim and S. W. Han, *Journal of Physics: Condensed Matter*, 2013, **25**, 256005.
227. X.-C. Liu, E.-W. Shi, Z.-Z. Chen, B.-Y. Chen, W. Huang, L.-X. Song, K.-J. Zhou, M.-Q. Cui, Z. Xie, B. He and S.-Q. Wei, *Journal of Alloys and Compounds*, 2008, **463**, 435-439.
228. A. K. Yadav, S. M. Haque, S. Tripathi, D. Shukla, M. A. Ahmed, D. M. Phase, S. Bandyopadhyay, S. N. Jha and D. Bhattacharyya, *RSC Advances*, 2016, **6**, 74982-74990.
229. J. A. van Bokhoven and C. Lamberti, *X-Ray Absorption and X-ray Emission Spectroscopy: Theory and Applications*, John Wiley & Sons, Chichester (UK), 2016.
230. [http://ixs.iit.edu/subcommittee\\_reports/sc/err-rep.pdf](http://ixs.iit.edu/subcommittee_reports/sc/err-rep.pdf) A Report of the Standards and Criteria Committee, IXS Standards and Criteria Committee in July 26, 2000).
231. M. Lorenzo, G. Diego, B. Fabrizio, P. Carmelo, E. S. Kumar, F. Bellarmine, M. Ramanjaneyulu, L. Carlo and M. S. R. Rao, *Journal of Physics: Condensed Matter*, 2013, **25**, 385402.
232. S. C. Das, R. J. Green, J. Podder, T. Z. Regier, G. S. Chang and A. Moewes, *The Journal of Physical Chemistry C*, 2013, **117**, 12745-12753.
233. I. N. Demchenko, J. D. Denlinger, M. Chernyshova, K. M. Yu, D. T. Speaks, P. Olalde-Velasco, O. Hemmers, W. Walukiewicz, A. Derkachova and K. Lawniczak-Jablonska, *Physical Review B*, 2010, **82**, 075107.
234. S. Hüfner, J. Osterwalder, T. Riesterer and F. Hulliger, *Solid State Communications*, 1984, **52**, 793-796.
235. H. Zeng, G. Duan, Y. Li, S. Yang, X. Xu and W. Cai, *Advanced Functional Materials*, 2010, **20**, 561-572.
236. D. Das and P. Mondal, *RSC Advances*, 2014, **4**, 35735-35743.
237. Y. Liu, H. Liu, Z. Chen, N. Kadasala, C. Mao, Y. Wang, Y. Zhang, H. Liu, Y. Liu, J. Yang and Y. Yan, *Journal of Alloys and Compounds*, 2014, **604**, 281-285.

238. J. J. Lu, T. C. Lin, S. Y. Tsai, T. S. Mo and K. J. Gan, *Journal of Magnetism and Magnetic Materials*, 2011, **323**, 829-832.
239. O. Perales-Perez, A. Parra-Palomino, R. Singhal, P. M. Voyles, Y. Zhu, W. Jia and M. S. Tomar, *Nanotechnology*, 2007, **18**, 315606.
240. B. B. Li, X. Q. Xiu, R. Zhang, Z. K. Tao, L. Chen, Z. L. Xie, Y. D. Zheng and Z. Xie, *Materials Science in Semiconductor Processing*, 2006, **9**, 141-145.
241. A. K. Rana, Y. Kumar, P. Rajput, S. N. Jha, D. Bhattacharyya and P. M. Shirage, *ACS Applied Materials & Interfaces*, 2017, **9**, 7691-7700.
242. M. Deepak, P. Chinmay, B. Sohini, P. Arjun, D. Igor, A. Naushad, S. N. Jha, D. Bhattacharyya and M. Shailaja, *Journal of Physics D: Applied Physics*, 2014, **47**, 045308.
243. Y. Zuo, S. Ge, Z. Chen, L. Zhang, X. Zhou and S. Yan, *Journal of Alloys and Compounds*, 2009, **470**, 47-50.
244. H. Wang, Y. Chen, H. B. Wang, C. Zhang, F. J. Yang, J. X. Duan, C. P. Yang, Y. M. Xu, M. J. Zhou and Q. Li, *Applied Physics Letters*, 2007, **90**, 052505.
245. J. Mohapatra, D. K. Mishra, S. K. Kamilla, V. R. R. Medicherla, D. M. Phase, V. Berma and S. K. Singh, *physica status solidi (b)*, 2011, **248**, 1352-1359.
246. G. Venkataiah, M. R. S. Huang, H. L. Su, C. P. Liu and J. C. A. Huang, *The Journal of Physical Chemistry C*, 2010, **114**, 16191-16196.
247. B.-B. Li, X.-Q. Xiu, R. Zhang, Z.-K. Tao, L. Chen, Z.-L. Xie, Y.-D. Zheng and B. He, *Chinese Physics Letters*, 2006, **23**, 907.
248. A. Kuzmin and J. Chaboy, *IUCrJ*, 2014, **1**, 571-589.
249. N. N. Trofimova, Y. V. Zubavichus, O. I. Titova, E. A. Karpyuk, V. A. Ivanov, A. D. Pomogailo and Y. L. Slovokhotov, *Bulletin of the Russian Academy of Sciences: Physics*, 2013, **77**, 1127-1130.
250. R. Bhunia, A. K. Yadav, S. N. Jha, D. Bhattacharyya, S. Hussain, R. Bhar and A. K. Pal, *Polymer*, 2015, **78**, 1-12.
251. N. T. Mai, T. T. Thuy, D. M. Mott and S. Maenosono, *CrystEngComm*, 2013, **15**, 6606-6610.
252. R. W. Wagner CD, Davis LE, Moulder JF, Muilenberg GE *Handbook of X ray photoelectron spectroscopy*, Perkin Elmer, Eden Prairie, 1979.
253. G. H. Yu, L. R. Zeng, F. W. Zhu, C. L. Chai and W. Y. Lai, *Journal of Applied Physics*, 2001, **90**, 4039-4043.
254. Y. H. Jeong ES, Han SW, An SJ, Yoo J, Kim YJ, Yi GC, *J Korean Phys Soc*, 2008, **53**.
255. A.L. Roe, D.J.Schneider, RJ Mayer, JW Pyrz, LQ Jr *J Am Chem Soc*, 1984, **106**, 1676.
256. D. Joseph, S. Basu, S. N. Jha and D. Bhattacharyya, *Nuclear Instruments and Methods in Physics Research Section B: Beam Interactions with Materials and Atoms*, 2012, **274**, 126-128.
257. D. Joseph, A.K. Yadav, S.N. Jha and D. Bhattacharyya, *Bull. Mater. Sci.* , 2013, **36**.
258. N. L. Misra, A. K. Yadav, S. Dhara, S. K. Mishra, R. Phatak, A. K. Poswal, S. N. Jha, A. K. Sinha and D. Bhattacharyya, *Analytical Sciences*, 2013, **29**, 579-584.
259. X. Huang, G. Li, L. Duan, L. Li, X. Dou and L. Zhang, *Scripta Materialia*, 2009, **60**, 984-987.
260. J.F. Moulder, P.E. Sobol, K.D. Bomben, *Handbook of X-ray Photoelectron Spectroscopy, Physical Electronics*, Physical Electronics, Inc., USA, 1995.
261. R. Al-Gaashani, S. Radiman, A. R. Daud, N. Tabet and Y. Al-Douri, *Ceramics International*, 2013, **39**, 2283-2292.
262. K. R. Kittilstved, D. A. Schwartz, A. C. Tuan, S. M. Heald, S. A. Chambers and D. R. Gamelin, *Physical Review Letters*, 2006, **97**, 037203.

263. E.-S. Jeong, H.-J. Yu, Y.-J. Kim, G.-C. Yi, Y.-D. Choi and S.-W. Han, *Journal of nanoscience and nanotechnology*, 2010, **10**, 3562-3565.
264. Z. Wu, Y. Zhou, X. Zhang, S. Wei and D. Chen, *Applied Physics Letters*, 2004, **84**, 4442-4444.
265. P. Ballirano, C. Ruggero, *J. Appl. Cryst.*, 2001, **34**, 757-762.
266. Q. Ye, P. Y. Liu, Z. F. Tang and L. Zhai, *Vacuum*, 2007, **81**, 627-631.
267. N. Martin, C. Rousselot, D. Rondot, F. Palmino and R. Mercier, *Thin Solid Films*, 1997, **300**, 113-121.
268. Z. M. Tian, S. L. Yuan, Y. Q. Wang, J. H. He, S. Y. Yin, K. L. Liu, S. J. Yuan and L. Liu, *Journal of Physics D: Applied Physics*, 2008, **41**, 055006.
269. M. Sahoo, A. K. Yadav, S. N. Jha, D. Bhattacharyya, T. Mathews, N. K. Sahoo, S. Dash and A. K. Tyagi, *The Journal of Physical Chemistry C*, 2015, **119**, 17640-17647.
270. L. X. Chen, T. Rajh, Z. Wang and M. C. Thurnauer, *The Journal of Physical Chemistry B*, 1997, **101**, 10688-10697.
271. J. L. Gole, S. M. Prokes and O. J. Glembocki, *The Journal of Physical Chemistry C*, 2008, **112**, 1782-1788.
272. N. Khatun, Anita, P. Rajput, D. Bhattacharya, S. N. Jha, S. Biring and S. Sen, *Ceramics International*, 2017, **43**, 14128-14134.
273. S. Zhang, L. Zhang, H. Li, J. Li, Z. Jiang, W. Chu, Y. Huang, J. Wang and Z. Wu, *Journal of Synchrotron Radiation*, 2010, **17**, 600-605.
274. Q. R. Deng, X. H. Xia, M. L. Guo, Y. Gao and G. Shao, *Materials Letters*, 2011, **65**, 2051-2054.
275. D. H. Kim, J. S. Yang, K. W. Lee, S. D. Bu, D. W. Kim, T. W. Noh, S. J. Oh, Y. W. Kim, J. S. Chung, H. Tanaka, H. Y. Lee, T. Kawai, J. Y. Won, S. H. Park and J. C. Lee, *Journal of Applied Physics*, 2003, **93**, 6125-6132.
276. M. Newville, B. Ravel, D. Haskel, J. J. Rehr, E. A. Stern and Y. Yacoby, *Physica B: Condensed Matter*, 1995, **208-209**, 154-156.
277. W. H. Baur and A. A. Khan, *Acta Crystallographica B* 1971, **27**.
278. L. Zhang, L. Zhu, L. Hu, Y. Li, H. Song and Z. Ye, *RSC Advances*, 2016, **6**, 57403-57408.
279. T. E. de Souza, A. Mesquita, A. O. de Zevallos, F. Béron, K. R. Pirota, P. P. Neves, A. C. Doriguetto and H. B. de Carvalho, *The Journal of Physical Chemistry C*, 2013, **117**, 13252-13260.
280. Y. L. Soo, G. Kioseoglou, S. Kim, Y. H. Kao, P. S. Devi, J. Parise, R. J. Gambino and P. I. Gouma, *Applied Physics Letters*, 2002, **81**, 655-657.
281. S. J. Stewart, M. Fernández-García, C. Belver, B. S. Mun and F. G. Requejo, *The Journal of Physical Chemistry B*, 2006, **110**, 16482-16486.
282. F. M. F. de Groot, J. C. Fuggle, B. T. Thole and G. A. Sawatzky, *Physical Review B*, 1990, **41**, 928-937.
283. G. S. Henderson, X. Liu and M. E. Fleet, *Physics and Chemistry of Minerals*, 2002, **29**, 32-42.
284. J. P. Crocombette and F. Jollet, *Journal of Physics: Condensed Matter*, 1994, **6**, 10811.
285. J. G. Zhou, H. T. Fang, J. M. Maley, M. W. Murphy, J. Y. Peter Ko, J. N. Cutler, R. Sammynaiken, T. K. Sham, M. Liu and F. Li, *Journal of Materials Chemistry*, 2009, **19**, 6804-6809.
286. R. Ruus, A. Kikas, A. Saar, A. Ausmees, E. Nõmmiste, J. Aarik, A. Aidla, T. Uustare and I. Martinson, *Solid State Communications*, 1997, **104**, 199-203.

287. T. Ohtsuki, A. Chainani, R. Eguchi, M. Matsunami, Y. Takata, M. Taguchi, Y. Nishino, K. Tamasaku, M. Yabashi, T. Ishikawa, M. Oura, Y. Senba, H. Ohashi and S. Shin, *Physical Review Letters*, 2011, **106**, 047602.
288. K. Mamiya, T. Koide, A. Fujimori, H. Tokano, H. Manaka, A. Tanaka, H. Toyosaki, T. Fukumura and M. Kawasaki, *Applied Physics Letters*, 2006, **89**, 062506.
289. S. K. S. Patel, N. S. Gajbhiye and S. K. Date, *Journal of Alloys and Compounds*, 2011, **509**, S427-S430.
290. J. P. Xu, S. B. Shi, L. Li, J. F. Wang, L. Y. Lv, F. M. Zhang and Y. W. Du, *Journal of Physics and Chemistry of Solids*, 2009, **70**, 511-515.
291. J.-G. Li, R. Büchel, M. Isobe, T. Mori and T. Ishigaki, *The Journal of Physical Chemistry C*, 2009, **113**, 8009-8015.
292. W. K. Park, R. J. Ortega-Hertogs, J. S. Moodera, A. Punnoose and M. S. Seehra, *Journal of Applied Physics*, 2002, **91**, 8093-8095.
293. B. Santara, B. Pal and P. K. Giri, *Journal of Applied Physics*, 2011, **110**, 114322.
294. R. Bhunia, S. Das, S. Dalui, S. Hussain, R. Paul, R. Bhar and A. K. Pal, *Applied Physics A*, 2016, **122**, 637.
295. T. Thomas, G. Milan, S. Gisela, J. Gerhard, B. Sebastian and G. Eberhard, *New Journal of Physics*, 2008, **10**, 055009.
296. S. Abhinav Pratap, K. Ravi, P. Thakur, N. B. Brookes, K. H. Chae and W. K. Choi, *Journal of Physics: Condensed Matter*, 2009, **21**, 185005.
297. C. Guglieri, M. A. Laguna-Marco, M. A. García, N. Carmona, E. Céspedes, M. García-Hernández, A. Espinosa and J. Chaboy, *The Journal of Physical Chemistry C*, 2012, **116**, 6608-6614.
298. E. Sakai, K. Amemiya, A. Chikamatsu, Y. Hirose, T. Shimada and T. Hasegawa, *Journal of Magnetism and Magnetic Materials*, 2013, **333**, 130-133.
299. A. A. Freeman, K. W. Edmonds, N. R. S. Farley, S. V. Novikov, R. P. Champion, C. T. Foxon, B. L. Gallagher, E. Sarigiannidou and G. van der Laan, *Physical Review B*, 2007, **76**, 081201.
300. A. A. Freeman, K. W. Edmonds, G. van der Laan, R. P. Champion, A. W. Rushforth, N. R. S. Farley, T. K. Johal, C. T. Foxon, B. L. Gallagher, A. Rogalev and F. Wilhelm, *Physical Review B*, 2008, **77**, 073304.

# Appendix-A

## Tauc-Lorentz dispersion model

The measured spectroscopic ellipsometry data of thin film or bulk material are used to describe the sample based on a model of single or multiple layers of the given material. The layers are represented by wavelength dependent dielectric functions called dispersion relations that help to evaluate the material's optical properties by adjusting specific fit parameters. Following section deals with one such widely used dispersion formula known as Tauc-Lorentz dispersion [1] formula.

Jellison and Modine developed this model (1996) using the Tauc joint density of states and the Lorentz oscillator. The standard Lorentzian expression [2] of imaginary part of dielectric constant  $\epsilon_2 (= 2nk)$  for a single electronic transition is:

$$\epsilon_2(E) = 2nk = \frac{A_L E_0 C_L E}{(E^2 - E_0^2)^2 + C_L^2 E^2} \quad (\text{A.1})$$

where,  $E_0$  is the peak transition energy, while  $A_L$  and  $C_L$  determine the strength and broadening of the transition respectively.

The joint density of states for an amorphous material as suggested by Tauc[3] is given by:

$$\epsilon_2(E) = \frac{A_T (E - E_g)^2}{E^2} \quad (\text{A.2})$$

Assuming the amorphous material to be a collection of non-interacting atoms one obtains the following parametric expression for the imaginary part of the dielectric constant of the material ( $\epsilon_2$ ) by directly multiplying eqn. (A.1) with eqn. (A.2).

$$\begin{aligned}\epsilon_{2TL}(E) &= \frac{A_{TL}E_0C_L(E-E_g)^2}{\{(E^2-E_o^2)+C_L^2E^2\}E}, \quad E > E_g \\ &= 0 \quad E \leq E_g\end{aligned}\quad (A.3)$$

The expression for real part of dielectric constant can be obtained by Kramers-Kronig analysis as:

$$\begin{aligned}\epsilon_{1TL}(E) &= \epsilon_{1TL}(\infty) + \frac{1}{2} \frac{A_{TL}}{\pi} \frac{C_L}{\xi^4} \frac{a_{in}}{\alpha E_o} \ln \left[ \frac{(E_o^2 + E_g^2 + \alpha E_g)}{(E_o^2 + E_g^2 - \alpha E_g)} \right] - \frac{A_{TL}}{\pi \xi^4} \frac{a_{atan}}{E_o} \left[ \pi - a \tan \left( \frac{2E_g + \alpha}{C_L} \right) + \right. \\ &\quad \left. \tan^{-1} \left( \frac{-2E_g + \alpha}{C_L} \right) \right] \\ &\quad + 2 \frac{A_{TL}}{\pi \xi^4} \frac{E_o}{\alpha} \left\{ E_g (E^2 - \gamma_{TL}^2) \left[ \pi + 2 \tan^{-1} \left( 2 \frac{\gamma_{TL}^2 - E_g^2}{\alpha C_L} \right) \right] \right\} \\ &\quad - \frac{A_{TL}E_oC_L}{\pi \xi^4} \frac{E^2 + E_g^2}{E} \ln \left( \frac{|E - E_g|}{E + E_g} \right) + 2 \frac{A_{TL}E_oC_L}{\pi \xi^4} E_g \ln \left[ \frac{|E - E_g|(E + E_g)}{\sqrt{(E_o^2 - E_g^2)^2 + E_g^2 C_L^2}} \right]\end{aligned}\quad (A.4)$$

where,

$$a_{in} = (E_g^2 - E_o^2)E^2 + E_g^2 C_L^2 - E_o^2(E_o^2 + 3E_g^2)$$

$$a_{atan} = (E^2 - E_o^2)(E_o^2 + E_g^2) + E_g^2 C_L^2$$

$$\xi^4 = (E^2 - \gamma^2)^2 + \frac{\alpha^2 C_L^2}{4}$$

$$\alpha = \sqrt{4E_o^2 - C_L^2} / 2$$

$$\gamma_{TL} = \sqrt{E_o^2 - C_L^2} / 2$$

Thus in the TL model the dispersion of optical constants can be described by the five parameters  $A_{TL}, C_L, E_o, E_g$  and  $\epsilon_{1TL}(\infty)$ .

**References:**

1. G.E. Jellison Jr., F.A. Modine, Parameterization of the optical functions of amorphous materials in the interband region, *Appl. Phys. Lett.* 69 (1996) 371.
2. F. Wooten, *Optical Properties of Solids* (Academic, New York, 1972)
3. J. Tauc, R. Grigorovici, and A. Vanacu, *Phys. Status Solidi* 15, 627 (1966)

# Appendix-B

## Bruggeman Effective Medium Approximation

Since the thin film samples investigated under the scope of the thesis have been deposited by physical vapour deposition technique, most of the films are prone to have void in whole or in part of thin film layer structure. This has been accounted in ellipsometry modelling by assuming the thin film layer as an effective medium of mixture of bulk-like material and void. The refractive index of bulk like material is called intrinsic refractive index as opposed to the effective refractive index of the mixture of void and bulk material. Such effective medium model is applied under the assumption that the medium is microscopically inhomogeneous and macroscopically homogeneous i.e. each separate region (shown in below figure) in the medium is large enough to possess their own dielectric identities, but small compared to wavelength of light i.e.  $L_1, L_2, L_3 \ll \lambda$ .

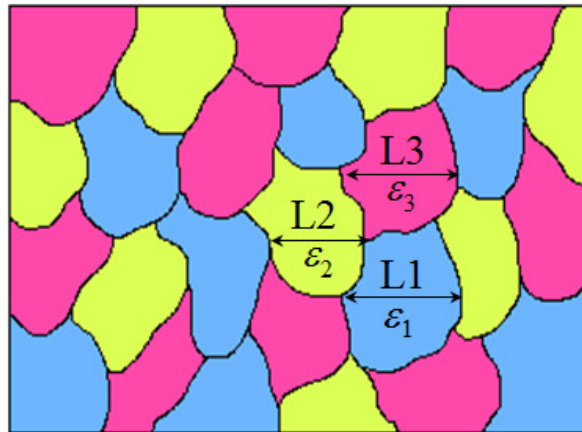


Fig. : Microscopically inhomogeneous medium to be treated under effective medium approximation (EMA).

Under this approximation, the constituent separate regions with different complex dielectric constants  $\epsilon_1, \epsilon_2, \epsilon_3, \dots$  are considered to be embedded in a host medium having complex dielectric constant of  $\epsilon_h$  and the effective complex dielectric function,  $\epsilon$  of the whole medium takes the general form given by-

$$\frac{\epsilon - \epsilon_h}{\epsilon + 2\epsilon_h} = V_1 \frac{\epsilon_1 - \epsilon_h}{\epsilon_1 + 2\epsilon_h} + V_2 \frac{\epsilon_2 - \epsilon_h}{\epsilon_2 + 2\epsilon_h} + \dots \quad (2.18)$$

$V_1, V_2, \dots$  represents the volume fraction of material having dielectric constants of  $\epsilon_1, \epsilon_2, \dots$ . There are various effective medium approximation (EMA) models and in different EMA model, the dielectric constant of host material is considered differently. For example, in Lorentz-Lorentz (LL) EMA model vacuum is considered as host material i.e.  $\epsilon_h$  is considered to be 1. In Maxwell Garnett (MG) EMA model any one of the inclusions is considered as host material. In Bruggeman EMA model the effective medium itself is considered as host material, i.e.  $\epsilon_h$  is considered to be same as  $\epsilon$ .